

# Computational studies for the characterization and design of dye sensitized solar cells (DSSCs) with improved efficiencies

THÈSE N° 6800 (2015)

PRÉSENTÉE LE 25 SEPTEMBRE 2015

À LA FACULTÉ DES SCIENCES DE BASE

LABORATOIRE DE CHIMIE ET BIOCHIMIE COMPUTATIONNELLES

PROGRAMME DOCTORAL EN CHIMIE ET GÉNIE CHIMIQUE

ÉCOLE POLYTECHNIQUE FÉDÉRALE DE LAUSANNE

POUR L'OBTENTION DU GRADE DE DOCTEUR ÈS SCIENCES

PAR

Negar ASHARI ASTANI

acceptée sur proposition du jury:

Prof. L. Emsley, président du jury  
Prof. U. Röthlisberger, directrice de thèse  
Prof. F. Buda, rapporteur  
Dr D. Varsano, rapporteur  
Prof. M. Graetzel, rapporteur



ÉCOLE POLYTECHNIQUE  
FÉDÉRALE DE LAUSANNE

Suisse  
2015



آفتاب آمد دلیل آفتاب  
گر دلیلت باید از وی رومتاب

Sun is itself a proof of sun,  
If you need a reason do not turn your back to it  
—Rumi

For maman Nasrin, baba Saeed, Ramtin and Hesamam ...



# Acknowledgements

Past four years of my PhD were among the sweetest years of my whole life. Doing a PhD next to the Lac Lemman and beautiful heights of Alps was an exceptional opportunity helping me to keep the balance between abstracts of science and beauty of life. The pleasure completed by presence of most special people around me helping me both emotionally and technically.

Getting accepted and working at LCBC was like a gift to me from the very beginning. I was following the updates of LCBC on their website when one day I saw my name there as "future PhD student". I can never explain the feeling I had at that moment. Working with Professor Ursula Röthlisberger, the pioneer of computational chemistry, was a dream come true. Yet I had no idea that her wonderful character will make it way better than my dreams.

Looking back, I know meeting Ursula was a turning point in my life. I was constantly amazed by her strong, sweet and thoughtful character. I tried to learn as much as possible from her and still I think I haven't learned enough.

She is one of the smartest people I know. Her wiseness together with her wide insight on different scientific subjects was the best guide all through my thesis. Despite having a large group, she manages to meet weekly with all the group members and personally I learned a lot from her during these weekly sessions and I appreciate that so much. Another thing about her that I admire a lot is her honest approach to science. Despite her sweet and kind character, she is absolutely strict when it comes to science. She reassesses the results over and over making sure that our contribution is absolutely accurate and practical. I really wish I have learned this one thing from her if not any other.

She let me follow subjects that I liked to work on and she was always there if I needed her support. She sent me to different conferences and helped me to expand my network via her connections. She was always advertising me (or better saying: overselling me) at her conferences and she was giving all the credits to us (her students).

All this made me become emotionally so attached to her that leaving her group and not seeing her is my biggest after-PhD nightmare. Only thing I can do is to wish her a long happy and healthy life so that many more students like me can benefit from her giving spirit.

When I was working on Grätzel solar cells in Iran for my master thesis I could never believe that one day I will be working in close contact with Prof. Michael Grätzel and his group. Four years of collaboration with the most prestigious group (LPI), I was lucky enough to experience working hand in hand with pioneers of science. Not only working with him, but I was so lucky that I had the chance to audit the course of statistical mechanics which was taught by Prof. Michael Grätzel himself. It was an exceptional experience to learn principles of solar cells

## Acknowledgements

---

directly from the inventor of one of most promising solar technologies.

His support for me lasted till the very end of my thesis and he kindly accepted to be in my thesis jury. Prof. Michael Grätzel and his wife Dr. Carole Grätzel were like family to me during my studies. I send my heartiest gratitudes to them and wish them happiness and health.

I also want to thank my two other jury members Prof. Fancesco Buda and Dr. Daniele Versano who kindly accepted to be in my jury and took the time to read my thesis. I also would like to thank Prof. Emsley who accepted to be the president of my defense session. I really appreciate their valuable comments and corrections.

I also would like to express my heartiest gratitudes to Prof. Michele Parrinello, Prof. Paolo Carloni, Prof. Maria Ramos and Prof Matteo Dal Peraro for coming with us to Iran. I also thank Dr. Reza Asgari for organizing the workshop.

During my private defense Dr. Daniele Versano mentioned that I should be thankful to my group for the fact that I could cover many different techniques in my thesis that would be impossible without my kind and generous colleagues. That's absolutely correct and here I would like to thank Dr. Simone Meloni, Dr. Basile Curchod, Dr. Elizabeth Brunk and Dr. Ivano Tavernelli for this very reason. When I first started at LCBC, Dr. Elizabeth Brunk or my friend Liz, who was a senior PhD student at the time, gave me the most precious advices without which I wouldn't survive. Although she was quite busy with her own thesis, she was nice enough to spend a lot of time sharing her knowledge and experience with me. Sharing the same office, I enjoyed a lot her company and our discussions every now and then on evolution, environment and politics were my favorite activities. Liz and her husband Christoph were among our best friends during our stay in Lausanne and we were so lucky for having them next to us.

Likewise, Dr. Basile Curchod who was a senior PhD student at the time, was a great help to me during the first two years of my PhD. He was the most passionate chemist I know. I had no quantum chemistry background and he patiently shared his knowledge with me. Later we collaborated on many different projects and I'm always very grateful for this fruitful collaborations.

Later close to the end of my PhD, Dr. Simone Meloni arrived in our lab and I was lucky to work with him on different projects. His pragmatic character helped us to have many projects done. I learned a lot from him. Both from his humble scientific character and his technical expertise in parallel computing and solid state physics. He was so humble that I dared expressing my ideas freely and after a while I became confident enough to have my own ideas. I wish I have learned this from him and I can give this confidence to undergraduates.

I'm also thankful to Dr. Ivano Tavernelli for his help, in particular his course on computational methods in quantum molecular mechanics, that I referred to it many times during my studies. In addition to my LCBC colleagues, I'm also so thankful to my LPI colleagues: Simon Mathew, Hauke Harms, Julien Frey, Lauren Polander, and Chenyi Yi. Having them next to us, I experienced the most fruitful collaborations between experiment and computation.

I'm also so thankful to Dr. Fransoic rötzingler from LPI. I benefited from our discussions and his valuable comments all through my PhD.

Four years of hard work wouldn't be possible if it wasn't because of the sweet environment

of our lab. Above all I want to thank Karin Pasche. In a way she takes care of all of us in the lab and the nice environment of LCBC is thanks to her presence. I would like to thank my lovely friend Siri for her lively and modest character, my sweet friend Elisa and her handsome Matteo, patient and peaceful Marta, beautiful and funny Giulia, our artist Esra, sweet-heart Ariadni, helpful Martin, kind Nick and patient Thibault. I very much enjoyed the company of my Greek office-mate Polydefkis for our discussions on politics, for him updating me with the latest football news so that I can show off in front of Hesam and of course for his sweet and supportive family. I'm also thankful to my Brazilian officemates Fernanda and Theresa. Though very short, but they made very memorable moments during their stay in Lausanne that I'll never forget. I should also thank my last officemate Matej, who is in my opinion the best officemate any one can have when writing the thesis. He was so quite that I would forget about his presence, yet his sudden funny comments was a chill-out every now and then.

During past four years, I mostly annoyed our system administratives: Matteo, Mathieu, Daniel, and Thibault. I would like to thank them all and apologize for my non-collaborative attitudes specially when I was under some kind of stress.

I also thank Anne-Lene Odegaard for her non-stop support during all these years. She's like an angel to the Ecole doctoral and I owe her a lot.

I would like to also acknowledge my Iranian friends in Lausanne, who have been absolutely supportive throughout these years and made life far away from home much less difficult: Nas-taran and Omid, Haleh and Mohsen, Marjan and Amin, Mitra, Arash and Delaram, Fatemeh and Behrooz, Maryam and Ramin, Maryam and Masih, Maryam, Ali, Melika and Rojin, Hamed and Shirin, Maryam, Ali and Kian, Sara and Alireza, Sara and Nasser, and Nasibeh and Sina, Elham Ghadiri, Roxana and Yoshi and Mahsa Silatani. I would like to also specially thank Shirin Saeedi and Seyed Hamed Hassani for their priceless helps with organizing the workshop on computational chemistry in Iran and our visit to Isfahan.

### **And Special thanks go to my family ...**

I don't even know how to start this part. I can never thank my family enough, specially in the few pages of this thesis. Everything I have achieved in my life was the easiest thing I could do at that time, since all the hard work was already taken care of by my parents Nasrin Jafary and Saeed Ashari. As far as I can remember, both my parents have been working so hard and the only thing I have done was to live like a princess. Although I might be a little bit spoiled, at least I know that I owe them a lot.

My problems were problems only before I shared them with my dad. He was the first person I would go to whenever I faced a problem. Sometimes I think how many times I shocked my dad with my troubles and how patiently he always comforted me. He would say: " That's it? That's what made my daughter cry?" It was always comforting to see how much he loves me and how little my problems become as soon as I tell my dad about them. He knew how weak I was yet he was the one believing in me. I remember we had regular math sessions on Tuesdays. My dad used to give me math problems to solve and he would sit next to me to work out the problem with me. I'm always his little girl and he is my only hero.

## Acknowledgements

---

My mum, my angel and my love, is the strongest woman I know. She was, is and will be my role model. I still remember how she stayed up every night to review my courses with me before my exams. Being a teacher she was always looking for the best schools and teachers for me. Although she was working outside the house, she never let us go to school without breakfast or lunch. I can't even think of doing what she did for me, for my future children. Above all she has always been my best friend. In her magic arms all my sorrows vanish. She is my patient listener and she is perhaps the only one who know the real me and yet she loves me!

I believe the most important thing I learned from my parents was their admirable love for each other which was always present at our house. My dad's single advice for me was to become like my mum and my mum's famous quote was that she was lucky to find my dad. I always admire them for this and I wish I have learned it from them. I also thank my brother Ramtin and his Mahta for their kind company and all the fun we have together when we go back to Iran. Ramtin, my little brother was my playmate as a kid and later he became my safe shoulder I can always lean on. I'm so happy that he could find a sweet-heart like Mahta.

I'm also so thankful to my other family, my in-laws!

Khale Nooshin and Amu Ahmad were happier than me when I was accepted for my PhD. They supported and encouraged me like they did for their own child. One small example of their sweetness was that they were always sending us prepared foods so that we don't waste time on cooking. I'm so thankful to both of them, because of their endless love. I also thank Ehsan and Shahrzad, for all the fun moments we have had together. In particular I thank Ehsan for always defending me in our childhood games.

Last but not least is my love, Hesam. I could never wish for a more supporting man (or better saying "Gaurdian angel"). This thesis exists only because he encouraged me to pursue a PhD and of course I would do anything to impress him. For me, every single page of this thesis is a reminder of dedications and sacrifices he made so that I worry about nothing but my studies (from helping in the housework and cooking, to helping me with maths, organizing the conference, emotional support and actual collaboration in my thesis<sup>1</sup>). I want to thank Hessam not only for his help and support (which of course are priceless) but for the very fact that he is **My Hessam**. As long as my studies is an excuse that brings me closer to him I'm ready to accept any challenge. As Leonard Cohen says: "I make my plans, like I always do, but when I look back, I was there for him".

I thank God for being so godly kind to me. I think I'm the luckiest girl for having all these angels around me. I wish I have learned from them and I can be helpful to someone one day.

*Lausanne, September 2015*

Negar Ashari Astani

---

<sup>1</sup>See chapter 6



# Abstract

During millions of years of evolution, all creatures have found their ways of harvesting, storing and utilizing the energy coming from the sun. Plants use photosynthesis to convert carbon dioxide to glucose. With a low efficiency of only 3%, plants still capture enough energy to grow their roots, fruits and leaves. Animals regulate their body temperature by basking in the sun or seeking a shadow when needed. Human beings are the only species that is not satisfied with this natural share. With the exponential population growth and a gross domestic product per capita that doubles every fifty years, finding a clean, secure, and sustainable source of energy is inevitable. Photovoltaic solar cells together with a proper energy storage technology, like water splitting and a fuel cell to burn the stored hydrogen, can form the promising green cycle that solves the energy problem.

Among different photovoltaic technologies, hybrid organic-inorganic solar cells, such as dye sensitized solar cells (DSSCs) or perovskite solar cells, are subject of active research due to their low-fabrication costs and easy production. In order to become commercially viable, these modules need to reach their theoretical Shockley-Queisser efficiency limit while acquiring enough durability and stability. In this context ab initio first-principles studies are of great help in order to give a fundamental insight of the chemistry and physics going on inside the cell. The main purpose of this dissertation is to make use of computational methods for a characterization of the fundamental processes in dye-sensitized and perovskite solar cells and the use of this knowledge for a rational design of solar cells with higher efficiencies.

Starting from a systematic investigation of bio-inspired porphyrin-based dyes focused on their light harvesting properties, we were able to outline some key guidelines for designing efficient dye sensitizers. The outcome of this study was an efficient light harvester, which when integrated in an optimized device achieved the record-breaking 13% efficiency porphyrin-based dye sensitized solar cell. While having good sensitizers is a necessary condition for a high performance DSSC, it is often not enough. It is essential to know the interactions of different components of a DSSC and how they work together. For this reason, we performed atomistic molecular dynamics simulations of a comprehensive model of a DSSC consisting of dye molecules, TiO<sub>2</sub> substrate, solvent and electrolyte.

In particular, in these simulations, we studied the accessibility of oxidized electrolyte to the TiO<sub>2</sub> substrate for different dye coverages and show that at medium to high coverage, peripheral alkyl groups of the dyes are highly efficient in shielding the TiO<sub>2</sub> substrate from direct contact with the oxidized electrolyte preventing recombination. In a next chapter, and as a proof of principles study, we investigated the importance of solvation effects on the

## Acknowledgements

---

stability of a carbocation (as a prototype for the cationic dye species after electron injection). The last two parts of this thesis focus on perovskite solar cells where we show the origins of the highly tunable band gap and propose a simple model in terms of orbital overlap that can be used to rationalize and predict variations of the band gap as a function of crystal structure and chemical composition of the perovskite. Finally, we study the efficient carrier transport properties of these materials and show that there is a direct correlation between the efficiency of carrier transport and the band gap.

**Keywords:** Dye sensitized solar cells (DSSCs), Perovskite, Photovoltaic, Density functional theory, Classical and Ab initio molecular dynamics simulations

# Résumé

Pendant des millions d'années d'évolution, toutes les créatures ont trouvé leurs façons de la récolte, le stockage et l'utilisation de l'énergie provenant du soleil. Les plantes utilisent la photosynthèse pour convertir le dioxyde de carbone en glucose. Avec une faible efficacité de seulement 3%, les plantes quand même captent d'énergie suffisant pour faire croître leurs racines, les fruits et les feuilles. Animaux réguler leur température corporelle en se prélassant au soleil ou à la recherche d'une ombre en cas de besoin. Les humains sont les seules espèces qui ne sont pas satisfaits de cette part naturelle. Avec la croissance exponentielle de la population et un produit intérieur brut par habitant qui double tous les cinq ans, de trouver une source d'énergie propre, sûre et durable est inévitable. Cellules solaires photovoltaïques avec une technologie de stockage d'énergie propre, comme le fractionnement de l'eau et une pile à combustible à brûler l'hydrogène stocké, peuvent former le cycle verte prometteuse qui résout le problème de l'énergie.

Parmi les différentes technologies photovoltaïques, cellules solaires hybrides organiques-inorganiques, comme les cellule solaire à colorant<sup>2</sup> ou de cellules solaires perovskites, sont objet de recherches actives en raison de leurs faibles coûts de fabrication et la production-facile. Afin de devenir commercialement viable, ces modules ont besoin d'atteindre leur limite théorique de l'efficacité Shockley-Queisser, tout en acquérant durabilité suffisant et de stabilité. Dans ce contexte la, ab initio principes-premiers des études sont d'une grande aide dans le but de donner un intuition fondamentale de la chimie et la physique passe à l'intérieur de la cellule. Le but principal de cette thèse est d'utiliser des méthodes de calcul pour une caractérisation des processus fondamentaux dans les cellule solaire à colorant et perovskite et l'utilisation de ces connaissances pour une conception rationnelle de cellules solaires avec des rendements plus élevés.

A partir d'une étude systématique des colorants bio-inspirés à base de porphyrine qui a été focalisé sur leurs propriétés de récolte de lumière, nous avons pu esquisser quelques directives essentiel pour la conception de "dye sensitizers" efficaces. Le résultat de cette étude était un collecteur lumière efficace, qui, lorsqu'il est intégré dans un appareil optimisé, a atteint l'efficacité record de 13% pour cellule solaire à colorant à base de porphyrine. Tout en ayant de bonnes sensibilisateurs est une condition nécessaire pour une DSSC de haute performance, il est souvent pas suffisant. Il est essentiel de connaître les interactions des différents composants d'un DSSC et comment ils travaillent tout ensemble. Pour cette raison, nous avons effectué des simulations de dynamique moléculaire atomistique d'un modèle

---

<sup>2</sup>Dye sensitized solar cells (DSSCs)

## Acknowledgements

---

global d'un DSSC constitué de molécules de colorant, substrat de  $\text{TiO}_2$ , solvant et l'électrolyte. En particulier, dans ces simulations, nous avons étudié l'accessibilité de l'électrolyte oxydé au substrat de  $\text{TiO}_2$  pour différentes couvertures de colorants et de montrer que, à moyen et à une couverture élevée, des groupes alkyle périphériques des colorants sont très efficaces dans la protection contre le substrat de  $\text{TiO}_2$  de contact direct avec le oxydé électrolyte, ce qui empêche la recombinaison. Dans un chapitre suivant nous avons étudié l'importance des effets de solvatation sur la stabilité d'un carbocation (comme un prototype pour l'espèce cationique de colorant après l'injection d'électrons).

Les deux dernières parties de cette thèse se concentrer sur les cellules solaires perovskite où nous montrons les origines de la "band-gap" très réglable et proposons un modèle simple en termes de chevauchement orbitale qui peuvent être utilisées pour rationaliser et de prédire les variations de la "band gap" en fonction de structure cristalline et la composition chimique de la perovskite. Enfin, nous étudions les propriétés de transport porteurs efficace de ces matériaux et de montrer qu'il existe une corrélation directe entre l'efficacité du transport porteurs et la "band gap".

Mots clefs : Cellules solaires à colorant (DSSCs), Perovskite, Photovoltaïque, Théorie de la fonctionnelle de la densité, Classique et ab initio simulations de dynamique moléculaire

# Contents

<b>Acknowledgements</b>	<b>i</b>
<b>Abstract (English/Français/Deutsch)</b>	<b>v</b>
<b>List of figures</b>	<b>xiii</b>
<b>List of tables</b>	<b>xxi</b>
<b>1 Introduction</b>	<b>1</b>
1.1 World energy consumption . . . . .	1
1.2 Shockley-Queisser limit . . . . .	3
1.3 Liquid-electrolyte DSSCs . . . . .	3
1.4 Solid-state DSSCs . . . . .	5
1.5 Chapters of this thesis . . . . .	7
<b>2 Theory and Methods</b>	<b>9</b>
2.1 The molecular Hamiltonian and the definition of the wave function . . . . .	9
2.1.1 Bloch function . . . . .	11
2.2 Density Functional Theory (DFT) . . . . .	12
2.2.1 Hohenberg-Kohn theorems . . . . .	13
2.2.2 Kohn-Sham Equations . . . . .	15
2.3 Time-Dependent Density Functional Theory (TDDFT) . . . . .	20
2.3.1 The Time-Dependent Kohn-Sham Equations . . . . .	20
2.3.2 Linear Response TDDFT . . . . .	21
2.3.3 TDDFT limitations and failures . . . . .	22
2.4 Electronic transport . . . . .	24
2.5 Ab initio and classical molecular dynamics simulations . . . . .	27
2.6 Mixed Quantum Mechanics/Molecular Mechanics (QM/MM) simulations . . . . .	28
2.7 Alchemical transformations . . . . .	29
<b>3 Computational characterization and design of porphyrin-based dye sensitizers: All the way up to 13% efficiency</b>	<b>31</b>
3.1 Introduction . . . . .	32
3.2 Methods . . . . .	33
3.2.1 Theoretical Concerns . . . . .	34

## Contents

---

3.3	Results and Discussion . . . . .	38
3.3.1	Systematic modifications of the donor, meso, central and acceptor moieties	38
3.3.2	Acceptor modifications . . . . .	39
3.3.3	Donor modifications . . . . .	41
3.3.4	Variations of the porphyrin moiety: modification of the substituent in meso position . . . . .	52
3.3.5	Changes of the central metal ion . . . . .	55
3.3.6	Combined dyes . . . . .	58
3.4	Conclusion . . . . .	63
<b>4</b>	<b>Atomistic Molecular Dynamics Simulation of a Porphyrin-Sensitized Solar Cell</b>	<b>65</b>
4.1	Introduction . . . . .	66
4.2	Methods and computational details . . . . .	67
4.2.1	Force field developement . . . . .	68
4.3	Results and discussion . . . . .	73
4.3.1	Validation of the dye force field . . . . .	73
4.3.2	System setup and analysis . . . . .	74
4.4	Conclusions . . . . .	77
<b>5</b>	<b>Making use of solvent effects to tune carbocation selectivity</b>	<b>83</b>
5.1	Introduction . . . . .	84
5.2	Results and discussions . . . . .	85
5.2.1	Stability differences between tert-butyl and sec-butyl isomers in gas phase and aqueous solution . . . . .	85
5.3	Tunning the relative stability of tert-butyl and sec-butyl cations via environment effects . . . . .	89
5.4	Systematic study of different solvents and quantification of free energy differences	91
5.5	Conclusion . . . . .	92
5.6	Methods . . . . .	93
<b>6</b>	<b>Valence and conduction band engineering in halide perovskites for solar cell applications</b>	<b>95</b>
6.1	Introduction . . . . .	96
6.2	Results . . . . .	97
6.3	Conclusions . . . . .	103
6.4	Methods . . . . .	103
6.4.1	Additional computational details . . . . .	104
6.4.2	Correlation between $q_B$ and $E_{CBM}$ . . . . .	106
6.4.3	Correlation between $q_B$ and $O_{TVB}$ . . . . .	106
6.4.4	Calculation of the variation of $E_{VBM}$ and $E_{CBM}$ with stoichiometry and crystal symmetry, and the dependence of $E_g$ on them . . . . .	108

<b>7 Computational study of carrier transport in halide perovskites via a semiclassical model of electron and hole dynamics</b>	<b>109</b>
7.1 Introduction . . . . .	110
7.2 Methods . . . . .	111
7.2.1 Brief discussion of $m^*$ calculation . . . . .	112
7.2.2 Effective mass calculation and significance of $\Delta k$ value for fitting . . . . .	113
7.2.3 GGA Vs. GGA+SOC for Cubic CsSnI <sub>3</sub> band diagrams with $C_{3v}$ symmetry . . . . .	114
7.3 Results and Discussion . . . . .	114
7.3.1 Lower gaps result in lower effective masses . . . . .	114
7.3.2 Effect of hydrogen bonding . . . . .	118
7.3.3 Effects of dopants and defects . . . . .	118
7.4 Conclusion . . . . .	122
<b>8 Conclusions and outlook</b>	<b>123</b>
<b>Appendices</b>	<b>137</b>
<b>A Tables for Chapter 4</b>	<b>139</b>
<b>B Band diagrams for Chapter 7</b>	<b>147</b>
B.1 Effect of doping . . . . .	148
<b>C Tight-binding formulation for simple cubic crystal of Na atoms (linear combination of s orbitals)</b>	<b>159</b>
<b>Curriculum Vitae</b>	<b>161</b>





# List of Figures

1.1	2015 latest chart of record cell efficiencies from the National Renewable Energy Laboratory (NREL) . . . . .	2
1.2	Schematic picture of a DSSC, porous TiO <sub>2</sub> layer composed of nanoparticles covered with dye molecules. . . . .	4
1.3	Schematic picture of different processes and their time scales in a DSSC. Picture taken from the thesis of Sophie Wenger <sup>1</sup> . . . . .	5
2.1	Jacob's ladder of DFT or today's taxonomy for xc functionals in DFT . . . . .	18
2.2	The total energy is a set of straight lines as a function of particle number, the red dashed-line shows how most functionals describe the energy. . . . .	19
2.3	Charge transfer in Donor-Acceptor molecules. . . . .	23
3.1	Orange box on the left: Electron-hole density map of the [S <sub>0</sub> → S <sub>1</sub> ] vertical transition for the reference dye: YD2-o-C8. The density difference contour plots ( $\rho_{S_1} - \rho_{S_0}$ ) show the electron distribution (blue) and the hole distribution (orange). Isovalue set to 0.0003. Blue box on the right: Frontier Kohn-Sham orbitals for YD2-o-C8 (isovalue is 0.02 a.u.) . . . . .	35
3.2	M06 able to capture slight shifts in the absorption spectrum (LD13 Vs. LD14). The experimental spectra (inset) is borrowed from Ref. <sup>2</sup> . . . . .	36
3.3	M06 is able to capture slight shifts in the absorption spectrum (YD2 Vs. YD2-o-C8). The experimental spectra (inset) from Ref. <sup>3</sup> . . . . .	37
3.4	General pattern of electron and hole localization on zinc-porphyrin-based dyes. Electron density is moving from the orange regions (holes-donors) to the blue (electrons-acceptor). X stands for meso positions, D for donor and A for the acceptor. . . . .	38
3.5	Different acceptor modifications of YD2-o-C8. . . . .	39
3.6	Calculated vertical Ionization energies (IE) (red) and negative of Electron affinities (EA) (blue) for acceptor-modified derivatives. . . . .	40
3.7	Calculated UV-visible absorption spectra for acceptor-modified derivatives. . . . .	40
3.8	Soret band electron and hole distribution in YD2-o-C8 and YD2-o-C8-2CN . . . . .	42
3.9	Electron-hole density map of the [S <sub>0</sub> → S <sub>1</sub> ] vertical transition for donor-modified derivatives. The density difference contour plots ( $\rho_{S_1} - \rho_{S_0}$ ) show the electron distribution in blue and the hole distribution in orange. Isovalue set to 0.0003 a.u. . . . .	43

## List of Figures

---

3.10 Frontier Kohn-Sham orbitals for donor modified derivatives (isovalue is 0.02 a.u.)	44
3.11 Electron-hole density map of the [S0 → S1] vertical transition for acceptor-modified derivatives. The density difference contour plots ( $\rho_{S1} - \rho_{S0}$ ) show the electron distribution (blue) and the hole distribution (orange). Isovalue set to 0.0003	45
3.12 Frontier Kohn-Sham orbitals for acceptor modified derivatives (isovalue=0.02 a.u.)	46
3.13 Different donor modifications on YD2-o-C8. The inset shows the general pattern of electron and hole distribution in Ullazine moiety.	47
3.14 Frontier Kohn-Sham orbitals for donor-modified derivatives (isovalue is 0.02 a.u.)	48
3.15 Calculated UV-visible absorption spectra for donor-modified derivatives.	49
3.16 Calculated vertical Ionization energies (IE) (red) and negative of Electron affinities (EA) (blue) for donor-modified derivatives.	49
3.17 Reduced steric hindrances in the bent structure (global minimum) versus the planar structure (local minimum): Also the dihedral angle is decreasing giving rise to a stronger electron push and consequently a red-shifted spectrum	50
3.18 Different meso position modifications of YD2-o-C8.	50
3.19 Calculated UV-visible absorption spectra for modifications applied to the meso position.	51
3.20 Dihedral angle formed between the aromatic meso substituents and the porphyrin base.	51
3.21 Electron-hole density map of the [S0 → S1] vertical transition for meso-modified derivatives. The density difference contour plots ( $\rho_{S1} - \rho_{S0}$ ) show the electron distribution in blue and the hole distribution in orange. Isovalue set to 0.0003 a.u.	52
3.22 Frontier Kohn-Sham orbitals for meso modified derivatives (isovalue is 0.02 a.u.)	53
3.23 Calculated vertical Ionization energies (IE) (red) and negative of Electron affinities (EA) (blue) for meso-modified derivatives.	54
3.24 Meta (blue) and Ortho (green) position of the the alkoxy group.	54
3.25 Calculated vertical Ionization energies (IE) (red) and Electron affinities (EA) (blue) for metal porphyrin derivatives.	56
3.26 Calculated UV-visible absorption spectra for different metal porphyrin derivatives.	56
3.27 Frontier Kohn-Sham orbitals for metal porphyrin derivatives (isovalue is 0.02 a.u.). HOMO and LUMO for Co and Cu-based porphyrins are just shown for consistency, otherwise the first optically allowed excitation of these two dyes are not HOMO/LUMO transitions.	57
3.28 Electron-hole density map of the [S0 → S1] vertical transition for Sn and Pb-centered porphyrin dyes, [S0 → S6] vertical transition of Cu-based porphyrin and [S0 → S11] vertical transition of Co-based compound. The density difference contour plots ( $\rho_{S^*} - \rho_{S0}$ ) show the electron distribution in blue and the hole distribution in orange. S* stand for the corresponding excited state for each compound. Isovalue set to 0.0003 a.u.	58

3.29	Some combinations of different donor, acceptor, metal, and meso position moieties. . . . .	59
3.30	Frontier Kohn-Sham orbitals for the combined dyes (isovalue is 0.02 a.u.) . . .	60
3.31	Electron-hole density map of the [S0 → S1] vertical transition for the combined dyes. The density difference contour plots ( $\rho_{S1} - \rho_{S0}$ ) show the electron distribution in blue and the hole distribution in orange. Isovalue set to 0.0003 a.u. . . . .	61
3.32	Calculated vertical Ionization energies (IE) (red) and negative of Electron affinities (EA) (blue) for the combined dyes. . . . .	62
3.33	Calculated UV-visible absorption spectra for modifications applied on the combined dyes. . . . .	62
4.1	Chemical structure of YD2-o-C8. . . . .	69
4.2	Fitted point charges for YD2-o-C8 and $\text{Co}(\text{bpy})_3^{3+}$ . . . . .	70
4.3	Atom types assigned according to AMBER convention. . . . .	70
4.4	Energy barriers for rotation around dihedrals 1,2,3 and 4 calculated from rigid scans of each dihedral separately at DFT/(M06) level of theory. . . . .	71
4.5	Fitting of the dihedral potential for rotation around the alkyne linker using two additional off-center interaction sites ("DU"). Without this torsional potentials, the vdW forces favor a perpendicular arrangement between the linker and the porphyrin base and/or the benzylic acid moiety. . . . .	72
4.6	Comparison of the thermal distributions for selected dihedral angles (deg) obtained from 200 ps of the MM simulation (green) and 5 ps of QM (red) simulations. 74	
4.7	Binding sites 1 (green) and 2 (orange). The dotted oval indicates the approximate area occupied by each dye. Non-dissociative molecular binding modes a and b with the proton pointing down and up, respectively. Dissociative binding mode c. 76	
4.8	Distribution of $\text{Co}(\text{bpy})_3^{3+}$ electrolytes. The ice blue colors show the density map of $\text{Co}(\text{bpy})_3^{3+}$ in 5 Å vicinity of dye molecules. . . . .	77
4.9	Occupation density map of peripheral alkyl chains around the dye molecules at high coverage density. The map is done by replacing each atom with a normalized Gaussian distribution of width (standard deviation) equal to the atomic radius. The Gaussian distribution for each atom is then weighted with the occupancy. The various Gaussians are added and distributed on a grid and represented in a contour plot. The ice blue ares correspond to an isosurface value of 0.01. . . . .	78
4.10	Occupation density map of peripheral alkyl chains around the dye molecules at normal coverage density. The map is done by replacing each atom with a normalized Gaussian distribution of width (standard deviation) equal to the atomic radius. The Gaussian distribution for each atom is then weighted with the occupancy. The various Gaussians are added and distributed on a grid and represented in a contour plot. The ice blue ares correspond to an isosurface value of 0.01. . . . .	79

## List of Figures

---

4.11	Occupation density map of peripheral alkyl chains around the dye molecules at low coverage density. The map is done by replacing each atom with a normalized Gaussian distribution of width (standard deviation) equal to the atomic radius. The Gaussian distribution for each atom is then weighted with the occupancy. The various Gaussians are added and distributed on a grid and represented in a contour plot. The ice blue areas correspond to an isosurface value of 0.01. . . .	80
4.12	Probability density profile for acetonitrile (top) and electrolyte (bottom) along the Z axis. . . . .	81
5.1	Relative energetics in the gas phase. The values shown are calculated at MP2/cc-pVDZ level of theory) between the various isomers of 2-butyl and tert-butyl. Displayed are regioisomers tert-butyl and sec-butyl. Shown in blue are various conformations of sec-butyl, including methyl-bridged (2a), hydrogen-bridged cis (1b), open-chain trans (2c), hydrogen-bridged trans (2d) and open-chain cis (2e). The most stable conformation of tert-butyl is the $C_s$ (1b) roughly 1 kcalmol <sup>-1</sup> lower than the $C_{3v}$ conformer (1a)) . . . . .	86
5.2	Conversion of different isomers during the course of the simulation . . . . .	87
5.3	The structuring of solvent molecules around tert-butyl and sec-butyl (2-butyl) is depicted by a contour density mapping. The high presence of solvent molecules is demonstrated by the darkened regions, which represent the most frequently occupied positions in the 4.5 Å vicinity around the solute during the 200 ps QM/MM simulation. . . . .	87
5.4	Radial distribution function of water molecules around tert-butyl and sec-butyl in QM/MM and MM simulations. . . . .	88
5.5	Thermodynamic cycle used for calculating the relative solvation free energies in different solvents . . . . .	89
5.6	Electrostatics versus vanderWaals contributions to the solvation free energy of perturbing tert-butyl to 2-butyl in different solvents. . . . .	91
5.7	Relative solvation free energy difference correlation with dipole/volume ratio. Two distinct domains are recognized within which the linear correlation holds. Aqua region shows the fluorinated solvents that satisfy the linear correlation in a separate domain probably due to their special solvation cages. . . . .	92

- 6.1 Configurations of the equilibrium structure of several perovskites. Images are ordered in such a way that the corresponding structures can be thought of as a series of structural or alchemical alterations starting from the CsPbI<sub>3</sub> cubic structure (A), with a lattice parameter  $a = 6.38\text{\AA}$  as a reference. In panels B and C the tetragonal and orthorhombic structures of CsPbI<sub>3</sub> are shown, respectively. They can be obtained from the cubic analogue by tilting the PbI<sub>6</sub> octahedra along their axis parallel to the tetragonal axis (tetragonal structure) or along all of their three axes (orthorhombic). Tetragonal CsSnI<sub>3</sub> is characterized by a tilting angle  $\theta_1 = 14.3^\circ$  and a pseudocubic lattice parameter  $a^* = \sqrt[3]{V} = 6.12\text{\AA}$  (where  $V$  is the volume of the unit cell). In the orthorhombic CsSnI<sub>3</sub>,  $\theta_1 \sim \theta_2 \sim \theta_3 = 8.5^\circ$  and  $a^* = 6.30\text{\AA}$ . (D) is obtained from the cubic CsPbI<sub>3</sub> by replacing Pb with Sn and I with Cl ( $\theta_1 = \theta_2 = \theta_3 = 0^\circ$  and  $a = 5.85\text{\AA}$ ). E, F and G are obtained from the cubic, tetragonal and orthorhombic CsPbI<sub>3</sub>, respectively, by replacing Cs with Li. Their tilting angle and pseudocubic lattice parameters are: E)  $a = 6.32\text{\AA}$ ; F)  $\theta_1 = 20.3^\circ$ ,  $a = 6.12\text{\AA}$ ; G)  $\theta_1 = 20.5^\circ$ ,  $\theta_2 = 18.8^\circ$ ,  $\theta_3 = 10.8^\circ$ ,  $a = 5.81\text{\AA}$ . (H) and (I) are obtained by replacing Cs<sup>+</sup> in the cubic CsPbI<sub>3</sub> with NH<sub>4</sub><sup>+</sup> and PH<sub>4</sub><sup>+</sup>, respectively. While PH<sub>4</sub>PbI<sub>3</sub> preserves the original cubic symmetry ( $a = 6.32\text{\AA}$ ), NH<sub>4</sub>PbI<sub>3</sub> is triclinic ( $\alpha = \beta = 85.8^\circ$ ,  $\gamma = 87.1^\circ$ ,  $a = 6.38\text{\AA}$ ) and the PbI<sub>6</sub> octahedra are highly distorted . . . . . 98
- 6.2 VBM (blue frame) and CBM (red frame) orbitals of selected systems. Panels (A), (B) and (C) shows how the tilting of BX<sub>6</sub> octahedra affects the overlap: in the cubic structure (A) X mp orbitals are aligned with B-X bonds and the absolute value of the negative overlap is maximal ( $O_{\text{VBM}} = -0.21$ ). In tetragonal (B) and orthorhombic (C) structures p orbitals are no longer well aligned, and the overlap diminishes (tetragonal  $O_{\text{VBM}} = -0.17$ , and  $\Delta E_{\text{VBM}} = -0.29$  eV is the energy variation with respect to the cubic case; orthorhombic  $O_{\text{VBM}} = -0.11$ ,  $\Delta E_{\text{VBM}} = -0.54$  eV). In the case of orthorhombic structures, the tilting along all the three axes of the octahedra further reduces the overlap, as shown from the lateral view of the crystal shown in the inset of panel (C). (D) Monovalent cations forming hydrogen bonds (green dashed lines) distort the framework reducing the overlap in analogy to the variations induced by tilting. In addition, hydrogen bonds polarize the VBM orbitals, resulting in an increase of electronic density on hydrogen bonded halide ions (red arrow), and a complementary reduction on the others halides (green arrow) and on bivalent cations. (E) and (F) CBM orbital in tetragonal CsPbI<sub>3</sub> and CsPbCl<sub>3</sub>. The effect of halide substitution along the series I<sup>-</sup>, Br<sup>-</sup>, Cl<sup>-</sup> is moving the CBM electronic charge from B to X. For example,  $q_{\text{B}} = 0.81$  and  $E_{\text{CBM}} = 0.76$  eV in CsPbI<sub>3</sub>, and  $q_{\text{B}} = 0.86$  and  $E_{\text{CBM}} = 0.34$  eV in CsPbCl<sub>3</sub>. A similar effect is produced by the change of crystal structure along the series cubic to tetragonal to orthorhombic, and with monovalent cations of varying hardness. . . . . 100

## List of Figures

---

- 6.3  $E_{\text{VBM}}$  ( $E_{\text{CBM}}$ ) vs  $O_{\text{VBM}}$  ( $O_{\text{CBM}}$ ) for Pb-based (right) and Sn-based (left) perovskites.  $E_{\text{BCB}}$  is shifted as explained in the Methods section. The relation  $E_{\text{VBM}}$  vs  $O_{\text{VBM}}$  is linear ( $R^2 \sim 0.93$  and  $\sim 0.53$  for Sn-based and Pb-based perovskites, respectively) and has a large negative slope. In the case of Pb perovskites, if we fit  $E_{\text{VBM}}$  vs  $O_{\text{TVB}}$  independently for each halides (continuous colored lines in the left panel) we obtain a much higher  $R^2$ ,  $\geq 0.85$ . The linear fitting of  $E_{\text{CBM}}$  vs  $O_{\text{CBM}}$  is poorer ( $R^2 \sim 0.33$  and  $\sim 0.38$  for Sn-based and Pb-based perovskites, respectively), and the slope is lower. . . . . 101
- 6.4  $E_{\text{VBM}}$  and  $E_{\text{CBM}}$  vs  $E_g$ . The top row refers to Pb-based systems, while the bottom row to Sn-based ones. On the left column we report results obtained including SOC, on the right column results obtained without SOC. . . . . 105
- 6.5 (see also Figure 6.1):  $E_{\text{VBM}}$  ( $E_{\text{CBM}}$ ) vs  $O_{\text{VBM}}$  ( $O_{\text{CBM}}$ ) without SOC. For Sn-based systems (right), the relation  $E_{\text{VBM}}$  vs  $O_{\text{VBM}}$  is linear and its slope is large.  $E_{\text{CBM}}$  vs  $O_{\text{CBM}}$ , instead, cannot be satisfactorily fit with a linear relation and presents a smaller negative slope. For the Pb-based systems (right), the linear fitting of both  $E_{\text{VBM}}$  vs  $O_{\text{CBM}}$  and  $E_{\text{CBM}}$  vs  $O_{\text{CBM}}$  is poor. At variance with the Sn-based perovskites case, here the slope of  $E_{\text{VBM}}$  vs  $O_{\text{VBM}}$  and  $E_{\text{CBM}}$  vs  $O_{\text{CBM}}$  fitting is comparable. . . . . 105
- 6.6  $E_g$  for the various crystal structures of  $\text{CsSnI}_3$ . Ortho 25% and Ortho 75% refer to the two orthorhombic structures identified by Kanatzidis and coworkers<sup>4</sup>. The fitting of crystallographic data required the adoption of a splitting position model for Cs and I atoms, with occupancy 25 and 75% of the two sites of each atomic species. The band gap reported is obtained from DFT calculations using the HSE exchange and correlation functional<sup>5</sup>. The SOC-corrected HSE  $E_g$  (see text above) of the Orthorhombic 75% phase, 1.14 eV, is in nice agreement with the experimental value, 1.3 eV<sup>4, 6</sup>. . . . . 106
- 6.7  $q_{\text{B}}$  and  $E_{\text{CBM}}$ . The top row refers to Sn-based systems, while the bottom row to Pb-based ones. On the left column we report results obtained including SOC, on the right column results obtained without SOC. . . . . 107
- 6.8  $q_{\text{B}}$  vs  $O_{\text{VBM}}$  for Sn-based (left) and Pb-based (right) perovskites . . . . . 108
- 6.9  $E_{\text{VBM}}$  and  $E_{\text{CBM}}$  energies of the orthorhombic structure of  $\text{CsSnX}_3$  perovskites 108
- 7.1 Importance of the grid size for fitting: The projection of the energy function on the  $x$  plane is demonstrated. . . . . 114
- 7.2 Band diagrams with and without SOC correction. Band splitting occurs when SOC is applied. . . . . 115
- 7.3 Two transversal and one longitudinal eigenvectors (principle axes of carrier transport) are shown. Lowest  $m^*$  in the highest overlap direction. . . . . 117
- 7.4 Gap and band edge energies versus minimum effective mass for Sn-based compounds . . . . . 118
- 7.5 Gap and band edge energies versus minimum effective mass for Pb-based compounds . . . . . 118

7.6 Antibonding overlap of the TVB orbitals versus the minimum hole effective masses $m_e^*$ for tin-based (left) and lead-based (right) compounds . . . . .	119
7.7 Effect of hydrogen bonding on effective masses. . . . .	120
7.8 Effect of Zn(II) dopant on the orbitals of the band edges . . . . .	121
7.9 Pb vacancy: depletion of equatorial iodide p orbitals that significantly affects TVB.121	121
B.1 Sn-Cubic structures . . . . .	148
B.2 Sn-Ortho25 structures . . . . .	148
B.3 Sn-Ortho75 structures . . . . .	149
B.4 Sn-Tetra structures . . . . .	149
B.5 Sn-Cubic structures . . . . .	149
B.6 Sn-Ortho25 structures . . . . .	150
B.7 Sn-Ortho75 structures . . . . .	150
B.8 Sn-Tetra structures . . . . .	150
B.9 Sn-Cubic structures . . . . .	151
B.10 Sn-Ortho25 structures . . . . .	151
B.11 Sn-Ortho75 structures . . . . .	151
B.12 Sn-Tetra structures . . . . .	152
B.13 Effect of Sr dopant on band structure . . . . .	153
B.14 Effect of Zn(II) dopant on band structure . . . . .	154
B.15 Charge defects . . . . .	155
B.16 Vacancy defects in CsPbI <sub>3</sub> . . . . .	156
B.17 Band diagrams of organic monovalent cation perovskites . . . . .	157





# List of Tables

3.1	$\Lambda$ parameters calculated for the dyes reported in this work . . . . .	35
4.1	Components of each simulation box . . . . .	68
4.2	Force field parameters developed in this work for the TiO <sub>2</sub> substrate and the chemisorbed water molecules. The full force field in AMBER format is given in Appendix A. . . . .	72
5.1	Displayed are the solvation free energy differences between tert-butyl and sec-butyl (negative values indicate tert-butyl is favored and positive values indicate sec-butyl is favored), the volume of each molecule in the solvent, the radius of the overall volume, and the dipole. a) Solvation free energies calculated from the differences in free energy between tert-butyl and sec-butyl in gas phase and solvent environment b) Volume was calculated by summing the volume of each atom in the molecule, using the respective van der Waals radius c) the radius of the volume of each molecule in the solvent d) 1-Alkyl-3-methyl imidazolium cation/Cl ion. . . . .	90
7.1	Average $m^*$ for MAPbI <sub>3</sub> using different grid sizes for fitting. $\Delta k'$ is giving the best $R^2$ value showing the significance of grid size on fitting procedure, grid is symmetric around the extremum which in the case of MAPbI <sub>3</sub> is slightly shifted from $\Gamma$ point. . . . .	113
7.2	Character table of $c_{3v}$ point group . . . . .	115
7.3	Product table of $c_{3v}$ point group . . . . .	115
A.1	Force field parameters implemented in this work for YD2-o-C8. . . . .	142
A.2	Force field parameters implemented in this work for the cobalt bipyridine complex. . . . .	145



# 1 Introduction

## 1.1 World energy consumption

Among the top ten problems of humanity for the next 50 years, sufficient and sustainable supply of energy stands at the first place<sup>7</sup>. Water, food, environment, poverty, war, disease, education, democracy, and population growth only come after that. The world energy consumption can be estimated as follows<sup>8</sup>:

$$E = N \times (GDP/N) \times (E/GDP) \quad (1.1)$$

Where  $N$  is the global population,  $GDP/N$  is the globally averaged gross domestic product (GDP) per capita, and  $E/GDP$  is the globally averaged energy intensity. Population growth and increases in income per person (GDP is expected to more than double in 50 years) are the key drivers behind the growing demand for energy. With the current population of about 7 billion people (10 billion in the next 50 years), finding a renewable source of energy seems inevitable.

The total world consumption of energy in year 2012 was 8,979 Mtoe (million of tonnes of oil equivalent)<sup>9</sup> from which renewable energies have a share of only 3.5% all together (with a growth of ca. 3% over 12 years since the year 2000). On the other hand, the solar energy (currently only 10% of the total renewable energy) received by earth in **one hour** is sufficient to meet the world demand for **one year**<sup>10</sup>. Even more interestingly, sun radiation maps show that only 4% of the world's deserted areas are sufficient to provide this photovoltaic (PV) power<sup>11</sup>. Currently, significant amount of solar energy is coming from solar plants which concentrate sunlight by means of hightech mirrors and use the heat to boil water or salts and run steam turbines<sup>11</sup>. Solar PV contributes one third of this amount and that is mainly from silicon-based panels. Single crystal silicon panels can give efficiencies as high as 25% (as discussed below, their highest theoretical efficiency is 30%), however, they require energy-demanding manufacturing, for the zone-melting process and wafer cutting of the single crystals that need to reach high temperatures and are highly expensive. The panels that are most widely used (the blue color panels on the roofs) are based on polycrystalline silicon, which are much

## Chapter 1. Introduction

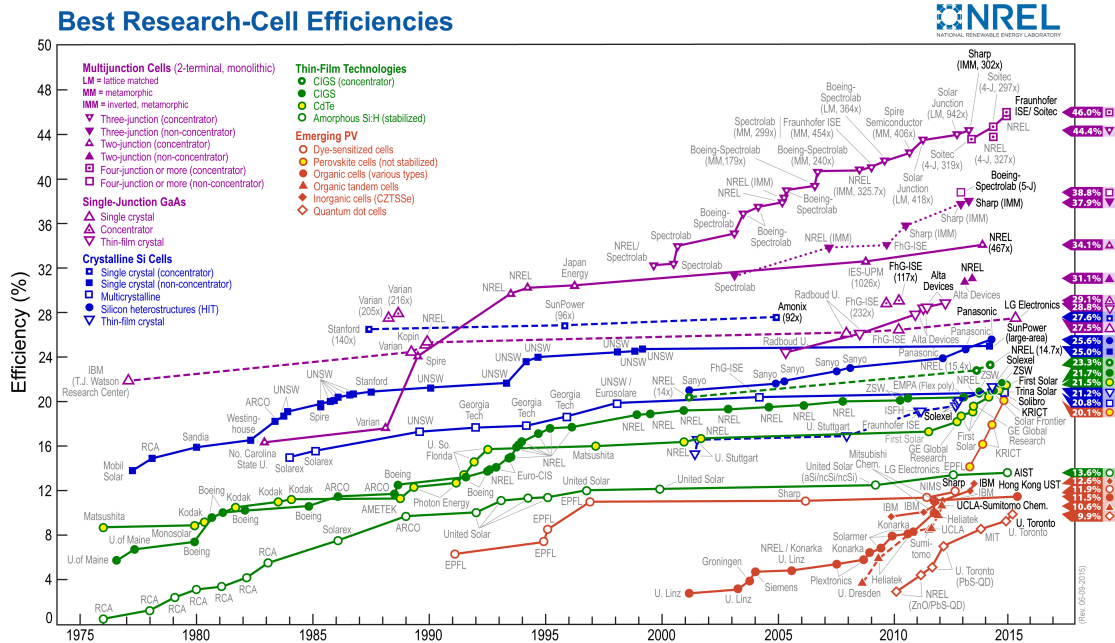


Figure 1.1: 2015 latest chart of record cell efficiencies from the National Renewable Energy Laboratory (NREL)

cheaper in production costs (distillation Siemens process) and their efficiency is about 21%<sup>12</sup>. These modules last, on average, 25-40 years. Thus, the energy payback time in these systems is around 1.5 years. The main issue with silicon PVs aside from their expensive manufacturing is the dumping process. In principle, these panels can be recycled. However, this requires heating up to 1800 F, i.e. a highly energy-demanding processing again.

Many different alternative technologies have emerged in parallel during the last decades which offer cheaper and cleaner technologies. Among them are second-generation thin-film panels. These technologies use less materials, however most of the involved compounds are rare or toxic. More recent third-generation photovoltaics are highly efficient and potentially of low cost. They include tandem and multi-junction solar cells, which can overcome the Shockley-Queisser limit<sup>13</sup>. The highest efficiency reached today without light-concentration is 38.8% for a five-junction solar cell, based on GaInP and GaInAs materials<sup>14</sup>. However, these technologies require delicate processing of expensive materials, and will probably not be feasible for mass production. Last but not least, are the emerging PV technologies. This class includes organic and hybrid organic-inorganic, dye-sensitized and perovskite photovoltaics. While most of them have not yet been commercially applied and are still in the research or development phase (due to low efficiencies and stability problems), intense research is going on in these fields as they promise a low-cost, high efficiency solution for the future. A quick look to the latest chart of record cell efficiencies from the National Renewable Energy Laboratory (NREL) (Figure 1.1), shows the intensive and rapid growth of these technologies during the recent years. Dye sensitized solar cells (DSSC) and perovskite solar cells are the major topic of this thesis.

## 1.2 Shockley-Queisser limit

Due to the irreversibility of the energy conversion process in a photovoltaic cell, these devices cannot reach higher efficiencies than their thermodynamic efficiency limit, the so called "Shockley-Queisser" limit ( $\eta_{max}=31\%$ ).

The origin of the irreversibility of the energy conversion is threefold: Non-equilibrium conditions due to power extraction, entropy of light (Carnot thermodynamic limitation), Free energy waste under polychromatic radiation (40% of loss)<sup>15</sup>. As a result, the overall efficiency of the solar cell is limited to the 31% theoretical maximum efficiency. In this section we address the last of these three factors. The optimization of the polychromatic radiation loss will be in fact one of the main objectives of this thesis.

Due to the polychromic nature of the solar spectrum with an absorber with threshold excitation wavelength  $\lambda_t$  in a somewhat idealized form, all parts of the solar spectrum with larger wavelengths than the threshold are not absorbed, all the lower wavelengths give rise to the same excitation with the excitation energy of  $hc/\lambda_t$  and the excess energy is transferred to the medium as radiation and heat. The fraction of absorbed energy which is stored as available energy is then given by the following equation:

$$\theta = \frac{\int_0^{\lambda_t} F_\lambda \frac{\lambda}{\lambda_t} d\lambda}{\int_0^\infty F_\lambda d\lambda}. \quad (1.2)$$

Where  $F_\lambda$  is the spectral radiation flux with wavelength  $\lambda$  incident on the converter from an external source. For a given spectral distribution of the incident radiation energy, an optimal threshold wavelength exists which yields a maximum  $\theta$ . For a Planckian radiation with a temperature  $T = 5200$  K (direct solar light at AM 1.5), the optimal wavelength is  $\lambda_t^{opt} = 953$  nm (1.3 eV) and accordingly  $\theta^{opt} = 0.44$ . This wavelength is near the absorption threshold of silicon solar cells.

## 1.3 Liquid-electrolyte DSSCs

Dye sensitized solar cells were first developed by O'Regan and Grätzel in 1991<sup>16</sup>. A schematic presentation of a DSSC is given in Figure 1.2. DSSC consist of three primary components: an anode which is made of a mesoporous layer of  $\text{TiO}_2$  nanoparticles deposited on a transparent glass (usually fluoride-doped tin dioxide ( $\text{SnO}_2:\text{F}$ ) or indium doped tin oxide ( $\text{SnO}_2:\text{I}$ )) which allows for light to penetrate to the sensitized  $\text{TiO}_2$  paste, the counter electrode (cathode) is made of a positively charged catalyst (typically platinum or carbon) deposited on a conductive substrate (usually the same substrate used for the fabrication of the anode) and finally after sealing the cell the liquid electrolyte is induced which is usually a redox couple (e.g.  $\text{I}_3^-/\text{I}^-$  or  $\text{Co(II)}/\text{Co(III)}$ ).

The photochemical cycle in a DSSC starts with the absorption of an incident photon by the dye molecules. The excited sensitizers will then inject the excited electrons into the  $\text{TiO}_2$ . The

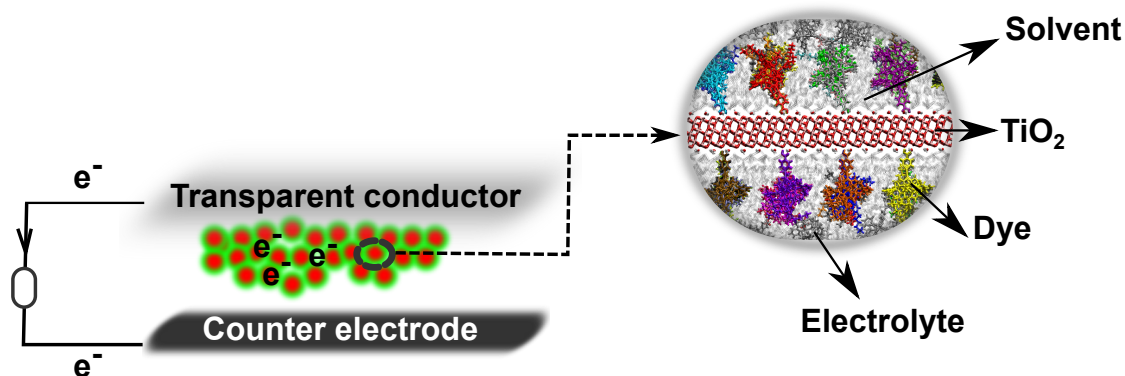


Figure 1.2: Schematic picture of a DSSC, porous  $\text{TiO}_2$  layer composed of nanoparticles covered with dye molecules.

nanoporous  $\text{TiO}_2$  layer contains spherical anatase particles with a diameter between 20-30 nm and a band gap of about 3.2 eV. The material is weakly n-doped due to oxygen vacancies in the lattice. The most thermodynamically stable lattice plane for the  $\text{TiO}_2$  nanoparticles is (101), which is the dominant exposed facet. Upon injection of the excited electron (from the dye), the semiconductor will act as an electron transporter. The electrons will then be externally transferred to the positively charged counter electrode (cathode) and meanwhile they lose energy by doing work. These electrons will reduce the electrolyte at the interface of cathode/electrolyte and will finally go back and regenerate the dye molecules once the reduced electrolyte reaches the oxidized dye.

The alignment of the relevant energy levels and time scales for the various competing processes are illustrated in Figure 1.3. In contrast to a conventional p-n junction solar cell, the functions of light absorption and charge carrier transport are separated. As a result, there should be no exciton recombination occurring inside the  $\text{TiO}_2$  itself. As mentioned above, the dye in its ground state  $S_0$  absorbs light and will be promoted to its excited state  $S_0^*$ . The electrons are then injected from the excited state into the conduction band of the  $\text{TiO}_2$  on a time scale of 50 fs-10ps and thereby the sensitizer is turned into oxidized  $S^+$ . In this step, the dye molecule in its cationic form needs to be stable enough so that no back electron recombination occurs. At least not until an electrolyte can approach the dye and regenerate it. This very fact is the motivation for Chapter 5 of this thesis, where as a proof of principles study, the stability of carbocations in different solvents is established computationally. The regeneration process occurs within  $0.1 \mu\text{s} - 30 \mu\text{s}$  where upon the dye has regained its initial state  $S_0$ . The oxidized form of the redox mediator diffuses to the counter electrode where it is regenerated.

On its own,  $\text{TiO}_2$  only absorbs a very small part of the solar spectrum, therefore usually sensitizers are used (e.g. dye molecules) to cover larger areas of the visible spectrum. Some times also co-sensitizers are used (other dyes) so that they act as a complementary sensitizing system to harvest together as much light as possible. Dye molecules are diffused and infiltrated into the porous  $\text{TiO}_2$  nano particles and ideally cover all the accessible surfaces. A uniform and homogeneous dye uptake can play an important role for device fabrication as we shall see in

## Chapter 4.

The fast-paced growth of this technology is due to the low cost and easy fabrication process that makes DSSCs the perfect choice to commercialize. Moreover, the flexible, light, colorful, and transparent structure of DSSCs makes them particularly interesting for use in architecture and design.

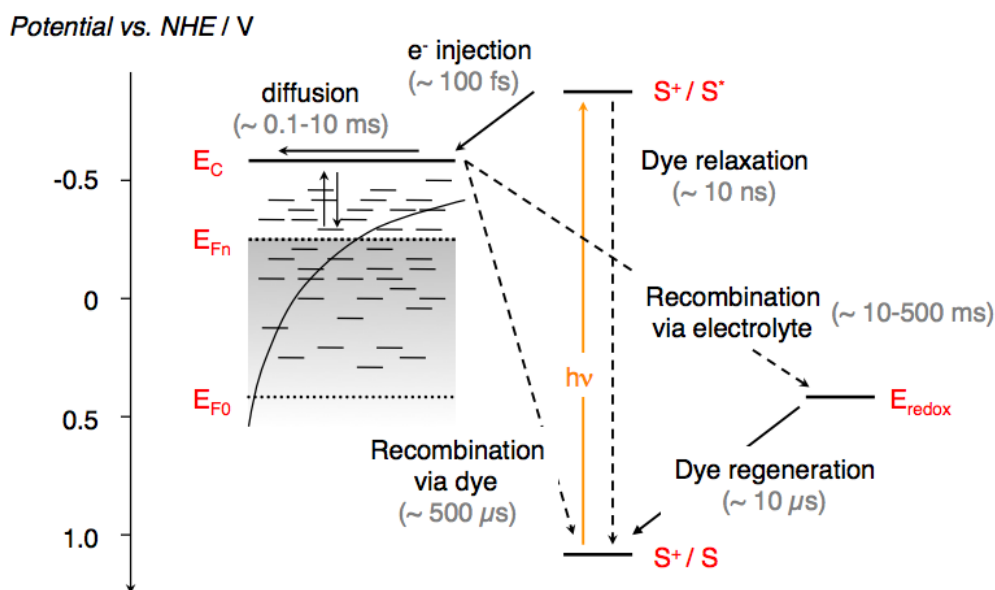


Figure 1.3: Schematic picture of different processes and their time scales in a DSSC. Picture taken from the thesis of Sophie Wenger<sup>1</sup>.

## 1.4 Solid-state DSSCs

Since the first report in 1998<sup>16</sup>, solid-state DSSCs followed a slower evolution almost always lagging behind liquid-based DSSCs. Materials that typically comprise a solid-state DSSC are a blocking layer, oxide film, a sensitizer, a hole transporting material (HTM), and a metal electrode. The first challenge is charge recombination across the interface of the TiO<sub>2</sub>/spiro-MeOTAD heterojunction which was later circumvented by incorporation of 4-tert-butylpyridine (tBP) and lithium bis(trifluoromethanesulfonyl)imide (LiTFSI) Li<sup>+</sup>[CF<sub>3</sub>SO<sub>2</sub>]<sub>2</sub>N<sup>-</sup>, in spiro-MeOTAD, which resulted in a PCE of 2.56%<sup>17</sup>. Another difficulty in solid-state DSSCs is that the thickness of the TiO<sub>2</sub> layer is limited to the optimized value of 2 μm because the mean free path of holes in spiro-MeOTAD is limited. Therefore, in order to increase the light harvesting other ways than thickening the oxide level had to be implemented. Thus later improvements were based on designing more efficient sensitizers. An efficiency of 4% was achieved by changing the dye from the conventional N719 to Z907 or the purely organic D102. Unlike liquid-based DSSCs, due to the thickness limitation of solid-state devices, dyes with higher absorption coefficients are preferred to more red-shifted dyes. D102 and Z907 are good

## Chapter 1. Introduction

---

examples for this concept. While Z907 absorption starts at lower energies, D102 was showing higher performances.

With this idea in mind, new dyes were designed with high molar absorption coefficients. Among them are the ruthenium-based C104<sup>18</sup> or the purely organic C220<sup>19</sup> with molar absorption coefficients five times higher than that of Z907. The next step was taken through improvements of the conductivity of the spiro-MeOTAD HTM via doping which resulted in a remarkable efficiency of 7.2%<sup>20</sup>.

In parallel, the search for alternatives for spiro-MeOTAD was going on which yielded the conjugated polymer poly-(3-hexylthiophene) (P3HT) as a suitable substitute<sup>21</sup>.

In 2012, a breakthrough in spiro-based solid-state DSSCs took place. CH<sub>3</sub>NH<sub>3</sub>PbI<sub>3</sub> perovskite was used as sensitizer and yielded an overall efficiency of 9.7%<sup>22</sup>. Perovskites were first used as sensitizer in DSSC, by Masayaka's group<sup>23</sup> in 2009 and then later by Park's group<sup>24</sup> in 2011 with the efficiencies of 3.5% and 6.5%, respectively. This breakthrough was further enhanced by incorporating CH<sub>3</sub>NH<sub>3</sub>PbI<sub>3-x</sub>Cl<sub>x</sub> compounds<sup>1</sup>, surpassing 10% efficiency<sup>26</sup>. Ever since, the improvements in the PCEs of perovskites have been very rapid, so much so that recently a certified efficiency of 20.1% was reached<sup>27</sup>. The massive scrutiny on these compounds show that the ambi-polar organometallic compounds owe their success to a combination of favorable properties such as the easy fabrication process, the small band-gaps, the high extinction coefficients, and the high carrier mobility<sup>28</sup>.

Perovskites were named after a Russian mineralogist who first characterized them to have an ABX<sub>3</sub> structure where X can be halogen or oxygen and A and B are 12 and 6 coordinated with X. An empirical value for the stability and distortion of the perovskite structure is given by the ratio of the (A-X) distance with respect to the (B-X) distance, called the tolerance factor:

$$t = \frac{R_A + R_X}{\sqrt{2}(R_B + R_X)} \quad (1.3)$$

The cubic phase is stabilized when  $t=1$  and the structure is distorted when  $t$  deviates from 1. The band gap energy of CH<sub>3</sub>NH<sub>3</sub>PbI<sub>3</sub> and CH<sub>3</sub>NH<sub>3</sub>PbBr<sub>3</sub> was measured using ultraviolet photoelectron spectroscopy (UPS) and UV-vis spectroscopies to be about 1.5 and 2.25 eV, respectively. While the energetics of TiO<sub>2</sub>/perovskite/spiro-MeOTAD suggests a good matching for charge transfer to happen (like for liquid DSSCs), there are pieces of evidence showing that perovskites on their own act as electron and hole transporters. The former was proved by utilizing Al<sub>2</sub>O<sub>3</sub> instead of TiO<sub>2</sub> which lead to devices that performed with a significant efficiency of 10%<sup>26</sup>, and the latter was proved when devices with pure perovskite and no HTM were made, yielding a considerable efficiency of 5.5%<sup>29</sup>.

Later, Seok's group<sup>27</sup> improved the efficiency up to 12% using the wider band gap CH<sub>3</sub>NH<sub>3</sub>PbBr<sub>3</sub>, which was expected to perform less good considering its lower photocurrent. The reason was due to the high photovoltage that compensated the lack in photocurrent.

Recent breakthroughs have been made through doping the electron transporter TiO<sub>2</sub>-EL layer which yielded 19.3%<sup>30</sup> efficiency. Seok's group<sup>31</sup> took another approach and mixed

---

<sup>1</sup>Later turned out that these chloride does not enter the lattice but only affects the formation of perovskite structures<sup>25</sup>



$\text{CH}_3\text{NH}_3\text{PbI}_3$  with formamidinium organic cation perovskites  $\text{FAPbI}_3$  to obtain an efficiency of 20.1%, the highest efficiency to date.  $\text{FAPbI}_3$  has carrier diffusion lengths that are longer than those of  $\text{CH}_3\text{NH}_3\text{PbI}_3$  and in addition it has a shallow band gap, which makes it a better light harvester. The only unsolved issue with this compound is its instability, since the perovskite phase of  $\text{FAPbI}_3$  is unstable at room temperature. With the fast pace in perovskite DSSC, future improvements to overcome this problem do not seem far to reach.

In Chapters 6 and 7 of this thesis, we will make use of ab initio electronic structure methods to investigate the key parameters that control the band gap in various perovskite compounds and then use the semi-classical carrier mobility model, as a first estimation for the efficiency of the carrier transport in different perovskite materials.

### 1.5 Chapters of this thesis

Based on the overview given in the previous sections, the chapters of this thesis are each designated to a computational study that targets the optimization of a specific component (sometimes more than one component) of DSSCs.

In Chapter 3, we start by studying the electronic structure of porphyrin-based dye molecules. The main objective of this section is to rationalize and automatize the design of dye molecules with improved absorption spectra. We perform a systematic study to establish the effects of chemical variations in the donor, bridge and acceptor moieties of these dyes by means of static calculations at the level of density functional theory (DFT) and time-dependent density functional theory (TDDF).

Later, we study the effect of more mesoscopic properties such as solvent effects and dye packing. As mentioned earlier the oxidized dye needs to remain as a stable cation before getting regenerated by electrolyte, otherwise the injected electron is recombined. In Chapter 5 we carry out a proof of principles investigation where we show how changing the solvent can affect the stabilization of different carbocations.

In Chapter 4, we model the complete DSSC by means of classical force fields that we developed for this purpose. These molecular dynamics simulations are then used to assess the accessibility of the electrolyte to the semiconductor surface or the dye-solvent, dye-dye interactions that influence the overall packing of dye molecules on the substrate.

In Chapter 6, we switch our attention to solid-state DSSCs and investigate the systematic variations of the band gap in perovskite materials.

In the last part, Chapter 7, we study the efficiency of carrier transport in a semi-classical approach and show how the effective masses are correlated with the band gap.

All chapters of this thesis are based on advanced manuscripts that are being submitted for publication. In addition, a series of publications (listed in my resume at the end of this thesis) have already appeared as part of investigations in this thesis.



## 2 Theory and Methods

In this chapter, an overview is given of the main theoretical concepts used in this thesis starting with definition of the wave function  $\psi$  in the case of molecules and solid crystals in terms of molecular orbitals and band structures. Later, the main electronic structure methods will be discussed. This chapter is mainly adopted from Ullrich's book<sup>32</sup> for density functional theory and time-dependent density functional theory, Hutter's book<sup>33</sup> for ab initio molecular dynamics, Chipot's book<sup>34</sup> for alchemical transformations, the review by Brunk and R othlisberger<sup>35</sup> for quantum mechanical/molecular mechanics simulations, and text book of Kittel, Yu, and Ashcroft<sup>36-38</sup> for solid state physics.

### 2.1 The molecular Hamiltonian and the definition of the wave function

Due to the wave like nature of electrons, electronic structure methods have been applied with the aim of finding approximate solutions to the time-independent, non-relativistic Schr odinger equation (Equation 2.1).

$$\hat{H}\psi(\{\mathbf{R}_\alpha\}, \{\mathbf{r}_i\}) = E\psi(\{\mathbf{R}_\alpha\}, \{\mathbf{r}_i\}) \quad (2.1)$$

where  $\hat{H}$  is the Hamiltonian for a molecular system consisting of  $M$  nuclei (indexed with  $\alpha$ ,  $N$  electrons (indexed with  $i$ ) in atomic units, and the position of the nuclei and electrons as  $\mathbf{R}$  and  $\mathbf{r}$ , respectively:

$$\hat{H} = -\frac{1}{2} \sum_{\alpha=1}^M \frac{1}{M_\alpha} \nabla_\alpha^2 - \frac{1}{2} \sum_{i=1}^N \nabla_i^2 - \sum_{i=1}^N \sum_{\alpha=1}^M \frac{Z_\alpha}{r_{i\alpha}} + \sum_{i=1}^{N-1} \sum_{j>i}^N \frac{1}{r_{ij}} + \sum_{\alpha=1}^{M-1} \sum_{\beta>\alpha}^M \frac{Z_\alpha Z_\beta}{R_{\alpha\beta}} = \hat{T}_e + \hat{T}_n + \hat{v}_{en} + \hat{v}_{ee} + \hat{v}_{nn} \quad (2.2)$$

The first two terms are the kinetic energy operators of the nuclei and electrons, respectively. The third and fourth are the electron-nuclei and the electron-electron interaction terms and the last term is the nucleus-nucleus interaction.  $r_{ij}$  and  $R_{\alpha\beta}$  refer to the distance between

## Chapter 2. Theory and Methods

---

electrons  $i$  and  $j$  and nuclei  $\alpha$  and  $\beta$ , respectively. The wave function  $\psi(\{\mathbf{R}_\alpha\}, \{\mathbf{r}_i\})$  is the eigenfunction (eigenstate) of  $\hat{H}$  with eigenvalue  $E$ .

Even the simplest molecule,  $He$ , consists of three particles, and its Schrödinger equation can not be solved analytically. Therefore all quantum chemical methods adopt the Born-Oppenheimer approximation, which takes note of the great difference in masses of electrons and nuclei. Because of this difference, the electrons can respond almost instantaneously to displacements of the nuclei. Therefore, instead of trying to solve the Schrödinger equation for all the particles simultaneously, we regard the nuclei as fixed in position and solve the Schrödinger equation for the electrons in the static potential arising from the nuclei in that particular arrangement.

Thus, the wave function  $\psi^{elec}$  for fixed nuclei where  $\hat{T}_n = 0$  is determined by the defined  $\mathbf{R}_\alpha$  as fixed set

$$\hat{H}^{elec}(\{\mathbf{r}_i\}; \mathbf{R}_\alpha) \psi^{elec}(\{\mathbf{r}_i\}; \mathbf{R}_\alpha) = E^{elec} \psi^{elec}(\{\mathbf{r}_i\}; \mathbf{R}_\alpha) \quad (2.3)$$

with

$$\hat{H}^{elec} = \hat{T}_e + \hat{v}_{en} + \hat{v}_{ee} + \hat{v}_{nn} \quad (2.4)$$

Note that  $\hat{v}_{nn}$  does not act on  $\{\mathbf{r}_i\}$  and only results in a trivial shift of the electronic energy.

By solving the Equation ( 2.3), integrating over electronic degrees of freedom gives:

$$E^{elec}(\{\mathbf{R}_\alpha\}) = \int \psi^{*elec}(\{\mathbf{r}_i\}; [\mathbf{R}_\alpha]) \hat{H}^{elec}(\{\mathbf{r}_i\}; [\mathbf{R}_\alpha]) \psi^{elec}(\{\mathbf{r}_i\}; [\mathbf{R}_\alpha]) d\mathbf{r} \quad (2.5)$$

which is only parametrically depending on the nuclear coordinates.

The Born-Oppenheimer approximation is very reliable for ground electronic states, but it is less reliable for excited state. To include effects beyond the BO approximation, the total electronic-nuclear wave function can be expanded in the complete orthonormal set of eigenfunctions of  $\hat{H}^{elec}$  (Equation 2.3) with the nuclear wave function as the expansion coefficients. The solutions of the Schrödinger equation will then include coupling terms in which  $\hat{T}_n$  acts on the electronic states. If we neglect the coupling terms and the quantum nature of the nuclei all together, downgrading them to classical particles leaves us with the total energy expression as a function of the nuclear coordinates and classical momenta  $\{\mathbf{P}_\alpha\}$

$$E(\{\mathbf{R}_\alpha\}, \{\mathbf{P}_\alpha\}) = E^{elec}(\{\mathbf{R}_\alpha\}) + T_n = E^{elec}(\{\mathbf{R}_\alpha\}) + \sum_{\alpha=1}^M \frac{\mathbf{P}_\alpha^2}{2M_\alpha} \quad (2.6)$$

in the total electronic energy is defined by

$$E^{elec} = \min_{\psi \rightarrow \psi_0} \frac{\langle \psi^{*elec} | \hat{H} | \psi^{elec} \rangle}{\langle \psi^{*elec} | \psi^{elec} \rangle} \quad (2.7)$$

Equations (2.6) and (2.7) can be used to perform on-the-fly ab initio molecular dynamics, where the nuclei move according to classical mechanics, over a potential energy surface that

## 2.1. The molecular Hamiltonian and the definition of the wave function

is calculated on-the-fly from an ab initio electronic structure method.


Up to this point the initial Schrödinger equation is simplified considerably, yet, even exact solution to this simplified problem is a difficult task. Many different electronic structure methods have been developed to give an approximate solution to Equation (2.3). Before moving to next section where the electronic structure methods used in this thesis are discussed, we shall examine the general properties of the Schrödinger equation for an electron in a periodic potential when we move from molecular systems (Chapters 3-5) to solid-based perovskite solar cells (Chapters 6 and 7).

### 2.1.1 Bloch function

The nuclei in a perfect crystal are arranged in a regular periodic array which allows for the nuclear potential to be described as a periodic function:

$$U(\mathbf{r} + \mathbf{R}) = U(\mathbf{r}) \quad (2.8)$$

for all Bravais lattice vectors  $\mathbf{R}$ . The electron in such a potential are called Bloch<sup>1</sup> electrons (in contrast to "free electrons") and they have the following very important property stated in Bloch's theorem:

 The eigenstate  $\psi$  of the one-electron Hamiltonian  $\hat{H} = -\frac{\nabla^2}{2} + U(\mathbf{r})$ , can be chosen to have the form of a plane wave times a function with periodicity of the Bravais lattice:

$$\psi_{n\mathbf{k}}(\mathbf{r}) = e^{i\mathbf{k}\cdot\mathbf{r}} u_{n\mathbf{k}}(\mathbf{r}) \quad (2.9)$$

where

$$u_{n\mathbf{k}}(\mathbf{r} + \mathbf{R}) = u_{n\mathbf{k}}(\mathbf{r}) \quad (2.10)$$

Any periodic function can be expanded in Fourier series, thus the periodic potential can be written as follows:

$$u(\mathbf{r}) = \sum_{\mathbf{G}} c_{n\mathbf{k}}(\mathbf{G}) e^{i\mathbf{G}\cdot\mathbf{r}} \quad (2.11)$$

where  $\mathbf{G}$  is the reciprocal lattice vector. Thus, we can rewrite the wave function in equation

---

<sup>1</sup>Bloch was a Swiss physicist.

2.10:

$$\psi_{n\mathbf{k}}(\mathbf{r}) = \sum_{\mathbf{G}} c_{n\mathbf{k}}(\mathbf{G}) e^{i(\mathbf{G}+\mathbf{k})\cdot\mathbf{r}} \quad (2.12)$$

If we solve  $\psi_{(n\mathbf{k})}^* \hat{H} \psi_{(n\mathbf{k})} = \varepsilon_{n\mathbf{k}}$  for various  $\mathbf{k}$  points inside the first Brillouin zone, we can have the band structure of the system. In Chapter 7 we make extensive use of this method.

Among all electronic structure methods like Hartree Fock and post-Hartree Fock wave function-based methods, only density functional theory (DFT) is applicable to the large systems considered in this thesis. This method and its time-dependent extension (TD-DFT) will be discussed in the following section.

## 2.2 Density Functional Theory (DFT)

As discussed in previous sections, the wave function tells us all we can wish to know about the quantum state of our system. Yet there remains a major drawback as Dirac (1929) aptly stated in his famous quote:



‘ The fundamental laws necessary for the mathematical treatment of a large part of physics and the whole of chemistry are thus completely known, and the difficulty lies only in the fact that application of these laws leads to equations that are too complex to be solved. ’

As for today, except for special cases like one-electron systems or systems with high symmetry the problem has remained intractable. Let us now ask a rather provocative question: Should we set our goal to search for the full many-body wave function? According to Kohn (1999) we should not!





‘In general the many-electron wavefunction  $\psi(x_1, \dots, x_N)$  for a system of  $N$  electrons is not a legitimate scientific concept, when  $N \gtrsim 10^3$ .’

What he meant is that the number of parameters needed to construct  $\psi$  grows exponentially with respect to the number of electrons (the so called “exponential wall”) and therefore it will be no longer feasible to neither calculate nor store such huge wave function. The essence of DFT is indeed to take this task off our shoulders.


### 2.2.1 Hohenberg-Kohn theorems

The theoretical foundation of DFT dates back to 1964<sup>39</sup> when Hohenberg and Kohn stated their theorems:

 In a finite, interacting N-electron system with given particle-particle interactions, there exists a one-to-one correspondence between the external potential  $v(r)$  (or energy) and the ground state density  $n_0(r)$ .

 Rayleigh-Ritz variational principle holds. That is the total energy is minimum for the ground state density  $n_0(r)$ .

Since the Hamiltonian is a functional of the external potential ( $\hat{T}$  and  $\hat{W}$  are fixed operators), it is also a functional of the ground state density. According to the Schrödinger equation this means that all the eigenstates are density functionals as well. In other words:

 All ground state properties of an N-electron system can be evaluated having the ground state density.

The extension of Hohenberg-Kohn theorems to the cases with degenerate ground states is straightforward<sup>40</sup>. Along with the theorems of Hohenberg and Kohn, Kato (1854)<sup>41</sup> and E. Bright Wilson (1968)<sup>42</sup> made the following observation which can be seen as the first proof of the theorem for atoms and molecules. Assume that we have the exact ground-state density ( $n_0$ ) of an unknown system (from X ray diffraction methods for example), the total number of electrons can be obtained for this system trivially by integration:

$$N = \int n_0 d\mathbf{r} \quad (2.13)$$

the position of the nuclei ( $R$ ) is exactly where the density has cusps and the magnitude and the slope of the density at the cusps dictate the nuclear charges  $Z_i$  at  $R_i$ .

$$Z_i = - \frac{1}{2n(\mathbf{r})} \frac{\partial \bar{n}(\mathbf{r})}{\partial \mathbf{r}} \Big|_{\mathbf{r}=R_i} \quad (2.14)$$

Where  $\bar{n}(\mathbf{r})$  denotes the spherical average of the density. Since we constructed the Hamiltonian solely using the ground state density, the system is completely defined. According to the second Hohenberg-Kohn theorem, there is a lower limit for  $E_{v_0}[n]$  which is  $E_0$ . Moreover the integral over the density has to be equal to the number of the electrons ( $N$ ). This implies that we need to look for a minimum subjected to a constraint, viz. we need to solve the following

equation

$$\frac{\partial}{\partial n(r)} \left[ E_{v_0}[n] - \mu \int d^3 r' n(r') \right] = 0 \quad (2.15)$$

where  $\mu$  is the Lagrange multiplier. The significance of this equation is that we can find the ground-state density without solving the Schrödinger equation. If we rewrite  $E_{v_0}[n]$  in Equation 2.15 as

$$E_{v_0}[n] = F[n] + \int d^3 r n(r) v_0(r) \quad (2.16)$$

where  $F[n]$  is the universal energy functional consisting of  $\hat{W}$  and  $\hat{T}$ . So If the universal functional is known (which is the only but the highly nontrivial issue) then  $n_0(r)$  can be obtained as:

$$\frac{\partial F[n]}{\partial n(r)} + v_0(r) = \mu. \quad (2.17)$$

Many attempts have been made over the years for deriving approximations for the universal functional (we will see the improvements in the following sections), however, two fundamental issues yet remain concerning the two Hohenberg-Kohn theorems and Equation (2.17) that have to be addressed:

1. Is the density derived from Equation (2.17),  $v$ -representable? That is, how does one know that this density corresponds to the ground state density of a local potential?
2. Is  $F[n]$  differentiable?

Levy (1979) and Lieb (1983) addressed the first issue with the so called Levy<sup>43</sup> constrained search. A weaker constrain of N-representability (The density is representing an antisymmetric wavefunction) was used by Levy. Their proposition though is not so practical, plays a very important formal and conceptual role in DFT.



According to Levy's constrained search the search for the antisymmetric manybody wavefunction (Equation 2.18) can be performed in two steps: 1) Look for the wavefunctions which produce a given density 2) look among these wavefunctions for the one that minimizes the energy Equation (2.19).

$$E_0 = \min_{\psi} \langle \psi | \hat{T} + \hat{V}_0 + \hat{W} | \psi \rangle \quad (2.18)$$

$$E_0 = \min_n \left\{ \min_{\psi \rightarrow n} \langle \psi | \hat{T} + \hat{V}_0 + \hat{W} | \psi \rangle \right\} \quad (2.19)$$

The second issue has been reviewed by van Leeuwen (2003)<sup>44</sup>.



### 2.2.2 Kohn-Sham Equations

Although the fact that one could express in principle all the energy terms as functionals of the ground-state density is highly valuable, it never became practical. Only after the key insight of Kohn and Sham (1965), DFT calculations became practical. Kohn and Sham wisely took advantage of an effective single particle picture to transform DFT to a tool that is widely used today.

If we consider a noninteracting system the Hamiltonian would become  $\hat{H}_s$ :

$$\hat{H}_s = \hat{T} + \hat{v}_s = \sum_{j=1}^N \left( -\frac{\nabla_j^2}{2} + v_s(r_j) \right) \quad (2.20)$$

Now the Lagrange equation takes the following form 2.21 and the ground-state density in principle can be calculated. However, the kinetic operator of a non interacting system as a functional of pure density  $\hat{T}_s[n]$  is only approximately known (e.g Thomas-Fermi model gave a poor description of chemical bonding<sup>45-47</sup>).

$$\frac{\partial E_{v_s[n]}}{\partial n(\mathbf{r})} = \frac{\partial \hat{T}_s[n]}{\partial n(r)} + v_s = \mu \quad (2.21)$$

where  $\mu$  is the Lagrange multiplier which is also the chemical potential.

Solving the Schrödinger equation for a noninteracting system with the same ground state density as the interacting system, is much easier as the many-body ground-state wave function reduces to a single Slater determinant.

$$\psi_s(\mathbf{r}_1, \dots, \mathbf{r}_N) = \frac{1}{\sqrt{N!}} \begin{vmatrix} \varphi_1(\mathbf{r}_1) & \varphi_2(\mathbf{r}_1) & \dots & \varphi_3(\mathbf{r}_1) \\ \varphi_1(\mathbf{r}_2) & \varphi_2(\mathbf{r}_2) & \dots & \varphi_3(\mathbf{r}_2) \\ \vdots & \vdots & \dots & \vdots \\ \varphi_1(\mathbf{r}_N) & \varphi_2(\mathbf{r}_N) & \dots & \varphi_N(\mathbf{r}_N) \end{vmatrix} \quad (2.22)$$

where  $\varphi_j(\mathbf{r}_j)$  satisfy the Schrödinger equation.

$$\left( -\frac{\nabla^2}{2} + v_s(\mathbf{r}) \right) \varphi_j(\mathbf{r}) = \varepsilon_j \varphi_j(\mathbf{r}) \quad (2.23)$$

And the ground-state density is:

$$n_0(\mathbf{r}) = n_s(\mathbf{r}) = \sum_{j=1}^N |\varphi_j(\mathbf{r})|^2 \quad (2.24)$$

If we now rewrite the total-energy functional in a clever way as Kohn and Sham did, we have

$$\begin{aligned} E_{v_0}[n] &= T[n] + W[n] + \int d^3\mathbf{r} n(\mathbf{r}) v_0(\mathbf{r}) = \\ &T_s[n] + \int d^3\mathbf{r} n(\mathbf{r}) v_0(\mathbf{r}) + \frac{1}{2} \int d^3\mathbf{r} \int d^3\mathbf{r}' \frac{n(\mathbf{r})n(\mathbf{r}')}{|\mathbf{r}-\mathbf{r}'|} + E_{xc}[n] \end{aligned} \quad (2.25)$$

Where the classical Coulomb (Hartree) energy is

$$E_H[n] = \frac{1}{2} \int d^3\mathbf{r} \int d^3\mathbf{r}' \frac{n(\mathbf{r})n(\mathbf{r}')}{|\mathbf{r}-\mathbf{r}'|} \quad (2.26)$$

The remaining part is swept under the new exchange-correlation energy term:

$$E_{xc}[n] = T[n] - T_s[n] + W[n] - \frac{1}{2} \int d^3\mathbf{r} \int d^3\mathbf{r}' \frac{n(\mathbf{r})n(\mathbf{r}')}{|\mathbf{r}-\mathbf{r}'|} \quad (2.27)$$

If we insert this into the Equation (2.15) we obtain:

$$\frac{\partial T_s[n]}{\partial n(\mathbf{r})} + v(\mathbf{r}) + \int d^3\mathbf{r}' \frac{n(\mathbf{r}')}{|\mathbf{r}-\mathbf{r}'|} + \frac{\partial E_{xc}}{\partial n(\mathbf{r})} = \mu \quad (2.28)$$

If we compare Equation (2.28) and Equation (2.21), it becomes clear that the two can be identical if we identify

$$v_s[n](\mathbf{r}) = v_0(\mathbf{r}) + \int d^3\mathbf{r}' \frac{n(\mathbf{r}')}{|\mathbf{r}-\mathbf{r}'|} + v_{xc}[n](\mathbf{r}), \quad (2.29)$$

It should be possible to find the ground-state density using the single-particle Schrödinger equation.

$$\left( -\frac{\nabla^2}{2} + v_s[n](\mathbf{r}) \right) \varphi_j(\mathbf{r}) = \varepsilon_j \varphi_j(\mathbf{r}) \quad (2.30)$$

$$n_0(\mathbf{r}) = \sum_{j=1}^N |\varphi_j(\mathbf{r})|^2 \quad (2.31)$$

Equations (2.30) and (2.31) are called the Kohn-Sham equations.

If we consider the kinetic energy

$$T_s[n_0] = \sum_{j=1}^N \int d^3\mathbf{r} \varphi_j^*(\mathbf{r}) \left( -\frac{\nabla^2}{2} \right) \varphi_j(\mathbf{r}) \quad (2.32)$$

$$= \sum_{j=1}^N \varepsilon_j - \int d^3\mathbf{r} n(\mathbf{r}) v_s[n_0](\mathbf{r}). \quad (2.33)$$

Inserting Equation (2.32) into Equation (2.26) gives a convenient expression for the exact ground-state energy of the interacting system:

$$E_{v_0}[n_0] = \sum_{j=1}^N \varepsilon_j - \frac{1}{2} \int d^3\mathbf{r} \int d^3\mathbf{r}' \frac{n_0(\mathbf{r})n_0(\mathbf{r}')}{|\mathbf{r}-\mathbf{r}'|} \quad (2.34)$$

$$- \int d^3\mathbf{r} n_0(\mathbf{r}) v_{xc}[n_0](\mathbf{r}) + E_{xc}[n_0]. \quad (2.35)$$

$E_{xc}$  remains the only unknown part in DFT which is usually the smallest part of the total energy. However,  $E_{xc}$  contributes significantly to the binding energy of matter and thus finding good

approximation to  $E_{xc}$  is extremely important.

One strategy for finding better functionals is by satisfying more and more exact properties concerning orbital energies, band gaps, asymptotics, self-interaction, and derivative discontinuities.

### Approximate functionals

The simplest approximation to  $E_{xc}$  and  $v_{xc}$  is the local density approximation or LDA was originally proposed by Kohn and Sham<sup>48</sup>. They expressed the xc energies of an inhomogeneous system as the integral over the xc energy of homogeneous electron liquids with density  $\bar{n}$ , evaluated at the local density ( $n(\mathbf{r}) - \bar{n}$ )

$$E_{xc}^{LDA}[n] = \int d^3\mathbf{r} e_{xc}^h(\bar{n}(\mathbf{r}))|_{\bar{n}=n(\mathbf{r})} \quad (2.36)$$

By construction, LDA becomes exact in the uniform limit. For nonuniform systems it works best if the variation of density is slow enough. One major drawback of the LDA is due to its self interaction error which results in a wrong asymptotic behavior (i.e. the spurious interaction of an electron with itself). Rather than following  $-1/r$  for  $r \rightarrow \infty$ , LDA xc goes to zero exponentially. Owing to this asymptotic behavior, the Kohn-Sham energy values are underestimated. In addition  $v_{xc}^{LDA}$  like most other functionals does not have a derivative discontinuity (see next section) and thus it yields wrong band gaps and wrong dissociation limits for molecules.

Later generalized gradient approximations (GGA) were introduced that retain the locality of LDA and depend not only on the local density but also on its gradients. The general form of GGA functionals are thus

$$E_{xc}^{GGA}[n] = \int d^3\mathbf{r} e_{xc}^{GGA}(n(\mathbf{r}), \nabla n(\mathbf{r})) \quad (2.37)$$

GGAs are not constructed based on a systematic expansions in terms of density and gradients. Instead, explicit mathematical expressions are introduced that are parameterized by satisfying formal properties or with the help of empirical data. Some of the most famous GGA functionals are BLYP<sup>49,50</sup>, PW91<sup>51</sup>, PBE<sup>52</sup>.

While LDA and GGA have been instrumental for the progress of DFT, they have yet to achieve "chemical" accuracy (i.e 1kcal/mol or 0.043eV) many improved schemes have been suggested. Perdew and Schmidt introduced the Jacob's ladder for DFT functionals of increasing accuracy (Figure 2.1) which today is the standard taxonomy for xc functionals. The first rung of the Jacob's ladder corresponds to LDA or LSD (local spin density) followed by GGAs with a function that make use of the Kohn-Sham orbital kinetic energy densities ( $\tau$ ), and hybrid functionals that include a percentage of exact exchange by borrowing part of HF exchange. The fifth rung is represented by functionals that make use of unoccupied orbitals and perturbation methods to approximate correlation energies.

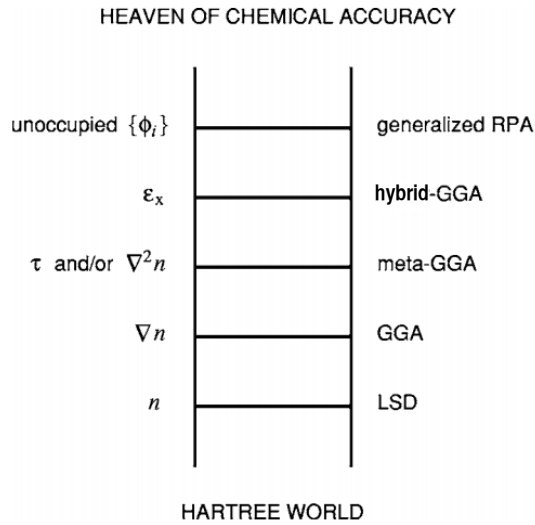


Figure 2.1: Jacob's ladder of DFT or today's taxonomy for xc functionals in DFT

### Kohn-Sham eigenvalues, band gaps and derivative discontinuities

Solid state physics distinguishes between several different gaps: single particle gap, the (quasi) particle gap, and the optical gap. One can probe the optical gap by means of optical spectroscopy. The optical gap refers to the energy difference between the ground-state and first optically allowed excited-state of a system for a *fixed* particle number  $N$ . Optical gaps can be calculated successfully by means of TDDFT (Except for excitons! See next section).

The fundamental band gap  $E_g$  in an insulating or semiconductor periodic solid is an example of a particle gap, involving ground-state energies of systems with *different* particle numbers:

$$E_g(N) = \epsilon_{N+1}(N+1) - \epsilon_N(N) \quad (2.38)$$

Where  $\epsilon_{N+1}$  and  $\epsilon_N$  are the HOMO level of two different systems. Thus  $E_g(N)$  is the difference between the ionization energy and the electron affinity.

$$E_g(N) = I(N) - A(N) \quad (2.39)$$

where  $I(N)$  is the ionization energy and  $A(N)$  the electron affinity.

If we define the KS gap for a noninteracting system as follows:

$$E_{g,s}(N) = \epsilon_{N+1}(N) - \epsilon_N(N) \quad (2.40)$$

we can relate the two gaps by:

$$E_g = E_{g,s} + \Delta \quad (2.41)$$

Where  $\Delta$  would be the correction to the KS gap (we will soon see that  $\Delta$  is indeed  $\Delta_{xc}$ ).

$$\Delta = \epsilon_{N+1}(N+1) - \epsilon_{N+1}(N) \quad (2.42)$$

It turns out that  $\Delta$  can be related to a very fundamental property of density functionals, known as derivative discontinuity. If we consider an open system of  $N$  particles connected to a particle reservoir with fixed chemical potential  $\mu$ , where  $\mu$  lies between HOMO and LUMO of our system, if the potential changes in a way that LUMO falls below  $\mu$ , an additional particle will be allowed to come in and the total number of particles changes abruptly from  $N$  to  $N+1$  and  $\mu$  would change consequently. That is,  $\mu$  and thus the energy ( $E$ ) is a piecewise constant function as illustrated in Figure 2.2.

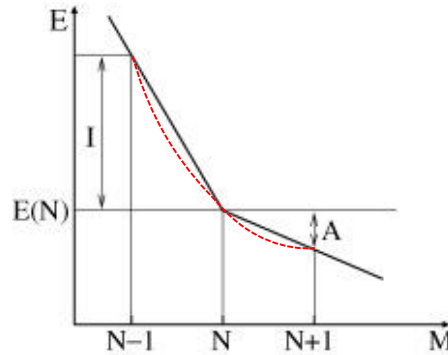


Figure 2.2: The total energy is a set of straight lines as a function of particle number, the red dashed-line shows how most functionals describe the energy.

Since  $\frac{\partial \mu}{\partial N}$  is discontinuous, also the left hand side of the Euler-Lagrange equation (i.e.  $\frac{\partial E}{\partial n}$ ) has to change abruptly for integer electron numbers. This means that the functional derivative is discontinuous, too. Perdew et al. suggested that in this picture particle number is treated continuous if we think of an statistical ensemble which mixes systems with  $N$  and  $N+1$  particles via a density operator  $\hat{\rho} = (1 - \omega)|\psi_0^N\rangle\langle\psi_0^N| + \omega|\psi_0^{N+1}\rangle\langle\psi_0^{N+1}|$ . An important outcome of this formalism is that the energy is a set of straight lines connecting values at integer particle numbers  $E(N + \omega) = (1 - \omega)E(N) + \omega E(N + 1)$ (Figure 2.2). If we subtract the fundamental gap of the interacting and non-interacting systems, we will get the relation between the gap correction and the functional derivatives as follows:

$$\Delta_{xc} = \left. \frac{\partial E_{xc}[n]}{\partial n(r)} \right|_{N+} - \left. \frac{\partial E_{xc}[n]}{\partial n(r)} \right|_{N-} \quad (2.43)$$

Therefore the many-body correction to the Kohn-Sham band gap is the derivative discontinuity of the xc energy arising from the non-uniqueness of the potential with respect to an additive constant.


Approximate xc functionals do not reproduce the discontinuity and thus the molecular properties such as IE and molecular dissociation are affected.

## 2.3 Time-Dependent Density Functional Theory (TDDFT)

The success of density functional theory for ground state properties has prompted its extension to time-dependent systems. A very attractive feature of time-dependent density functional theory (TDDFT) is that it allows a first principles calculation of excitation energies and forces at a moderate computational cost. TDDFT is currently quite an active area of research; in the following sections, its basic ideas and working equations are outlined.

### 2.3.1 The Time-Dependent Kohn-Sham Equations

In analogy to the first Hohenberg-Kohn (HK) theorem of ground-state DFT, the Runge-Gross theorem<sup>53</sup> states that

 **T** here exists a one-to-one mapping between the time-dependent one-body density  $n(\mathbf{r}, t)$  and the time-dependent external potential  $v_{ext}(\mathbf{r}, t)$  plus a spatially constant purely time-dependent function  $C(t)$ .

Up to a phase factor  $\alpha$ , the time-dependent wavefunction is then determined by the initial stationary wavefunction  $\psi(t_0)$  and the time-dependent density  $n(\mathbf{r}, t)$

$$\psi(t) = \psi[n, \psi(t_0)] \exp[-i\alpha(t)]. \quad (2.44)$$

By introducing again a fictitious system with non-interacting electrons in time-dependent orbitals  $\phi_i(\mathbf{r}, t)$  we can write down the time-dependent KS equations

$$\left[-\frac{1}{2}\nabla^2 + v_{eff}(\mathbf{r}, t)\right]\phi_i(\mathbf{r}, t) = i\frac{\partial}{\partial t}\phi_i(\mathbf{r}, t) \quad (2.45)$$

where

$$v_{eff}(\mathbf{r}, t) = v_{ext}(\mathbf{r}, t) + \int \frac{n(\mathbf{r}', t)}{|\mathbf{r} - \mathbf{r}'|} d\mathbf{r}' + v_{xc}(\mathbf{r}, t). \quad (2.46)$$

Usually applications of TDDFT imply the *adiabatic* approximation (ALDA) in which the exchange-correlation potential is approximated as

$$v_{xc}[n](\mathbf{r}, t) \approx \frac{\delta E_{xc}[n_t]}{\delta n_t(\mathbf{r})} = v_{xc}[n_t](\mathbf{r}), \quad (2.47)$$

where  $n_t$ , denotes the density evaluated at one particular time  $t$ . The xc-potential is thus independent of the time evolution of the density but depends only on the density at that particular time. Thus ground state functionals can also be used in excited states. This approxi-

mation assumes that the xc-potential instantaneously follows changes in the charge density, neglecting possible retardation effects.

### 2.3.2 Linear Response TDDFT

If the system is perturbed by a weak electric field at time  $t = 0$ , the evolution of the density can be described by propagating the time-dependent KS equations (Equation 2.45) which is the approach used in real time propagation RT-TDDFT<sup>54</sup>. The Fourier transform of the time-dependent dipole moment yields the optical absorption of the system. Assuming that the perturbation is weak, we can also apply linear response time dependent density functional theory (LR-TDDFT), which is done by most quantum chemistry codes. This treatment has the advantage that it is formulated on the basis of pure ground state properties. If we apply a periodic perturbation  $v_{appl}(\mathbf{r}, t)$  to the system, LR-TDDFT consists in evaluating the first order change of the density  $\delta n$ , which is related to the linear response of the density matrix  $\delta P(\omega)$  of the KS reference system in frequency space:

$$\delta n(\mathbf{r}) = \sum_{ij}^{\text{all orbitals}} \phi_i(\mathbf{r}) \delta P_{ij} \phi_j(\mathbf{r}). \quad (2.48)$$

The frequency dependent *generalized susceptibility* of the non-interacting reference system reads

$$\chi_{ij}(\omega) = \frac{f_i - f_j}{\omega - (\epsilon_j - \epsilon_i)}, \quad (2.49)$$

where  $\epsilon_i$  are the energies of the orbitals and  $f_i$  their occupation numbers. The generalized susceptibility connects the first order change of the effective potential  $\delta v_{ij}^{eff}(\omega)$  with the first order change of the density matrix:

$$\delta P_{ij}(\omega) = \frac{f_i - f_j}{\omega - (\epsilon_i - \epsilon_j)} \delta v_{ij}^{eff}(\omega). \quad (2.50)$$

Here,  $\delta v_{ij}^{eff}(\omega)$  contains the frequency dependent perturbation  $v_{appl}(\omega)$  and the linear response of the SCF potential  $\delta v_{ij}^{SCF}$ , which in turn, can be evaluated by  $\delta P(\omega)$  and the coupling matrix  $K_{ij}$ ,

$$\delta v_{ij}^{SCF} = \sum_{kl} K_{ij,kl}(\omega) \delta P_{kl}. \quad (2.51)$$

The coupling matrix is defined as

$$K_{ij,kl} = 2(ij|f_H|kl) + (ij|f_{XC}|kl), \quad (2.52)$$

and is determined by purely ground state properties through the Hartree kernel  $f_H$  and the xc-kernel, defined as

$$f_{XC}(\mathbf{r}, \mathbf{r}') = \frac{\delta^2 E_{XC}[n]}{\delta n(\mathbf{r})\delta n(\mathbf{r}')}, \quad (2.53)$$

when the ALDA is used. Assuming that the perturbation takes the form of an oscillating time-dependent electric field,  $\delta P(\omega)$  can be used to compute the tensor components of the frequency dependent dynamic polarizability. Excitation energies are obtained as the poles of the dynamic polarizability. Determination of these poles and thus of the excitation energies can be done by solving the following matrix equations, also known as the Casida equations<sup>55</sup>

$$\begin{bmatrix} \mathbf{A} & \mathbf{B} \\ \mathbf{B} & \mathbf{A} \end{bmatrix} \begin{pmatrix} \mathbf{X}_I \\ \mathbf{Y}_I \end{pmatrix} = \omega_I \begin{bmatrix} +1 & \mathbf{0} \\ \mathbf{0} & -1 \end{bmatrix} \begin{pmatrix} \mathbf{X}_I \\ \mathbf{Y}_I \end{pmatrix}, \quad (2.54)$$

where the matrices  $\mathbf{A}$  and  $\mathbf{B}$  are defined as

$$\begin{aligned} A_{ia,jb} &= +\delta_{i,j}\delta_{a,b}(\epsilon_a - \epsilon_i) + 2(i a | f_H | j b) \\ &\quad - c_X (i j | f_H | a b) \\ &\quad + (1 - c_X) (i a | f_X | j b) \\ &\quad + (i a | f_C | j b) \\ B_{ia,jb} &= +2(i a | f_H | b j) - c_X (i b | f_H | a j) \\ &\quad + (1 - c_X) (i a | f_{XC} | b j) \\ &\quad + (i a | f_C | b j). \end{aligned} \quad (2.55)$$

For the case of a hybrid XC-functional with an amount  $c_X$  of exact exchange, and  $f_X$  and  $f_C$  being the GGA exchange and correlation kernels, defined in analogy to (2.53). By setting  $c_X = 1$  and neglecting the term containing  $\hat{f}_C$ , time-dependent Hartree-Fock (TDHF) are recovered. In the same way as the Tamm-Dancoff Approximation (TDA) is applied in TDHF by setting the matrix  $\mathbf{B} = 0$ , also TDDFT-TDA can be obtained. The TDDFT-TDA provides a simplification of the eigenvalue problem and has been shown to give similar results as the full LR-TDDFT treatment for most closed shell systems at equilibrium geometries. In contrast to the TDA to TDHF, which is equivalent to configuration interaction singles (CIS), no other route exists in deriving the TDDFT-TDA.

### 2.3.3 TDDFT limitations and failures

**Charge Transfer** Charge transfer (CT) states illustrated in Figure 2.3 are usually underestimated due to the incorrect long range behavior of current standard xc functionals.

The excitation energy  $\Omega_{CT}$  to transfer an electron from the donor to the acceptor can be



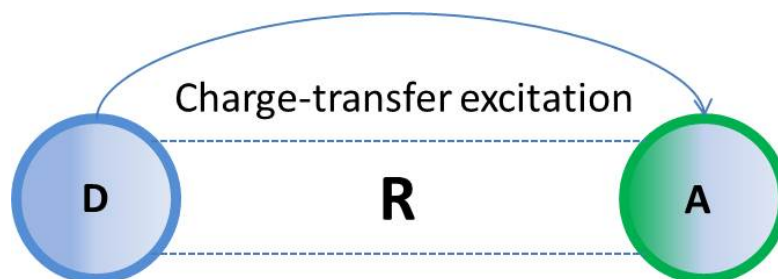


Figure 2.3: Charge transfer in Donor-Acceptor molecules.

described by:

$$\Omega_{CT} \approx IP^D - EA^A - \int d^3\mathbf{r} \int d^3\mathbf{r}' \frac{|\phi'_D(\mathbf{r})|^2 |\phi'_A(\mathbf{r}')|^2}{|\mathbf{r} - \mathbf{r}'|}. \quad (2.56)$$

where  $|\phi'_D(\mathbf{r})|^2$  and  $|\phi'_A(\mathbf{r}')|^2$  are the electronic density after CT. Here, one removes an electron from the donor, takes it to infinity (for which one has to overcome the ionization potential  $IP$ ) and then brings it back from infinity to the acceptor (for which one gains the electron affinity  $EA$ ). Since in this process a hole is created that interacts with the transferred electron, there is an additional term which is the Coulomb interaction between the hole on the donor and the additional electron on the acceptor. This term has to decrease with  $(1/R)$ , as a function of the donor-acceptor distance  $R$ . However, if we expand the integrand in TDDFT (Equation 2.52) with a single-pole approximation as in Equation (2.57), the corresponding potential does not exhibit the correct  $(1/R)$  asymptotic behavior.

$$\Omega_{CT} \approx IP^D - EA^A - \int d^3\mathbf{r} \int d^3\mathbf{r}' \phi'_D(\mathbf{r}) \phi'_A(\mathbf{r}') f_{xc}(\mathbf{r}, \mathbf{r}', \Omega_{CT}) \phi'_D(\mathbf{r}) \phi'_A(\mathbf{r}'). \quad (2.57)$$

In Equation 2.57, the last term consists of multiplication of two electron orbitals ( $\phi'_D(\mathbf{r}) \phi'_A(\mathbf{r}')$ ) which have very small overlap with each other as they belong to two distant regions in the molecule (D and A). Therefore, these two multiplications, on the left and right hand side of time-independent exchange-correlation kernel ( $f_{xc}$ ), go exponentially to zero as the distance  $R$  gets increases. If the exact Kohn-Sham xc-potential were known, because of the derivative discontinuity of the xc potential for changing number of electrons (Section 2.2), a charge transfer excitation would cause discontinuities in the derivative of the xc-potential with respect to density (xc-kernel). This singularity in the xc-kernel could compensate for the zero overlap of donor and acceptor orbitals and the correct  $1/R$  behavior would be found<sup>56</sup>.

Unfortunately the exact xc-functional is not known and almost all of the popular functionals like B3LYP and BLYP do not have the correct asymptotic behavior. For example, B3LYP the most widely used functional for ground state calculations, actually predicts an asymptotic behavior as  $-0.2/R$  rather than the correct  $-1/R$  form. Therefore various schemes have been

devised to handle CT problems, among them are long-range corrected (LC) functionals<sup>57</sup> including the Coulomb-attenuating method (CAM)<sup>58</sup>, which are range-separated hybrids<sup>59</sup> that were developed to eliminate or reduce the spurious long-range interaction. In this thesis, some of such functionals are tested that include long range corrections and the long range exchange is treated using exact orbitals created exactly by calculating the exchange integral with KS orbitals, rather than using a local functional.

- LC-wPBE<sup>60</sup>, The acronym wPBE refers to the short-range exchange functional derived by integration of the model PBE exchange hole.
- CAM-B3LYP, Combines the hybrid qualities of B3LYP and the long-range correction<sup>58</sup>.
- M06-2X<sup>61</sup>, Minnesota meta-hybrid functionals. M06 is parametrized including both transition metals and nonmetals, whereas the M06-2X functional is a highly non-local functional with a double amount of nonlocal exchange (2X), and it has been parametrized only for nonmetals. M06 is good for excitations with intermediate CT character (spatial overlap ( $\Lambda$ ) > 0.4 ), whereas M06-2X performs best for higher CT character excitations (spatial overlap ( $\Lambda$ ) > 0.23 )<sup>62</sup>.

**DFT limitations affect TDDFT accuracy** In DFT the Koopman's theorem<sup>63</sup> is only valid for the highest occupied KS state, HOMO. However, due to the approximations in the xc-functionals the energy of the HOMO,  $\epsilon_{HOMO}$ , is not in general a good approximation of the ionization potential. For this reason, in order to calculate electron removal energies we use the difference between the ground state energy of the (N-1)-electron system and that of corresponding (N)-electron system (As discussed also in Chapter 3).

## 2.4 Electronic transport

Electrons in the conduction band and holes in the valence band of a semiconductor can carry electrical current. Hence they are referred to as free carriers. In this section we study the effect of an external field on free carriers via a "quasi-classical" approach. But first we need to introduce "the effective mass approximation" which is widely used for describing the behavior of an electron in a system with impurities or defects.

Imagine a substitution defect of having a P atom in a lattice of a Si semiconductor. Since P has an extra electron which is loosely bound to P nucleus, it brings a so called "donor electron" in to the lattice. Since the donor electron is moving inside the semiconductor, its motion is affected by the crystal potential in addition to the impurity potential  $V_s$ . The Schrödinger equation of the donor electron is:

$$\begin{aligned}(H_0 + U)\psi(r) &= E\psi(r) \\ U &= -|e|V_s\end{aligned}\tag{2.58}$$

Since the defect breaks the symmetry, solving Equation ( 2.58) requires extensive numerical calculations. The most common approach for solving it is to utilize the effective mass approximation. This approximation makes use of the known band structure properties of a perfect crystal such as effective masses and is useful not only for calculating defect energy levels but also for studying electrons under any weak external perturbation. Among different methods for studying the electronic transport, in this section (which will be used in Chapter 7) we use the effective mass approximation to treat free carriers as having classical charge and renormalized masses.

There are two approaches for deriving the effective mass theory: One uses Wannier functions whereas the other one uses Bloch functions only. The Wannier functions are Fourier transform of Bloch functions, so the two approaches give the same result at the end. The Wannier function  $a_n(r; \mathbf{R}_i)$  is related to the Bloch function  $\psi(n\mathbf{k})$  as follows:

$$a_n(r; \mathbf{R}_i) = N^{-1/2} \sum_{\mathbf{k}} e^{-i.\mathbf{k}.\mathbf{R}_i} \psi(n\mathbf{k}) \quad (2.59)$$

$$\psi(n\mathbf{k}) = N^{-1/2} \sum_{\mathbf{R}_i} e^{(-i.\mathbf{k}.\mathbf{R}_i)} a_n(r; \mathbf{R}_i) \quad (2.60)$$

where  $\mathbf{R}_i$  is a lattice vector,  $n$  the band index,  $\mathbf{k}$  the wave vector in the reduced zone scheme, and  $N$  the number of unit cells in the crystal.

One main property of Wannier functions is that they are eigenfunctions of a "lattice vector operator"  $\mathbf{R}_{op}$  defined by

$$\mathbf{R}_{op} a_n(r - \mathbf{R}_i) = \mathbf{R}_i a_n(r - \mathbf{R}_i) \quad (2.61)$$

The effect of  $\mathbf{R}_{op}$  on a wave function

$$\Psi(r) = \sum_{n,\mathbf{k}} A_{n,\mathbf{k}} \psi(n\mathbf{k}) \quad (2.62)$$

can be represented approximately as

$$\mathbf{R}_{op} \Psi(r) \approx \sum_{n,\mathbf{k}} \left( i \frac{\partial}{\partial \mathbf{k}} A_{n,\mathbf{k}} \right) \psi(n\mathbf{k}) \quad (2.63)$$

We can use this to simplify the Schrödinger Equation ( 2.58). For simplicity from now on the index "op" will be dropped and both the lattice vector and its operator will be indicated as  $\mathbf{R}$ . If we expand the wave function 2.64 as a linear combination of Wannier functions:

$$\Psi(r) = N^{-1/2} \sum_{n,i} C_n(\mathbf{R}_i) a_n(r - \mathbf{R}_i) \quad (2.64)$$

where  $n$  is the band index and the  $C_n(\mathbf{R}_i)$  are coefficients analogous to  $A_{n,\mathbf{k}}$  in Equation ( 2.64). Thus the  $C_n(\mathbf{R}_i)$  can be regarded as the amplitudes of Wannier functions and since

they are also solutions to a wave equation, so they are known as envelope wave functions. If we represent the eigenvalues of the unperturbed Hamiltonian  $H_0(r)$  in Equation ( 2.58) as  $W_n(\mathbf{k})$  then it can be proven that:

$$[W_n(-\frac{i\partial}{\partial\mathbf{R}}) + U(\mathbf{R})]C_n(\mathbf{R}) \approx EC_n(\mathbf{R}) \quad (2.65)$$

This is a rather useful equation indeed. We can use it to solve the energies of a donor electron. If we assume that the lowest conduction band for the semiconductor is isotropic, nondegenerate, and parabolic, with the band minimum located at the zone center, its energy is thus given by

$$W_n(\mathbf{k}) = E_c(0) + \frac{\hbar^2\mathbf{k}^2}{2m^*} \quad (2.66)$$

Where  $m^*$  is the effective mass of this conduction band and  $E_c(0)$  the band edge. Since we consider only one band the index n is dropped. If we substitute ( 2.66) in ( 2.65) we will have:

$$\left[ -\left(\frac{\hbar^2}{2m^*}\right)\frac{\partial^2}{\partial\mathbf{R}^2} + U(\mathbf{R}) \right] C(\mathbf{R}) \approx [E - E_c(0)]C(\mathbf{R}) \quad (2.67)$$

which is equivalent to the Schrödinger equation for a particle with effective mass  $m^*$  moving in a potential U. In other words, the net effect of the crystal potential on the donor electron inside the crystal is to change the electron mass from the value in free space to the effective mass  $m^*$ . As a result this approach is known as the effective mass approximation. In a quasi-classical approach, the wave equation for the time evolution of an electron in a semiconductor under the influence of  $\phi$  is given by

$$(H_0 - e\phi)\psi(r, t) = i\hbar\frac{\partial\psi}{\partial t} \quad (2.68)$$

Here  $H_0$  is the one-electron Hamiltonian in the absence of an electrical field,  $e$  is the electronic charge and  $\psi(r, t)$  is the wave function in presence of the external field  $\phi$ . Within the effective mass approximation the wave equation for the envelope functions can be written as

$$\left[ E_c(0) - \frac{\hbar^2}{2m^*}\frac{\partial^2}{\partial\mathbf{R}^2} - e\phi(\mathbf{R}) \right] C(\mathbf{R}, t) \approx -\frac{i\hbar\partial}{\partial t}C(\mathbf{R}, t) \quad (2.69)$$

Instead of solving ( 2.69) in a quasi-classical approach, it can be argued that the net effect of the crystal lattice on the donor electron is the change in the magnitude of its effective mass  $m^*$ . So that the motion of this particle can be followed by classical equations of motion:

$$m^*\frac{d^2\mathbf{r}}{dt^2} + \frac{m^*}{\tau}\left(\frac{d\mathbf{r}}{dt}\right) = -e\mathbf{F} \quad (2.70)$$

Where  $\mathbf{r}$  is the position of the electron and  $\tau$  is a phenomenological scattering time introduced to account for the scattering of the electron by impurities and phonons. Equation ( 2.70) is considered quasi-classical because the concept of an effective mass for the electron motion has been derived quantum mechanically. The effective mass approximation will be used in

Chapter 7 in calculating the transport properties of perovskites.

## 2.5 Ab initio and classical molecular dynamics simulations

Molecular dynamics simulations rely on the ergodicity hypothesis, that is for an ergodic system we are allowed to replace the ensemble average (Equation 2.71) with the time average (Equation 2.72) of an arbitrary expectation value  $\langle A \rangle$ :

$$\langle A \rangle = \lim_{T_{max} \rightarrow \infty} \frac{\sum_t^{T_{max}} A(\mathbf{R}_\alpha(t), \mathbf{P}_\alpha(t)) e^{-\beta E(\mathbf{R}_\alpha(t), \mathbf{P}_\alpha(t))}}{\sum_t^{T_{max}} e^{-\beta E(\mathbf{R}_\alpha(t), \mathbf{P}_\alpha(t))}} \quad (2.71)$$

$$\langle A \rangle = \lim_{T_{max} \rightarrow \infty} \frac{\sum_t^{T_{max}} A(\mathbf{R}_\alpha(t), \mathbf{P}_\alpha(t))}{t} \quad (2.72)$$

Where again  $\alpha$  is an index of the nuclei. The total energy (within the Born-Openheimer approximation and classical description of the nuclei) is the sum of kinetic energy of classical nuclei and the potential energy  $E_p(\mathbf{R}_\alpha)$ :

$$E(\mathbf{R}_\alpha, \mathbf{P}_\alpha) = E_p(\mathbf{R}_\alpha) + T_n(\mathbf{P}_\alpha) \quad (2.73)$$

To sample  $\langle A \rangle$  along  $t$ , we can use Newton's equations of motion:

$$-\nabla_{\mathbf{R}} E_p(\mathbf{R}_\alpha) = M_\alpha \frac{d^2 \mathbf{R}}{dt^2} \quad (2.74)$$

Which are typically solved by numerical integration schemes, such as the popular velocity Verlet algorithm. The potential energy surface  $E_p(\mathbf{R})$  can be obtained at various levels of theory. For example a classical force field:

$$E_p = \sum_{bonds} K_r (r - r_0)^2 + \sum_{angles} K_\theta (\theta - \theta_0)^2 + \sum_{dihedrals} \frac{K_\phi}{2} [1 + \cos(n\phi - \gamma)] + \sum_{i < j} \left[ \frac{A_{ij}}{r_{ij}^{12}} - \frac{B_{ij}}{r_{ij}^6} + \frac{q_i q_j}{r_{ij}} \right] \quad (2.75)$$

Where in first three bonded terms,  $K_r$ ,  $K_\theta$ , and  $K_\phi$  refer to the force constant for the harmonic oscillator approximation of bonds, angles and dihedrals, respectively and  $\gamma$  is the phase. The last two terms are non-bonded van der Waals and Coulombic energies.  $r_{ij}$  is the distance between atoms  $i$  and  $j$  and  $q_x$  refers to the point charge of atom  $x$  and  $A$  and  $B$  are Lennard-Jones parameters. On the other hand in ab initio molecular dynamics (AIMD),  $E_p$  is obtained via one of the electronic structure methods (mostly DFT). One method commonly used in AIMD is the Car-Parrinello (CP) method.

In CP, the classical nuclei and electrons, represented by single-particle wave functions  $\psi_i$ , are

propagated simultaneously according to the extended Lagrangian:

$$L_{CP} = \frac{1}{2} \sum_{\alpha} \frac{1}{M_{\alpha}} \mathbf{V}_{\alpha}^2 + \frac{1}{2} \mu \sum_i \int d\mathbf{r} \dot{\psi}_i^*(\mathbf{r}) \dot{\psi}_i(\mathbf{r}) + E^{elec}[\{\psi_i\}; \{\mathbf{R}_{\alpha}\}] + \sum_{i,j} \Lambda_{ij} \left( \int d\mathbf{r} \psi_i^*(\mathbf{r}) \psi_j(\mathbf{r}) - \delta_{ij} \right) \quad (2.76)$$

Where  $\mu$  is a fictitious classical inertia attributed to the electronic degrees of freedom.  $\dot{\psi}_i$  refers to the time derivative of the electronic single particle orbital  $i$ . The Lagrange multipliers  $\Lambda_{ij}$  enforce orthogonality of the orbitals.

## 2.6 Mixed Quantum Mechanics/Molecular Mechanics (QM/MM) simulations

The development of the hybrid QM/MM approaches is motivated by the general idea that large chemical systems may often be partitioned into an electronically important region which requires a quantum chemical treatment and a remainder which only acts in a perturbative fashion and thus admits a classical description.

Using this approach, it is possible to reduce the size of the quantum system, and treat the rest of the system, the environment, at a classical molecular mechanics level. In this way, the amount of computer time and memory storage capacity required for the computation of complex systems made of thousands of atoms like for instance proteins, can be substantially reduced.

The original molecular Hamiltonian for the QM system in the Born-Oppenheimer approximation

$$\hat{H}_{tot}^{QM} = -\frac{1}{2} \sum_n \nabla_n^2 + \sum_{I < J} \frac{Z_I Z_J}{|\mathbf{R}_I - \mathbf{R}_J|} - \sum_{In} \frac{Z_I}{|\mathbf{R}_I - \mathbf{r}_n|} + \sum_{n < m} \frac{1}{|\mathbf{r}_m - \mathbf{r}_n|} \quad (2.77)$$

is modified into

$$\hat{H}_{tot}^{QM/MM} = -\frac{1}{2} \sum_n \nabla_n^2 + \sum_{I < J} \frac{Z_I Z_J}{|\mathbf{R}_I - \mathbf{R}_J|} - \sum_{In} \frac{Z_I}{|\mathbf{R}_I - \mathbf{r}_n|} + \sum_{n < m} \frac{1}{|\mathbf{r}_m - \mathbf{r}_n|} - \sum_{Kn} \frac{Q_K}{|\mathbf{R}_K - \mathbf{r}_n|} \quad (2.78)$$

where  $K$  is the index of MM atoms with charge  $Q_K$ . The QM/MM interaction Hamiltonian also includes the bonded and vdW interactions between QM and MM systems that are treated at the classical level. The last term in Equation (2.78) describes the interaction of the electrons of the QM sub-system with the charges of the MM atoms. What is still missing but can easily be added is the part of the MM Hamiltonian dealing with the molecular bonded-interactions that

are parametrized by a classical force-field. We make use of this method in Chapter 5 where the effects of different solvents on the stability of carbocations are studied.

## 2.7 Alchemical transformations

One of the ways for calculating the relative free energies of compounds with different chemical composition is "alchemical transformation". In this framework chemical systems can be transformed or gently 'perturbed' into one another. These calculations are very useful in cases where we are interested in the free energy difference of two systems differing only in a small portion (like finding the binding free energy of different ligands to a protein or like in our case (Chapter 5) to calculate relative solvation free energies. For such applications, we are interested in calculating the free energy difference between one system described by the Hamiltonian  $H_0$ , and a target system with Hamiltonian  $H_1$ :

$$H_1(x, p_x) = H_0(x, p_x) + \Delta H(x, p_x) \quad (2.79)$$

where  $\Delta H(x, p_x)$  consists of all terms in  $H_1(x, p_x)$  that describes the 'unique' subsystem and its interacting environment.

The Helmholtz free energy between the target and reference systems  $\Delta A$  is evaluated by

$$\Delta A = -k_B T \ln \frac{Z_1}{Z_0} = -k_B T \ln \frac{\int e^{-\frac{H_1(x, p_x)}{k_B T}} dx dp_x}{\int e^{-\frac{H_0(x, p_x)}{k_B T}} dx dp_x} \quad (2.80)$$

Where  $Z_0$  and  $Z_1$  refer to the partition functions of state 0 and 1 which are defined by position  $x$  and momentum  $p_x$ .

The free energy difference is computed using the thermodynamic integration approach, in which a parameterized Hamiltonian,  $H_\lambda(x, p_x)$ , is defined using an order parameter,  $\lambda$ , such that when  $\lambda = 0$ ,  $H_\lambda = H_0$  and when  $\lambda = 1$ ,  $H_\lambda = H_1$ . i.e.  $H_\lambda$  interpolates smoothly between the states 0 and 1. The Helmholtz free energy  $A$  is then a function of  $\lambda$  given by

$$\frac{dA}{d\lambda} = \frac{\int \frac{\partial H_\lambda(x, p_x)}{\partial \lambda} e^{-\frac{H_\lambda(x, p_x)}{k_B T}} dx dp_x}{\int e^{-\frac{H_\lambda(x, p_x)}{k_B T}} dx dp_x} = \left\langle \frac{\partial H_\lambda(x, p_x)}{\partial \lambda} \right\rangle_\lambda \quad (2.81)$$

If  $H_\lambda$  interpolates linearly between 0 and 1, Equation (2.81) reduces to:

$$\frac{dA}{d\lambda} = \langle H_1(x, p_x) - H_0(x, p_x) \rangle_\lambda \quad (2.82)$$





### 3 Computational characterization and design of porphyrin-based dye sensitizers: All the way up to 13% efficiency



T

his chapter is based on a collaboration with Basile F.E. Curchod, Andrey Laktionov, Giulia Palermo and Ivano Tavernelli from LCBC<sup>a</sup> and Simon Mathew and Chenyi Yi from LPI<sup>b</sup>.

<sup>a</sup>Laboratory of Computational Biochemistry and Chemistry

<sup>b</sup>Laboratory of Photonics and Interfaces

### Chapter 3. Computational characterization and design of porphyrin-based dye sensitizers: All the way up to 13% efficiency

---

This work is a review on the vast series of first-principles computations of the structural and electronic properties of porphyrin-based dye sensitizers which led to the designed record-breaking dye SM315 with 13% efficiency. Considering systematic variations in the donor (D), bridge, (B) and acceptor (A) moieties as well as in the metal center, we were able to engineer dyes with improved light-harvesting properties. Some of the key guiding principles that emerge from these studies are: 1) maintenance of planarity of the porphyrin bridge is crucial to ensure efficient long-distance charge transfer as well as low energy electronic transitions in the long-wavelength region; 2) proper orientation of the charge-transfer excitation along the D-B-A molecule that favors electron injection.

## 3.1 Introduction

Ever since their invention, dye sensitized solar cells (DSSCs)<sup>64</sup> have attracted a lot of attention due to their low fabrication costs and their tunable properties. The photovoltaic cycle in a DSSC starts with the photon excitation of the sensitizer molecule, which injects the excited electron into TiO<sub>2</sub> nanoparticles that act as a conductor that takes the electrons to the counter electrode. At this point, the electrolyte (redox couple) is reduced and can then serve to regenerate the oxidized dye completing the cycle. Aside from a variety of possible modifications of different DSSCs components like the TiO<sub>2</sub> nanoparticles, the redox couple, the co-adsorbents and the solvent, the design and the molecular engineering of better performing sensitizers which can absorb light more efficiently is of great importance for the geometry optimization of the device performance. Ru-based dyes were for a long time the dominant class of sensitizers used in DSSCs<sup>65,66</sup>; however, their further improvement is hampered by their low molar extinction coefficients (e.g.,  $\epsilon < 10000 M^{-1} cm^{-1}$  for the metal to ligand charge transfer (MLCT) band of the black dye<sup>67</sup>) and the limited availability of the precious ruthenium metal. Together with purely organic dyes, porphyrin-based sensitizers are a successful alternative, which in recent years has altered the interests of many researchers<sup>68-70</sup>. Inspired by nature, these chlorophyll-like sensitizers are now among the best performing dyes yielding the highest reported efficiencies for DSSCs so far<sup>3,71</sup>.

Porphyrin-based dyes absorb light in a broad range of visible light. For a dye with the HOMO-LUMO gap of  $E_{0-0}$ , all the photons with energies below this value would only heat up the system and won't get absorbed. On the other hand photons with higher energy than the gap would release their excess energy as heat via vibration. Only a small portion of these photons will be able to inject electrons because most of the higher excited states ( $S_2, S_3, \dots$ ) have too short electron lifetimes for proper injection to happen<sup>72</sup>. For this reason there is an optimum wavelength ( $\lambda_{opt}$ ) for which the photon energy contribution to the photovoltaic available energy is maximum. This optimum wavelength for a Planckian radiation is ca. 970 nm (1.3 eV)<sup>73</sup>. Therefore to increase the photocurrent, dyes that absorb in the red region of the solar spectrum are preferred.

Another important criterion to guide the design of new dyes is to obtain a favorable energy alignment with other components in the cell and in particular with the electrolyte (redox

couple). Depending on the nature of electrolyte that is used (iodide based or cobalt-based), the HOMO energy level of the dye should lie below the oxidation potential of the redox couple, ensuring proper dye regeneration. Cobalt-based electrolytes are colorless and do not compete with the dye for light absorption. Moreover, their oxidation potential aligns better than that of the iodide-based electrolytes improving therefore the open circuit voltage  $V_{OC}$ . Equally important is the LUMO energy level which needs to lie slightly above the Fermi energy level of  $\text{TiO}_2$  for proper injection.

Considering the aforementioned challenges in the design of better performing dyes, ab initio computational methods can be of great help. Certain theoretical concerns though need to be considered which will be discussed later in the "Theoretical concerns" section. In this article, using linear response time-dependent density functional theory (LR-TDDFT) and density functional theory (DFT), we show how a thorough screening of a series of dyes properties including absorption spectra, energy levels and charge distribution can help guiding the design of better performing dyes.

The current record efficiency DSSC is based on a new porphyrin-based dye (SM315) with the efficiency of 13%<sup>71</sup>, which is the first in its family to give such a high efficiency without using any co-sensitizers. In this article, we report the underlying computational screening of different dyes, which along with experimental results paved the way to the design of SM315. Performing systematic studies of dyes with variations in the donor, bridge and acceptor moieties as well as in the central metal ion, it has been possible to establish some fundamental structure-function relationships that govern this class of compounds.

## 3.2 Methods

Full geometry optimization of all of the compounds in their singlet ground state were performed with DFT using the M06 functional with the effective core potential and basis set LANL2DZ<sup>74</sup> for zinc, cobalt, copper, lead and tin. A 6-31G\* basis set<sup>75</sup> is used for the remaining atoms except for the fluorine for which 6-31G++ diffuse basis set<sup>76</sup> is used. Ultrafine grid, and tight geometrical convergence criteria were applied within the Gaussian 09 package<sup>77</sup>. The polarizable continuum model (PCM) using the integral equation formalism variant (IEF-PCM)<sup>78</sup> is employed for treating solvation effects. A relative permittivity of 7.43 is applied for tetrahydrofuran (THF). Bulky electronically passive long alkoxy chains were replaced by methoxy groups. Geometry optimizations were followed by frequency calculations for further assessment of the minimum energy configuration. For each compound, LR-TDDFT/M06/IEF-PCM (THF) calculations were performed for the first 30 excited states, using the same basis set and xc-functional used for the optimization. As discussed before, M06 is capable of describing transitions with a small amount of charge transfer (CT) character, which is the case in porphyrin-based dyes. Vertical ionization energy (IE) and electron affinity (EA) were computed at (U)DFT/M06 level of theory. Graphical representation of the molecules and their orbitals were obtained with the software VMD v.1.9.0<sup>79</sup>. The geometries of different rotamers with

### Chapter 3. Computational characterization and design of porphyrin-based dye sensitizers: All the way up to 13% efficiency

---

respect to the phenyl ring on the donor were optimized and the energy difference between them (0.05 eV) was within the error of the theoretical methods used. The TDDFT method was used to calculate the spectra, molecular orbital distribution, and electron density distribution of the most important excited states. The theoretical electronic spectra were broadened with a Lorentzian function with a full-width at half-maximum (FWHM) of  $1500\text{ cm}^{-1}$ .

#### 3.2.1 Theoretical Concerns

A very attractive feature of TDDFT is that it allows first principles calculation of excitation energies and forces at a moderate computational cost. Not surprisingly, TDDFT has been used extensively to help DSSCs meet their theoretical maximum efficiency<sup>80-83</sup>. The use of TDDFT for the investigation of this type of compounds, however, requires particular care because of its well-known and well-documented failures.

**Charge Transfer** Due to their special design, these elongated donor-bridge-acceptor porphyrin-based dyes are prone to have charge transfer electronic transitions. Charge transfer states are usually underestimated in TDDFT because of the incorrect long range behavior of standard exchange correlation (XC) functionals<sup>84</sup> and the adiabatic approximation inherent to LR-TDDFT<sup>32</sup>. A typical absorption spectrum of a porphyrin compound consists of two distinct electronic transitions: the so-called Soret band (higher energy) and the Q-band (lower energy). The later transition is more of a charge transfer (CT) character, while the former is of valence type. Furthermore, some excitations close to the Soret band are believed to exhibit double-excitation character which can't be described through adiabatic TDDFT<sup>85,86</sup>. Various schemes have been devised to handle CT problems. Among them are the modified functionals based on long-range coulomb-attenuation correction: LC-wPBE<sup>87</sup>, CAM-B3LYP<sup>88</sup>, and M06-2X<sup>89</sup>.

To obtain a reliable protocol for our calculations we first tested a series of LC functionals verifying their accuracy by comparing with available experimental results. For the reference dye YD2-o-C8, M062X and CAM-B3LYP overestimate the first transition by 0.4 eV and 0.2 eV respectively. With M06<sup>89</sup> the error drops to 0.03 eV which is within DFT/TDDFT precision. While this transition clearly exhibits a donor-to-acceptor character, the overlap of the orbitals taking part to this vertical excitation is still considerable. The  $\Lambda$ -parameter<sup>90</sup> provides a measure of the degree of spatial overlap for a LR-TDDFT transition ( $0 < \Lambda < 1$ , the smallest the value of  $\Lambda$ , the smallest the degree of spatial overlap). Computing this parameter for the first transition of YD2-o-C8 gives a value of 0.65 (other  $\Lambda$  values are reported in Table 3.1). It is commonly accepted that GGA functionals should not be used for computing transitions with a  $\Lambda$ -parameter smaller than 0.4, while hybrid functionals can be used for transitions with  $\Lambda > 0.3$ . The existence of a certain amount of electron-hole overlap associated to this transition as it is also evident from inspection of the electron-hole distribution maps (coexistence of blue and orange spots on the porphyrin ring in Figure 3.1-orange box on the left) is the reason why M06 is yielding the closest excitation energy with respect to the experiment.

Incorporation of 20% HF exchange in M06, helps to provide a balanced description of the

Donor variations 1		Donor variations 2	
SM63	0.592	SM209	0.471
SM63-D1	0.522	SM371	0.56
SM63-D2	0.534	SM1	0.697
SM63-D3	0.595	SM0	0.58
SM63-D4	0.605	SM00	0.538
SM63-D5	0.734	SM01	0.692
		SM02	0.68
Meso position variations		Central metal	
Furan	0.659	Cu(II)	0.676
Thiophene	0.653	Mg(II)	0.669
Thiol- Thiophene	0.645	Co(II)	0.57
Phenyl	0.663	Pb(II)	0.656
-CH <sub>3</sub>	0.671	Sn(IV) with lig- ands	0.583
-F	0.672		
-OH	0.744		
-NH <sub>2</sub>	0.757		
Combined dyes		Acceptor variations	
Y486	0.511	CN-CN	0.58
Y690	0.533	CN-CF <sub>3</sub>	0.59
SM315	0.499	CF <sub>3</sub> -CF <sub>3</sub>	0.60
Y789	0.56	Pyrazine	0.60
Y789-D1	0.44	Pyrimidine	0.61
Y789-D2	0.558		

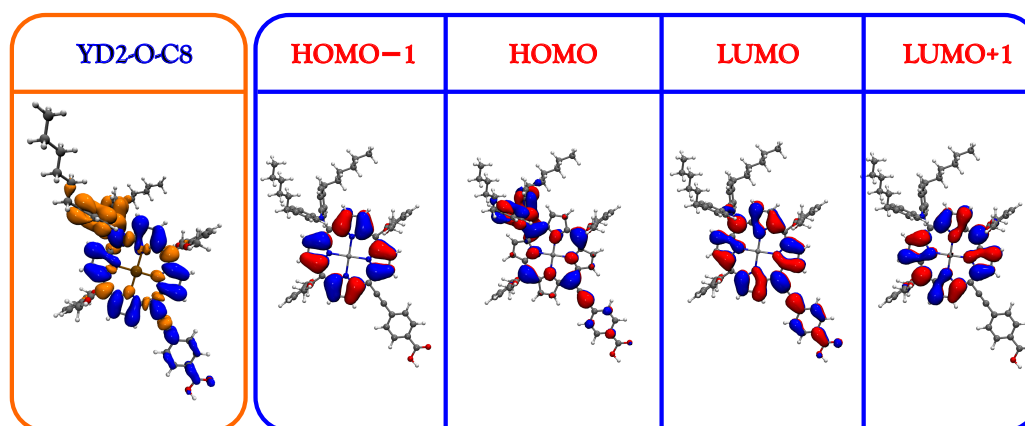
Table 3.1:  $\Lambda$  parameters calculated for the dyes reported in this work

Figure 3.1: Orange box on the left: Electron-hole density map of the  $[S_0 \rightarrow S_1]$  vertical transition for the reference dye: YD2-o-C8. The density difference contour plots ( $\rho_{S_1} - \rho_{S_0}$ ) show the electron distribution (blue) and the hole distribution (orange). Isovalue set to 0.0003. Blue box on the right: Frontier Kohn-Sham orbitals for YD2-o-C8 (isovalue is 0.02 a.u.)

### Chapter 3. Computational characterization and design of porphyrin-based dye sensitizers: All the way up to 13% efficiency

vertical transitions in porphyrin-based dyes. Functionals with no or smaller amount of HF exchange fail more rapidly in describing CT transitions. For example B3LYP functional underestimates the same transition by 0.1 eV. M06 was also able to predict the shifts observed in the experimental absorption spectra of the pair LD13 and LD14<sup>2</sup>, (Figure 3.2) and the pair YD2<sup>3</sup> and YD2-o-C8 (Figure 3.3).

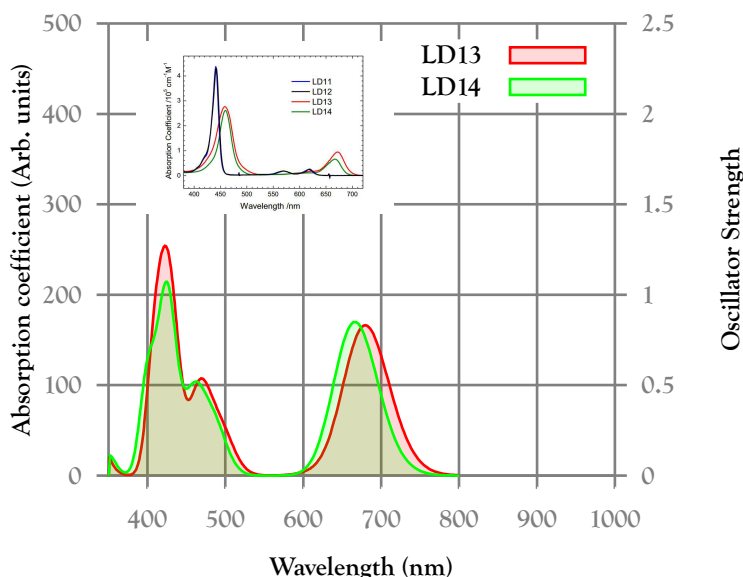


Figure 3.2: M06 able to capture slight shifts in the absorption spectrum (LD13 Vs. LD14). The experimental spectra (inset) is borrowed from Ref.<sup>2</sup>

Results of  $\gamma$ -tuning of LC-BLYP functional (for the SM315 dye) also yielded excitation energies similar to M06 as shown in our previous publication<sup>71</sup>. In the following, all calculations are performed using M06 functional.  $\Lambda$  parameters are also listed in a table in the supplementary information and will be used in the manuscript as a measure for the spatial charge separation in the dye.

**DFT limitations affect TDDFT accuracy** In exact DFT the Koopman's theorem<sup>91</sup> is only valid for the highest occupied KS state, HOMO. However, due to the approximations in the xc-functionals the energy of the HOMO,  $\epsilon_{\text{HOMO}}$ , is not in general a good approximation of the ionization potential. For this reason, in order to calculate electron removal energies we use the difference between the ground state energy of the (N-1)-electron system ( $E_{N-1}$ ) and that of corresponding (N)-electron system ( $E_N$ ). Electron affinities (EA) are also computed from  $E_N - E_{N+1}$ . Due to the intrinsic derivative discontinuities in the exact electronic energy plot as a function of number of electrons<sup>92</sup>, the values for IE and EA derived from GGA functionals are underestimated and overestimated respectively<sup>93</sup>. For this reason, the values reported in this thesis are just given in support of the general trends observed for the investigated dye series rather than an exact evaluation of their electrochemical properties.

**Solution Environment** The cavity model has been widely used to study solvent effects in

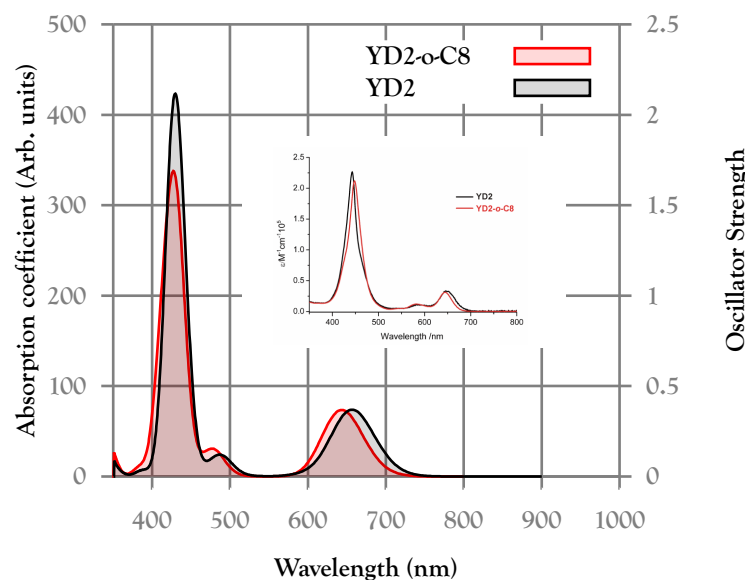


Figure 3.3: M06 is able to capture slight shifts in the absorption spectrum (YD2 Vs. YD2-o-C8). The experimental spectra (inset) from Ref.<sup>3</sup>

chemical and biological systems. This model represents the solvent by a homogeneous continuum medium, which is polarized by the solute placed in a cavity. Such implicit treatment of solvent molecules in quantum mechanical calculations reduces significantly the computational cost and makes these calculations more feasible. Polarizable Continuum Model (PCM) combined with DFT and LR-TDDFT has become a standard protocol for taking solvent effects on molecular properties implicitly into account<sup>94</sup>.

The accuracy of PCM and its efficiency when combined with LR-TDDFT has been reviewed in numerous studies<sup>95–97</sup>, which show that for non-hydrogen bonding solvents, PCM provides an accurate description of solvent effects. Tetrahydrofuran (*THF*) and Chloroform are the solvents commonly used for absorption spectra measurements of porphyrin-based dyes. Possessing very small dielectric constants (7.42 and 4.71, respectively), they are considered rather apolar solvents which don't exhibit significant hydrogen bonding capabilities with porphyrin dyes. While treating the solvent molecules explicitly can be important in processes where large solvent reorganization are expected (e.g. relaxation in an excited state prior to fluorescence or adiabatic relaxation after oxidation), in the cases described here, the porphyrin-based molecule, which is a rather rigid molecule, is optimized at its ground state geometry and the PCM takes into account polarization effects due to the vertical transitions (the non-equilibrium solvation). In the following calculations we are using the integral equation formalism of PCM (IEF-PCM) for describing the THF solvent. For PCM LR-TDDFT calculations of dyes in water or in highly polar solvents, an explicit solvent simulation should assess the quality of a PCM calculation.

**Dye adsorption on the TiO<sub>2</sub> slab** For the dye screening purpose of this work, we addressed the UV/visible spectra of the dyes in solution. It has been seen<sup>71</sup> that upon adsorption on

## Chapter 3. Computational characterization and design of porphyrin-based dye sensitizers: All the way up to 13% efficiency

the TiO<sub>2</sub> surface, porphyrin dyes experience a slight blue shift in their spectra, however, the character of the transitions remain intact. Interesting works have been published that study the changes induced to the electronic structure and the energy alignments for smaller dyes upon adsorption<sup>98-100</sup>.

### 3.3 Results and Discussion

#### 3.3.1 Systematic modifications of the donor, meso, central and acceptor moieties

We started our investigations with some systematic changes of the YD2-o-C8 dye (previous champion dye reported in 2012<sup>3</sup>) monitoring their absorption spectra using Linear response (LR) TDDFT. Subtracting the ground state electron density from that of the excited state, a general pattern for electron and hole localization is recognized for almost all of the zinc porphyrin-based compounds. The negative region corresponds to electronic density depletion (holes), while the positive regions shows an increase of density (electron) (Figure 3.4). The benzoic acid acceptor group accommodates most of the excited electron whereas the remaining excited electron density and part of the hole resides on the porphyrin ring. The largest part of the hole within the ring is localized on the four nitrogens surrounding zinc and on the linking carbon atoms with the meso side groups (orange spots in Figure 3.4).

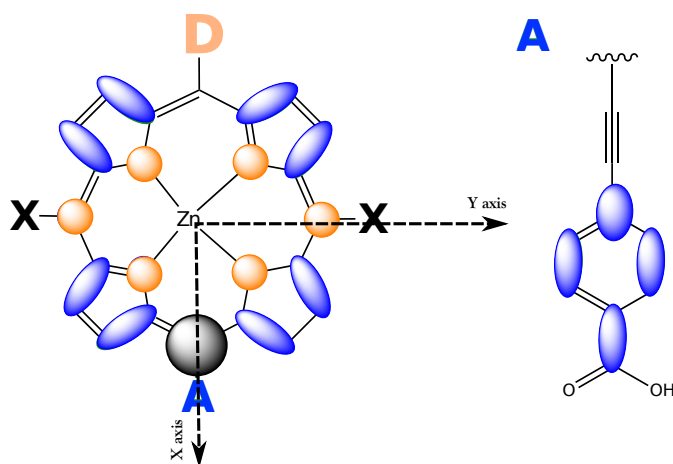


Figure 3.4: General pattern of electron and hole localization on zinc-porphyrin-based dyes. Electron density is moving from the orange regions (holes-donors) to the blue (electrons-acceptor). X stands for meso positions, D for donor and A for the acceptor.

The character of the first transition [ $S_0 \rightarrow S_1$ ] is mainly the same in all compounds (for some metal center modifications this first transition has zero oscillator strength). This lowest energy transition is composed of ca. 80% of HOMO to LUMO transition plus about 20% of HOMO-1 to LUMO+1 transition. As it is evident from the inspection of the YD2-o-C8 orbitals (Figure



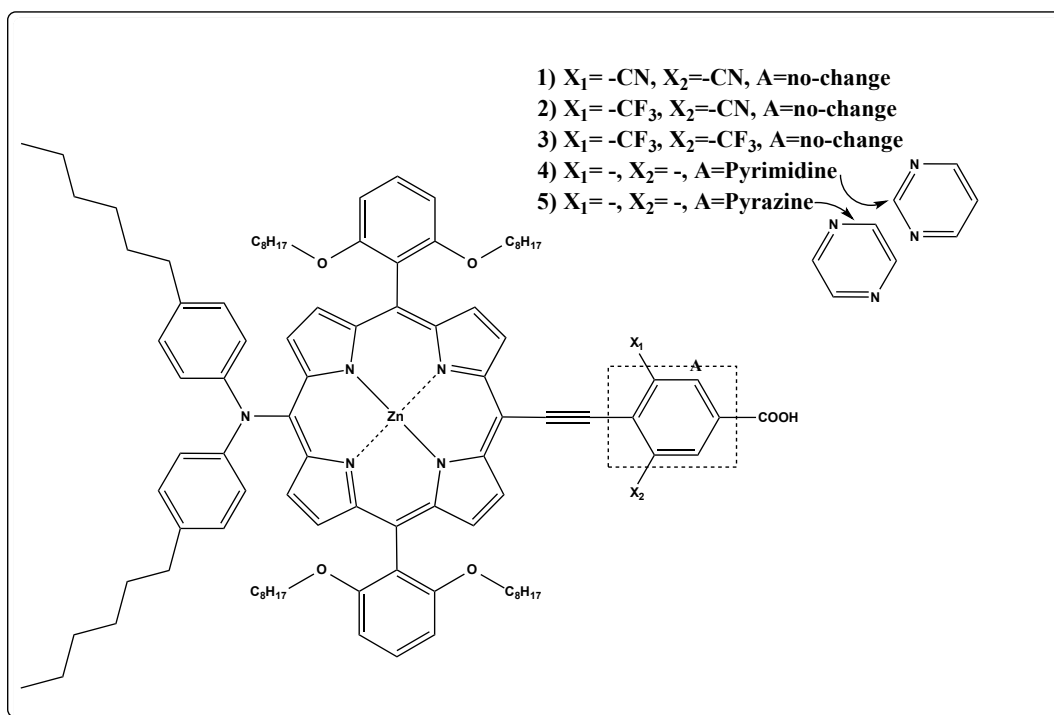


Figure 3.5: Different acceptor modifications of YD2-o-C8.

3.1), in the HOMO to LUMO excitation the electron is pushed from the donor to the acceptor whereas in the HOMO-1 to LUMO+1 transition the electrons and the hole remain confined within the porphyrin ring. In the following sections we follow the changes happening to the electronic structure of YD2-o-C8 through systematic modifications at meso, acceptor, donor and porphyrin positions.

### 3.3.2 Acceptor modifications

In a first series of variations, the acceptor unit was substituted with different typical electron withdrawing groups (EWG) to enhance the electron accepting power and thus redshift the donor to acceptor transition (Figure 3.5). As expected, acceptor variations mostly affect the energetics of the LUMO (Figure 3.6).

Electron deficient functional groups characterized by high Hammett constants<sup>101</sup> stabilize the LUMO and reduce the band gap. In addition, as evident in Figure 3.7, introducing stronger EWG in the acceptor splits the Soret band in two or more main transitions and broadens the spectrum. This feature is usually attributed to the asymmetry induced by increasing the conjugation along donor-acceptor axis and a consequent reduction of conjugation along the perpendicular axis<sup>71</sup>. In the fully symmetric tetramethylporphyrin, the Soret band is composed of two perpendicular axial and vertical degenerate transitions corresponding to excitations along the axial and the (perpendicular) vertical direction (Bx and By respectively).

**Chapter 3. Computational characterization and design of porphyrin-based dye sensitizers: All the way up to 13% efficiency**

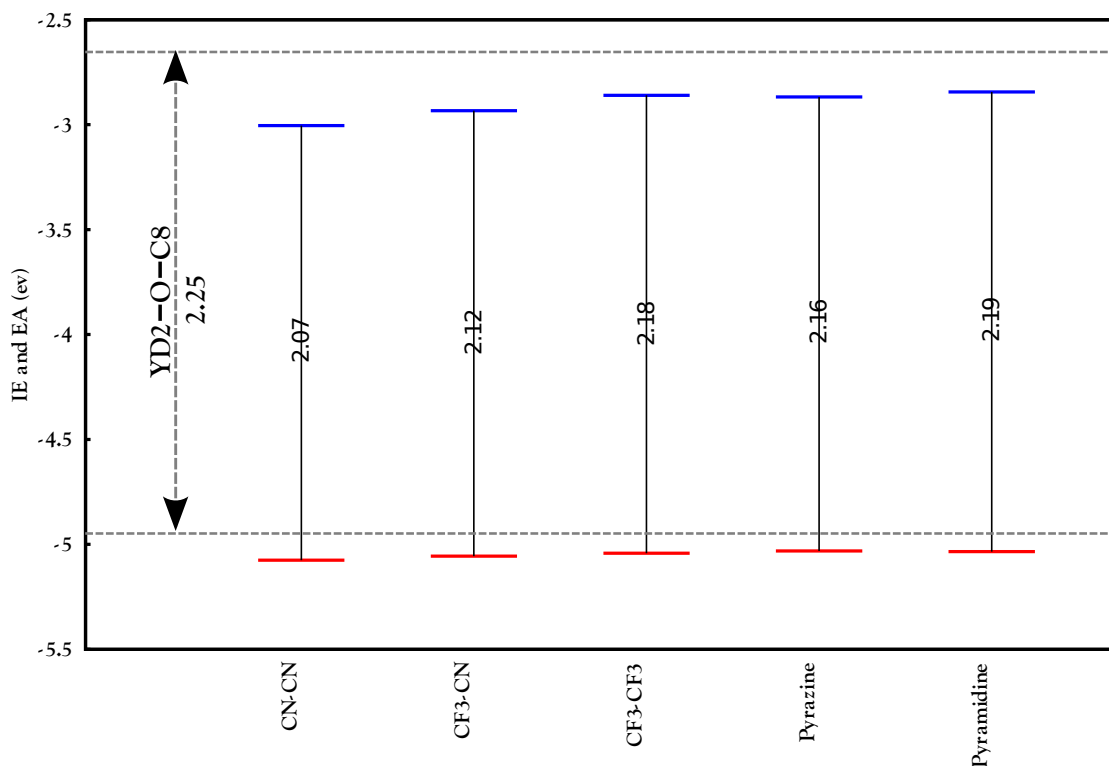


Figure 3.6: Calculated vertical Ionization energies (IE) (red) and negative of Electron affinities (EA) (blue) for acceptor-modified derivatives.

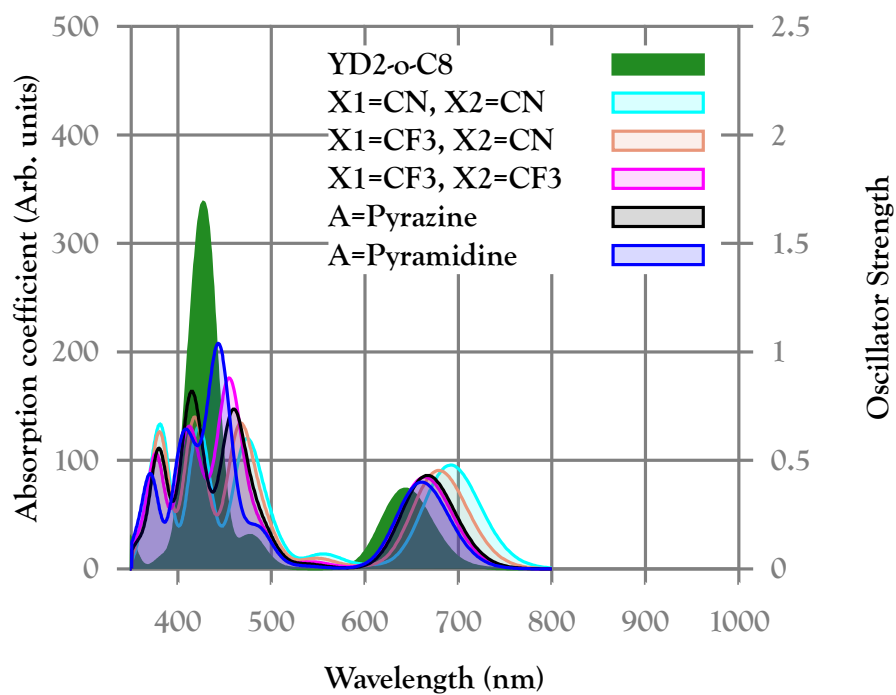


Figure 3.7: Calculated UV-visible absorption spectra for acceptor-modified derivatives.

By functionalizing porphyrin dyes with different donors and acceptors, conjugation along the x-axis<sup>3.4</sup> can be increased, which breaks the symmetry and lifts the degeneracy of the B<sub>x</sub> and B<sub>y</sub> transitions. For instance, the Soret band in YD2-o-C8 is composed of three electronic transitions at 412 nm, 429 nm, and 477 nm with oscillator strengths of 0.21, 1.99, and 0.89 respectively. All three transitions are mostly localized on the porphyrin ring with a small portion on the donor (Figure 3.8). Introducing two cyano groups in the benzoic acid (acceptor) changes the composition of the Soret band (Figure 3.8). Three electronic transitions constitute the Soret band (421 nm, 471 nm, and 495 nm with oscillator strengths of 0.83, 0.76, and 0.23 respectively) are in general red-shifted with respect to YD2-o-C8. Unlike YD2-o-C8, these transitions are not localized on the bridge only. At 471 nm (S<sub>0</sub> → S<sub>5</sub>), 56% of the transition is distributed along the x-axis. Employing the strong electron-withdrawing cyano group in the acceptor induces more extended charge transfer (CT) transitions. The oscillator strength of this transition (B<sub>x</sub>) is comparable with the B<sub>y</sub> transition while their energies are no longer similar, leading to a wider splitting of Soret band.

Cyano groups are highly efficient EDG but due to their limited stability and potential toxicity they are not ideal substituents and are avoided if possible also in the case of Ru-based dyes<sup>65,102</sup>. In some cases, cyanides can be replaced with EWGs like the electron deficient benzothiadiazole (BTD) group or quinoxaline acceptors. We will shortly discuss their effects in the "Combined modifications" section. Cyano groups strongly pull the electrons as can be seen from Figures 3.11 and 3.12, whereas no electron density is located on F atoms in the acceptor.

#### 3.3.3 Donor modifications

For donor modifications, substitution with electron rich donor groups were tested. Many of these groups have already shown good performances in organic dyes<sup>65,70</sup>. SM371 bears electron donating alkoxy-biphenyl (o,p-dibutoxyphenyl) in para position on the amine, which is known for back recombination features<sup>103</sup>. This donor has a pronounced electron push ability which results in a broad absorption spectrum with a lowest energy transition at 650 nm. The twist present in the biphenyl moiety diminishes the electron conjugation and consequently the charge transfer propensity (Figures 3.9 and 3.10).

In contrast to SM371, SM209 benefits from a planar fluorene donor, which brings the electron donating alkoxy groups in conjugation with the central amine. As a result the charge is spread in a more delocalized manner (lower overlap or  $\Lambda$  value) thus, the SM209 spectrum is significantly red shifted compared to that of SM371 (Figure 3.9).

In SM0 the alkyl chains on the phenyl rings of the amine donor are replaced by alkoxy groups. This small change induces a slight red shift in the spectrum by destabilizing the HOMO. HOMO-1 is no longer localized on the porphyrin ring only but and is also a bit extended over the donor (look at the decrease in  $\Lambda$  value). Since 18% of [S<sub>0</sub> → S<sub>1</sub>] transition are due to HOMO-1 to LUMO+1 excitations, this can further contribute to the slight red shift. A similar

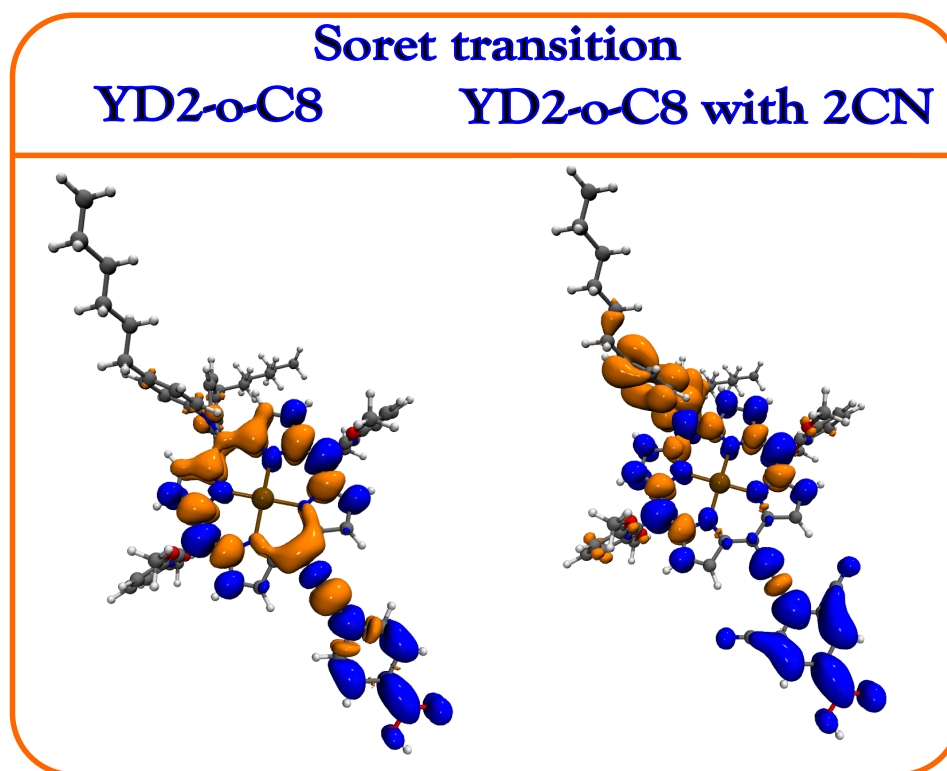


Figure 3.8: Soret band electron and hole distribution in YD2-o-C8 and YD2-o-C8-2CN

effect can be observed between SM01 and SM00 where the donor is based on a triphenyl group and the addition of the terminal alkoxy group for SM00 results again in a slight red shift together with a lower  $\Lambda$  parameter which implies a stronger CT character of the transition.

Incorporating phenylethynyl groups as linkers between the porphyrin and the donor expands the  $\pi$ -conjugation along the  $x$ -axis. Using it in both left and right hand side of the porphyrin, however, will create a push-pull dye. Depending on the strength of the terminal groups at each side, electrons move towards the direction with the stronger electron-withdrawing group. The long highly conjugated system with two phenylethynyl moieties along the  $x$ -direction (D-A axis in general) promotes the charge transfer (ICT) along this axis.

This however, does not apply for systems with a relatively weak donor where there is no preferred direction for the excited electrons to move along. Chen-Fu et al.<sup>104</sup> have extensively investigated this by incorporating different terminal donor groups. As expected, devices made with dyes with nitroxy  $-\text{NO}_2$  (with highly positive Hammett constant 0.78) substituted donors demonstrate the lowest photoconversion efficiencies, whereas dimethylamine with its highly negative Hammett constant can push the electrons towards the acceptor of the molecule more efficiently. The same effect is observed here for SM01 and SM02. Introducing an ethynyl link on the donor (SM02) side triggers more ICT resulting in a more red-shifted spectrum. With three phenyl groups, the SM02 donor is richer in electrons compared to the dimethylamine moiety in LD14. Moreover, bulky donor moieties generally perform better in real devices as

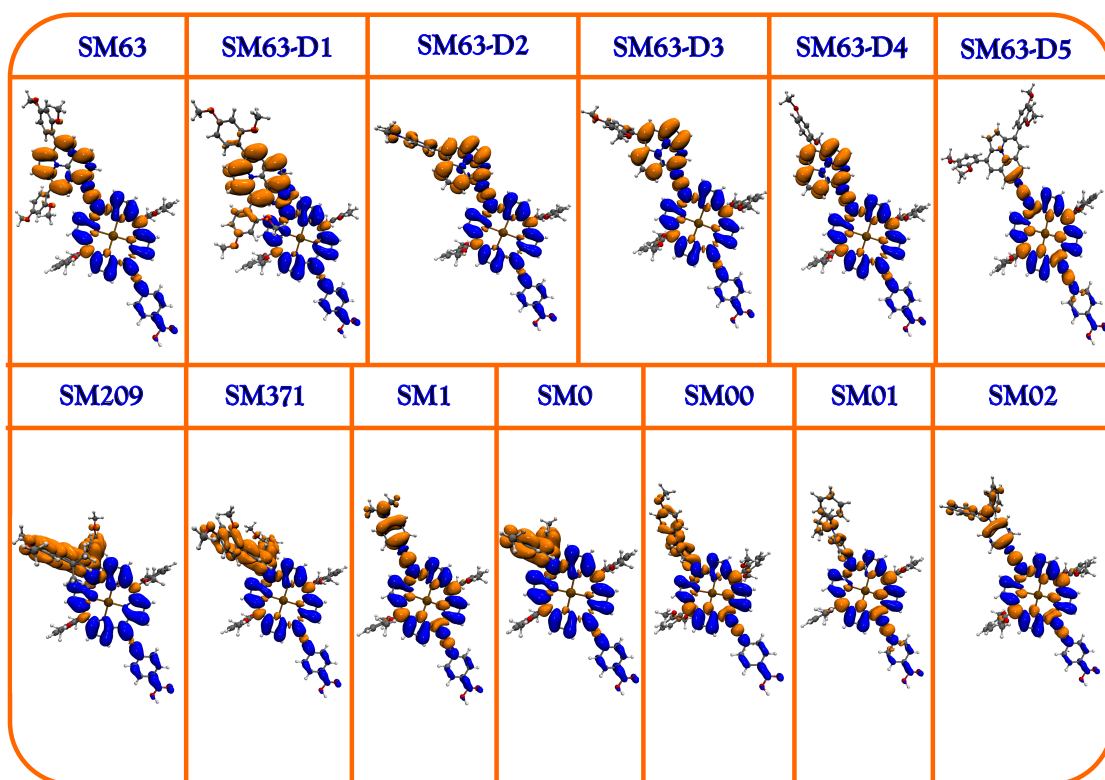


Figure 3.9: Electron-hole density map of the  $[S_0 \rightarrow S_1]$  vertical transition for donor-modified derivatives. The density difference contour plots ( $\rho_{S_1} - \rho_{S_0}$ ) show the electron distribution in blue and the hole distribution in orange. Isovalue set to 0.0003 a.u.

Chapter 3. Computational characterization and design of porphyrin-based dye sensitizers: All the way up to 13% efficiency

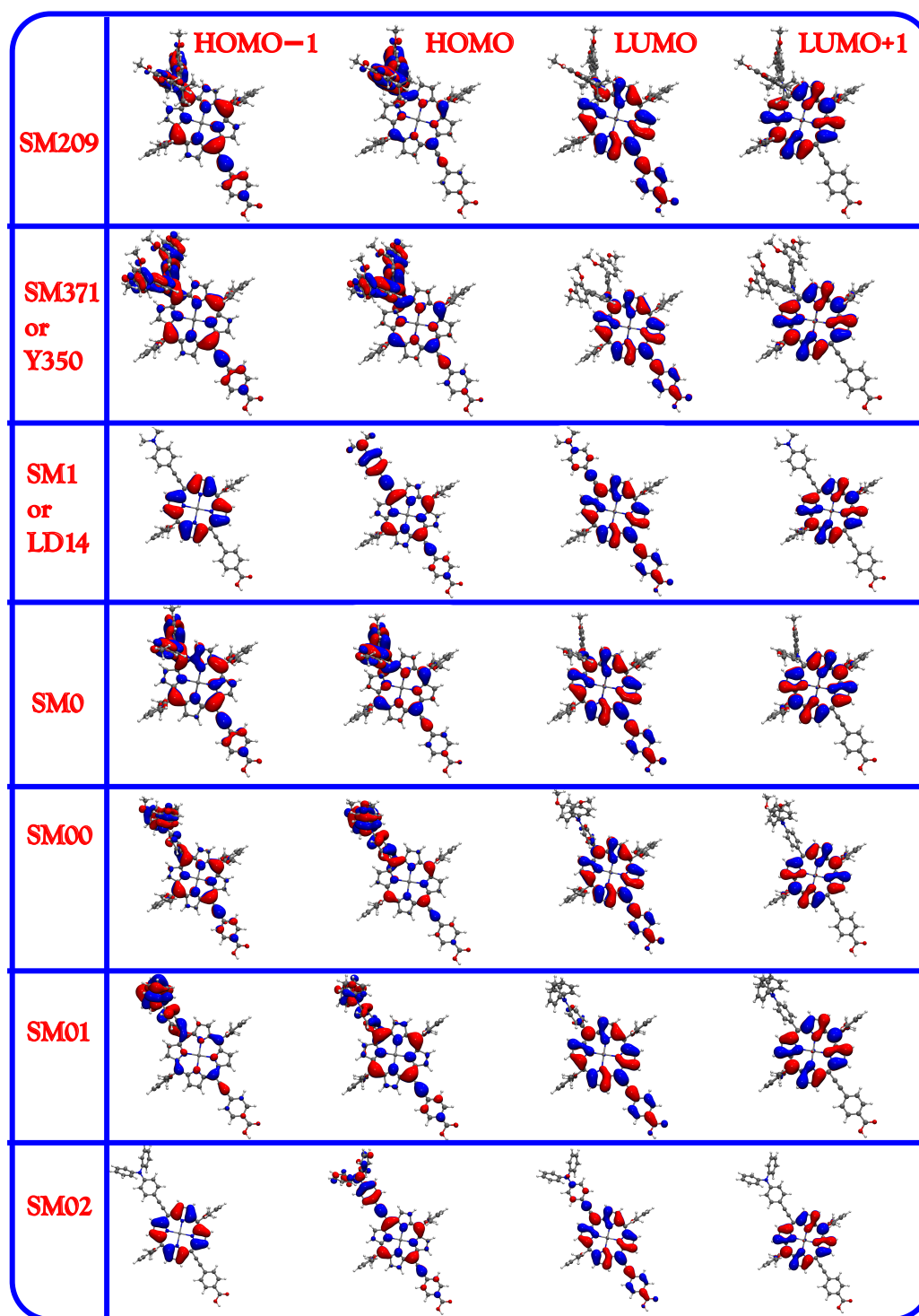


Figure 3.10: Frontier Kohn-Sham orbitals for donor modified derivatives (isovalue is 0.02 a.u.)

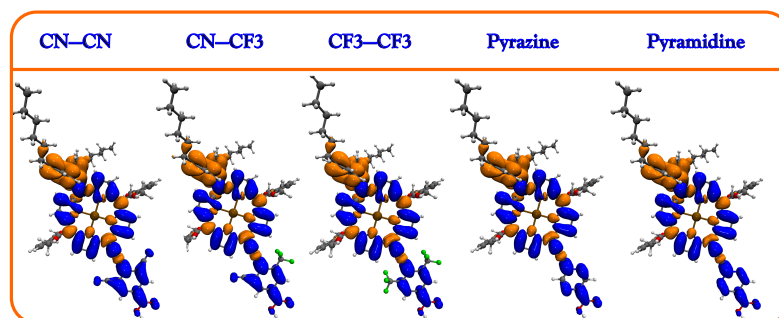


Figure 3.11: Electron-hole density map of the  $[S_0 \rightarrow S_1]$  vertical transition for acceptor-modified derivatives. The density difference contour plots ( $\rho_{S_1} - \rho_{S_0}$ ) show the electron distribution (blue) and the hole distribution (orange). Isovalue set to 0.0003

they can reduce charge recombination by preventing the electrolyte from approaching the surface of the semiconductor.

This has motivated the search for a bulky highly conjugated donor group with, at the same time, a strong electron push character. Recently ullazine has been introduced for application in organic<sup>104</sup> and porphyrin-based dyes (work under preparation). The electron-rich ullazine unit<sup>105,106</sup> is a 16  $\pi$ -electron nitrogen-containing heterocyclic annulene system which thanks to its planar structure promotes ICT and possesses both electron-donating (pushing) and electron withdrawing (pulling) properties. In addition, it is known to form stable cations<sup>105</sup>. Not surprisingly, among the donors we tested in this work (Figure 3.13), ullazine-based donors on average show a superior ability to harvest the light. Possessing multiple possible substitution sites (left inset in Figure 3.13) makes it a good candidate for molecular engineering.

Due to its ambivalent nature (that can function both as a donor or as an acceptor group), ullazine's electronic properties can be so sensitive to the binding site through which it is incorporated. The general pattern of electron and hole distribution for ullazine (left inset in Figure 3.13) suggests that the hole (orange) resides mostly on the periphery, whereas the electron (blue) is localized on the upmost carbon with respect to the imminium motif<sup>106</sup>. Considering the predominant  $[HOMO \rightarrow LUMO]$  nature of the first excitation, the aforesaid pattern holds for most of our studied ullazine-based compounds (look at HOMO expanding on ullazine moiety in Figure 3.14), for SM63-D5 however, the lowest energy excitation has a different character. Here (in line with previous reports of Feng. et al on organic dyes<sup>106</sup>) the first excited state  $S_1$  is mainly (70%) composed of  $[HOMO - 1 \rightarrow LUMO]$  transition and unlike the five other compounds, H-1 doesn't expand to the ullazine periphery. Looking at the  $\Lambda$  parameters, indeed SM63-D5 acquires the highest value among all (see table 3.1).

This implies that electron and hole overlap in this compound is maximum. That is, this excitation has just a little charge transfer character and that's why it gives the most blue shifted spectrum of all (Figure 3.15). More precisely, incorporation of ullazine via its 6th binding site, intercepts any electronic communication with the rest of the dye. This was expected already from the wave function node present in the frontier orbitals of ullazine at this binding site

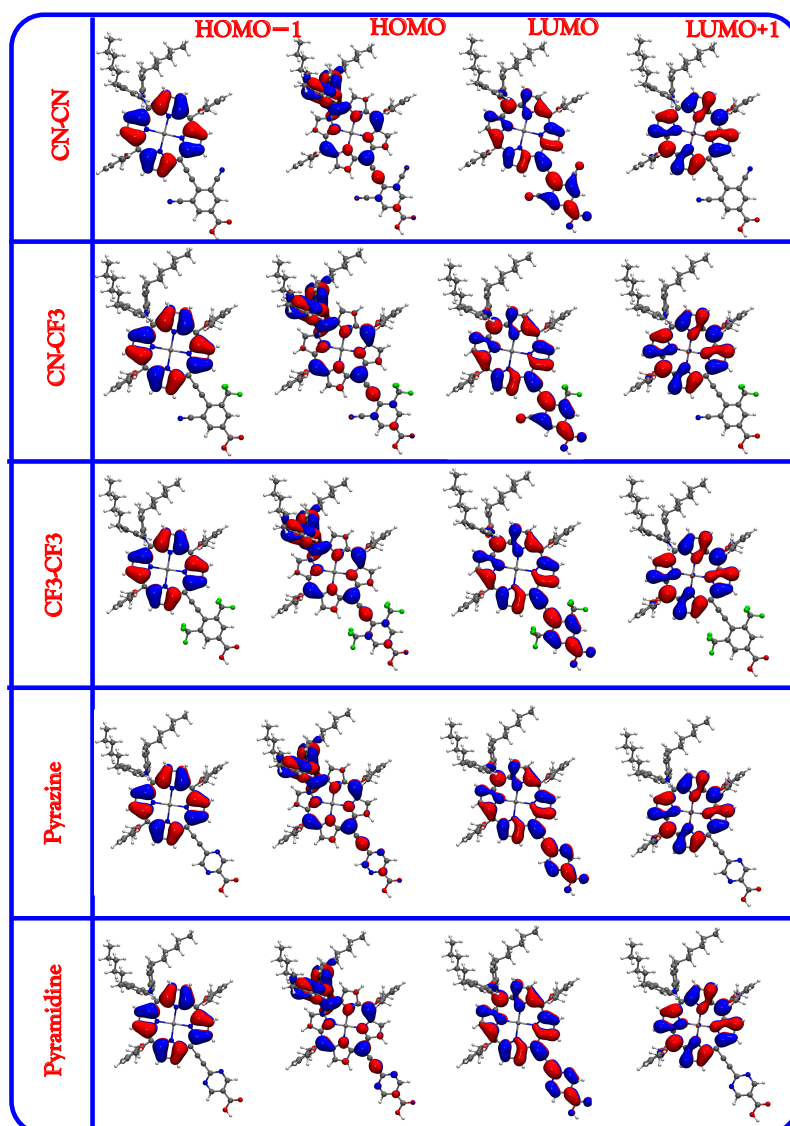


Figure 3.12: Frontier Kohn-Sham orbitals for acceptor modified derivatives (isovalue=0.02 a.u.)



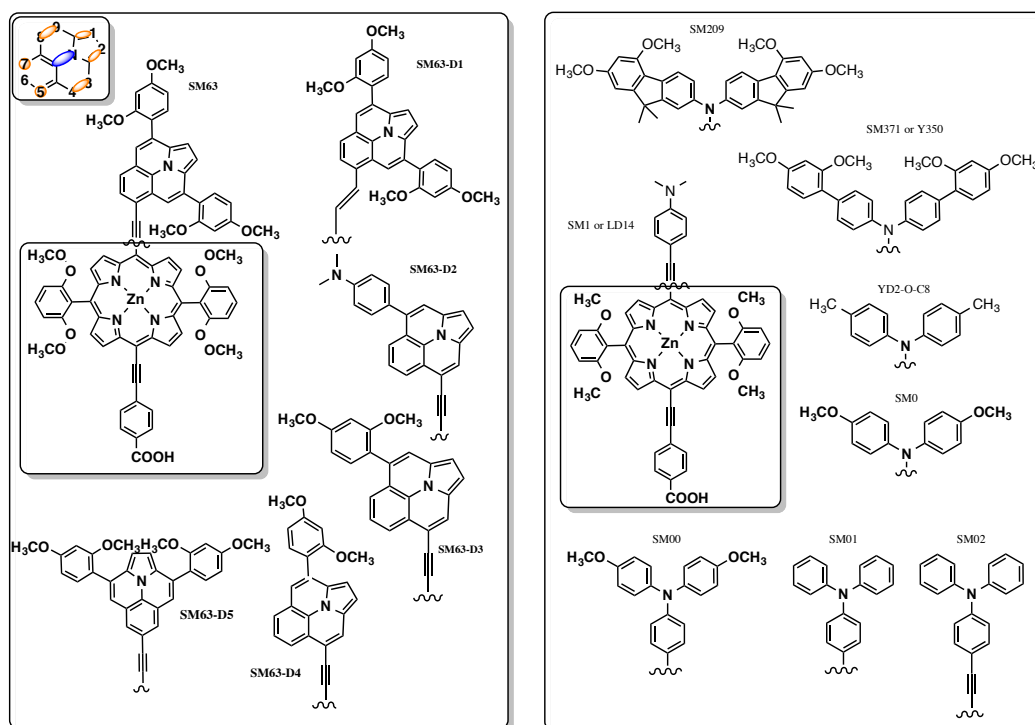


Figure 3.13: Different donor modifications on YD2-o-C8. The inset shows the general pattern of electron and hole distribution in Ullazine moiety.

(look at the inset in Figure 3.13).

Similar to the aforementioned case of the porphyrin base and its meso position substituents, a non-zero dihedral angle is also present between the heterocyclic annulene of ullazine and its peripheral substituents. Comparing SM63-D2 and SM63-D3 which have substituents at similar binding site of the ullazine (site 8) while differing by terminal aniline and phenyl methoxy substituents respectively, we can see that in SM63-D3 the phenyl moiety rotates slightly with respect to the ullazine plane due to the subsistent steric hindrance between the ortho methoxy and the ullazine itself (forming a dihedral angle of ca.  $52^\circ$ ). In SM63-D2, this angle is reduced by  $5^\circ$  and consequently an extension of the hole to the attached functional group (aniline substituent) is observed (orange regions in Figure 3.9, also look at the decrease in  $\lambda$  parameter). All SM63 derivatives, have destabilized HOMO energy levels (Figure 3.16).

Chapter 3. Computational characterization and design of porphyrin-based dye sensitizers: All the way up to 13% efficiency

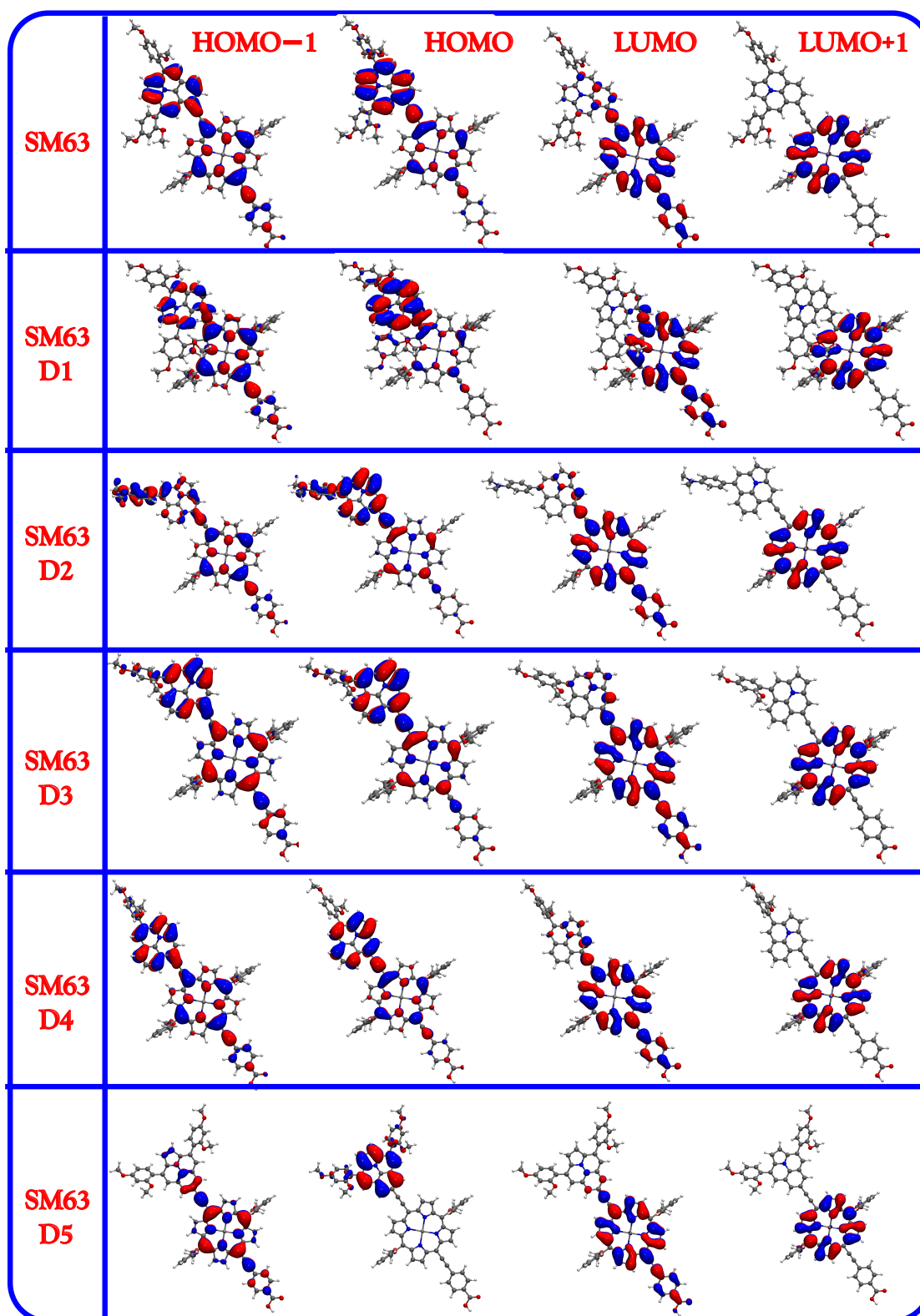


Figure 3.14: Frontier Kohn-Sham orbitals for donor-modified derivatives (isovalue is 0.02 a.u.)

### 3.3. Results and Discussion

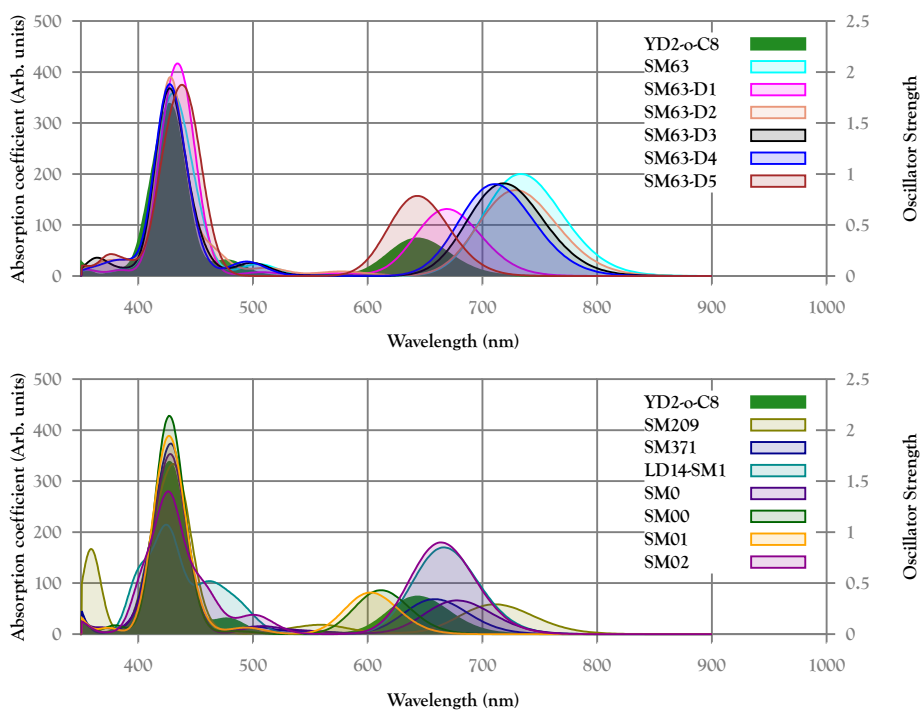


Figure 3.15: Calculated UV-visible absorption spectra for donor-modified derivatives.

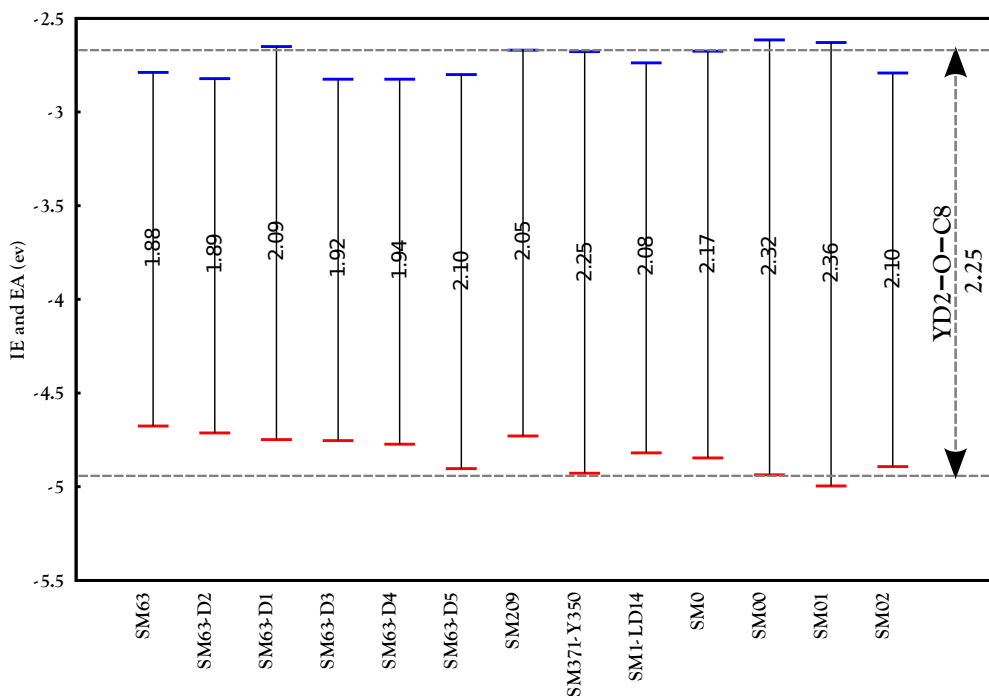


Figure 3.16: Calculated vertical Ionization energies (IE) (red) and negative of Electron affinities (EA) (blue) for donor-modified derivatives.

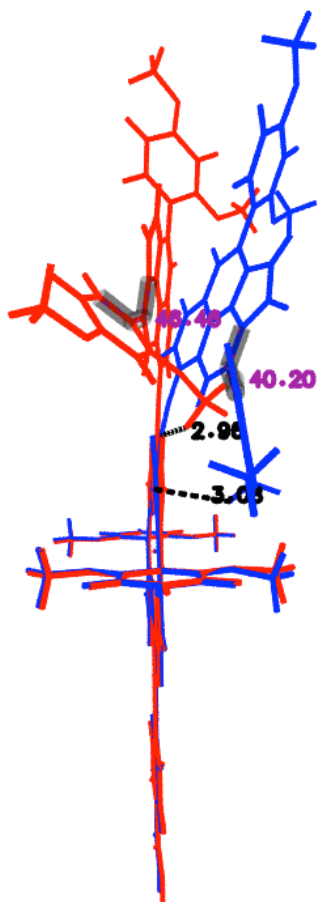


Figure 3.17: Reduced steric hindrances in the bent structure (global minimum) versus the planar structure (local minimum): Also the dihedral angle is decreasing giving rise to a stronger electron push and consequently a red-shifted spectrum

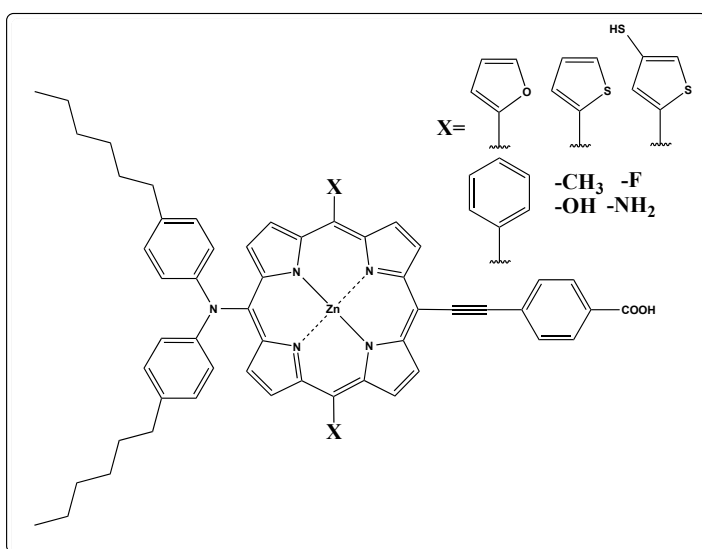


Figure 3.18: Different meso position modifications of YD2-o-C8.

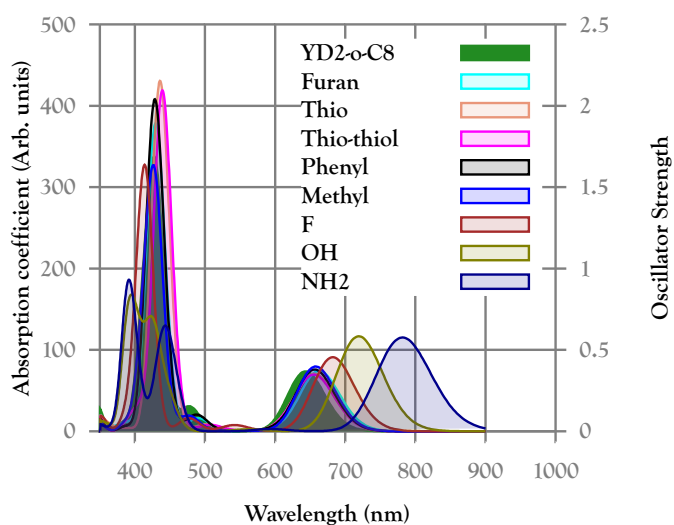


Figure 3.19: Calculated UV-visible absorption spectra for modifications applied to the meso position.

Inclining the donor moiety downward (bowing), SM63, sacrifices some of electron conjugation to gain stability through establishing Van der Waals interactions with the vertically rotated phenyl methoxy at porphyrin's meso position. Our calculations show that the bent structure is 4 Kcal/mol more stable than the planar structure where the electron conjugation was stronger. The Van der Waals nature of this difference in energy was assessed using the BLYP<sup>107,108</sup> functional which is known for not describing the dispersion interactions correctly. Indeed BLYP functional favors the planar structure by 4 Kcal/mol. Adding the Grimme correction<sup>109</sup> to BLYP for treating dispersion forces, the stability is once more reversed confirming the fact that the bowed structure is indeed the result of weak VDW interactions.

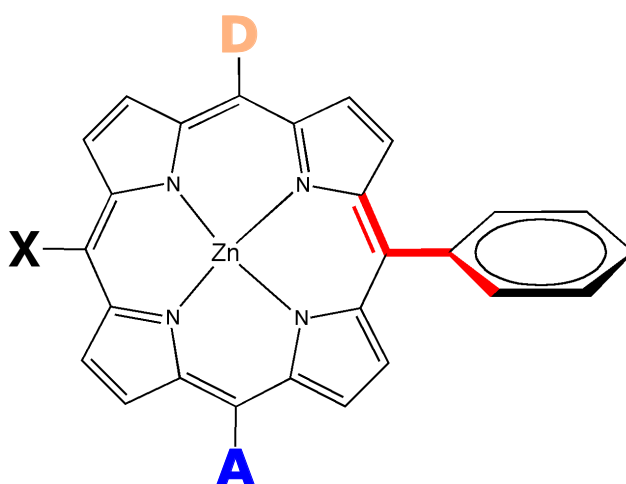


Figure 3.20: Dihedral angle formed between the aromatic meso substituents and the porphyrin base.

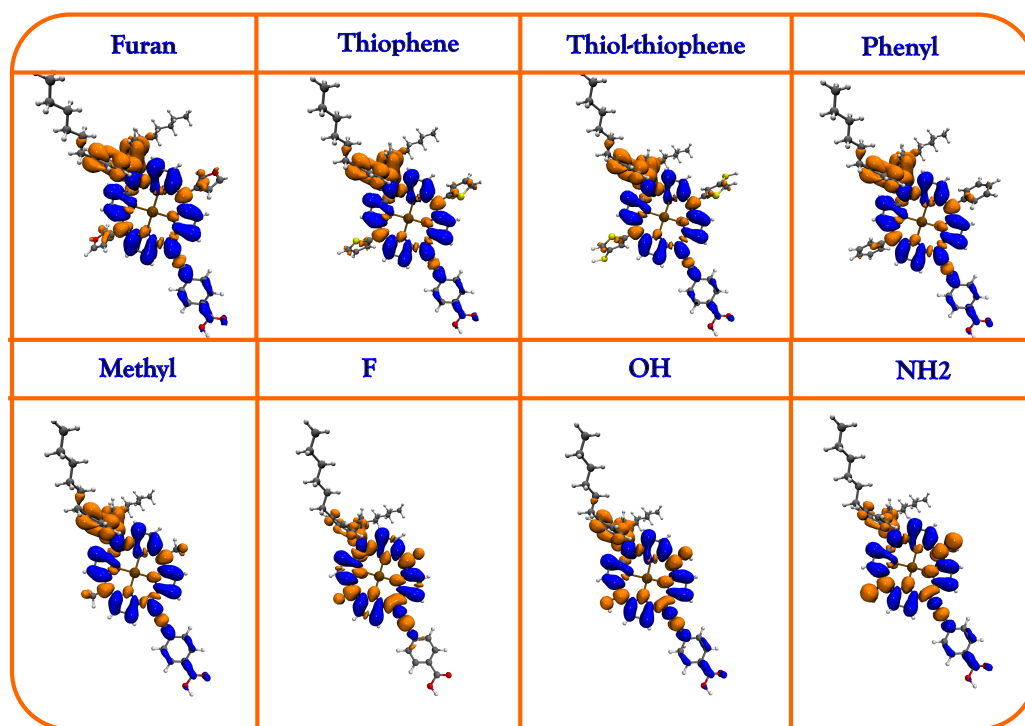


Figure 3.21: Electron-hole density map of the  $[S_0 \rightarrow S_1]$  vertical transition for meso-modified derivatives. The density difference contour plots ( $\rho_{S_1} - \rho_{S_0}$ ) show the electron distribution in blue and the hole distribution in orange. Isovalue set to 0.0003 a.u.

Among all ullazine-based compounds, the bent structure is only observed for SM63 where the periphery substituent of ullazine is close to the porphyrin ring. Moreover, substituting phenylmethoxies in site 3 of the ullazine, creates steric clashes between the periphery of ullazine and the porphyrin base (Figure 3.17). Introducing an ethylene bond (SM63-D1) instead of the alkyne bond we can try to reduce the structural conflict, however, this breaks the planarity of the molecule and its electronic conjugation, which shifts the spectrum towards blue. The small  $\Lambda$  value or small spatial overlap of the first transition is due to the broken electron conjugation rather than the charge transfer character of  $S_1$ .

### 3.3.4 Variations of the porphyrin moiety: modification of the substituent in meso position

According to the electron/hole pattern in Figure 3.4, the meso position participated in hole accommodation. Electron donating groups (EDG) in this position should thus have a stabilizing effect. A number of textbook EDG groups (Figure 3.18) were thus scanned as possible meso substituents. The general trend that can be observed is that the more basic functional groups (with negative Hammett constants) introduce a red shifted spectra (Figure 3.19). The largest red shift is observed for  $-\text{NH}_2$  substituent. Aromatic groups do not shift the spectrum considerably. Interestingly F substituent is among the red shifted spectra.

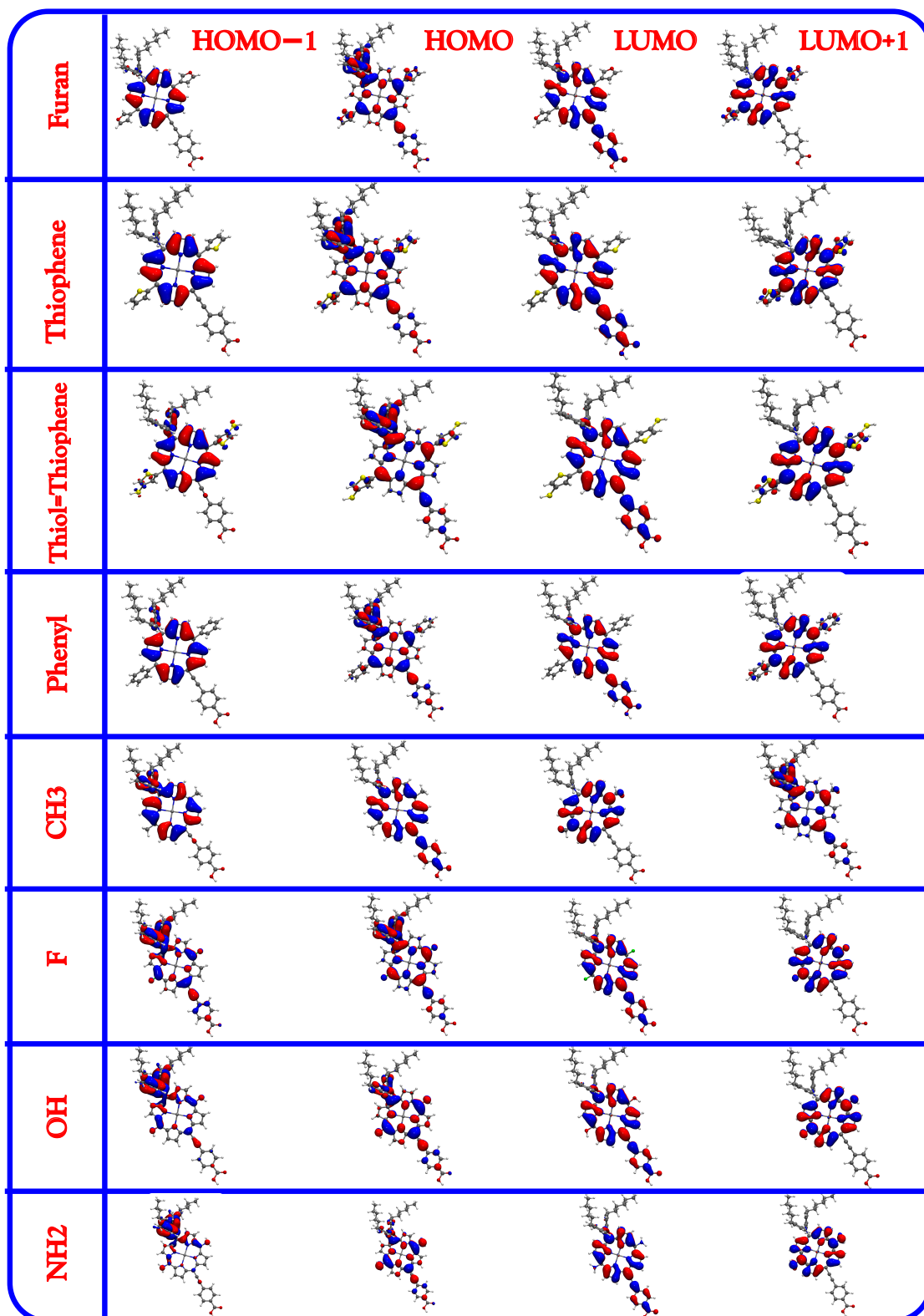


Figure 3.22: Frontier Kohn-Sham orbitals for meso modified derivatives (isovalue is 0.02 a.u.)

**Chapter 3. Computational characterization and design of porphyrin-based dye sensitizers: All the way up to 13% efficiency**

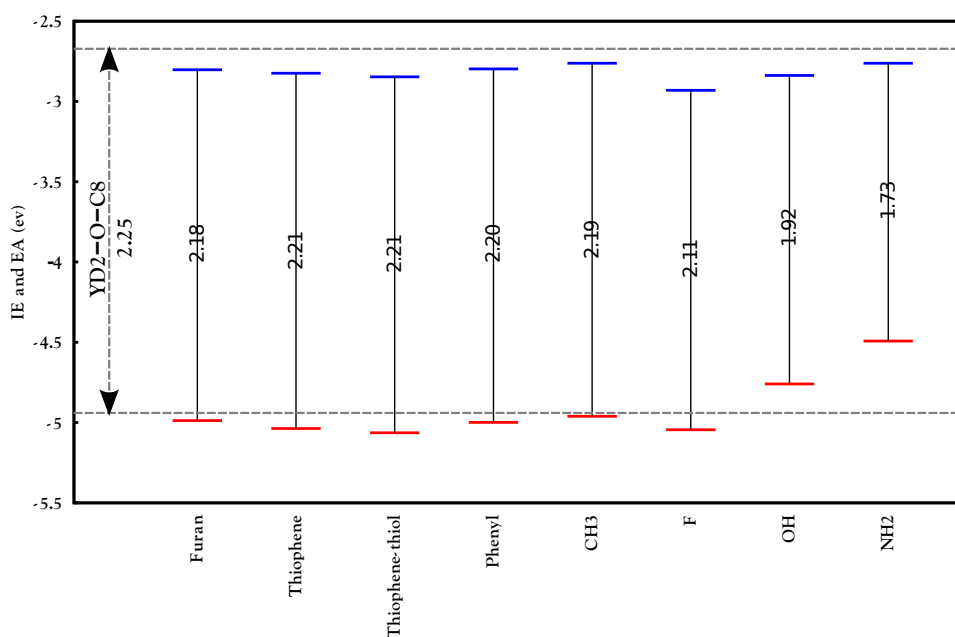


Figure 3.23: Calculated vertical Ionization energies (IE) (red) and negative of Electron affinities (EA) (blue) for meso-modified derivatives.

For some of the bulkier heterocyclic substituents, steric hindrance with the porphyrin rings leads to twisting characterized by the dihedral angle shown in Figure 3.20. This rotation reduces or even breaks electronic conjugation between the porphyrin and the aromatic substituents.

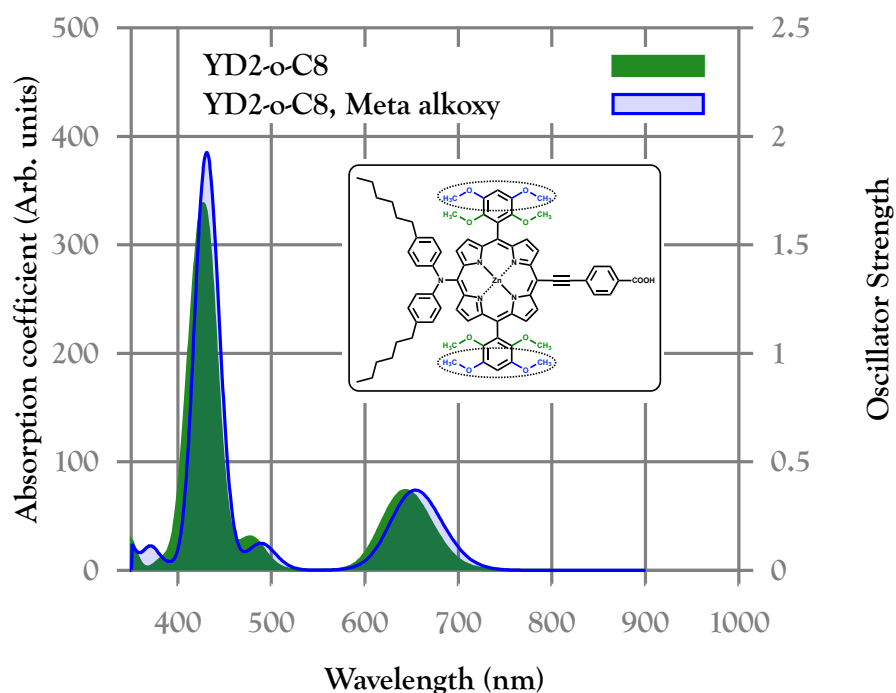


Figure 3.24: Meta (blue) and Ortho (green) position of the the alkoxy group.



Larger dihedral angles ( $60^\circ$ ) prevent electron communication entirely and shift the spectrum to the blue. Furan induces the smallest twisting from the plane (ca.  $58^\circ$ ) among all the aromatic substituents: phenyl, thiophene, thiol-thiophene and phenylmethoxy (reference YD2-o-C8) which give twisting angles of  $60.1^\circ$ ,  $62.2^\circ$ ,  $65.8^\circ$ , and  $88.7^\circ$ , respectively. The furan substituted dye indeed results in the largest red shift, confirming that a certain amount of planarity is needed for keeping the electronic communication. The electron-hole density map of furan (Figures 3.21 and 3.22) indeed displays a stronger donating effect on the bridge compared to that of thiophene, thiol-thiophene, phenylmethoxy (Figure 3.1) and phenyl substituents (orange spots on the furan heterocyclic group). Clearly aromatic substituents do not fall into the general trend we expected from the general electron and hole pattern (because of the rotation);

However, for non-aromatic groups as expected from the general electron and hole distribution (Figure 3.4), substitutions at meso position mainly affect the HOMO energetics and leave the LUMO almost unchanged (Figure 3.23). F substituent is only inducing a better red-shift w.r.t the aromatic groups because the sterical rotation do not let the aromatics to contribute electronically.

In the reference compound YD2-o-C8, the methoxy groups in ortho position of the phenyl groups lead to an essentially orthogonal orientation of the porphyrin base and the phenyl methoxy substituent in meso position breaking any electron conjugation effects. This can be avoided by moving the methoxy groups to the meta position of the phenyl groups which induces a twisting angle of  $68^\circ$  and a red shifted spectrum (Figure 3.24).

#### 3.3.5 Changes of the central metal ion

In this section we investigated in a systematic way, the effect of modifications of the porphyrin metal. Mimicking from nature we chose Mg(II) and Cobalt(II) which are central ions in chlorophylls and cobalamins, respectively. We also tested Cu(II), Pb(II) and Sn(IV) metallated porphyrins already employed for water purification and optical applications<sup>110–113</sup>. As a general rule, these compounds all satisfy simple criteria: the central metal have an ionic radius between 40 and 60 pm to fit inside the porphyrin ring and its oxidation state is between II and III. Large size of Sn IV (69pm) and Pb II (79 pm) ions, introduce distortion to the molecule, which in turn gives rise to a significant red shift due to the broken symmetry. Adding axial ligands to Sn IV can restore the planarity and stability to the molecule, however, its HOMO and LUMO energetic levels are quite different from the other bivalent cations (Figure 3.25). Among all, Pb and Sn show the most red-shifted spectra. While for Pb this can be due to the distorted structure, this is not the case for Sn with axial ligands, which, as mentioned before, preserves planarity.

**Chapter 3. Computational characterization and design of porphyrin-based dye sensitizers: All the way up to 13% efficiency**

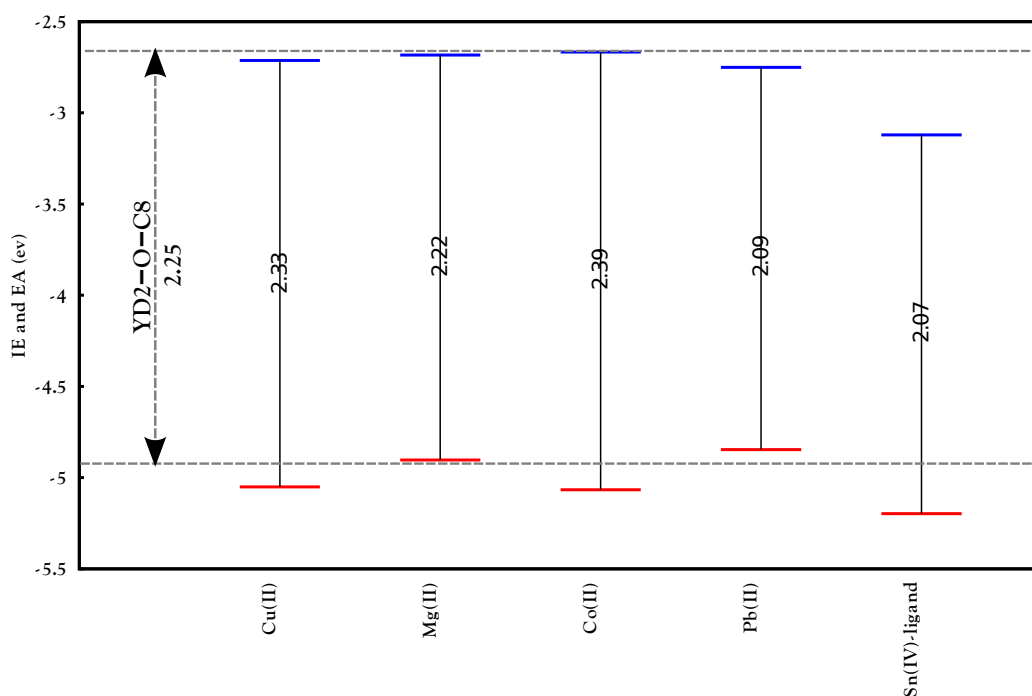


Figure 3.25: Calculated vertical Ionization energies (IE) (red) and Electron affinities (EA) (blue) for metal porphyrin derivatives.

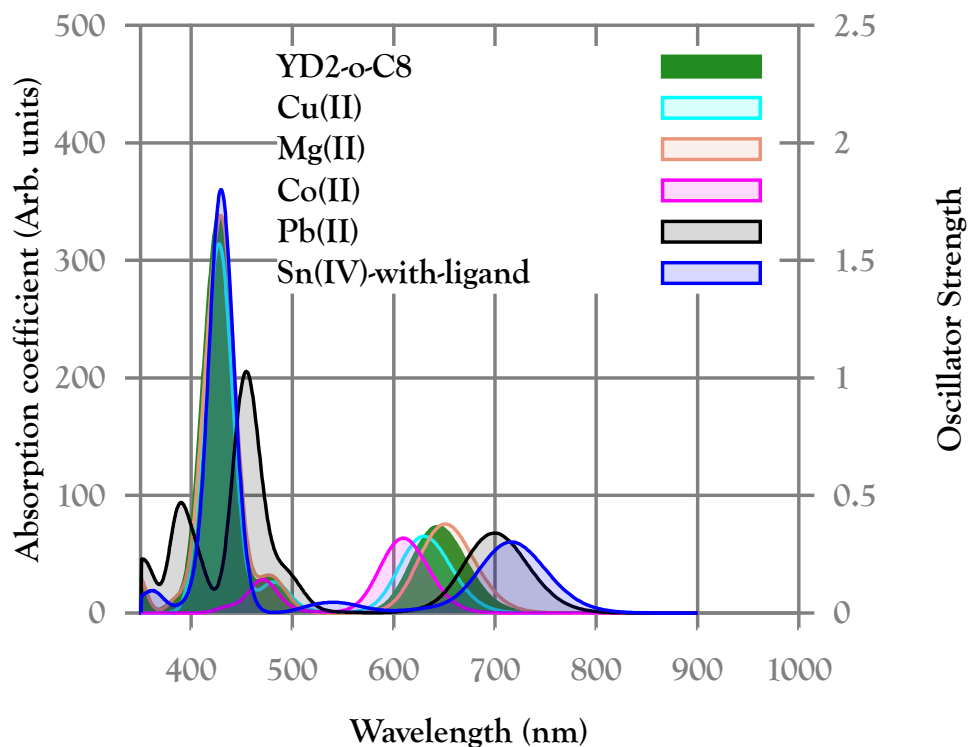


Figure 3.26: Calculated UV-visible absorption spectra for different metal porphyrin derivatives.

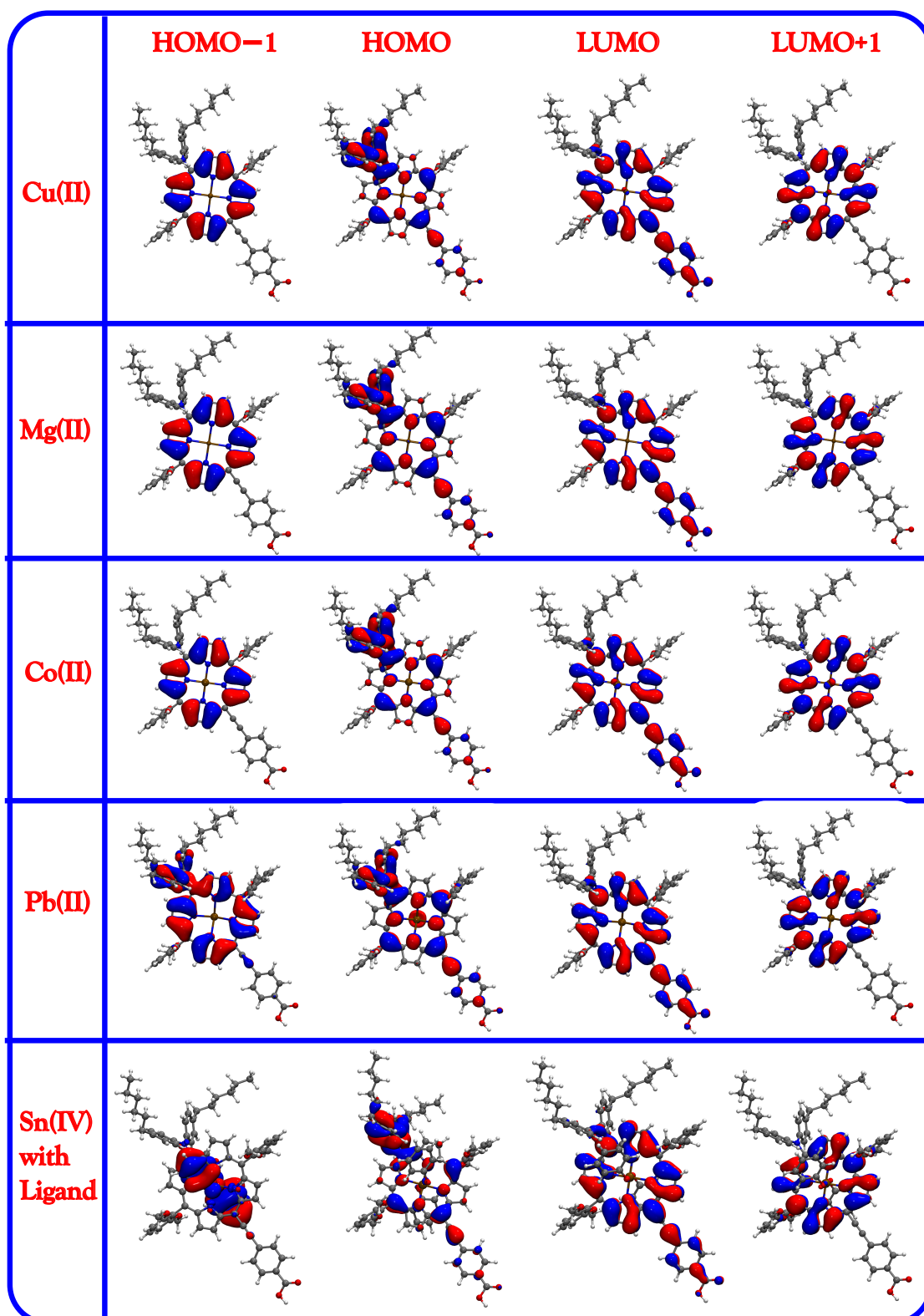


Figure 3.27: Frontier Kohn-Sham orbitals for metal porphyrin derivatives (isovalue is 0.02 a.u.). HOMO and LUMO for Co and Cu-based porphyrins are just shown for consistency, otherwise the first optically allowed excitation of these two dyes are not HOMO/LUMO transitions.

### Chapter 3. Computational characterization and design of porphyrin-based dye sensitizers: All the way up to 13% efficiency

Even though our calculations for Pb-porphyrins give converged results for the absorption spectra (Figure 3.26), it is possible that the system is not stable in practice and that metal free porphyrin is produced instead. Cobalt compounds eliminate the Soret band due to a depletion of the electron density in the porphyrin ring (Figures 3.27 and 3.28), Teng et al.<sup>114</sup> observed the same effect by incorporating Co in free porphyrins.

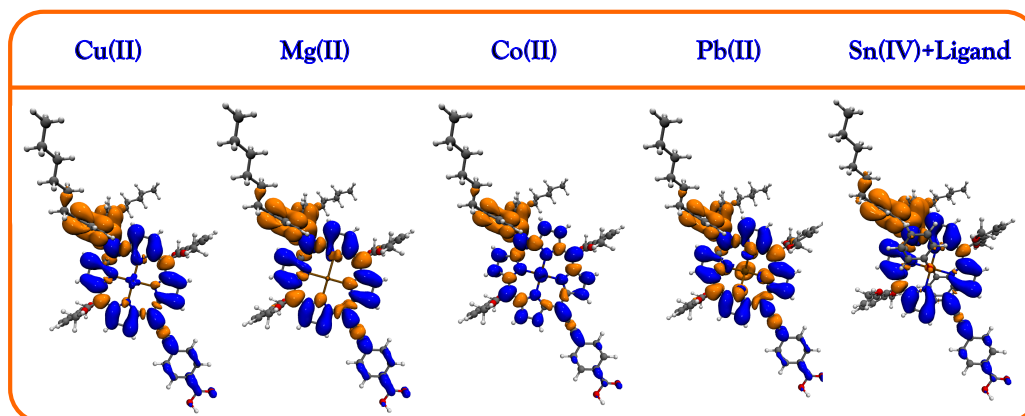


Figure 3.28: Electron-hole density map of the [S0 → S1] vertical transition for Sn and Pb-centered porphyrin dyes, [S0 → S6] vertical transition of Cu-based porphyrin and [S0 → S11] vertical transition of Co-based compound. The density difference contour plots ( $\rho_{S^*} - \rho_{S0}$ ) show the electron distribution in blue and the hole distribution in orange.  $S^*$  stand for the corresponding excited state for each compound. Isovalue set to 0.0003 a.u.

The lowest energy transitions in Co and Cu-based porphyrins have zero oscillator strength. Their first (lowest energy) considerable excitation (high oscillator strength) is for [S0 → S11] and [S0 → S6] transitions respectively. Since higher excited states have short lifetimes, these dyes are not expected to show proper electron injection. In conclusion, ligated Sn-based porphyrin seem to be the most promising compound except for its pretty low LUMO energy which can hamper the electron injection.

#### 3.3.6 Combined dyes

Based on the previously gained knowledge in donor, acceptor and porphyrin variations, some combined variations of different components were also tested (Figure 3.29). Incorporating bulky donor and acceptor groups, with extended  $\pi$  system, the electron conjugation can be maximized. However, not all these transitions necessarily enhance the photocurrent. As an electron-withdrawing group, quinoxaline has been employed as an electron acceptor substitution in the meso position (Y789 and its derivatives Y789-D1 and D2) to enhance the charge transfer character of the electronic transitions. For the same reason 2,1,3-benzothiadiazole (BTD) was introduced to SM315 as an acceptor. Interestingly, Y789 and Y789-D1 are both showing significant red shifted spectra, however from the corresponding electron/hole distributions, it becomes clear that the electronic excitation is not extended enough to deliver electrons to the carboxylic group (Figures 3.30 and 3.31).

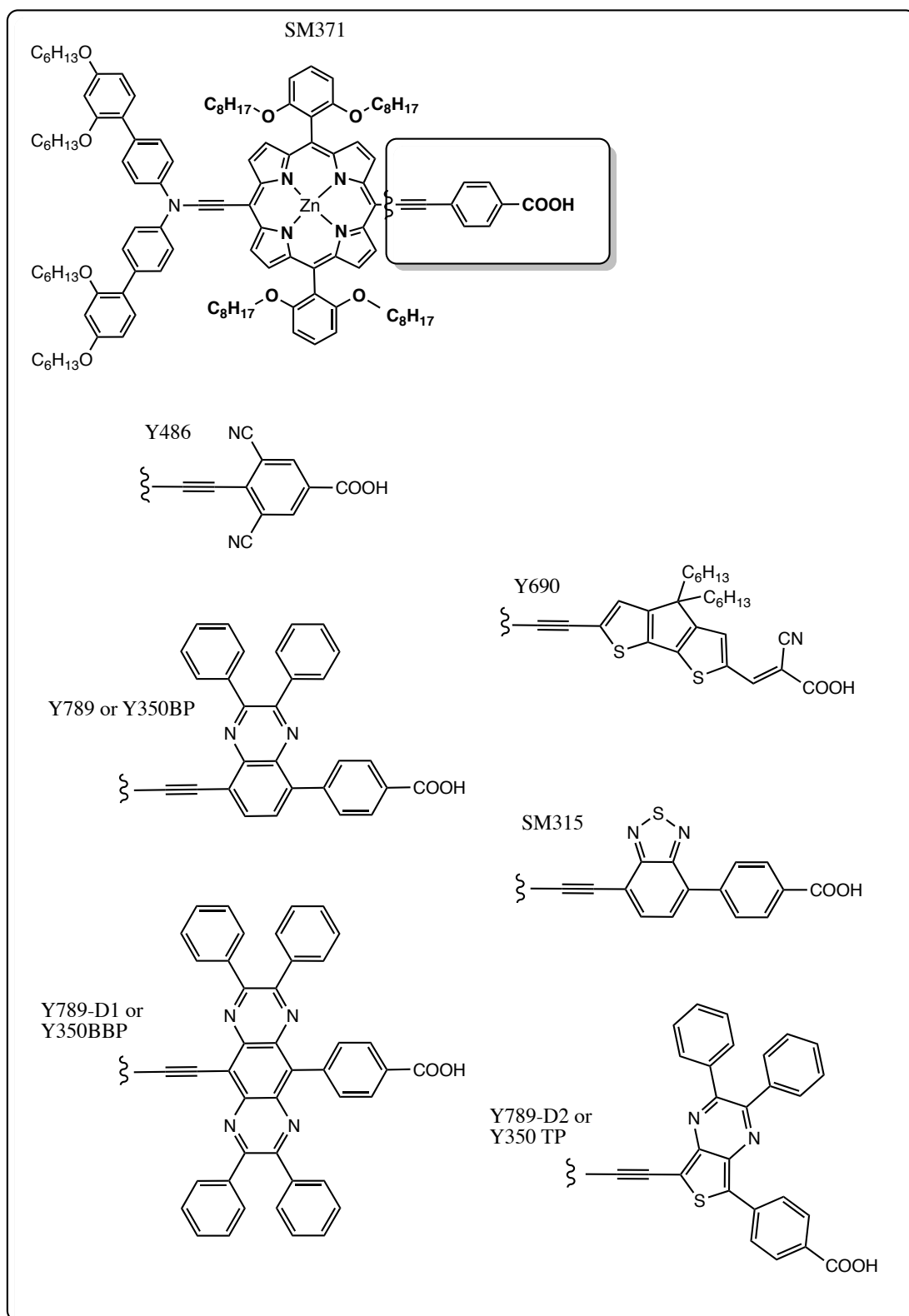


Figure 3.29: Some combinations of different donor, acceptor, metal, and meso position moieties.

Chapter 3. Computational characterization and design of porphyrin-based dye sensitizers: All the way up to 13% efficiency

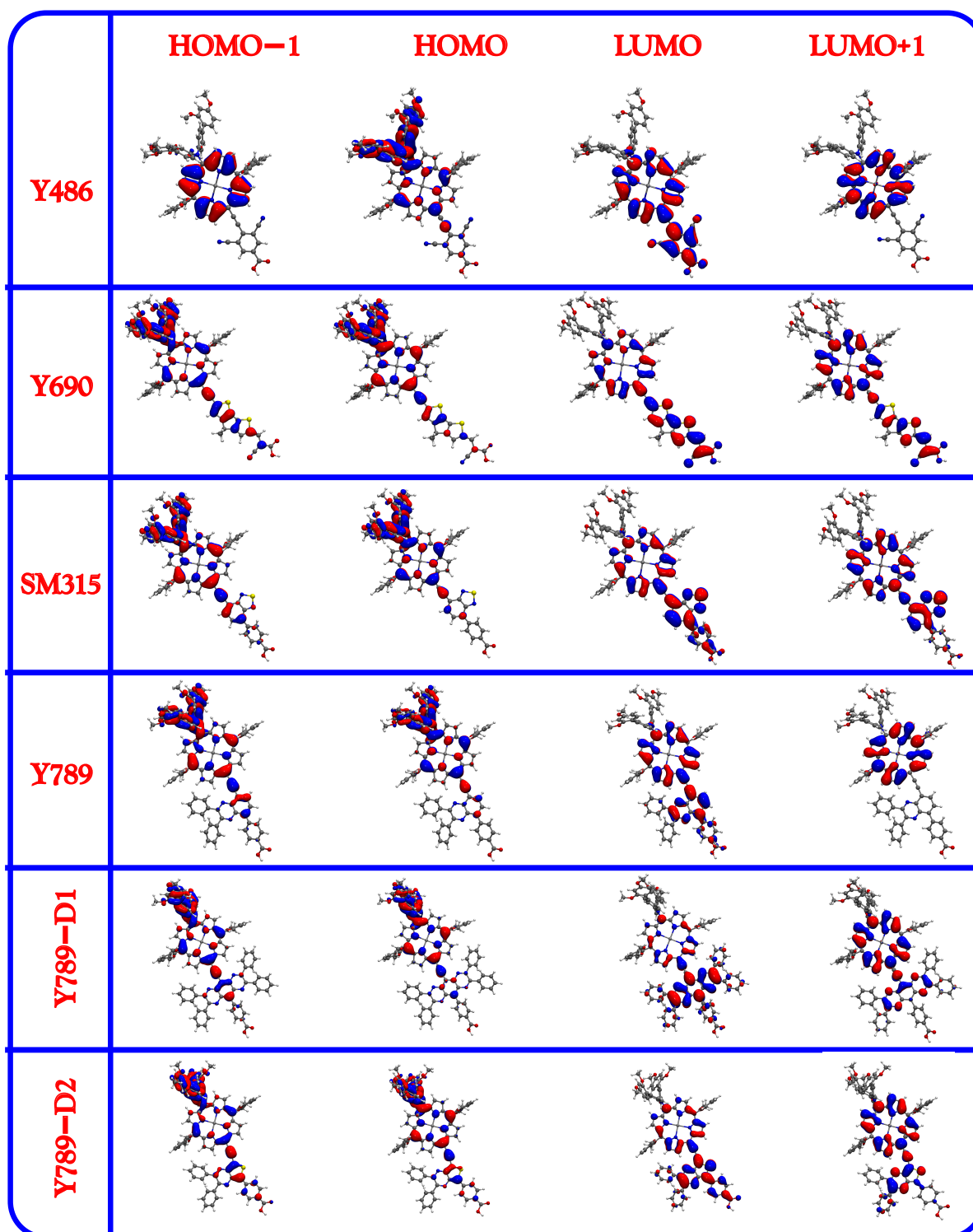


Figure 3.30: Frontier Kohn-Sham orbitals for the combined dyes (isovalue is 0.02 a.u.)

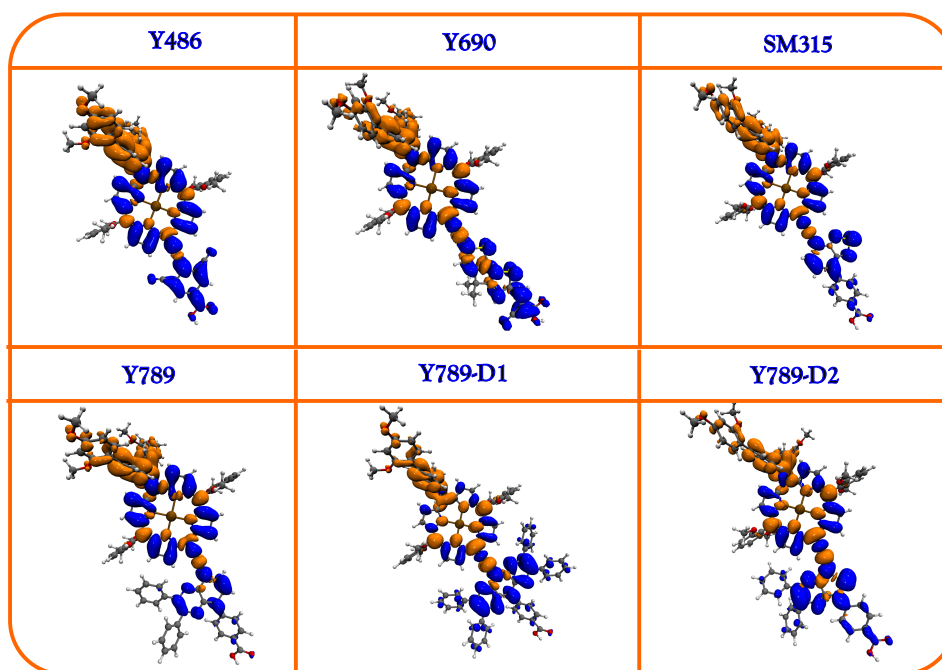


Figure 3.31: Electron-hole density map of the [S0 → S1] vertical transition for the combined dyes. The density difference contour plots ( $\rho_{S1} - \rho_{S0}$ ) show the electron distribution in blue and the hole distribution in orange. Isovalue set to 0.0003 a.u.

Moreover, Figure 3.32 shows that LUMO energy levels of Y789-D1 and Y789-D2 are lower than the reference YD2-o-C8 dye. Due to the intrinsic twist between the quinoxaline and the carboxylic moiety ( $52^\circ$ ), the charge transfer from the donor moiety ends at the quinoxaline group. SM315 with the  $\Lambda$  value of 0.49 for the first transition, indeed shows a higher CT character compared to Y789 with  $\Lambda = 0.56$ . As expected SM315 produces a higher photocurrent than Y789 ( $18.1 \text{ mA}\cdot\text{cm}^{-2}$ )<sup>71</sup> compared to  $17.4 \text{ mA}\cdot\text{cm}^{-2}$  of Y789 (Figure 3.31).

This may cause a problem in electron injection to the oxide electron transporter. This being said, electron injection can still happen through electron tunneling<sup>115</sup> which might explain the considerably high value of  $17.1 \text{ mA}\cdot\text{cm}^{-2}$  for Y789.

Y690 benefits from a cyclopentadithiophene (CPDT) acceptor, which owes its success to the both steric effects of the alkyl groups that prevent dye aggregation on the  $\text{TiO}_2$  surface and effective donor-acceptor communication through charge transfer excitations<sup>65</sup>. This acceptor has shown good performance in the two highest performing organic dyes, Y123 and JF419<sup>70</sup>. Y690 has been designed with an alkyne bridge connecting the porphyrin to CPDT. The steric hindrance that occurs upon direct connection induces a twisting angle of ca.  $60^\circ$  with the porphyrin plane. Adding the alkyne group planarizes the whole structure enhancing the electronic communication through more conjugation. This is manifested in a considerable red shift of the absorption spectrum (Figure 3.33).

**Chapter 3. Computational characterization and design of porphyrin-based dye sensitizers: All the way up to 13% efficiency**

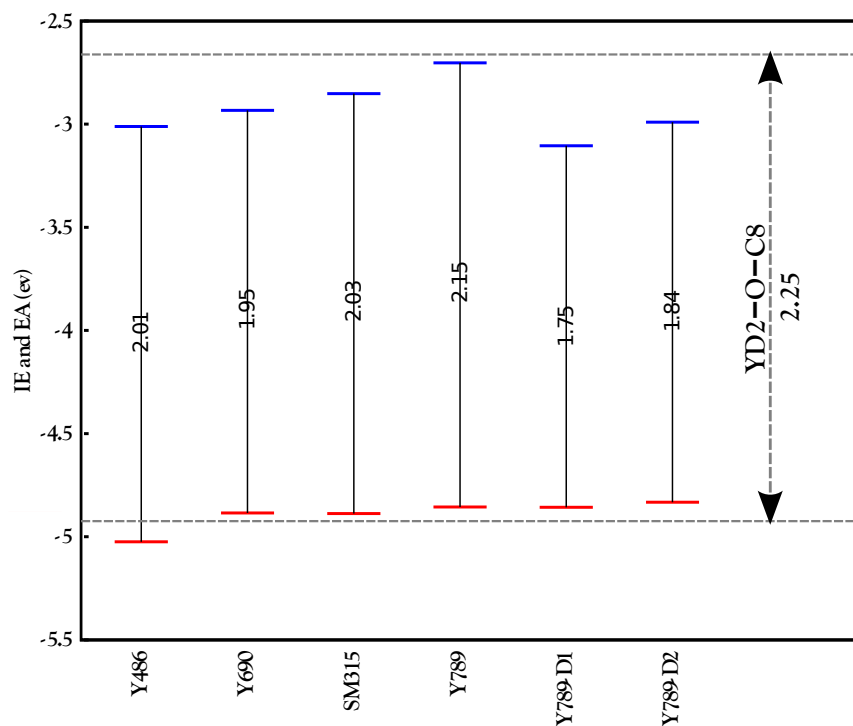


Figure 3.32: Calculated vertical Ionization energies (IE) (red) and negative of Electron affinities (EA) (blue) for the combined dyes.

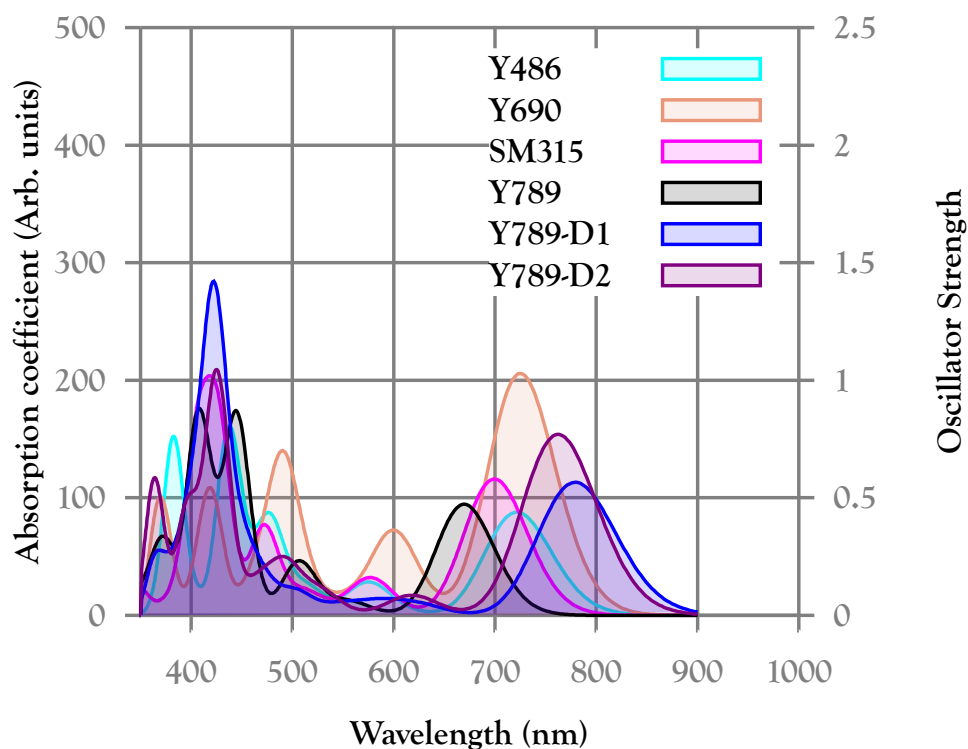


Figure 3.33: Calculated UV-visible absorption spectra for modifications applied on the combined dyes.



### **3.4 Conclusion**

We reported here a detailed theoretical investigation on different porphyrin-based dyes. We showed that different functional groups and metals can alter the electronic conjugation and thus the spectra. Red shifted spectra are not necessarily a guarantee to higher photocurrent but other properties including the efficiency of the push-pull mechanism along the molecular scaffold (from donor to acceptor) need also to be considered for an efficient injection into the TiO<sub>2</sub> nanoparticles. Bulky highly conjugated donor groups such as ullazine and dibutoxyphenyl while protecting the substrate TiO<sub>2</sub> from the electrolyte, can enhance the electron push if employed on the right binding site with preserved planarity. Ligated Sn-based porphyrins seem to function similar to Zn-porphyrins and even show better light harvesting properties. Meso position substitutions need not to rotate vertically with respect to the porphyrin plane to be able to contribute to the electronic density. Equally important, incorporating strong EWD acceptor groups (BTD, CPDT, quinoxaline) can help shifting the absorption spectrum to the red. However, adding up more conjugated moieties to the acceptor can mislead the electronic flow and drift the electrons from the carboxylic group. The effect of incorporation of long alkyl chains and bulky groups to shield the substrate from the reach of the electrolyte is discussed in our previous work for Ru-based dyes<sup>116</sup>. The static calculations presented here are followed by classical and ab-initio dynamic simulations in our next work to cover other aspects of DSSC design (e.g. dye-packing, electron recombination and alkyl chains shielding effect for porphyrin dyes).



## 4 Atomistic Molecular Dynamics Simulation of a Porphyrin-Sensitized Solar Cell



T

his chapter is based on a collaboration with Elizabeth Brunk, Basile F.E. Curchod, Ivano Tavernelli and Simone Meloni from LCBC<sup>a</sup>, Hauke Harms from LPI<sup>b</sup> and Raphael Jovita and Antoine van Muyden<sup>c</sup>.

<sup>a</sup>Laboratory of Computational Biochemistry and Chemistry

<sup>b</sup>Laboratory of Photonics and Interfaces (LPI)

<sup>c</sup>Student semester projects at LCBC

## Chapter 4. Atomistic Molecular Dynamics Simulation of a Porphyrin-Sensitized Solar Cell

---

Molecular dynamics simulations were performed for a comprehensive model of a liquid thin film solar cell including the TiO<sub>2</sub> substrate sensitized with the porphyrin dye YD2-o-C8, and Co(bpy)<sub>3</sub><sup>3+</sup> electrolyte in acetonitrile solution. To this end, force fields for the porphyrin dye as well as for the cobalt electrolyte were developed based on ab initio data. In this way, dye packing on the surface and electrolyte accessibility to the TiO<sub>2</sub> substrate could be studied for different dye coverages. The simulations show that the thickness of the dye layer is strongly affected by the coverage density. At >80% coverage, the peripheral octyl chains of the dye effectively shield the TiO<sub>2</sub> substrate from the electrolyte reducing the extent of electron recombination.

### 4.1 Introduction

Dye sensitized solar cells (DSSCs) are among the most promising thin-film based photovoltaics. Their colorful, transparent, and flexible structure makes DSSCs an aesthetic choice for any energy-optimized design; from small electronic devices for integration in electronic consumer goods to large modules, like the DSSC windows of the EPFL convention center in Switzerland). In contrast to their facile and cheap fabrication process, the chemical and physical processes that are involved in their functioning are far from trivial. Conventional DSSCs consist of a TiO<sub>2</sub> paste covered with sensitizer molecules (dyes) which get excited once exposed to an incident photon and inject electrons into the electron transporter TiO<sub>2</sub>. Oxidized dye molecules in turn are regenerated via an electrolyte redox couple (for Ru-based dyes I<sub>3</sub><sup>-</sup>/I<sup>-</sup> and for porphyrin-based dyes mostly Co<sup>III</sup>/Co<sup>II</sup>). The importance of a good energy level alignment between different components of the DSSC has been pointed out both experimentally<sup>117,118</sup> and computationally<sup>119,120</sup>. An optimal sensitizer should not only harvest as much light as possible (having a broad panchromatic absorption spectrum in the visible) but also should possess suitable redox properties. Using a one-electron, frozen orbital picture, the LUMO energy level should be slightly higher than the TiO<sub>2</sub> Fermi level. The HOMO level instead should be lower than the electrolyte redox potential for efficient regeneration (yet not so low that the absorption spectrum is affected). With this hindsight, different DSSC components have been optimized resulting in cells with efficiencies as high as 13% (for the porphyrin-based cell designed by Mathew et al.<sup>71</sup>). Among computational methods, DFT has by far given the greatest contribution to computational DSSC research. Using DFT, many different dye and electrolyte structures have been screened to guide and focus synthetic efforts. Yet, DFT applications remain limited to the study of individual components of DSSCs. Further improvements of DSSCs depends crucially on a better understanding of the effect of simultaneously altering different major cell components. Such comprehensive computational studies can currently be only performed using classical molecular dynamics simulations based on parameterized analytical force fields. Indeed force field approaches can be particularly useful for studying the influence of dye coverage on the semiconductor substrate and on dye packing, dye-dye interactions and electrolyte accessibility. Using molecular dynamics simulations, we were recently able to rationalize AFM images of Z907 sensitized TiO<sub>2</sub> surfaces as a function

of coverage.<sup>116</sup>. Here, we develop force fields for the porphyrin-based dye YD2-o-C8 and the cobalt bipyridine electrolyte while for the rest of the system ( $\text{TiO}_2$ ,  $\text{BF}_4^-$  counterions, and acetonitrile solvent), force field parameters were already available in the literature.

## 4.2 Methods and computational details

Classical MD simulations were carried out using the AMBER 12 package using the PMEMD module<sup>121</sup>. For the development of the force fields, full ab initio geometry optimization of the isolated dye molecule and electrolyte were performed using the Gaussian package<sup>77</sup> at DFT(M06)<sup>61</sup> level of theory with the effective core potential and basis set LANL2DZ<sup>122</sup> for zinc and cobalt, and a 6-31G\*<sup>76</sup> basis set for the remaining atoms together with ultrafine grid, and tight geometrical convergence criteria. Geometry optimizations were followed by frequency calculations for ensuring that the molecular configurations reached a true minimum on the potential energy surface. The optimized electron density was used for point charge analysis. Point charges were calculated with both population analysis (Bader and Voronoi<sup>123</sup>) and an electrostatic potential fitting procedure (RESP<sup>124</sup>).

5 ps of ab initio molecular dynamics was carried out for a  $20 \times 15$  double layered  $\text{TiO}_2$  slab covered with chemisorbed water molecules (see Table 4.1) using the CPMD code<sup>125</sup>. The average geometry was then used to set up the classical model. Analogous first-principles MD simulations were also carried out for the dye molecule in vacuum. In addition, two systems containing a single dye absorbed on a  $\text{TiO}_2$  slab together with explicit acetonitrile solvent molecules which were first equilibrated classically and then simulated fully quantum mechanically for 3 ps. In the first one, the dye was absorbed with a dissociative binding mode and in the second one with a molecular or non-dissociative mode. Individually equilibrated components (dye and water covered slab) were then assembled into an initial model for the classical MD studies using Materials Studio<sup>126</sup>.

Following Amber convention, each dye was defined as a residue denoted by resname DYE, each Ti atom together with two oxygens was described by a resname SLB, each chemisorbed water was denoted by resname CHW, ELC resname for each  $\text{Co}(\text{bpy})_3^{3+}$ , BF4 for  $\text{BF}_4^-$  and finally ACN resname for each acetonitrile molecule (a sample of AMBER topology and coordinate file is given in the Appendix A). The system was then solvated with an equilibrated box including the electrolyte, counter ions and acetonitrile. For the sake of comparison, one model with normal coverage was also simulated in gas phase. Production runs of 80 ns in the NVE ensemble were sampled after initial minimization and 5 ns of equilibration in the canonical ensemble using Nosé-Hoover thermostats at room temperature (300 K). Ab initio molecular dynamics (AIMD) simulations were performed using the Car-Parinello<sup>127</sup> scheme as implemented in the CPMD package<sup>125</sup>. A time step of 5 au and a fictitious electron mass of 800 au was used. The electronic structure was described at the DFT/BLYP level<sup>49,128</sup> using a plane-wave cutoff of 70 Ry in combination with norm-conserving Martins-Trouiller pseudopotentials<sup>129</sup> and dispersion-corrected atom-centered potentials.

All figures were generated with the VMD package<sup>130</sup>.

## Chapter 4. Atomistic Molecular Dynamics Simulation of a Porphyrin-Sensitized Solar Cell

	Component	Residue name	Abundance	Dimension of the cell ( $\text{\AA}^3$ )
Low density	Dye	DYE	26	$108.85 \times 75.52 \times 150$
	Cobpy(III) electrolyte	ELC	140	
	$\text{BF}_4^-$ counter ions	BF4	420	
	Acetonitrile solvent	ACN	12800	
	Chemisorbed water	CHW	650	
Normal density	Dye	DYE	50	$108.85 \times 75.52 \times 150$
	Cobpy(III) electrolyte	ELC	134	
	$\text{BF}_4^-$ counter ions	BF4	402	
	Acetonitrile solvent	ACN	12747	
	Chemisorbed water	CHW	650	
High density	Dye	DYE	98	$114.30 \times 79.296 \times 150$
	Cobpy(III) electrolyte	ELC	142	
	$\text{BF}_4^-$ counter ions	BF4	426	
	Acetonitrile solvent	ACN	13534	
	Chemisorbed water	CHW	784	

Table 4.1: Components of each simulation box

### 4.2.1 Force field development

#### Porphyrin Dye YD2-o-C8

The structure of the YD2-o-C8 molecule is shown in Figure 4.1. Like all porphyrin-based donor-bridge-acceptor dyes, YD2-o-C8 has an extended conjugated systems. The stability increase due to electron delocalization is a pure quantum mechanical effect that is emulated at the force field level using special improper dihedral potential that enforces planarity. In the case of YD2-o-C8, this conjugated system also includes an alkyne linker between the porphyrin and the acceptor moiety which necessitated some special adaptations of the standard AMBER force field in Equation 4.1 (vide infra). This extended conjugation systems rigidifies the acceptor unit keeping it from free rotation. Moreover, it provides the dye with sufficient stiffness for upright arrangements even in the presence of a single carboxylic anchoring group (vide infra). Other peripheral groups including the phenylalkoxy groups in the two meso positions and the donor moiety are easier to describe at the level of a mechanical force field since the forces governing their rotation are mostly repulsive vdW interactions.

A well balanced choice of the electrostatic interactions in the form of effective atomic point charges is also crucial for preserving the planarity of the porphyrin-base together with proper and improper dihedral angle potentials. The point charges determined using a RESP formulation<sup>124</sup> are shown in Figure 4.2. RESP charges were fitted in three steps: first with no constraints, second by imposing a mirror symmetry to account for the x-y symmetry of the molecule, and finally by fixing the point charges of the carboxylic anchoring group according to the work of Suchko et al.<sup>131</sup> to reproduce the correct 29.98 kcal/mol chemisorption energy to the  $\text{TiO}_2$  scaffold<sup>131</sup>. Voronoi and Bader point charges were also computed for comparison,

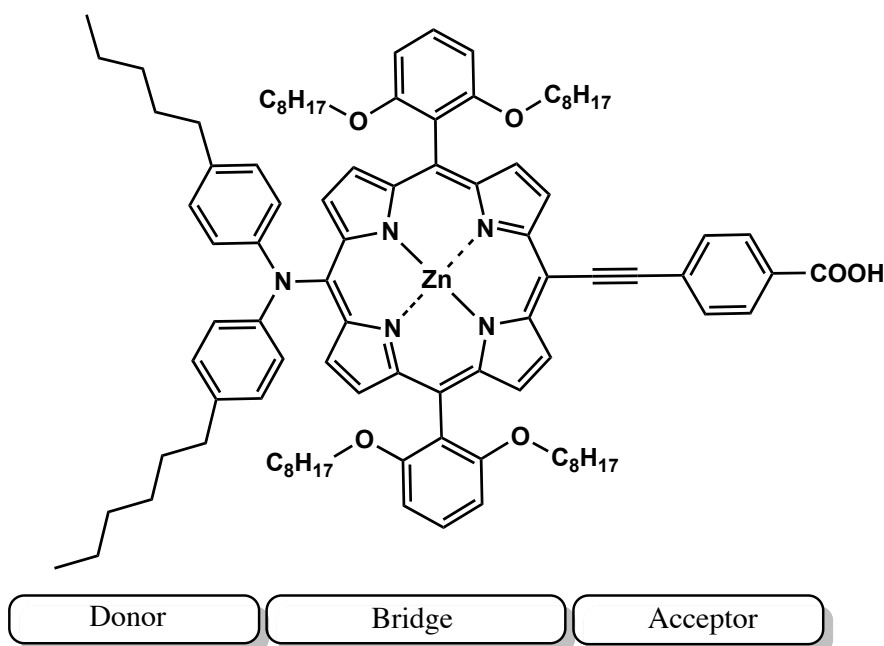


Figure 4.1: Chemical structure of YD2-o-C8.

yet their corresponding point charges couldn't preserve the planarity.

Equilibrium bond lengths and angles were derived from DFT (M06<sup>61</sup>) optimized geometries. The force constants were assigned according to the atom types selected by analogy to the existing AMBER force fields for the HEME cofactor<sup>132</sup> (Figure 4.3). Four rather important dihedral potentials shown in Figure 4.4 were fitted according to QM data following a three-step procedure: Quantum mechanical energy profiles for the torsion around each dihedral angle were calculated (denoted by "QM profile" in Figure 4.4).

The same energy profile was obtained from molecular mechanics (MM) calculations with a force field in which the corresponding dihedral potential to zero. The resulting torsional profile is solely given by 1-4 van der Waals interactions (MM<sub>0</sub> profile). Finally, the AMBER torsional energy function was fitted to the difference of the quantum profile and the remaining MM interactions (denoted as QM – MM<sub>0</sub>). The energy barrier for rotation around the dihedral angles 1,2 and 3 has its origins in sterical hindrances. Long alkyl chains in the donor moiety and the phenyl alkoxy groups at meso positions prevent this rotation (Look at the high energy barriers in Figure 4.4). Due to sterical repulsion between atom types OS of the meso group and the peripheral hydrogen atoms, dihedral 2 is forced to acquire an almost vertical (ca. 60 Å) configuration with respect to the porphyrin base. Quantum calculations show (Chapter 3) that the induced twist at this position has a crucial impact on the electronic influence of substituents at meso positions. On the other hand, the ca. 2 kcal/mol torsional energy barrier for dihedral 4, has its origins in pure electronic forces (e.g. exchange and correlation). This is evident from the fact, that Coulombic and vDW interactions (MM<sub>0</sub> profile) would favor perpendicular arrangements while the planar configuration is preferred in the QM description

## Chapter 4. Atomistic Molecular Dynamics Simulation of a Porphyrin-Sensitized Solar Cell

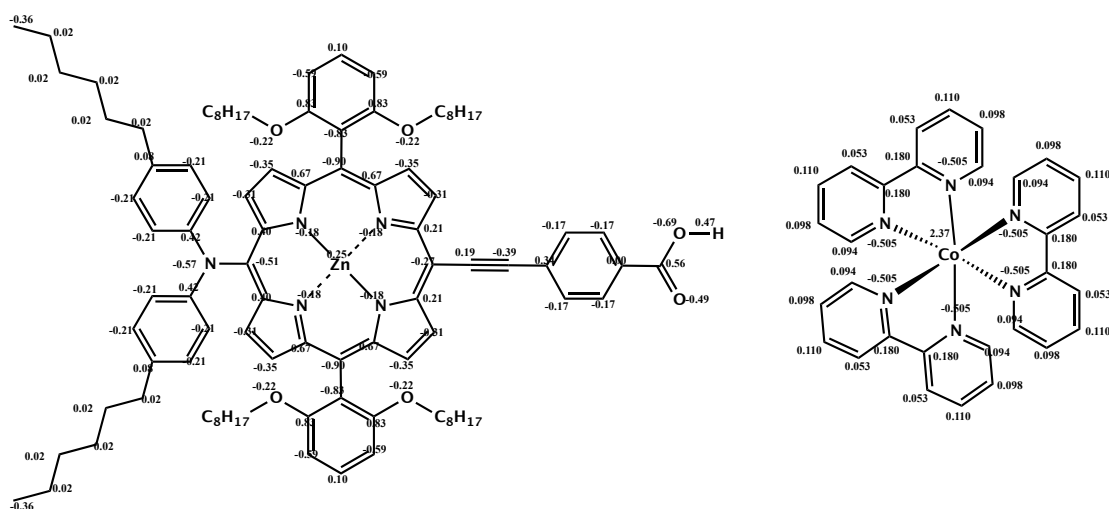


Figure 4.2: Fitted point charges for YD2-o-C8 and  $\text{Co}(\text{bpy})_3^{3+}$ .

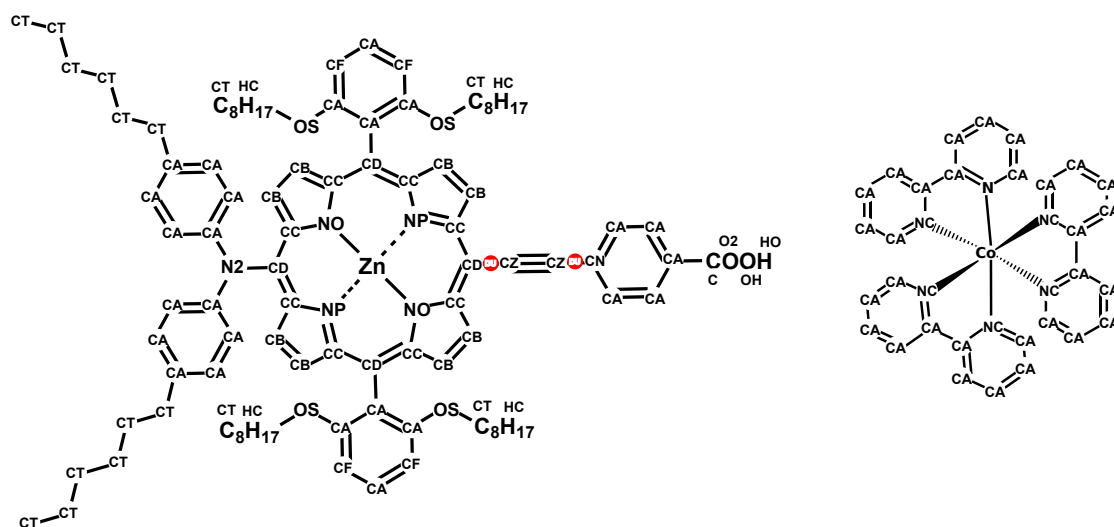


Figure 4.3: Atom types assigned according to AMBER convention.

when electron delocalization effects are included.

That is, if we neglect the electronic conjugation, the acceptor moiety would acquire a vertical position with respect to the base to maximize the distance between the negatively charged CA atoms of the acceptor moiety with negatively charged CB and CC atoms around the porphyrin base in order to reduce repulsion. While at first glance the CC-CD-CZ-CZ dihedral seems the logical choice to account for this torsional potential, the last three atoms are located on a line and therefore the definition of dihedral angle (the angle between a plane of three atoms with the fourth atom) is ill-defined. For this reason, we defined two dummy interaction sites with no vdW nor Coulomb interactions in the middle of the CZ-CD and CZ-CN bonds with bond connecting only to each other and CD and CA atoms in the porphyrin and the acceptor, respectively (Figure 4.5). Corresponding force field parameters are shown in Table A.1.



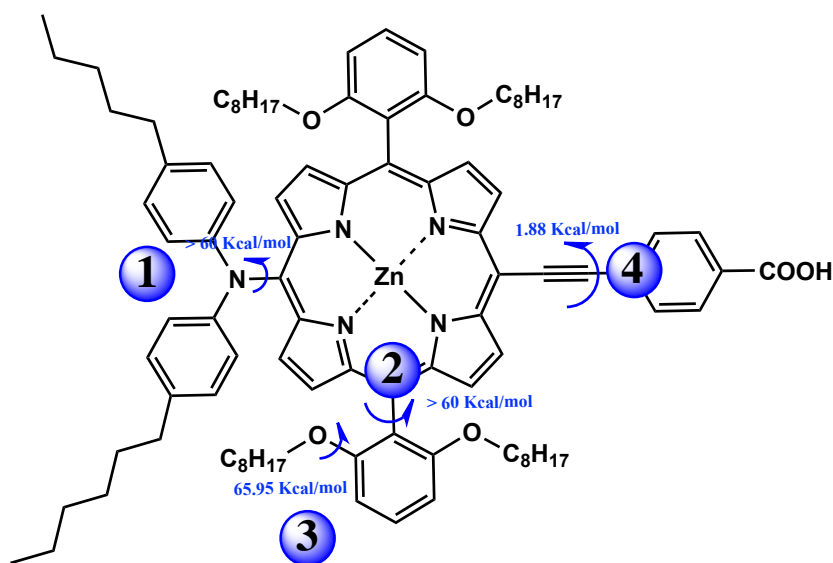


Figure 4.4: Energy barriers for rotation around dihedrals 1,2,3 and 4 calculated from rigid scans of each dihedral separately at DFT/(M06) level of theory.

### Redox mediator $\text{Co}(\text{bpy})_3^{3+}$ and $\text{BF}_4^-$ counter-ions

Cobalt-based electrolytes were first reported by Nusbaumer et al.<sup>133</sup> as a tunable alternative to the conventional  $\text{I}_3^-/\text{I}^-$  redox couples. The structure of the  $\text{Co}(\text{bpy})_3^{3+}$  complex allows for adjustment of the electrochemical potential and thus the final  $V_{\text{OC}}$  of the cell. Moreover, unlike  $\text{I}_3^-/\text{I}^-$ , cobalt complexes do not compete with the sensitizer in light absorption as they only harvest visible light very poorly<sup>134</sup>. The combination of  $\text{Co}(\text{bpy})_3^{2+/3+}$  electrolyte and the porphyrin-based dye SM315, is currently yielding the highest photoconversion efficiency of 13% reported for DSSCs<sup>71</sup>.

The entire set of developed force field parameters for  $\text{Co}(\text{bpy})_3^{3+}$  is given in Table A.2. The bulky shape of the ligands imposes a quasi octahedral form with little flexibility in the dihedral angles. Bader point charges were used for the central cobalt ion and the surrounding nitrogen atoms, the rest of the atomic point charges were fitted via a RESP procedure (Figure 4.2). Atom types were chosen by analogy with the force field available for ruthenium trisbipyridine<sup>135</sup>. Several non-coordinating anions such as TFSI or  $\text{PF}_6^-$  can be used as counter ions of cobalt trisbipyridine. In this work, we have used three  $\text{BF}_4^-$  counter ions for each  $\text{Co}(\text{bpy})_3^{3+}$  complex. Force field parameters for  $\text{BF}_4^-$  were taken from the work of Wu et al.<sup>136</sup>.

### $\text{TiO}_2$ substrate, chemisorbed water and acetonitrile solvent

We have used the modified SPC/E parameters for water chemisorbed on  $\text{TiO}_2$  developed by Alimohammadi et al.<sup>137</sup>. The vdW parameters used in this work (in the form of 12-6 Lennard Jones potentials in Equation 4.1) were fitted to reproduce the Buckingham potential reported in Alimohammadi's paper (Table 4.2). YD2-o-C8 is adsorbed on the substrate via its comparably small anchoring group, the carboxylic moiety.

## Chapter 4. Atomistic Molecular Dynamics Simulation of a Porphyrin-Sensitized Solar Cell

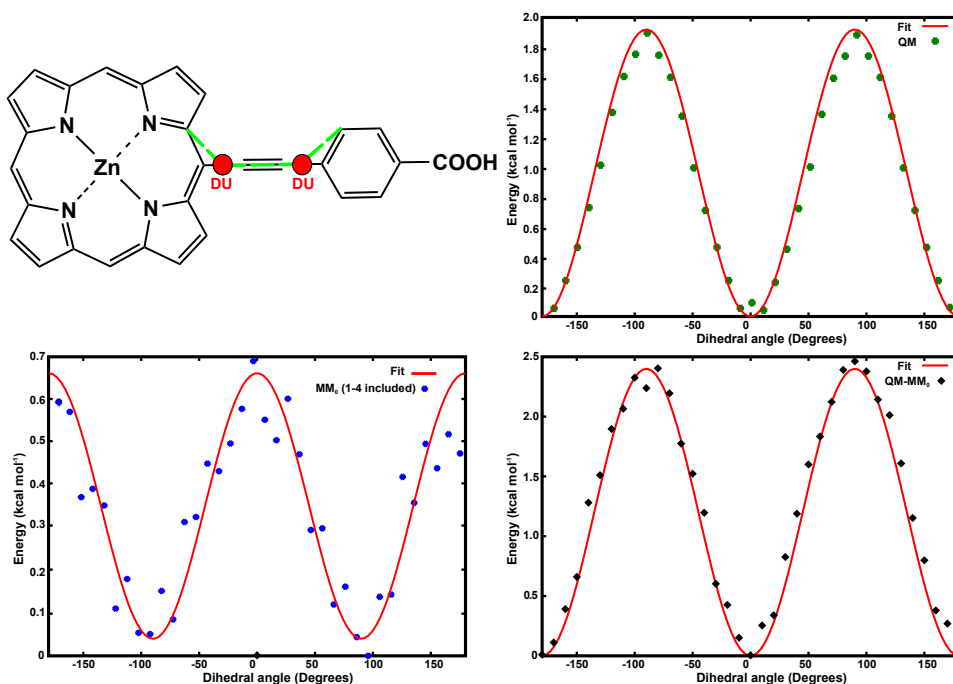


Figure 4.5: Fitting of the dihedral potential for rotation around the alkyne linker using two additional off-center interaction sites ("DU"). Without this torsional potentials, the vdW forces favor a perpendicular arrangement between the linker and the porphyrin base and/or the benzylic acid moiety.

Chemisorption-induced polarization of such small organic molecules (including the carboxylic group itself) has been shown to be negligible<sup>131</sup> and that the charges do not change so much once approaching the surface (0.2 |e| only). For this anchoring group, we used the point charges reported in Suchko et al.<sup>131</sup> for chemisorbed waters on TiO<sub>2</sub> and fixed them through RESP calculation of the dye molecule to reproduce the corresponding chemisorption energy. A united atom three site model OPLS force field was used for acetonitrile solvent molecules<sup>138</sup>.

LJ 12-6 parameters adapted from the Bandura-Kubicki model

Atom Type	$r^*$	$\epsilon_{ii}$	Charge
TI	1.1100	0.3887	2.156
OX	1.6600	0.2983	-1.098
OW (SPC/E)	1.7700	0.1541	-0.939
HW (SPC/E)	0.0000	0.0000	0.430
HW(chemisorbed)	0.0000	0.0000	0.42
OW(chemisorbed)	7.9317	0.0000	-0.846

Table 4.2: Force field parameters developed in this work for the TiO<sub>2</sub> substrate and the chemisorbed water molecules. The full force field in AMBER format is given in Appendix

### 4.3 Results and discussion

The components of the simulation system were chosen in such a way as to mimic a real DSSC as close as possible. According to the experiments and SEM images, the (101) facet of anatase is known to be the most exposed surface of the TiO<sub>2</sub> nanoparticles although not being the thermodynamically most stable surface in the bulk. The surface of the TiO<sub>2</sub> nanoparticles was thus modeled by two layers of anatase cleaved at the (101) facet on both sides and water terminated. TiO<sub>2</sub> surfaces are known to be highly hydrophilic<sup>139</sup>. Although stages of the cell fabrication are carried out in a glove box occasionally heat-treated in a furnace, water molecules can remain adsorbed on the substrate TiO<sub>2</sub> when the entire process is not completely sealed and protected. Many experimental and computational studies have been done to investigate the most stable configuration of chemisorbed water molecules on different facets of TiO<sub>2</sub> surface<sup>140,141</sup>. In this work, we used the average geometry obtained from 25 ps of ab initio Car-Parinello simulations of water on a TiO<sub>2</sub> (101) surface as a starting arrangement for the classical simulations. Dye molecules were distributed homogeneously on the substrate according to the corresponding coverage density reported in experiments, in which each dye molecule occupies an area of about 13 × 13 Å<sup>2</sup> (in the following we will refer to this as 'normal' density). The Co-based electrolyte Co(bpy)<sub>3</sub><sup>3+</sup> was added to reproduce the experimental 0.25 M concentration<sup>71</sup>. For every molecule of Co(bpy)<sub>3</sub><sup>3+</sup>, three BF<sub>4</sub><sup>-</sup> counter ions were added. Finally, the complete simulation box was solvated in acetonitrile solvent molecules (corresponding to a density of 0.786 gr/cm<sup>3</sup>). Although, this is the most comprehensive atomistic model of a DSSC so far, there are still, few components such as the co-adsorbent and electrolyte additives like chenodeoxycholic acid (cheno) which is believed to reduce dye aggregation and improve surface passivation that have been left out<sup>142</sup>. They could be added in a later even more comprehensive computational model. A classical force field of the AMBER<sup>143</sup> type (Equation 4.1) has been chosen to represent the porphyrin dye and the cobalt electrolyte, whereas the acetonitrile solvent was described by an OPLS force field<sup>144</sup> and the TiO<sub>2</sub> surface was modeled by a Bandura-Kubicki potential<sup>145</sup>.

$$E = \sum_{bonds} K_r (r - r_0)^2 + \sum_{angles} K_\theta (\theta - \theta_0)^2 + \sum_{dihedrals} \frac{K_\phi}{2} [1 + \cos(n\phi - \gamma)] + \sum_{i < j} \left[ \frac{A_{ij}}{r_{ij}^{12}} - \frac{B_{ij}}{r_{ij}^6} + \frac{q_i q_j}{r_{ij}} \right] \quad (4.1)$$

Where in three first bonded terms,  $K_r$ ,  $K_\theta$ , and  $K_\phi$  refer to the force constant for the harmonic approximation of bonds, angles and dihedrals, respectively and  $\gamma$  is the initial phase. The last two terms are non-bonded vdW and Coulombic energies.  $r_{ij}$  is the distance between atoms  $i$  and  $j$  and  $q_i$  refers to the point charge of atom  $i$  and  $A$  and  $B$  are Lennard-Jones parameters.

#### 4.3.1 Validation of the dye force field

To check the validity of the YD2-o-C8 force field, the equilibrium distribution of four key dihedral angles were compared with the ones obtained from ab initio MD simulations. The

## Chapter 4. Atomistic Molecular Dynamics Simulation of a Porphyrin-Sensitized Solar Cell

comparison is shown in Figure 4.6. The main features, in particular the location of extrema of the QM distribution are captured by the force field yet the thermal distribution is not exactly the same probably due to shorter time scale of QM simulations.

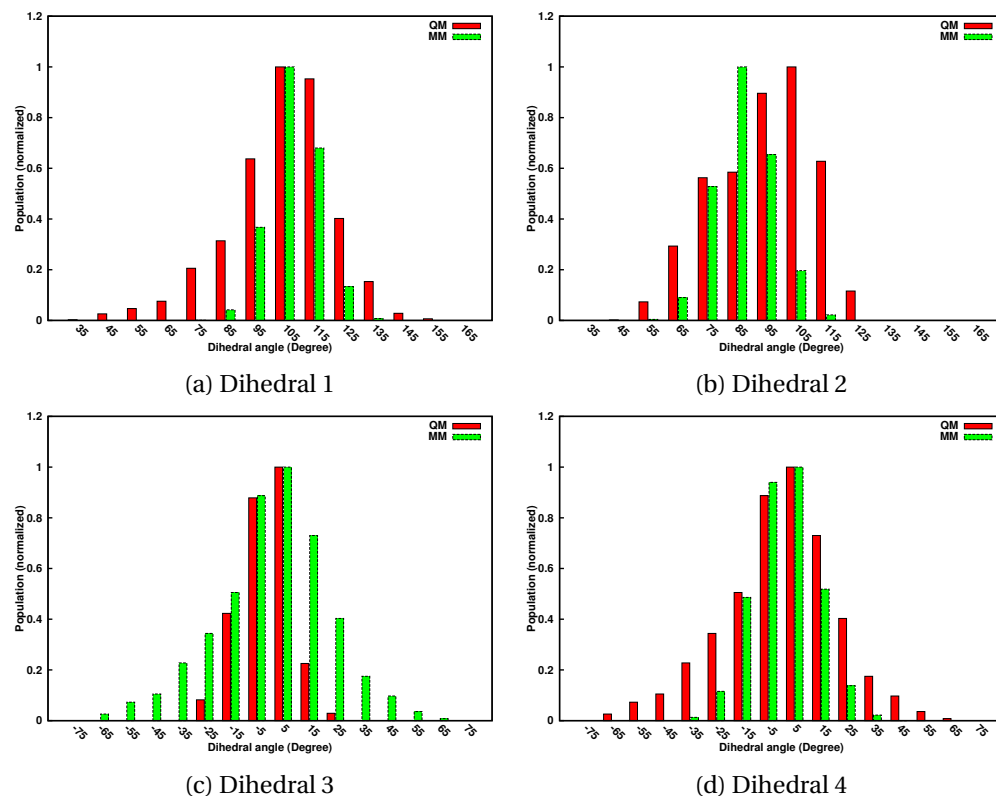


Figure 4.6: Comparison of the thermal distributions for selected dihedral angles (deg) obtained from 200 ps of the MM simulation (green) and 5 ps of QM (red) simulations.

### 4.3.2 System setup and analysis

We considered three systems with different dye coverages: low, normal, and high. All three systems were solvated in an equilibrated box consisting of the electrolyte  $\text{Co}(\text{bpy})_3^{3+}$ ,  $\text{BF}_4^-$  counter ions to ensure electroneutrality, and acetonitrile solvent molecules. According to the experiments<sup>71</sup>, assuming a uniform distribution of dye molecules on  $\text{TiO}_2$ , each porphyrin-dye occupies  $1.98 \text{ nm}^2$  of the substrate surface area<sup>71</sup>. This value has been reported for SM315 and we used the same coverage density for YD2-o-C8 since for the latter no direct data is available<sup>146</sup>. Having chosen the normal coverage density, we setup other two systems by doubling and halving the density resulting in the simulation systems labeled as "Low" and "high" coverage, respectively. According to our previous study on the Ru-based sensitizer Z907<sup>116</sup>, dye molecules have the tendency to spread uniformly on the substrate rather than aggregating, in other words the final arrangement is less driven by dye-dye interactions and more by the substrate templating. Although, this may not apply equally to porphyrin-based dyes, it can be a good guess to start with. Moreover, in case of inhomogeneity, the low-

coverage and high-coverage systems can account for the sparse and crowded areas on the substrate. Initial tests showed that the different binding modes dissociative reported e.g. for SM315<sup>71</sup> and non-dissociative hardly affect the space occupied by each dye (dotted area in Figure 4.7) and hence have thus little influence on the overall packing geometries. For all studies presented here, we have adopted a single, non-dissociative molecular binding mode. The possible binding sites on the TiO<sub>2</sub> surface are dictated by the choice of binding mode. Dissociative binding can only take place in site 1 as that is the only option where two successive 5-coordinated Ti atoms are close enough to bind with two oxygens of the anchoring group (Figure 4.7). Non-dissociative binding however, can involve site 1 or site 2. If the H proton of the carboxylic anchoring moiety points away from the surface, the dye occupies site 1 following the same geometric reasoning as for the dissociative mode, if the H proton is oriented towards the surface, it can form a hydrogen bond with one of the ridge oxygens and swaps between two neighboring ridge oxygens in the course of the simulation. However, due to the appreciable chemisorption energy of 30 kcal/mol and the additional confinement induced by solvent, we did not observe any detachment of dye molecules during the simulations. Compared to the simulations of the same system without solvent, where dye molecules show collective tilting and movements together, in solution and in the presence of bulky electrolyte molecules, dye-dye interactions are mostly substituted by dye-solvent interactions and therefore dye movement is considerably reduced and mainly limited to squiggly movements of the peripheral alkyl chains. Even at low coverages, the dye molecules hardly show any tilting and they soon establish their solvation cage. In parallel with classical simulations, we also carried out full ab initio MD simulations for a system containing one dye molecule adsorbed on a  $12 \times 24 \text{ \AA}^2$  surface area of TiO<sub>2</sub> with explicit acetonitrile solvent. Two systems were investigated in this way that differ in their dissociative versus non-dissociative binding mode. Due to the high computational cost, only 3 ps could be simulated in this case. During this short time scale, dye molecules hardly change their position (specially the dye in the dissociative mode stayed more solid than the one in the non-dissociative binding mode). However, in spite of the short simulation time of the former, both ab initio and classical molecular dynamics simulations suggest that in solution the solvent not only screen the dye-dye interactions but also the bulky electrolyte itself establishes direct interactions with dye molecules, in contrast to the gas phase where these interactions are substituted by dye-dye interactions.

According to our classical gas phase simulations dyes can occasionally detach from the substrate and adopt new binding modes. In solution, however, dye movements are mainly constrained to the donor moiety and the porphyrin base that can undergo some bending movements while the alkyl chains constitute the only really flexible parts.

## Chapter 4. Atomistic Molecular Dynamics Simulation of a Porphyrin-Sensitized Solar Cell

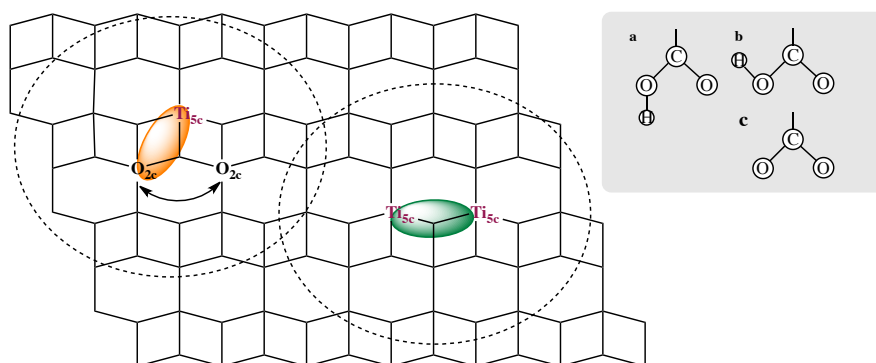


Figure 4.7: Binding sites 1 (green) and 2 (orange). The dotted oval indicates the approximate area occupied by each dye. Non-dissociative molecular binding modes a and b with the proton pointing down and up, respectively. Dissociative binding mode c.

As mentioned in the introduction, one main objective of this work is to study features of a DSS cell, such as dye-dye interactions, electrolyte accessibility to donor and TiO<sub>2</sub> substrate and the overall packing of sensitizer molecules on the surface. For this purpose, we carried out 80 ns of classical molecular dynamics simulations for each system. In Figure 4.8 the most likely areas where Co(bpy)<sub>3</sub><sup>3+</sup> molecules can approach dye molecules closer than 5 Å are shown in ice blue. It is evident from Figure 4.8 that for a uniform distribution of dye molecules close to experimental coverage densities, the space between dye molecules is too small to host bulky cobalt complexes. Moreover, alkyl chains are blocking the entrance by forming an effective shield on top of the dye molecules.

This effect gets even more pronounced when going to high coverage density. As demonstrated in Figures 4.11, 4.10, and 4.9, alkyl chain shielding is more efficient (covers larger areas) going to higher densities. At low coverage however, electrolyte molecules can penetrate in between the dye molecules and high probability areas are seen at close distances to the substrate (Figure 4.12). From a device-making point of view, it is thus essential to have a uniform distribution of dyes without spaces with sparse distribution such electron recombination from the electrolyte to the substrate is prevented. Density profiles of acetonitrile and cobalt bipyridine are shown in Figure 4.12. For higher coverages, the acetonitrile density is much lower close to the substrate. Layered structuring of acetonitrile is evident close to the TiO<sub>2</sub> surface (5 distinct peaks close to the substrate). The two first peaks disappear for the high density system showing the hampered solvent accessibility in this system.

Looking at occupancy density maps of the alkyl chains around the molecules, it becomes apparent that the alkyl chains try to cluster together optimizing hydrophobic interactions. This local packing of hydrocarbon chains leads to an effective hydrophobic coating of each dye molecule. From Figure 4.9, one can see that in all three systems two of the alkyl side chains are stretched around the molecule while the other two are extended towards top and bottom. The function of these latter octyl chains are especially important because by shielding the bottom part, electrons can thus be safely injected into the semiconductor without the risk of recombination due to the close proximity of oxidized electrolyte.

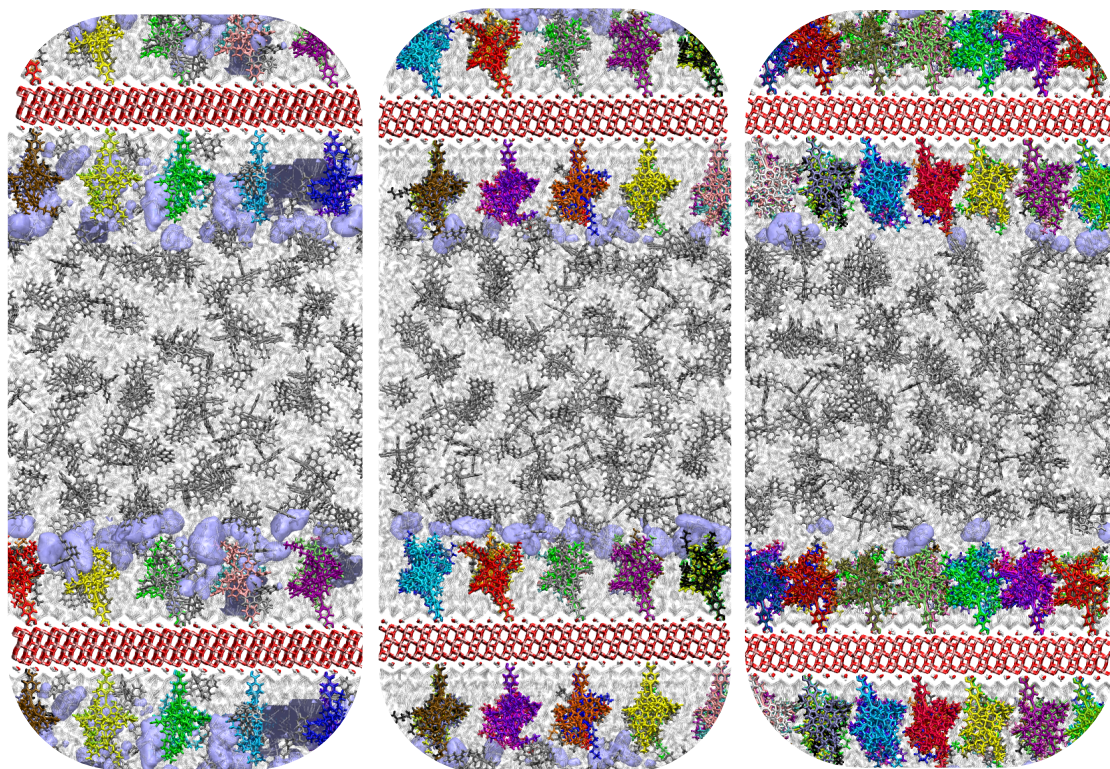


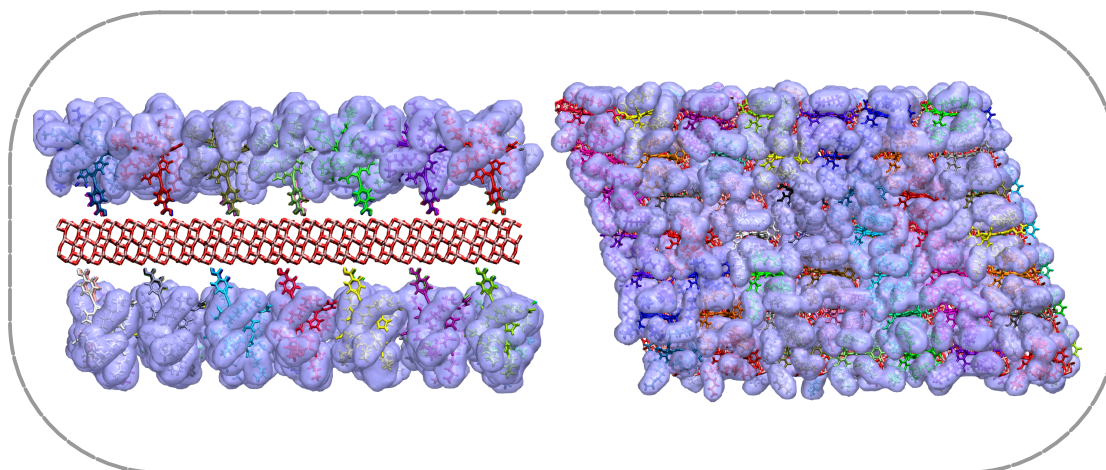
Figure 4.8: Distribution of  $\text{Co}(\text{bpy})_3^{3+}$  electrolytes. The ice blue colors show the density map of  $\text{Co}(\text{bpy})_3^{3+}$  in 5 Å vicinity of dye molecules.

#### 4.4 Conclusions

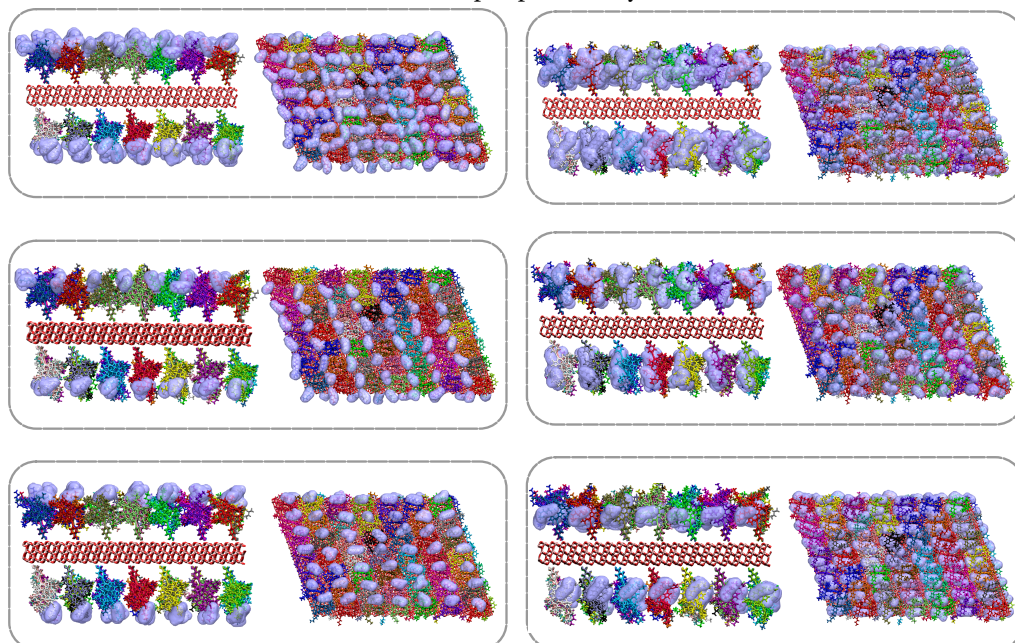
We developed a full force field for all the components in a porphyrin/Co electrolyte based DSSC based on ab initio data. By using this force field for classical molecular dynamics simulations, the effect of dye coverage on dye-packing, dye-dye interactions and solvent and electrolyte distributions was studied systematically. At standard to high dye coverage, the peripheral alkyl chains of the dye molecule can effectively hamper electrolyte diffusion to the  $\text{TiO}_2$  surface and thus prevent electron recombination between the injected electrons and oxidized electrolyte. While higher densities and more regularly packed arrangements can enhance this shielding effect, at the same time alkyl chains stop the electrolyte molecules way earlier not letting them make the necessary contact with the donor moiety of the dye compound. Thus standard dye coverages seem already to be the best compromise between the risk of recombination and the need for dye regeneration.

Octyl side chains effectively shield the acceptor moiety and this is even more pronounced at higher coverages where the dyes are so entangled that the diffusion of electrolyte and solvent molecules to the acceptor is basically suppressed. According to our results, different binding modes and packing pattern do not have a significant influence since at difference to e.g. ruthenium-based sensitizers, dye-dye interactions are shielded by solvent and the relative tilt angle of the dyes with respect to the surface remains almost unchanged during the simulation.

**Chapter 4. Atomistic Molecular Dynamics Simulation of a Porphyrin-Sensitized Solar Cell**



(a) Six peripheral alkyl chains

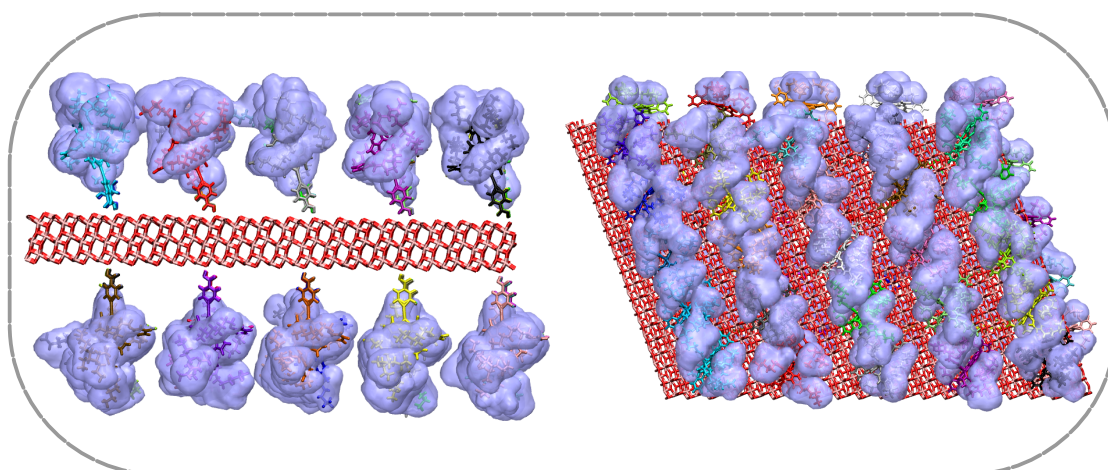


(b) Alkyl chains of the donor moiety: both chains (top), right side chain (middle), and left side chain (bottom)

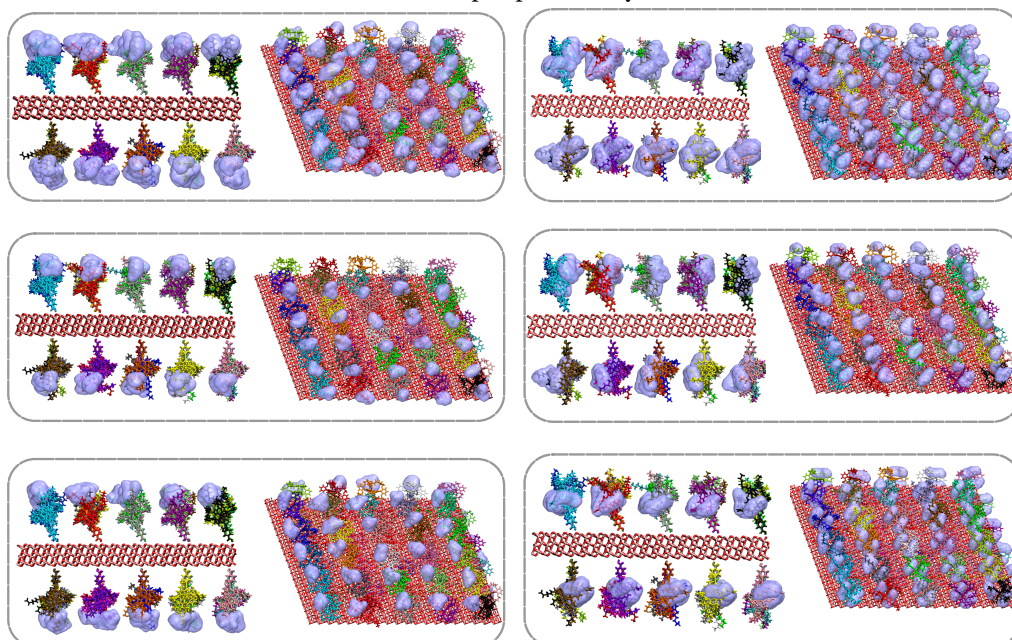
(c) Peripheral alkyl chains at meso positions: both sides (top), right side chains (middle), and left side chains (bottom)

Figure 4.9: Occupation density map of peripheral alkyl chains around the dye molecules at high coverage density. The map is done by replacing each atom with a normalized Gaussian distribution of width (standard deviation) equal to the atomic radius. The Gaussian distribution for each atom is then weighted with the occupancy. The various Gaussians are added and distributed on a grid and represented in a contour plot. The ice blue ares correspond to an isosurface value of 0.01.





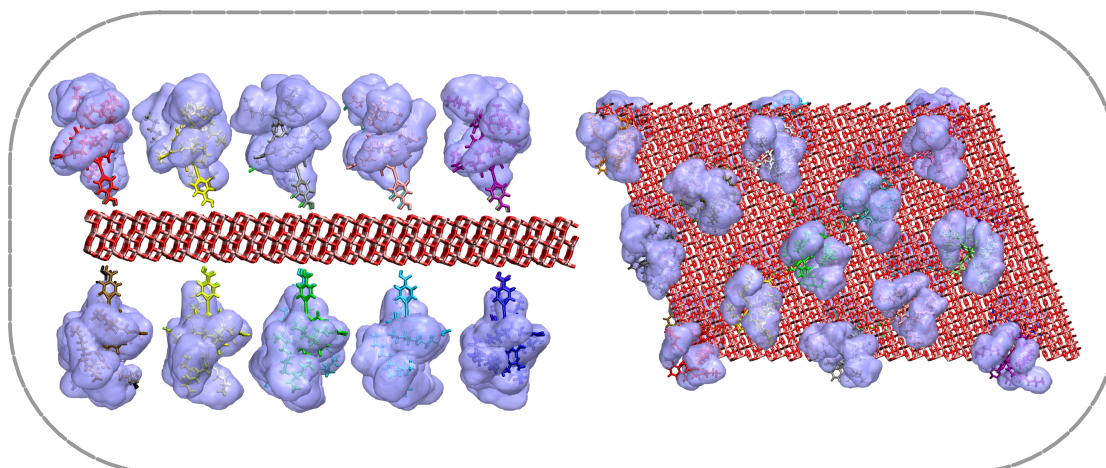
(a) Six peripheral alkyl chains



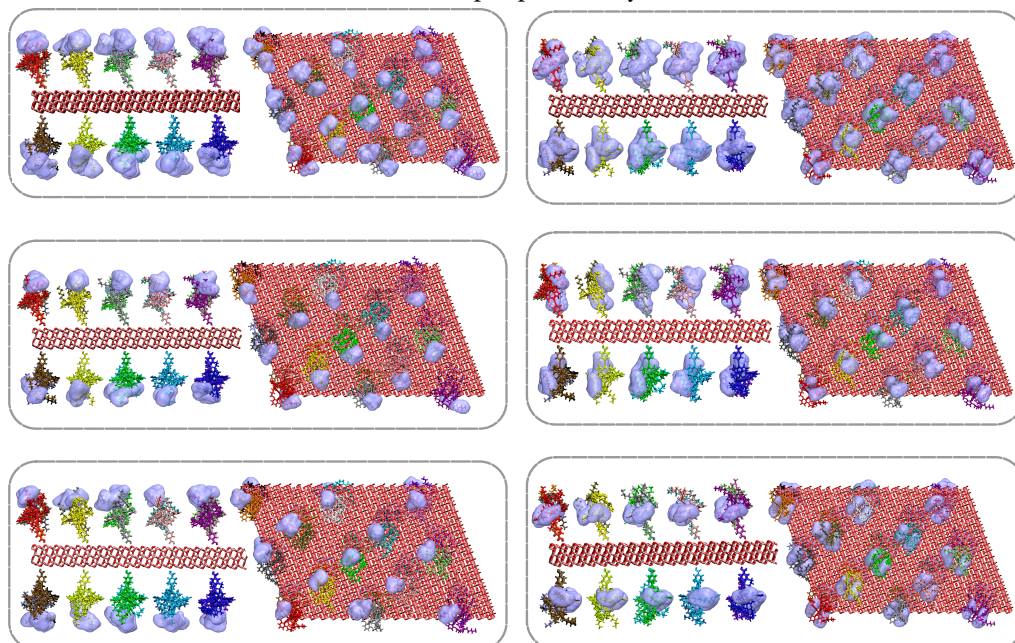
(b) Alkyl chains of the donor moiety: both chains (top), right side chain (middle), and left side chain (bottom)

(c) Peripheral alkyl chains at meso positions: both sides (top), right side chains (middle), and left side chains (bottom)

Figure 4.10: Occupation density map of peripheral alkyl chains around the dye molecules at normal coverage density. The map is done by replacing each atom with a normalized Gaussian distribution of width (standard deviation) equal to the atomic radius. The Gaussian distribution for each atom is then weighted with the occupancy. The various Gaussians are added and distributed on a grid and represented in a contour plot. The ice blue areas correspond to an isosurface value of 0.01.



(a) Six peripheral alkyl chains



(b) Alkyl chains of the donor moiety: both chains (top), right side chain (middle), and left side chain (bottom)

(c) Peripheral alkyl chains at meso positions: both sides (top), right side chains (middle), and left side chains (bottom)

Figure 4.11: Occupation density map of peripheral alkyl chains around the dye molecules at low coverage density. The map is done by replacing each atom with a normalized Gaussian distribution of width (standard deviation) equal to the atomic radius. The Gaussian distribution for each atom is then weighted with the occupancy. The various Gaussians are added and distributed on a grid and represented in a contour plot. The ice blue areas correspond to an isosurface value of 0.01.

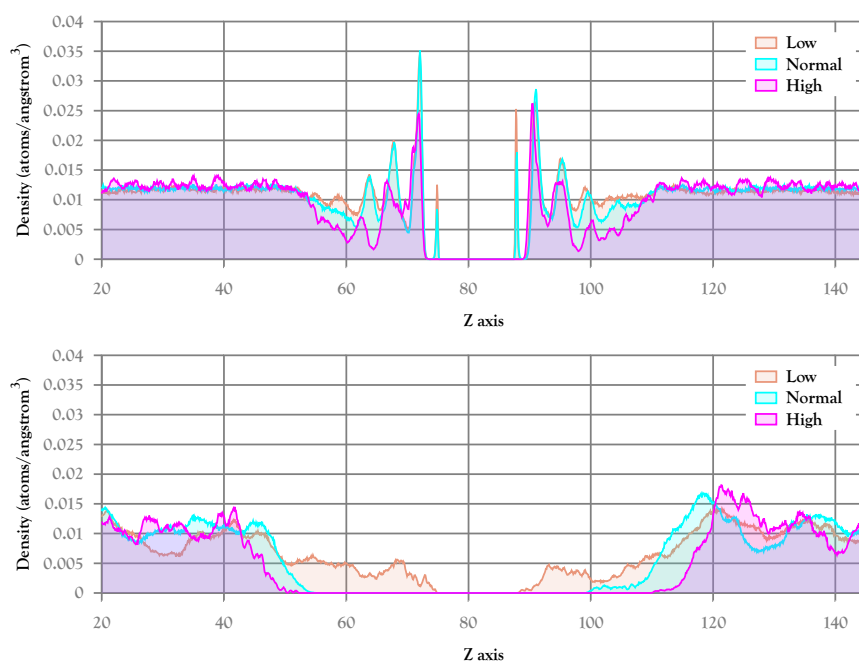


Figure 4.12: Probability density profile for acetonitrile (top) and electrolyte (bottom) along the Z axis.

Except for some small and quick swapping between neighboring ridge oxygens, dye molecules are rather rigid and basically remain in a vertical position.



## 5 Making use of solvent effects to tune carbocation selectivity



T

his chapter is based on a collaboration with Elizabeth Brunk from LCBC<sup>a</sup>.

<sup>a</sup>Laboratory of Computational Biochemistry and Chemistry

Solvents are usually considered as inert and passive reaction media but they also have the potential to influence the relative stability of chemical products and intermediates. Using classical and mixed quantum mechanical/molecular mechanical (QM/MM) molecular dynamics simulations, we investigate the effects of different solvents on the stability of prototypical butyl carbocations and show that the relative thermodynamic stability tert-butyl > sec-butyl can be tuned in different reaction media. We show that solute-solvent electrostatic interactions as well as the molecular shape of the solute and the structure of the solvent cage play an important role in stabilizing sec-butyl over tert-butyl, in fact the linear structure of the sec-butyl carbocation makes it more exposed to solvent molecules than its more bulky tertiary counterpart. We suggest an empirical parameter, the ratio of solvent dipole moment and van der Waals volume as a simple proxy for the strength of the electrostatic solute-solvent interactions and the size of the solvation cage. Using this ratio to scan different solvents, it is possible to identify conditions that destabilize the more stable tert-butyl cation with respect to its sec-butyl isomer. These findings suggest that solvents can be used as active reaction components that allow for a highly selective tuning of chemical reactivity.

### 5.1 Introduction

Solvents are usually considered as mere spectators in chemical reactions. This however is not always the case and solvents can in fact play an important role in stabilizing/destabilizing reaction intermediates and in actively modulating chemical reactivity (e.g. in the Menshutkin reaction<sup>147</sup>). Likewise, for a long time, solvent effects have been mostly ignored in computational chemistry and only by the introduction of implicit solvent models in the 1990s some progress to include solvation phenomena has started<sup>148</sup>. More recently, the introduction of first-principles molecular dynamics and mixed quantum mechanical/molecular mechanical (QM/MM) molecular dynamics simulations has enabled an explicit treatment of solvation effects<sup>35</sup>. Here, we investigate the possible role of different solvents for the preferential stabilization/destabilization of carbocations as prototypical and frequently encountered reaction intermediates. Carbocations are involved in many reactions that are commonly used for organic feedstock in industrial processes, including the synthesis of primary alcohols or the alkylation of hydrogenic compounds<sup>149,150</sup>. Although olefin hydration is readily performed with the help of a variety of catalysts, it is generally difficult to obtain primary alcohols over thermodynamically more favoured products since in these reactions, in accordance with the fact that higher substituted carbocations are thermodynamically more stable (primary < secondary < tertiary) and in agreement with Markovnikov's rule, protons preferably bind to the less substituted carbon atom, rendering the selective production of primary alcohols a difficult task.

In the case of anti-Markovnikov olefin hydration, extensive efforts have been made to establish a direct synthetic approach by developing new catalysts and novel precursors<sup>149,150</sup>. It has been demonstrated that using tertiary-butanol (tert-BuOH) as a solvent in combination with a palladium catalyst containing chloride ligands (PdCl<sub>2</sub>) results in exceptionally high (38:1)

anti-Markovnikov selectivity. Although solvent effects have generally been considered to have a minor effect on carbocation stability, these findings could suggest that solvent molecules indeed act as more than mere bystanders and lead one to ask the question: Is it possible to use solvent effects in a systematic way to obtain products with a given regioselectivity? And if yes, is it possible to predict the optimal solvent? Understanding how to fine-tune the solvent environment would thus provide numerous possibilities in the design of chemical reactions with tailored properties. Here, we have chosen the textbook butyl carbocation  $C_4H_9^+$ , as simple example of a relevant carbenium ion. In this case, tertiary-butyl (tert-butyl) and secondary-butyl, (sec-butyl) are the only experimentally observed species while the primary butyl carbocation is too unstable to be detected. The direct observation of the thermodynamically more stable tert-butyl ion was made by Olah and coworkers in 1963<sup>151</sup> while the more elusive sec-butyl cation was first observed by Saunders et al.<sup>152</sup> In the gas phase, tert-butyl has been reported to be significantly more stable than sec-butyl but due to the difficulty in defining appropriate stability measures, the actual experimental values are scattered over a wide range from 13-22 kcal/mol. Based on electrostatic arguments and the assumption that the degree of solvation does not vary largely, it has been argued that the relative stability of different carbocations is not significantly affected by solvation<sup>153</sup>. However, quantitative data is only available for few media: a value of 14.5 kcal/mol has been estimated for  $SbF_5/SO_2ClF$  matrices and 11.7 kcal/mol for aqueous solutions suggesting that the relative stability difference could possibly be reduced in solution<sup>154</sup>. Since their discovery, butyl carbocations have been studied and modelled extensively<sup>152,155,156</sup>. However, a comprehensive understanding of their stability in different polar, aprotic, and nucleophilic solvents is still lacking. Many factors, both subtle and apparent, can contribute to the relative stability of different carbocation species in solution, (e.g. energetic versus entropic effects or electrostatic as well as steric effects). Therefore, predicting changes in relative stabilities induced by solute-solvent interactions becomes a multifaceted problem. Here, we use classical and QM/MM molecular dynamics simulations in combination with thermodynamic integration (TI) to quantify the relative stabilities of carbocations in various solvent environments. As a proof-of-principles study, we focus on the classic carbocations, tert-butyl and sec-butyl to investigate if their relative stability can be altered or even reversed in different solvents.

## 5.2 Results and discussions

### 5.2.1 Stability differences between tert-butyl and sec-butyl isomers in gas phase and aqueous solution

The relative stability of  $C_4H_9^+$  isomers in the gas phase has been studied extensively both theoretically and experimentally. In agreement with previous quantum chemical calculations, our DFT (BLYP/plane waves) calculations identify the  $C_s$  symmetric structure of tert-butyl as the most stable isomer (1.1 kcalmol<sup>-1</sup> lower than that of the corresponding  $C_{3v}$  structure (1a in Figure 5.1), which has been rationalized in terms of hyperconjugation, the bending of C-H bonds as a result of their interactions with the vacant “p” orbitals at the carbenium

ion center<sup>157</sup>. Similar to the findings of Sieber et al.<sup>152</sup>, our gas phase DFT optimizations of the sec-butyl isomer reveal that the methyl-bridged (see 2a in Figure 5.1), open chain cis (2e) and trans (2c), and hydrogen-bridged cis (2b) and trans (2d) structures are all minima on the gas phase potential energy surface. Among these isomers, 2a has the lowest energy while the other forms are 2-4 kcalmol<sup>-1</sup> higher in energy. On the other hand, the most stable form of sec-butyl (2a) is roughly 12 kcalmol<sup>-1</sup> higher in energy than the lowest tert-butyl isomer (1b in Figure 5.1) in good agreement with the results from high-level quantum chemical methods at the MP2 level. This helps narrowing down the experimental values to the lower range.

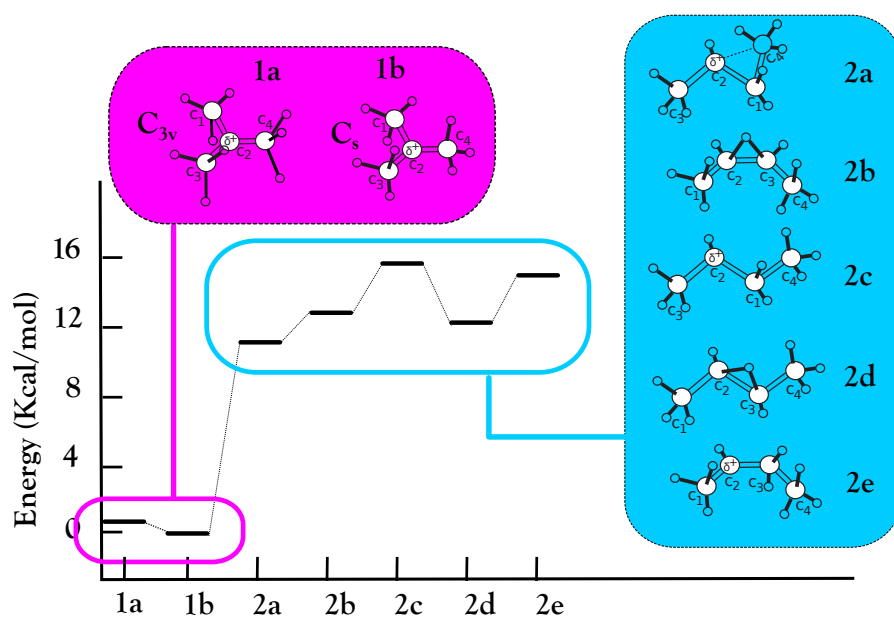


Figure 5.1: Relative energetics in the gas phase. The values shown are calculated at MP2/cc-pVDZ level of theory) between the various isomers of 2-butyl and tert-butyl. Displayed are regioisomers tert-butyl and sec-butyl. Shown in blue are various conformations of sec-butyl, including methyl-bridged (2a), hydrogen-bridged cis (1b), open-chain trans (2c), hydrogen-bridged trans (2d) and open-chain cis (2e). The most stable conformation of tert-butyl is the C<sub>s</sub> (1b) roughly 1 kcalmol<sup>-1</sup> lower than the C<sub>3v</sub> conformer (1a))

To gain insight into possible solvation effects, we first investigated the stability of butyl-cations in water. To this end, we performed QM/MM first-principles molecular dynamics simulations of both tert-butyl and sec-butyl, in which the solutes were treated quantum mechanically while the water molecules were described with the (TIP3P model) force field. In case of the less stable sec-butyl, several conformational transitions take place among different sec-butyl isomers during the 200 ps of QM/MM simulations, involving all conformers. This dynamic nature of sec-butyl, is in agreement with NMR, IR, and solvolysis experiments that conclude that a symmetrically bridged form of sec-butyl is in equilibrium with an unsymmetrically bridged form<sup>152</sup> (Figure 5.2) In contrast to the gas phase where the trans methyl bridged structure (2a) is the lowest energy isomers of sec-butyl, the QM/MM simulations show the asymmetric open-chain cis (2e) form as the most abundant isomer. The relative populations of



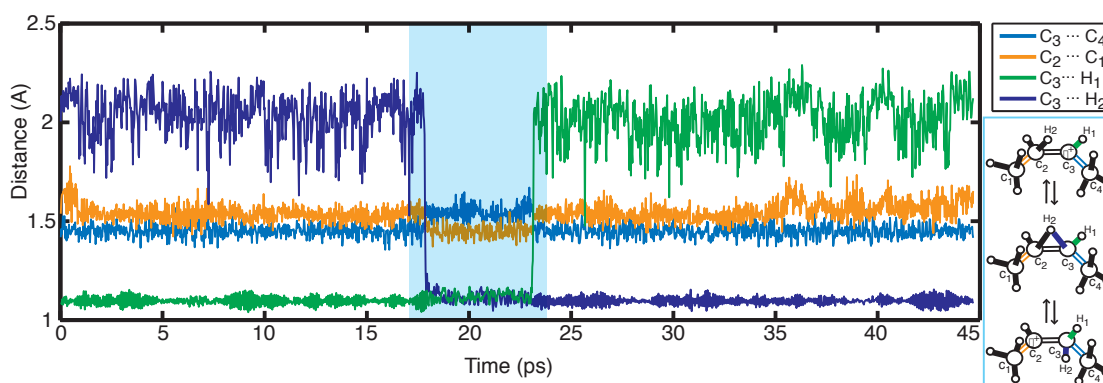


Figure 5.2: Conversion of different isomers during the course of the simulation

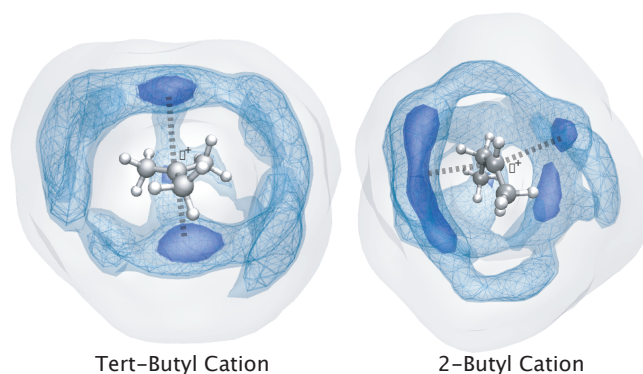


Figure 5.3: The structuring of solvent molecules around tert-butyl and sec-butyl (2-butyl) is depicted by a contour density mapping. The high presence of solvent molecules is demonstrated by the darkened regions, which represent the most frequently occupied positions in the 4.5 Å vicinity around the solute during the 200 ps QM/MM simulation.

2a, 2d, 2b, 2c and 2e during the QM/MM simulations are 3.2, 0.5, 0.3, 20, and 76%, respectively. In addition to the interconversions between sec-butyl isomers, a 2,3-hydride shift occurs at a frequency of 10-15 ps [See Figure 5.2], which has the effect of changing the position of the positively charged carbon centre forming a precursor for the structure (2a). This suggests that solvation can indeed affect the relative stabilities of different butyl isomers at least within the interconverting sec-butyl forms and raises the question which solvent interactions could be responsible for this preferential stabilization of the least stable isomer of sec-butyl? A closer analysis of the nature of the solvent cage (Figure 5.3) shows that the solvation structure of the different isomers can vary considerably. In the most stable form, the regions that are most frequently occupied by solvent molecules are directly adjacent to the C<sub>2</sub> and C<sub>3</sub> atoms, which prevents the possibility of accommodating a bridging hydrogen atom. For this reason, the open chain structures (2c and 2e) are more persistent in water over the symmetrically bridged and methyl-bridged structures. Given the fact that the relative stabilities of sec-butyl isomers undergoes significant alteration in aqueous solution, one can wonder if similar effects also affect the stability of tert-butyl versus sec-butyl.

## Chapter 5. Making use of solvent effects to tune carbocation selectivity

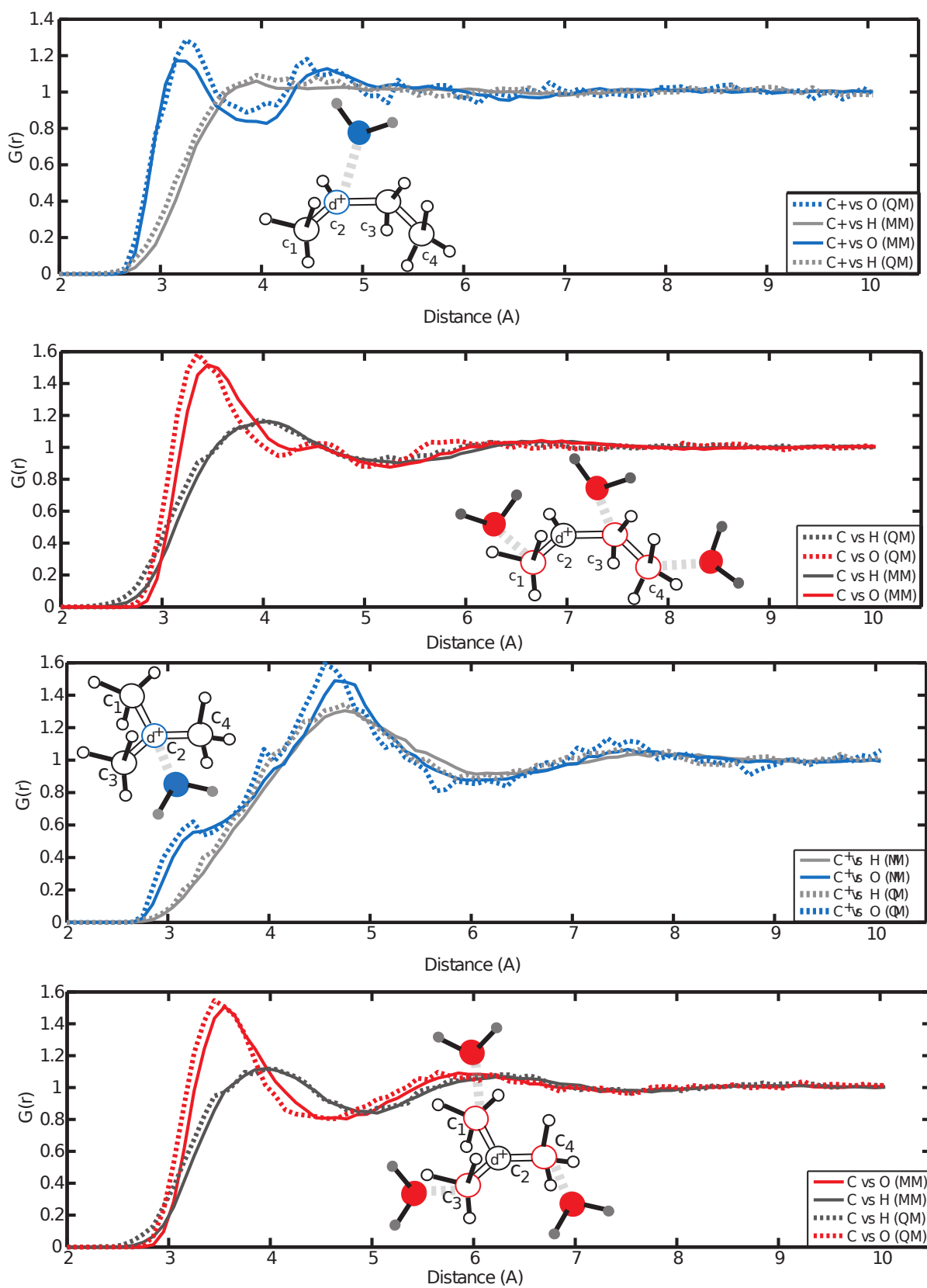


Figure 5.4: Radial distribution function of water molecules around tert-butyl and sec-butyl in QM/MM and MM simulations.

### 5.3. Tuning the relative stability of tert-butyl and sec-butyl cations via environment effects

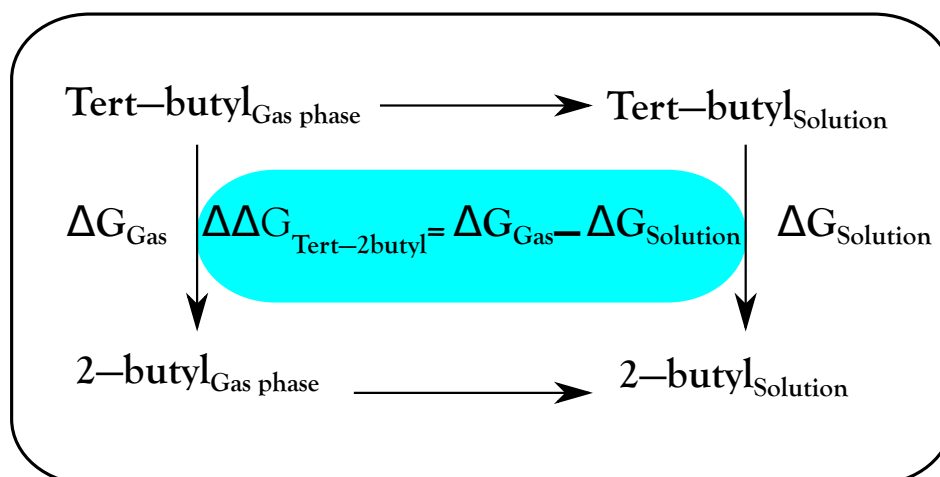


Figure 5.5: Thermodynamic cycle used for calculating the relative solvation free energies in different solvents

The substantial activation barrier ( $30 \text{ kcal mol}^{-1}$  in gas phase) separating tert-butyl and sec-butyl isomers prevents spontaneous interconversion of the two forms in aqueous solution within the 200ps time scale accessible in our simulations. Due to this, the free energy difference between the two forms cannot be directly estimated from their relative populations. However this quantity can be estimated using the thermodynamic cycle in Figure 5.5 via alchemical thermodynamic integration/free energy perturbation at the classical MD level. Closer analysis of the solvation pattern shows that there are distinct differences between the solvation cages of sec-butyl and the thermodynamically more favored tert-butyl. The highest occupied solvent regions around tert-butyl are situated right above and below the positively charged carbon ion. However, although on average both regions are essentially equally populated, (see Figure 5.3) (a) and (b)) the radial distribution function of water shows that this symmetry is broken in solution by cooperative effects leading to an asymmetric solvation pattern in which on average only one water molecule is found within the 1st solvation shell ( $r = 3.4 \text{ \AA}$ ). In contrast, an average of as much as five solvent molecules is found within the 1st solvation shell of sec-butyl (albeit at a larger average solute-solvent distance of  $3.8 \text{ \AA}$ ) (Figure 5.4). This suggests that the geometry of this isomer may be subject to a higher number of solute-solvent interactions, which, depending on the choice of solvent, and the strength of solute-solvent interactions could lead to preferential stabilization of this elusive isomer.

### 5.3 Tuning the relative stability of tert-butyl and sec-butyl cations via environment effects

In order to scan a wide range of solvents, we have used the method of alchemical transformation in combination with thermodynamic integration<sup>158</sup>, to determine the relative solvation free energy differences in a series of solvents.

## Chapter 5. Making use of solvent effects to tune carbocation selectivity

Solvent	$\Delta\Delta G_{tert-2but}^a$	Coulombic	van der Waals	Volume $\text{\AA}^{3b}$	$\mu(D)^c$
Acetonitrile	4.83	-8.92	13.75	78.44	3.92
DMSO	5.65	-8.56	14.21	123.70	3.96
N-methyl acetamide	5.76	-8.41	14.17	130.9	3.70
Ionic Liquid <sup>d</sup>	4.89	-8.02	12.91	-	-
Pyridine	4.80	-7.92	12.72	154.64	2.15
Water	7.89	-7.32	15.21	29.17	1.86
Methyl Hydroxide	5.15	-8.07	13.22	64.21	1.69
Carbon dichloride	2.67	-7.56	10.24	79.95	1.60
Carbon trichloride	1.97	-4.95	6.92	95.17	1.02
Carbontetrachloride	1.40	-2.18	3.58	110.38	0
Carbon tetrafluoride	1.09	-4.3	5.39	73.80	0
Carbon difluoride	0.26	-10.09	10.35	61.67	1.97
Carbon trifluoride	0.05	-9.86	9.91	55.60	1.65
Pyridazine	5.76	-9.02	14.78	142.40	2.2
Methyl fluoride	-0.07	-10.63	10.56	67.73	1.81

Table 5.1: Displayed are the solvation free energy differences between tert-butyl and sec-butyl (negative values indicate tert-butyl is favored and positive values indicate sec-butyl is favored), the volume of each molecule in the solvent, the radius of the overall volume, and the dipole. a) Solvation free energies calculated from the differences in free energy between tert-butyl and sec-butyl in gas phase and solvent environment b) Volume was calculated by summing the volume of each atom in the molecule, using the respective van der Waals radius c) the radius of the volume of each molecule in the solvent d) 1-Alkyl-3-methyl imidazolium cation/Cl ion.

Based on the thermodynamic cycle shown in Figure 5.5, the solvation free energy differences between tert-butyl and sec-butyl ( $\Delta\Delta G_{tert-2but}$ ) are calculated and listed in Table 5.1.

Among all different solvents considered, our simulations suggest that water can indeed provide an environment more conducive to hosting the sec-butyl cation. The values indicate that the free energy difference between the two isomers in the gas phase ( $13 \text{ kcal mol}^{-1}$ ) is considerably reduced in some polar solutions such as water. However it is well established that water immediately reacts with small carbocations and thus in a classical description this reaction is missed. However, other solvents such as pyridine, N-methyl acetamide, pyridazine and DMSO with values slightly lower than that of water can be promising solvents for converting the stability of the two isomers. In the following parts we will try to analyze the origin of this reversal in relative stability.

Free energy differences can be decomposed into two types of contributions, electrostatic (the charging and discharging of the transformed atoms) and van der Waals (the transformation of intermolecular forces between the transformed atoms, such as covalent bonds). Our findings suggest that van der Waals interactions play an important role in favoring sec-butyl over its counterpart (positive  $\Delta\Delta G_{tert-2but}$ ). The absolute difference of the two contributions dictates the final stability of one isomer over its counterpart. As shown in Figure 5.6, almost all of the solvents considered in this work lie in the blue zone where the absolute value of the van der Waals component is larger than that of the electrostatic contribution. The solvent  $\text{CH}_3\text{F}$ , is

## 5.4. Systematic study of different solvents and quantification of free energy differences

the only solvent with larger electrostatic component, which results in a positive total solvation free energy difference (Table 5.1). Considering the fact that most of these halogenated solvents are in gas phase at room temperature, their effect is closer to the effect of vacuum (gas phase), viz. tert-butyl is more stable than sec-butyl.

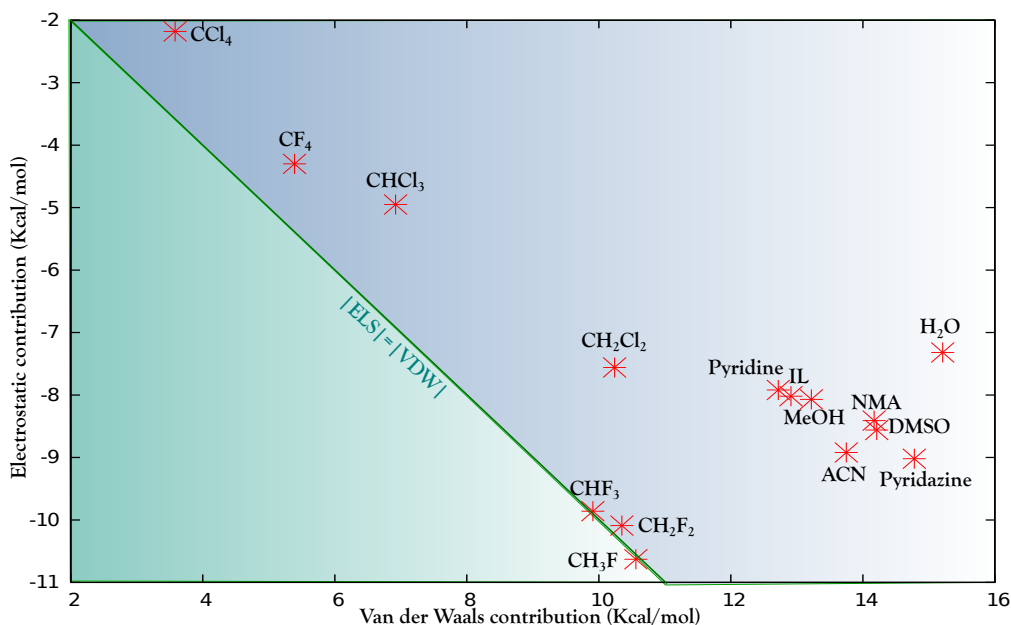


Figure 5.6: Electrostatics versus vanderWaals contributions to the solvation free energy of perturbing tert-butyl to 2-butyl in different solvents.

## 5.4 Systematic study of different solvents and quantification of free energy differences

At first glance the recipe to invert the stability seems to be simple: using a solvent with higher van der Waals (vdW) contribution than electrostatic contribution should revert the stability of one isomer over the one of its counterpart. In practice however, apart from the molecular properties (dipole moment or vdW volume), details of the solvation structure (e.g. solvation cage) seems to play an important role. Not surprisingly, solvents with higher dipole moments generally show higher electrostatic contributions (DMSO, ACN, and NMA) and non-polar molecules such as  $\text{CCl}_4$  and  $\text{CF}_4$  have only a small electrostatic contribution. However, among them, certain solvents do not follow this trend. Likewise, not all the voluminous solvents have higher VDW contributions (e.g. pyridine, pyridazine,  $\text{CCl}_2$ ). For water, although it is smaller than many bulkier solvents such as pyridine and DMSO, but since it is a relatively small molecule, more molecules are found in the first solvation shell which consequently increases the vdW interactions. A ratio between the two parameters of volume and dipole moment ( $10 \times (\text{dipole}/\text{volume})$ ), seems to correlate linearly with the relative solvation free energy (Figure 5.7). Water has the highest ratio, however as mentioned earlier, since our simulations did

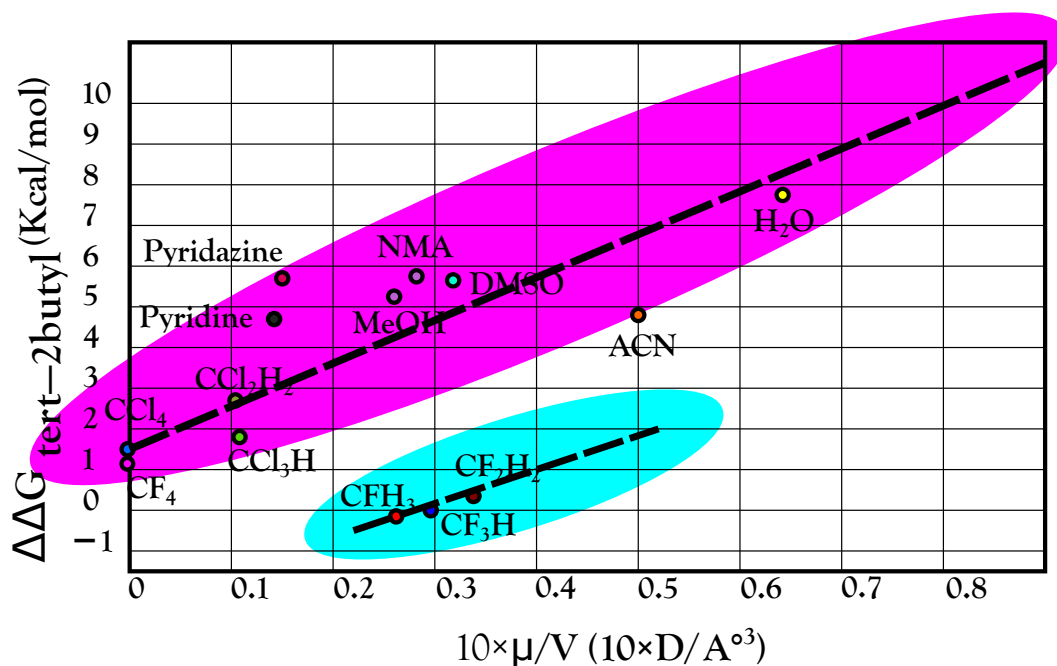


Figure 5.7: Relative solvation free energy difference correlation with dipole/volume ratio. Two distinct domains are recognized within which the linear correlation holds. Aqua region shows the fluorinated solvents that satisfy the linear correlation in a separate domain probably due to their special solvation cages.

not treat water molecules quantum mechanically, the well-known water trapping<sup>159</sup> wasn't captured in our simulations. Bulkier solvents with positive  $\Delta\Delta G_{tert-2but}$ , however, can be used to change the stability of the two isomers without entering any reaction with the solute.

## 5.5 Conclusion

The main question that this contribution poses is: "Can solvent be tuned to alter the inherent stability differences between tertiary and secondary or even primary carbocations? Our findings suggest that different solvent systems can provide diverse enough environments that are capable of changing the relative stability of secondary and tertiary carbocations. We have assessed the molecular details involved in the favoring of tert-butyl over sec-butyl, and vice versa and suggest a simple measure to estimate the general trends. How can fine-tuning of solvent be used to design chemical reactions with tailored properties? By selecting a solvent system based on its capability to favor a desired reaction intermediate over its thermodynamically more stable counterpart, reactions can be designed to be readily executable and produce high yields of the desired product. Our findings might be transferable to other reactions involving carbocations as well as to other reaction types. Our investigations suggest that it is worthwhile to consider solvent as an active player instead of a mere spectator and that an judicious choice of solvent can constitute an additional degree of freedom in tuning e.g. regioselectivity.

## 5.6 Methods

Computational models of tert-butyl and trans sec-butyl were constructed and optimized using the Gaussian 09<sup>77</sup> suite of programs in gas phase. Optimizations were performed at different levels of theory including DFT/B3LYP, MP2 and CCSD(T) with basis sets ranging from 6-31G(d,p), cc-PVDZ, aug-cc-PVDZ to cc-PVTZ. Relative energy differences in the gas phase including zero point energy (ZPE) corrections from scaled frequencies and thermal corrections were computed by calculations of the vibrational partition function within a harmonic oscillator approximation with Gaussian 09. For the classical MD simulations, solvent was added using the xleap program in AMBER 10<sup>121</sup> and the AMBER 99(SB) force field<sup>160</sup>. All of the solvents were simulated under standard conditions. The classical force fields for the carbocations were parameterized using the RESP procedure. Each structure was solvated with solvent molecules in a cubic periodic box with dimensions  $27 \times 27 \times 27 \text{ \AA}$ . For each system, molecular dynamics simulations were performed for 30-50 ns using periodic boundary conditions and the Particle Mesh Ewald (PME)<sup>161</sup> method to treat long-range electrostatic interactions with a real-space cutoff of 10  $\text{\AA}$ . The SHAKE algorithm was used to constrain all bonds that involve hydrogen atoms. A Langevin thermostat was employed to gradually bring each system to the target standard temperature. To ensure constant pressure (NPT) conditions during equilibration, we used a barostat with a relaxation time of 2 ps. A Nose-Hoover thermostat was then used to sample the canonical ensemble during the production run<sup>162-164</sup>. Free energy perturbation methods, in combination with thermodynamic integration (FEP/TI), was used within the sander module of AMBER 10. Using a dual topology paradigm, two topologies (state 0 and state 1) for each transformation were constructed from the solvated and equilibrated structures. The electrostatic and Lennard Jones terms were decoupled by performing three separate alchemical transformations: (i) decharging state 0 using 20 lambda points (ii) transforming the unique atoms in state 0 into those of state 1 using 20 lambda points and (iii) recharging state 1 using 20 lambda points. Convergence was tested by extending the duration of the MD run and by increasing the number of lambda points. In each transformation, all lambda points were individually minimized, equilibrated, and data was collected during a production phase of 3 ns. The change in the potential energy as a result of the perturbation was integrated over the lambda values to obtain the  $\Delta\Delta G$  for each alchemical transformation. For the QM/MM simulations, we use an extension of CPMD<sup>127,165</sup> and described the QM atoms by the DFT/BLYP functional<sup>49,128</sup>, which has been applied to many hydrogen-bonded systems<sup>166-168</sup>, and norm-conserving Martins-Trouiller pseudopotentials<sup>169</sup>. The QM atoms include the carbocations. The wave functions are expanded in a plane wave basis set with a 70 Ry cutoff inside an orthorhombic quantum box with dimensions  $10 \times 15 \times 15 \text{ \AA}$ . Long-range interactions were decoupled using the Martyna-Tuckerman scheme<sup>170,171</sup>. The MM subset is described by a classical AMBER 99 and temperature, using a Nose-Hoover thermostat. The system was equilibrated for 15 ps before performing production phase simulations for 200 ps.





## 6 Valence and conduction band engineering in halide perovskites for solar cell applications



T

his chapter is based on a collaboration with Simone Meloni and Giulia Palermo from LCBC<sup>a</sup>.

<sup>a</sup>Laboratory of Computational Biochemistry and Chemistry

## Chapter 6. Valence and conduction band engineering in halide perovskites for solar cell applications

---

We performed ab initio simulations aimed at identifying the atomistic and electronic structure origin of the valence and conduction band, and band gap tunability of halide perovskites  $ABX_3$  upon variations of the monovalent and bivalent cations A and B and the halide anion X. We found that the two key ingredients are the overlap between atomic orbitals of the bivalent cation and the halide anion, and the electronic charge on the metal center. In particular, lower gaps are associated with higher negative antibonding overlap of the states at the valence band maximum (TVM), and higher charge on the bivalent cation in the states at the conduction band minimum (CBM). Both TVM orbital overlap and CBM charge on the metal ion can be tuned over a wide range by changes in the chemical nature of A, B and X, as well as by variations of the crystal structure. On the basis of our results, we provide some practical rules to tune the valence band maximum, respectively the conduction band minimum, and thus the band gap in this class of materials.

### 6.1 Introduction

Mixed organic/inorganic and fully inorganic halide perovskites of the formula  $ABX_3$  (A = organic or inorganic monovalent cation, B = bivalent cation, X = halogen – See Figure 6.1), recently emerged as very efficient light harvesting materials and charge carrier transporters for solar cells<sup>172, 173, 174</sup>. Power Conversion Efficiencies (PCE), i.e. the percentage of solar light converted into electric current, as high as a certified 20.1% have been reported for perovskite based solar cells<sup>175</sup>.

Several strategies have been attempted to increase the PCE of halide perovskites, some targeting the quality of perovskite films, e.g. its uniformity<sup>172</sup>, others focusing on their intrinsic optical and electronic properties, such as tuning of the band gap,  $E_g$ ,<sup>176-178</sup>. In the latter case, the objective is obtaining a compound with a band gap close to the ideal value of 1.3 eV<sup>13</sup>. Seok and coworkers have shown that in mixed I/Br perovskites,  $ABl_{3-x}Br_x$ ,  $E_g$  can be tuned by changing the halide composition,  $x$ <sup>176</sup>. In particular, in methyl ammonium lead iodine/bromine perovskite,  $MAPbI_{3-x}Br_x$ , (MA = methyl ammonium), the band gap widens with increasing  $x$ . Kanatzidis and coworkers<sup>179</sup> studied the dependence of the valence band maximum (VBM) and conduction band minimum (CBM) as a function of with chemical composition, and concluded that in  $MASnI_{3-x}Br_x$  the widening of the band gap with the amount of Br is due to an increase in CBM rather than a lowering of VBM.

Snaith and coworkers confirmed the findings of Reference<sup>176</sup>, and showed that a correlation exists between  $E_g$  and the pseudocubic lattice parameter of the crystalline sample<sup>178</sup>. This relation inspired them to use the size of the monovalent cation, A, as a tuning parameter for changing  $E_g$ . An analogous strategy has been developed in parallel by Grätzel and coworkers<sup>174</sup>, who also explored the effect of using a mixture of MA and formamidinium (FA) cations. None of these studies have investigated a possible “active” role of A on the electronic structure of the system, e.g. via the formation of hydrogen bonds or other strong interactions with the halides ions of the framework.

The effect of cations and structural variations of the PbI framework of perovskites (e.g. the X-B-X angle) on  $E_g$  has also been discussed by Amat et al.<sup>180</sup>. They concluded that larger cations, which favor a more cubic-like structure of perovskites, red-shift the band gap. This result is somewhat counterintuitive in the light of the results of Reference<sup>178</sup>, where it is shown that FASnBr<sub>3</sub>, which has a cubic structure and smaller lattice constant, has a larger band gap than the tetragonal FASnI<sub>3</sub>. This apparently conflicting result suggests that there is a significant interplay between changes in the chemical composition and variations of the structure of the perovskite, and the combined effect of these two parameters on the band gap is non trivial.

The intricacy of the relation between chemical composition, crystal structure and the electronic properties of perovskites call for a comprehensive theory. Such a theory should aim at rationalizing experimental and computational results in terms of the effect of all essential variables such as the chemical composition, the lattice size, and distortions in the form of tilting angles, on the electronic structure, and thus on the optical properties of perovskites. This is the objective of the present work. We consider a wide range of perovskites, differing in the chemical nature of the bivalent (Pb and Sn) and monovalent (Na, Li and Cs) cations, halogen composition (I, Br, Cl), and crystal symmetry (cubic, tetragonal and orthorhombic). We also considered lead-iodide perovskites with A= NH<sub>4</sub><sup>+</sup> and PH<sub>4</sub><sup>+</sup> to investigate the effect of hydrogen bonding on the electronic structure of the system.

We performed ab initio calculation and analyzed the structure of VBM and CBM in terms of atomic orbitals and give a simple and intuitive interpretation of our and literature results. We also show that strategies for tuning VBM and CBM energy levels, and the bandgap must be crystal symmetry-dependent since cubic and tetragonal/orthorhombic structures follow different design guidelines.

## 6.2 Results

Halide perovskites are made by corner sharing BX<sub>6</sub> octahedra leaving cuboctahedral cavities, which are occupied by the A ions. In the cubic crystal, BX<sub>6</sub> polyhedra are oriented such that all B-X-B angles are 180°, i.e. zero tilting angles  $\theta_1 - \theta_3$  (Figure 6.1A). In tetragonal (Figure 6.1B) and orthorhombic (Figure 6.1C) crystals, the BX<sub>6</sub> polyhedra are rotated (tilted) with respect to their orientation in the cubic structure. The tetragonal structure is characterized by one tilting angle  $\theta_1$  different from 0, while in the orthorhombic structure all of them are non zero.

The chemical nature of halides and bivalent cations affects mainly the lattice size (Figure 6.1D), as expected on the basis of the well-established empirical relations between the ionic radii and the perovskite lattice size<sup>181</sup>. The effect of substituting the monovalent cation, on the other hand, depends on the crystalline symmetry of the reference system. If the system is cubic, the replacement of the original cation results in a corresponding change of the lattice parameter of the crystal: if the new cation is bigger the lattice expands, if it is smaller the lattice shrinks (Figure 6.1E). The value of the tilting angles  $\theta_1$ ,  $\theta_2$  and  $\theta_3$ , which measure the rotation of BX<sub>6</sub> octahedra around the three main axes with respect to the orientation in the cubic case

## Chapter 6. Valence and conduction band engineering in halide perovskites for solar cell applications

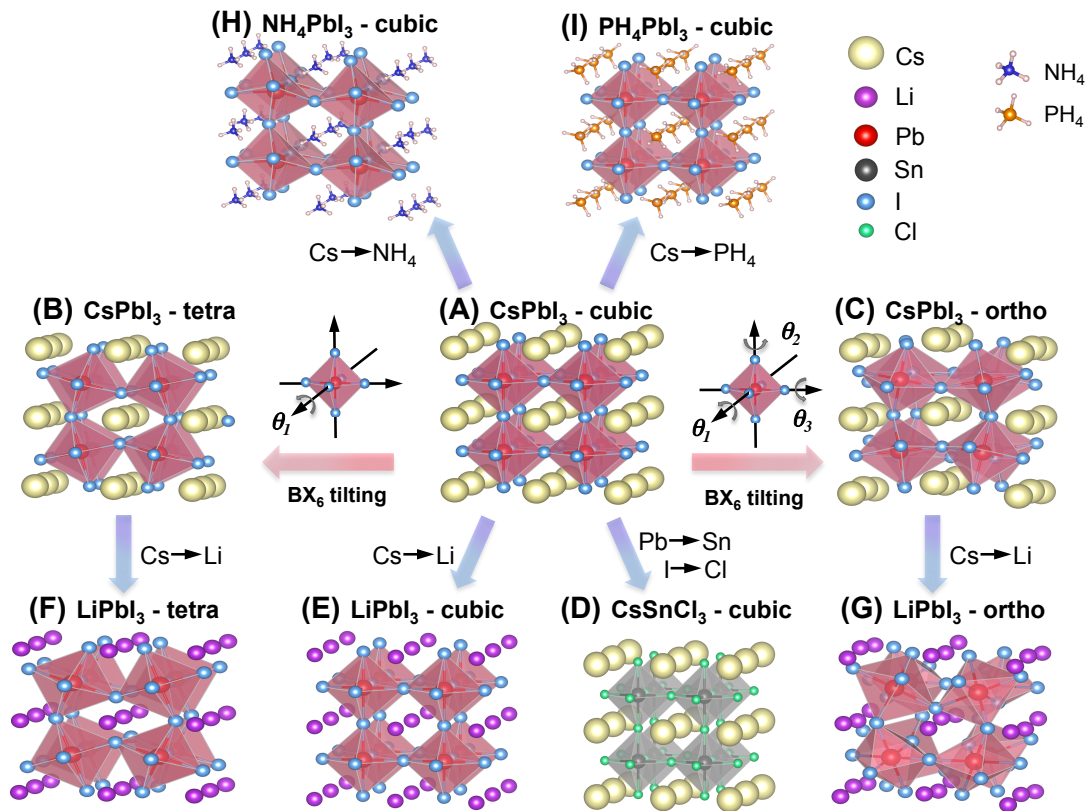


Figure 6.1: Configurations of the equilibrium structure of several perovskites. Images are ordered in such a way that the corresponding structures can be thought of as a series of structural or alchemical alterations starting from the CsPbI<sub>3</sub> cubic structure (A), with a lattice parameter  $a = 6.38\text{\AA}$  as a reference. In panels B and C the tetragonal and orthorhombic structures of CsPbI<sub>3</sub> are shown, respectively. They can be obtained from the cubic analogue by tilting the PbI<sub>6</sub> octahedra along their axis parallel to the tetragonal axis (tetragonal structure) or along all of their three axes (orthorhombic). Tetragonal CsSnI<sub>3</sub> is characterized by a tilting angle  $\theta_1 = 14.3^\circ$  and a pseudocubic lattice parameter  $a^* = \sqrt[3]{V} = 6.12\text{\AA}$  (where  $V$  is the volume of the unit cell). In the orthorhombic CsSnI<sub>3</sub>,  $\theta_1 \sim \theta_2 \sim \theta_3 = 8.5^\circ$  and  $a^* = 6.30\text{\AA}$ . (D) is obtained from the cubic CsPbI<sub>3</sub> by replacing Pb with Sn and I with Cl ( $\theta_1 = \theta_2 = \theta_3 = 0^\circ$  and  $a = 5.85\text{\AA}$ ). E, F and G are obtained from the cubic, tetragonal and orthorhombic CsPbI<sub>3</sub>, respectively, by replacing Cs with Li. Their tilting angle and pseudocubic lattice parameters are: E)  $a = 6.32\text{\AA}$ ; F)  $\theta_1 = 20.3^\circ$ ,  $a = 6.12\text{\AA}$ ; G)  $\theta_1 = 20.5^\circ$ ,  $\theta_2 = 18.8^\circ$ ,  $\theta_3 = 10.8^\circ$ ,  $a = 5.81\text{\AA}$ . (H) and (I) are obtained by replacing Cs<sup>+</sup> in the cubic CsPbI<sub>3</sub> with NH<sub>4</sub><sup>+</sup> and PH<sub>4</sub><sup>+</sup>, respectively. While PH<sub>4</sub>PbI<sub>3</sub> preserves the original cubic symmetry ( $a = 6.32\text{\AA}$ ), NH<sub>4</sub>PbI<sub>3</sub> is triclinic ( $\alpha = \beta = 85.8^\circ$ ,  $\gamma = 87.1^\circ$ ,  $a = 6.38\text{\AA}$ ) and the PbI<sub>6</sub> octahedra are highly distorted

(see Figure 6.1), is  $0^\circ$ . If the original system is tetragonal or orthorhombic, the substitution of A alters both the size of the lattice and the tilting angles.

The effect of substitution on the lattice size is analogous to the cubic case: larger cations expand the lattice, and vice versa. The tilting angle(s), instead, increases if the new cation is smaller, and decreases if it is bigger (see Figures 6.1G and 6.1E). This affects the linearity of the B-X-B angles: the more the structure is tilted, the more the B-X-B angles depart from the  $180^\circ$  value of the cubic structures. We observed values of  $\theta$  in the range  $\sim 7 - 19.5^\circ$  for the non-zero tilting angles in the tetragonal structures, and  $\sim 6.5 - 23^\circ$  in the orthorhombic ones (where all tilting angles are non zero, in this latter case). Monovalent cations that form hydrogen bonds with the halides of the framework are a special case. Depending on the strength of the hydrogen bond, the cubic structure may or may not be a (meta)stable form. In fact, the structure obtained by replacing  $\text{Cs}^+$  with  $\text{NH}_4^+$  in the cubic  $\text{CsPbI}_3$  is triclinic, with crystallographic angles  $\alpha = \beta = 85.8^\circ$  and  $\gamma = 87.1^\circ$ . Moreover, strong hydrogen bonds induce deformations of the  $\text{BX}_6$  polyhedra (Figure 6.1H). If we replace, instead,  $\text{Cs}^+$  by with a weaker hydrogen bond donor cation, e.g.  $\text{PH}_4^+$ , we obtain a stable cubic structure (Figure 6.1I).

An interesting feature of all perovskites considered in this work is the universality of the electronic characteristics of their VBM and CBM. In fact, in all systems, VBM is formed by an antibonding combination of B ns and X mp orbitals, namely Sn-5s or Pb-6p, and Cl-3p, Br-4p or I-5p (see Figure 6.2). This orbital has a high covalent character, with a typical B/X atomic orbital contribution of  $\sim 30 - 40/70 - 60\%$ , depending on the chemical nature of A, B and X, and the crystal symmetry. CBM is also characterized by an antibonding combination, this time by B np and X ms orbitals (see also Reference<sup>182</sup>). In contrast to VBM, CBM is more ionic, with B orbitals contributing  $\sim 70 - 90\%$ .

To understand the effect of all the alterations considered in experiments, we have investigated the effect of variations of the chemical nature of A, B and X, and the crystalline symmetry on the VBM and CBM. It is worth nothing remarking that simple hypotheses to explain the observed phenomenology, e.g. that the energy of VBM and CBM changes because the energy of the corresponding atomic orbitals changes with the nature of the halide, are inadequate. Our calculations show that the difference between the VBM and CBM energy of perovskites of formed by different halides change in a range of  $\sim 2$  eV (see Figure 6.4), and sometimes have an opposite sign with respect to the difference of energy between p atomic orbitals of the different halides ( $\Delta E_{\text{I/Br}} \sim \Delta E_{\text{Br/Cl}} = 0.5 - 0.6$  eV). Thus, it is clear that other effects, discussed in the following, are responsible for the high tunability of the valence and conduction band energy, and, thus, the band gap of halide perovskites.

Concerning the VBM level, the effect of changing symmetry, from cubic to tetragonal to orthorhombic, is reducing the overlap between B ns and X mp orbitals (see Figure 6.2A, 6.2B and 6.2C). In the cubic structure X mp orbitals are aligned along the B-X bond. This alignment is worse in the other two structures; in particular it decreases along the series cubic  $\rightarrow$  tetragonal  $\rightarrow$  orthorhombic. As for monovalent cation substitution, an effect is observed that depends on

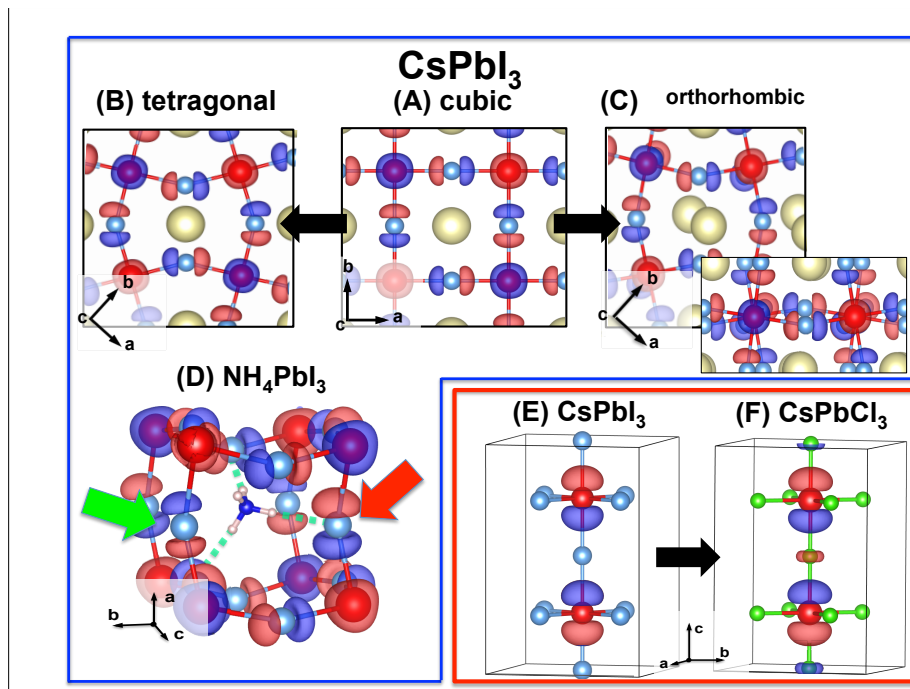


Figure 6.2: VBM (blue frame) and CBM (red frame) orbitals of selected systems. Panels (A), (B) and (C) shows how the tilting of  $BX_6$  octahedra affects the overlap: in the cubic structure (A) X mp orbitals are aligned with B-X bonds and the absolute value of the negative overlap is maximal ( $O_{VBM} = -0.21$ ). In tetragonal (B) and orthorhombic (C) structures p orbitals are no longer well aligned, and the overlap diminishes (tetragonal  $O_{VBM} = -0.17$ , and  $\Delta E_{VBM} = -0.29$  eV is the energy variation with respect to the cubic case; orthorhombic  $O_{VBM} = -0.11$ ,  $\Delta E_{VBM} = -0.54$  eV). In the case of orthorhombic structures, the tilting along all the three axes of the octahedra further reduces the overlap, as shown from the lateral view of the crystal shown in the inset of panel (C). (D) Monovalent cations forming hydrogen bonds (green dashed lines) distort the framework reducing the overlap in analogy to the variations induced by tilting. In addition, hydrogen bonds polarize the VBM orbitals, resulting in an increase of electronic density on hydrogen bonded halide ions (red arrow), and a complementary reduction on the others halides (green arrow) and on bivalent cations. (E) and (F) CBM orbital in tetragonal CsPbI<sub>3</sub> and CsPbCl<sub>3</sub>. The effect of halide substitution along the series  $I^-$ ,  $Br^-$ ,  $Cl^-$  is moving the CBM electronic charge from B to X. For example,  $q_B = 0.81$  and  $E_{CBM} = 0.76$  eV in CsPbI<sub>3</sub>, and  $q_B = 0.86$  and  $E_{CBM} = 0.34$  eV in CsPbI<sub>3</sub>. A similar effect is produced by the change of crystal structure along the series cubic to tetragonal to orthorhombic, and with monovalent cations of varying hardness.

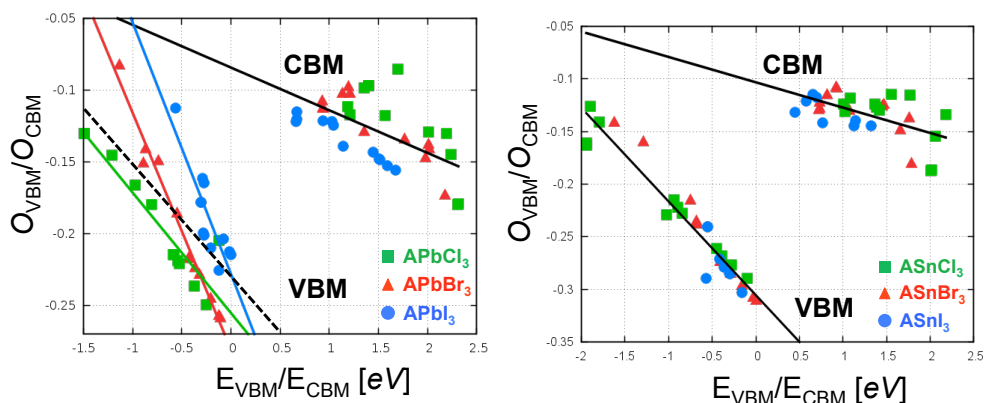


Figure 6.3:  $E_{\text{VBM}} (E_{\text{CBM}})$  vs  $O_{\text{VBM}} (O_{\text{CBM}})$  for Pb-based (right) and Sn-based (left) perovskites.  $E_{\text{BCB}}$  is shifted as explained in the Methods section. The relation  $E_{\text{VBM}}$  vs  $O_{\text{VBM}}$  is linear ( $R^2 \sim 0.93$  and  $\sim 0.53$  for Sn-based and Pb-based perovskites, respectively) and has a large negative slope. In the case of Pb perovskites, if we fit  $E_{\text{VBM}}$  vs  $O_{\text{TVB}}$  independently for each halides (continuous colored lines in the left panel) we obtain a much higher  $R^2$ ,  $\geq 0.85$ . The linear fitting of  $E_{\text{CBM}}$  vs  $O_{\text{CBM}}$  is poorer ( $R^2 \sim 0.33$  and  $\sim 0.38$  for Sn-based and Pb-based perovskites, respectively), and the slope is lower.

the symmetry of the crystal. In cubic systems, in which the size of A affects only the size of the lattice, we observe an increase or decrease of the (negative) B-ns/X-mp overlap with the size of the cation. In tetragonal and orthorhombic crystals, in which the size of A affects both the lattice size and the tilting angles, two competing effects are present: increase or decrease of the B-ns/X-mp overlap due to i) size of the lattice and ii) tilting angle. The overlap increases with the shrinking of the lattice, like in the case of cubic systems, and decreases with the increase of  $\theta$ . Simulations show that, typically, the second effect dominates, and the overlap is reduced in systems with smaller A. The chemical nature of A can affect the VBM orbital also in a more direct way, by polarizing it. This occurs when A can establish a relative strong bond with the halide of the framework, like for instance hydrogen bonds (Figure 6.2D). The effect is twofold in this case. First, because the structure is highly distorted, the alignment of X-mp orbitals with B-X bonds is very poor. Second, the electron density on the X ion hydrogen bonded to A is higher, with corresponding charge depletion on the adjacent B and the remaining X ions. Both effects cooperate in reducing the negative B-ns/X-mp overlap. Finally, concerning the effects of halide substituting the halide, the change of the chemical nature of this species affects mainly the geometry of the system by shrinking/expanding the lattice. However, the size of the p orbitals of X do not shrink/expand by the same amount, thus producing a change in the antibonding overlap with the halide composition of the perovskite.

In summary, for what concerns the tunability of the VMB, all the changes induced by variations in chemical composition and crystal structure can be rationalized in terms of the overlap between the B ns and X mp atomic orbitals forming this state. According to a tight binding formulation, the energy of a crystal orbital depends on the overlap among the relevant atomic orbitals. In particular, the larger is the negative (antibonding) overlap the higher is the energy

## Chapter 6. Valence and conduction band engineering in halide perovskites for solar cell applications

---

of the state. This argument, together with the above analysis, suggests that the key observable correlating with  $E_{\text{VBM}}$  is the orbital overlap, and A, B and X substitutions, and the crystal symmetry are all effective ways to alter the B ns/X mp overlap. To validate this idea we computed the overall overlap in the VBM orbital,  $O_{\text{VBM}} = \text{Re} \left( \sum_{i \in X-mp} \sum_{j \in B-ms} c_{\text{VBM},i}^* c_{\text{VBM},j} \mathcal{O}_{ij} \right)$ , with  $\mathcal{O}_{ij} = \int dr \Phi_i^*(r) \Phi_j(r)$  being the overlap between pairs of X and B atomic orbitals, and  $c_j$  and  $c_i$  projection coefficients of crystal orbitals onto the atomic basis. In Figure 6.3,  $O_{\text{VBM}}$  vs  $E_{\text{VBM}}$  is shown. The fitting of this correlation with a linear function is rather good for Sn-based perovskites (regression coefficient  $R^2 \sim 0.93$ ), while it is somewhat poorer for Pb-based systems ( $R^2 \sim 0.52$ ). However, if one focuses on Pb perovskites of a single halide, the linear trend ( $R^2 \geq 0.85$ ) is much clearer, with a VBM energy ordering following the series  $\text{Cl} < \text{Br} < \text{I}$ . This small but nonnegligible effect is due to the energy variations of X np orbitals, which grows along the series just introduced. The chemical nature of the halide is more important in the case of Pb-based perovskites because the VBM orbital is more ionic than in corresponding Sn-based systems. We also notice that the slope of the linear fitting is high in both Sn and Pb-based perovskites, indicating a high correlation between  $O_{\text{VBM}}$  vs  $E_g$ . This confirms our analysis, that all the modifications considered in experiments affect the band gap via the B ms and X np overlap.

The above argument could be also invoked to explain the dependence of the CBM on chemical composition and crystal symmetry. Also in this case,  $O_{\text{CBM}}$  vs  $E_{\text{CBM}}$  data show the expected trend of a decrease of the energy of the CBM with the overlap. However, data are more scattered and the slope is lower, suggesting a poorer correlation between the two observables. In the case of the CBM, the change of energy is mainly due to the electron density transfer from B to X (or vice versa) induced by the change of chemical composition and crystal structure (see Figures 6.2E and 6.2F, and 6.7). Since the region around B is positive, and that around X is negative, moving charge from B to X increases the electrostatic energy of the orbital. This explanation is proven to be correct by computing the correlation between the charge on the B ion,  $q_{\text{B}}$ , and  $E_{\text{CBM}}$ . Indeed, there is a clear linear correlation between these two observables for the various perovskites of given B and X ions. The effect of changing halides from I to Br to Cl is to shift this linear correlation to higher energy values. This is because the Cl environment, which is more negative, is more repulsive to an additional electron than Br, which, in turn, is more repulsive than I.

It is remarkable that the composition and structural parameters affecting  $q_{\text{B}}$  in the direction of increasing  $E_{\text{BCB}}$  affect  $O_{\text{VBM}}$  and  $E_{\text{CBM}}$  in the opposite direction (Figure 6.8). Thus, a single parameter,  $O_{\text{VBM}}$ , can be used to explain the entire experimental and computational phenomenology. The consequence of this fact is twofold. First, that chemical or structural alterations affect  $E_g$  by a synergic action on  $E_{\text{VBM}}$  and  $E_{\text{CBM}}$ : they change simultaneously in the direction of opening or closing the band gap (Figure 6.4). Second, at variance with other light harvesting materials, it is therefore not easy to tune the energy of the valence and conduction band of perovskites independently to optimize at the same time light harvesting and charge injection into the hole and electron transport materials. However, this does not mean that specific changes cannot affect more one or the other band. In fact, we found that



specific modifications affect the two bands in different ways. Rather, we must conclude that for halide perovskites it is not possible to derive simple design principles to selectively change the energy of VBM and CBM.

### 6.3 Conclusions

We can summarize our findings as follows: chemical and structural changes increasing the negative overlap between orbitals of B and X ions result in a shrinking of the band gap. We can then use this principle for suggesting practical rules for tuning (lowering) the gap. The increase of the overlap can be achieved by choosing B and X so as to reduce the ratio between the size of the lattice and the size of their s and p orbitals. More practical is to use ionic radii as a proxy for the lattice size<sup>181</sup>, and covalent radii as a proxy for the size of B and X orbitals. For example, the variation of  $E_g$  with halide composition follows the trend of the ratio  $\alpha = r_I/r_C$ , between their ionic ( $r_I$ ) and covalent ( $r_C$ ) radii:  $\alpha_I = 1.47$ ;  $\alpha_{Br} = 1.58$ ;  $\alpha_{Cl} = 1.67$ . As for the substitution of the monovalent cation, In the case of tetragonal and orthorhombic structures A must be large so as to reduce the tilting angles, which makes the structure as cubic-like as possible. At the same time, it should not make strong bonds with the perovskite framework. Thus, cations that do not form hydrogen bonds are preferable. For example,  $\text{PH}_4^+$  is better than  $\text{NH}_4^+$ : the former is larger than the latter, and it forms weaker hydrogen bonds.

Another remark is that tuning individual bands of perovskites to improve charge carrier transfer to hole and electron transport materials is complex because, in general, the parameters affecting the energy of VBM also affect the energy of CBM in the opposite direction.

### 6.4 Methods

Density Functional Theory (DFT) calculations are performed using the Quantum Espresso suite of codes<sup>183</sup>. We use the Generalized Gradient Approximation (GGA) to Density Functional Theory in the Perdew-Burke-Ernzerhof (PBE) formulation<sup>52</sup> and, for selected systems, the range separable hybrid exchange and correlation functional of Heyd, Scuseria, and Ernzerhof (HSE)<sup>5</sup>. The interaction between valence electrons and core electrons and nuclei is described by ultrasoft pseudopotentials. Norm conserving pseudopotentials are used in the case of HSE calculations. In GGA calculations, Kohn-Sham orbitals are expanded on a planewave basis set with a cutoff of 40 Ry, and a cutoff of 240 Ry for the density in the case of ultrasoft pseudopotentials. HSE calculations are performed with a cutoff of 60Ry. The Brillouin zone is sampled with a  $3 \times 3 \times 3$  and  $4 \times 4 \times 4$  Monkhorst-Pack  $k$ -points grid<sup>184</sup> for cubic and tetragonal/orthorhombic structures, respectively. The above values are chosen by checking the convergence of total energy, band gap and atomic forces.

Sn-based computational systems are prepared starting from experimental structures for  $\text{CsSnBr}_3$ <sup>6</sup>, replacing  $\text{Cs}^+$  with  $\text{Na}^+$ ,  $\text{Li}^+$ ,  $\text{NH}_4^+$  and  $\text{PH}_4^+$ ; and  $\text{Br}^-$  is replaced with  $\text{Cl}^-$  and  $\text{I}^-$ , as needed. Structures (atomic positions and lattice parameters) are then relaxed. Cubic samples

## Chapter 6. Valence and conduction band engineering in halide perovskites for solar cell applications

---

consist of a  $2 \times 2 \times 2$  supercell containing 8 stoichiometric units. For the body-centered tetragonal structures, we considered the simple tetragonal analogue, which contains 4 stoichiometric units. Finally, for the orthorhombic structure we used the experimental unit cell, which already contains 4 stoichiometric units. Pb-based samples are created using the same protocol starting from experimental structures of Refs. <sup>185</sup> and <sup>186</sup>.

Comparing the energy of Kohn-Sham (KS) orbitals in solid-state systems is difficult because there is no reference value. To overcome this problem, so as to be able to study the trend of  $E_{\text{VBM}}$  and  $E_{\text{CBM}}$  with chemical composition and crystal symmetry, we rigidly shifted the Kohn-Sham eigenvalues of each set of perovskites of given B so as to align low lying pure Sn/Pb states. We expect that the energy of these states, which are made by semi-core orbitals of the bivalent cations and are not directly involved in chemical bonds, is constant. Thus, these states represent a convenient reference. Energies are further shifted so as to set the highest value of  $E_{\text{VBM}}$  to 0 eV.

### 6.4.1 Additional computational details

We performed calculations with and without SOC corrections. The effect of SOC corrections to the GGA-PBE band gap ( $E_g$ ) is, typically, of the order of 0.3 – 0.4 and  $\sim 0.7 - 1.3$  eV toward smaller band gaps for Sn and Pb-based perovskites, respectively. SOC corrections do not change the qualitative conclusions of our study: i) both VBM and CBM are important in the tuning of the band gap (Figure 6.4), ii) the energy of the VBM is mostly affected by the overlap (Figure 6.5), and iii) that of the CBM mostly by the charge on the B ion (Figure 6.7). In Reference <sup>187</sup> it is shown that the good agreement between experimental and GGA-PBE computational results for MAPbI<sub>3</sub> is due to a fortuitous cancellation of errors, due to the fact that the underestimation of the band gap in the absence of many-body effects is exactly compensated by the overestimation associated with the lack of SOC corrections.

This compensation is not as efficient in the case of Sn-based perovskites. We also tested the effect of a functional including range-separated exact exchange (HSE<sup>5</sup>). In fact, it might be the exact exchange in the relatively localized VBM and CBM orbitals that lead to the main correction with respect to the GGA results. To test this hypothesis we computed the HSE band gap,  $E_g^{\text{HSE}}$ , of the CsSnI<sub>3</sub> perovskites (in the cubic, tetragonal and orthorhombic phases), added SOC corrections (described below), and compared computational and experimental results (see Figure 6.6). SOC corrections are computed from the difference of GGA-PBE results with and without SOC:  $\Delta E_g^{\text{SOC}} = E_g^{\text{SOC}} - E_g$ . The so computed band gap of orthorhombic CsSnI<sub>3</sub> (1.05-1.14 eV) is in fair agreement with the recent experimental values of 1.2 eV<sup>4, 6</sup>. For this reason in all the figures of this work CBM energies of all Sn containing systems are rigidly shifted so that  $E_g$  of the orthorhombic CsSnI<sub>3</sub> is 1.14 eV, i.e. our best DFT estimate of the band gap of this system including exact exchange and SOC effects

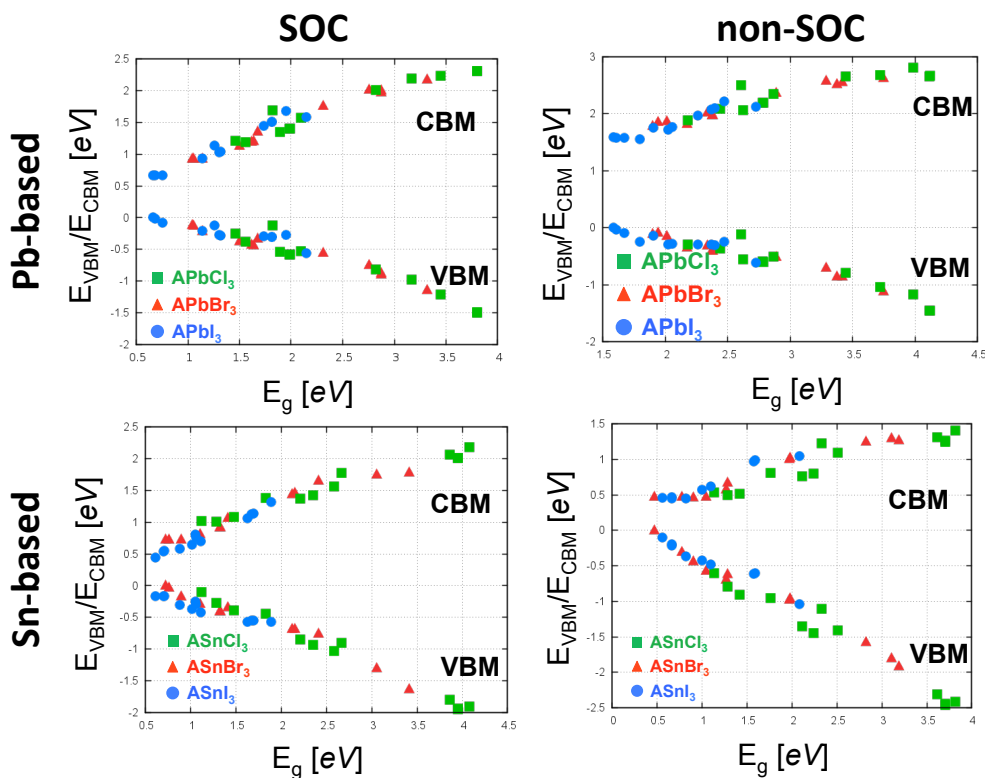


Figure 6.4:  $E_{VBM}$  and  $E_{CBM}$  vs  $E_g$ . The top row refers to Pb-based systems, while the bottom row to Sn-based ones. On the left column we report results obtained including SOC, on the right column results obtained without SOC.

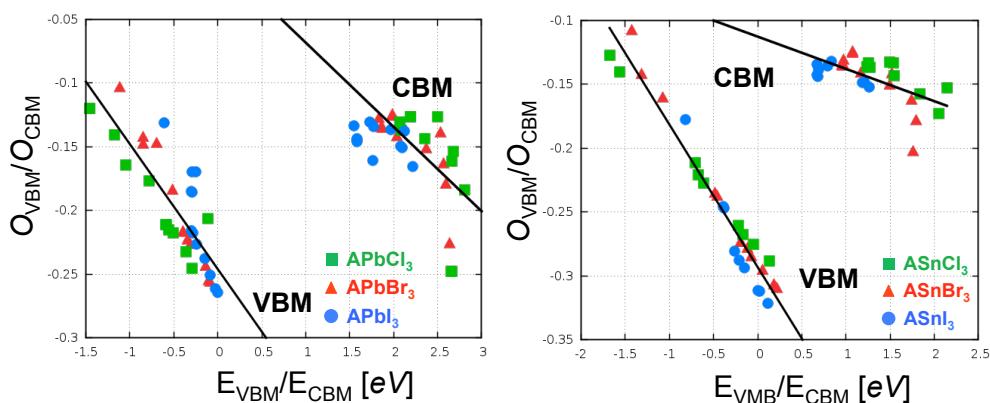


Figure 6.5: (see also Figure 6.1):  $E_{VBM}$  ( $E_{CBM}$ ) vs  $O_{VBM}$  ( $O_{CBM}$ ) without SOC. For Sn-based systems (right), the relation  $E_{VBM}$  vs  $O_{VBM}$  is linear and its slope is large.  $E_{CBM}$  vs  $O_{CBM}$ , instead, cannot be satisfactorily fit with a linear relation and presents a smaller negative slope. For the Pb-based systems (right), the linear fitting of both  $E_{VBM}$  vs  $O_{CBM}$  and  $E_{CBM}$  vs  $O_{CBM}$  is poor. At variance with the Sn-based perovskites case, here the slope of  $E_{VBM}$  vs  $O_{VBM}$  and  $E_{CBM}$  vs  $O_{CBM}$  fitting is comparable.

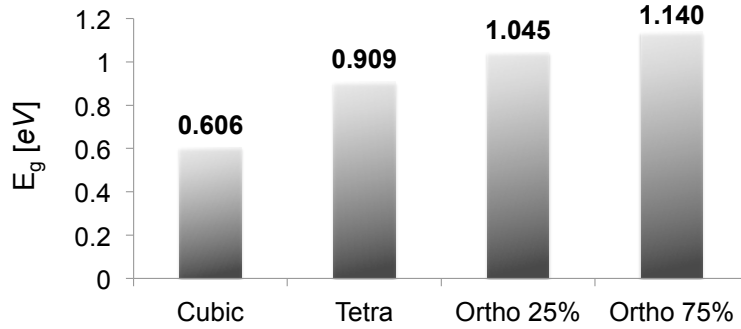


Figure 6.6:  $E_g$  for the various crystal structures of  $\text{CsSnI}_3$ . Ortho 25% and Ortho 75% refer to the two orthorhombic structures identified by Kanatzidis and coworkers<sup>4</sup>. The fitting of crystallographic data required the adoption of a splitting position model for Cs and I atoms, with occupancy 25 and 75% of the two sites of each atomic species. The band gap reported is obtained from DFT calculations using the HSE exchange and correlation functional<sup>5</sup>. The SOC-corrected HSE  $E_g$  (see text above) of the Orthorhombic 75% phase, 1.14 eV, is in nice agreement with the experimental value, 1.3 eV<sup>4, 6</sup>.

#### 6.4.2 Correlation between $q_B$ and $E_{\text{CBM}}$

In Figure 6.7,  $q_B$  vs  $E_{\text{CBM}}$ .  $q_B = \sum_{i \in B} c_i^2$ , values are reported with  $c_i$  being the projection coefficient of the CBM state onto B atomic orbitals and  $q_B$  as a measure of the amount of CBM charge on B atoms. Figure 6.7 shows a clear correlation between  $E_{\text{CBM}}$  and  $q_B$ : the higher is the charge on B the lower is  $E_{\text{CBM}}$ . As explained in the main text,  $E_{\text{CBM}}$  grows with the shrinking of  $q_B$  because part of its charge is moved from the attractive  $B^{2+}$  environment to the more repulsive X one. We notice that the trend of  $E_{\text{CBM}}$  with  $q_B$  depends on the halide, with an almost rigid shift toward higher  $E_{\text{CBM}}$  values along the series  $\text{I} \rightarrow \text{Br} \rightarrow \text{Cl}$ . This is not surprising because along this series the partial negative charge on the halide increases, and so does the electrostatic energy associated to the CBM charge on X. Results with and without SOC present an analogous trend, confirming that the qualitative picture one could gain from pure GGA calculations is correct.

#### 6.4.3 Correlation between $q_B$ and $O_{\text{VBM}}$

In the main text we explained that bands and band gap tuning strategies can be based on the overlap in the VBM crystal orbital because there is a correlation between this observable, determining the energy of the VBM, and  $q_B$ , determining the energy of the CBM. This is shown in Figure 6.8, where we report  $q_B$  vs  $O_{\text{VBM}}$ . We notice that  $q_B$  decreases with  $O_{\text{VBM}}$ , which results in a cooperative action in reducing/increasing the gap: when  $O_{\text{VBM}}$  changes in the sense of reducing the energy of the VBM,  $q_B$  changes in the direction of increasing the energy of the CBM, and vice versa.

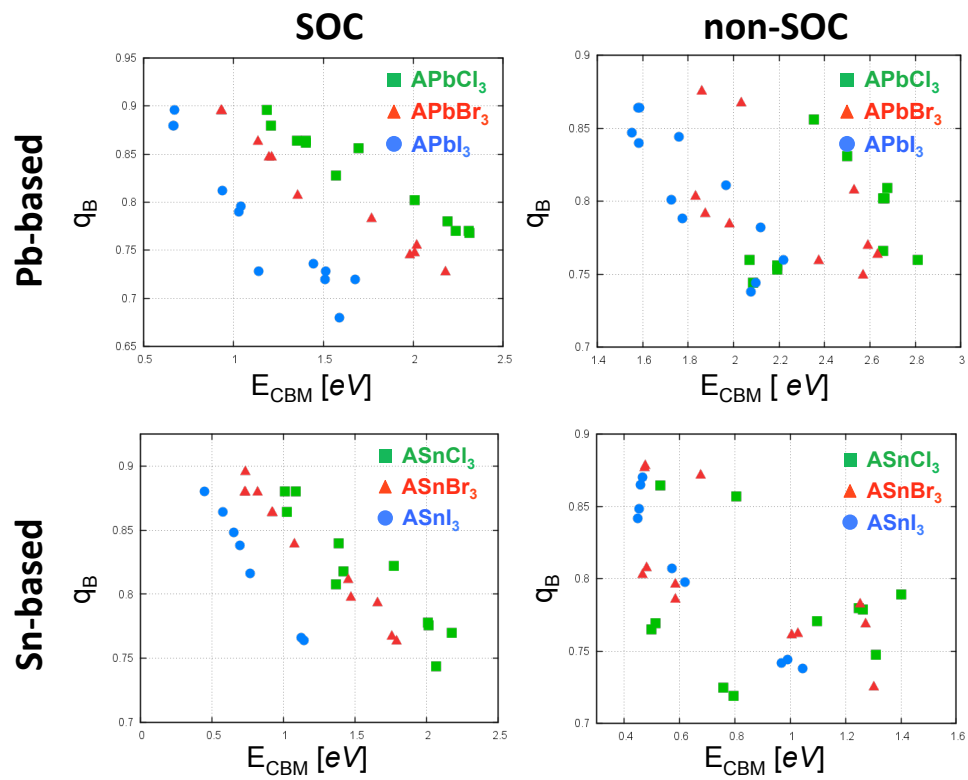


Figure 6.7:  $q_B$  and  $E_{CBM}$ . The top row refers to Sn-based systems, while the bottom row to Pb-based ones. On the left column we report results obtained including SOC, on the right column results obtained without SOC.

## Chapter 6. Valence and conduction band engineering in halide perovskites for solar cell applications

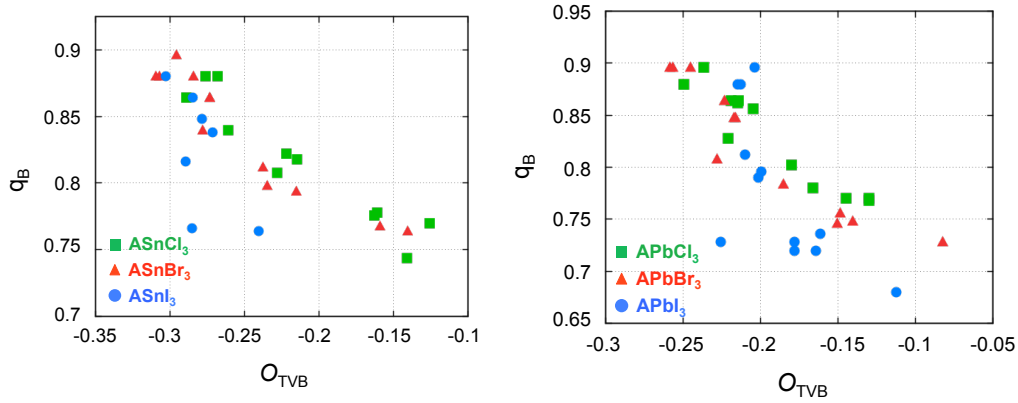


Figure 6.8:  $q_B$  vs  $O_{TVBM}$  for Sn-based (left) and Pb-based (right) perovskites

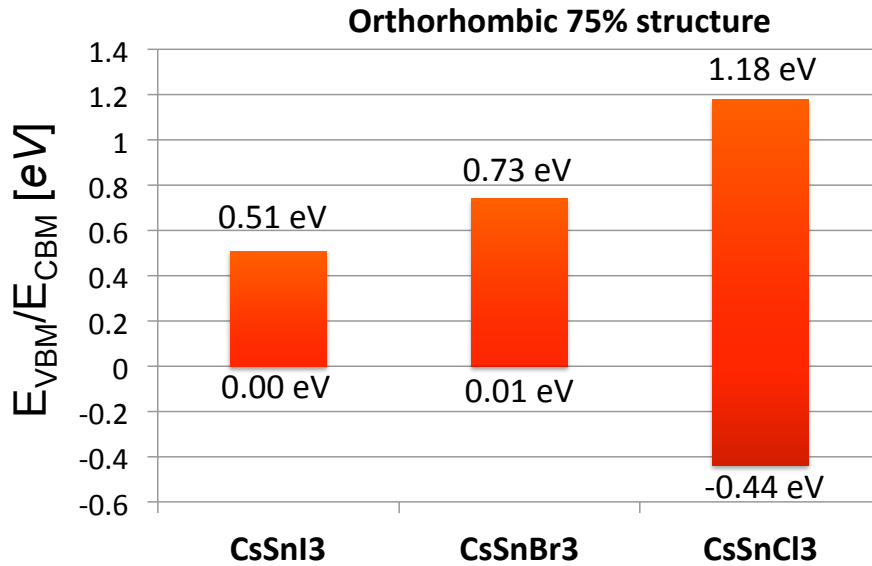


Figure 6.9:  $E_{VBM}$  and  $E_{CBM}$  energies of the orthorhombic structure of  $CsSnX_3$  perovskites

### 6.4.4 Calculation of the variation of $E_{VBM}$ and $E_{CBM}$ with stoichiometry and crystal symmetry, and the dependence of $E_g$ on them

Figure 6.4 shows that the energy of VBM and CBM change by  $\sim 2$  and  $1.5$  eV, respectively, in the systems investigated. Thus, we must conclude that the change of  $E_g$  in the perovskites set is determined by both states. This is only apparently conflicting with the experimental results of Ref. <sup>179</sup>. In fact, considering the systems investigated in this latter work we also observe that the change in the band gap is mostly determined by the change in the CBM (Figure 6.9).

# 7 Computational study of carrier transport in halide perovskites via a semi-classical model of electron and hole dynamics



This chapter is based on a collaboration with Simone Meloni and Giulia Palermo from LCBC<sup>a</sup>, my husband Amir Hesam Salavati from LCAV<sup>b</sup> and Qin Peng from LPI<sup>c</sup>.

<sup>a</sup>Laboratory of Computational Biochemistry and Chemistry

<sup>b</sup>Laboratory of Communications Audiovisual

<sup>c</sup>Laboratory of Photonics and Interfaces

## Chapter 7. Computational study of carrier transport in halide perovskites via a semiclassical model of electron and hole dynamics

---

Carrier transport in halide perovskites is studied using a semi-classical model of electron and hole dynamics. Effective masses are calculated for a variety of perovskites differing in chemical composition and crystal structures. We show that effective masses are highly correlated with the band gap energy. Using the **k.p** model for the bottom of the conduction band and a tight binding model for the top of the valence band, this trend can be rationalized in terms of two key properties, the orbital overlap between halogens and lead atoms and the charge on the bivalent cation. The highest anisotropy in the effective mass tensor is observed for the tetragonal structures. Most of the systems studied in this work show the effective masses characteristic of good carrier transporters ( $m^* < 1.5 m_0$ ) for both electron and holes, however, the introduction of some vacancies or dopants can change this value more considerably. While some dopants like Zn(II) flattens the conduction band edges ( $m_e^* = 1.7 m_0$ ) and adds an isolated energy level in the band gap, vacancies and more specifically  $\text{Pb}^{2+}$  vacancies make the valence band edge more shallow ( $m_h^* = 0.9 m_0$ ). From a device-performance point of view, modifications that increases the orbital overlap could be helpful by both decreasing the band gap and increasing carrier transport.

### 7.1 Introduction

Twenty years after their first discovery as possible robust transistors<sup>188</sup>, halide organic/inorganic perovskites (HOPs) with the composition of  $\text{ABX}_3$  (A = organic or inorganic monovalent cation, B = bivalent cation, X = halogen) have attracted a lot of attention due to the breakthrough they made in third-generation solar cells<sup>189–191</sup>. Efficiencies as high as 18.4%<sup>192</sup> and 20.1% (confirmed by U.S. National Renewable Energy Laboratory) have been reported for perovskite solar cells and the future efficiency of 30% (close to Shockley-Queisser limit) seems feasible. Perovskites owe their superb performance to the high open circuit voltage ( $V_{OC}$ )<sup>193</sup>, long carrier lifetime<sup>194</sup> and low non-radiative carrier recombination<sup>195</sup>. The apt bandgap of  $\sim 1.5$  eV makes them the perfect light harvester and puts them in the class of highly efficient thin-film solar cells like CdTe.

Hand in hand with experimental studies, theoretical methods have been involved from the start trying to shed light on the origin of the robust electronic properties of halide perovskites. Using density functional theory (DFT), the effect of halide and cation variations on the optical band gap, band structure, crystal defects and the perovskites/ $\text{TiO}_2$  interface have been studied intensively<sup>196–198</sup>. Even when spin-orbit coupling (SOC) effects that can be sizable in heavy elements such as Pb and Sn are neglected and despite the failure of DFT in describing many body effects, DFT is surprisingly able to predict the band gap close to the experimental measurements. Using GW methods, Umari et al. showed that this coincidence is due to the cancellation of errors which luckily compensates for DFT deficiencies in predicting the energetics. They also showed that the band structure properties are on the other hand mostly affected by SOC effects and DFT+SOC can give a proper description of band dispersion without the need for including many body effects<sup>199</sup>.

In Chapter 7 we demonstrated how one can rationalize and predict the various effects of



chemical composition and crystal symmetry on electronic properties of perovskites via two key parameters, the overlap between metal and halide orbitals and the charge on the divalent cation. We interpreted the band gap variations via an atomic orbital framework and showed how the overlap between the involved orbitals in the top of the valence band (TVB) and the electronic charge on the B ion are correlated with the energetics of the band edges. In this work we delve deeper into another equally important property of HOPs: carrier transport. In the field of semiconductors people have benefited a lot from the semi-classical model of electrons and holes by assigning effective masses ( $m^*$ ) to the carriers<sup>200</sup>. Saving a large part of simplicity inherited from the model of free electrons in gas phase, effective masses give a first quantitative measurement for the efficiency of carrier transport. Recently, this model has been applied also to HOP by different groups<sup>201-210</sup>. Despite the diversity of possible approaches for calculating the effective masses, all the reported values unanimously are in the range of good carrier transporters in accordance with the experimental measurements of carrier mobility<sup>211</sup>. The chemical origin of this property, however, remains an open question. In this work, after a brief discussion of different methods usually applied to derive the effective masses, we calculate  $m^*$  over a wide range of Sn and Pb-based perovskites, differing in the chemical nature of the monovalent cation (Na, Li, Cs, and some organic molecules), halogen (I, Br, Cl), and the crystal symmetry (cubic, tetragonal and orthorhombic). Looking at the general trends present in our results we see that small effective masses are again the result of high orbital overlap. The correlation with the band gap energy observed and reported by many different groups, is indeed the immediate result of this simple fact. We also investigate the influence of vacancies and doping on the effective masses. While doping might be beneficial in view of increasing the concentration of free charge carriers, it turns out that Zn(II) doping can have some detrimental effects on carrier transport in some cases.

## 7.2 Methods

Variable cell relaxation of all the structures was performed at Density Functional Theory (DFT)/Perdew-Burke-Ernzerhof (PBE)<sup>52</sup> level of theory as implemented in the Quantum Espresso suite of codes.<sup>183</sup> Fully relativistic SOC calculations were performed on top of DFT/PBE for band structure calculations. Relativistic ultrasoft PBE pseudopotentials with an energy cutoff of 40 Ry and 280 Ry for the density were used for all of the atoms. The Brillouin zone is sampled with a  $3 \times 3 \times 3$  and  $4 \times 4 \times 4$  Monkhorst Pack  $k$ -points grid<sup>184</sup> for cubic and tetragonal/orthorhombic structures, respectively. The above values are chosen by checking the convergence of total energy, band gap and atomic forces. A quadratic least square fit of the dispersion of the band structure at the band gap was performed using the "lsqcurvefit" function of MATLAB 7.12<sup>212</sup>. The quality of the fit was assured having the *resnorm* value always smaller than  $1.5 \times 10^{-9}$ . The fit is done with 27 data points distributed on a  $3 \times 3 \times 3$  grid around the extremum (27 points is the optimum number for having fits with small *resnorm* values). As discussed in the text, the grid size  $\Delta k$  is also optimized for each system.

### 7.2.1 Brief discussion of $m^*$ calculation

By definition, effective mass is the curvature of the dispersion curve  $E(k)$  at a certain  $k$  extremum. Having the full tabulation of the band energies, curvature can be estimated either via the  $\mathbf{k}, \mathbf{p}$  method (Equation (7.1)) (extended up to the second order perturbation) or through Taylor expansion (Equation (7.2)) (again expanded up to the second order).

$$E_k^n = E_{k_0}^n + \frac{\hbar^2 k^2}{2m} + \frac{\hbar^2}{m^2} \sum_m \frac{|k \cdot \langle u_{k_0}^{(m)} | p | u_{k_0}^{(n)} \rangle|^2}{E_{k_0}^n - E_{k_0}^m} \quad (7.1)$$

$$E_k^n = E_{k_0}^n + \sum_i \frac{\delta E^n(k)}{\delta k_i} \Big|_{k=k_0} \Delta k_i + \frac{1}{2} \sum_{i,j} \frac{\delta^2 E^n(k)}{\delta k_i \delta k_j} \Delta k_i \Delta k_j, \quad (7.2)$$

where  $u$  stands for the band potentials and  $p$  stands for the momentum operator. Either way a parabolic shape is assumed for the band edge around the extremum<sup>213</sup>. In this work using the former approach, we calculated DFT (SOC) derived  $E(k)$  for a three dimensional grid ( $\Delta k$  of which was chosen in a way to give the minimum residual value) around the BCB and TVB extrema, and then fitted the resulting data to a nonlinear curve in a least squares sense (Equation 7.3).

$$\begin{bmatrix} e_1 \\ e_2 \\ \cdot \\ \cdot \\ \cdot \\ e_{27} \end{bmatrix} = \frac{1}{2} \begin{bmatrix} k_{ix} - k_{0x} \\ k_{iy} - k_{0y} \\ k_{iz} - k_{0z} \end{bmatrix} \begin{bmatrix} \frac{\delta_\epsilon}{\delta k_x \delta k_x}, \frac{\delta_\epsilon}{\delta k_x \delta k_y}, \frac{\delta_\epsilon}{\delta k_x \delta k_z} \\ \frac{\delta_\epsilon}{\delta k_y \delta k_x}, \frac{\delta_\epsilon}{\delta k_y \delta k_y}, \frac{\delta_\epsilon}{\delta k_y \delta k_z} \\ \frac{\delta_\epsilon}{\delta k_z \delta k_x}, \frac{\delta_\epsilon}{\delta k_z \delta k_y}, \frac{\delta_\epsilon}{\delta k_z \delta k_z} \end{bmatrix} \begin{bmatrix} k_{ix} - k_{0x} \\ k_{iy} - k_{0y} \\ k_{iz} - k_{0z} \end{bmatrix} \quad (7.3)$$

We used the *lsqcurvefit* function of MATLAB<sup>212</sup> to fit our band structures. The Hessian matrix is then diagonalized to yield three principal axes of carrier transport (eigenvectors) with their corresponding effective masses (eigenvalues). As a first benchmark system, we have chosen the well studied MAPbI<sub>3</sub><sup>201–203</sup> to establish the best numerical procedure for an accurate evaluation of  $m^*$ .

Despite the generally good agreement of the small magnitude of  $m^*$  for halide perovskites from both computational and experimental studies<sup>211,214</sup>), some random large values have occasionally been reported using the same theoretical model and electronic structure calculations<sup>205,215</sup>. While previously, these large values were attributed to the absence of SOC effects in pure DFT(GGA) calculations<sup>216</sup> we speculate and will show that appearance of such large values is due to the parabolic assumption often under-represented in  $m^*$  calculation. In Table 7.1 the values of  $m^*$  are calculated for MAPbI<sub>3</sub> using three different 3D grids around the extremum ( $\Delta k < \Delta k' < \Delta k''$ ).  $\Delta k$  values are fractions of the reciprocal lattice parameter  $\vec{b}$ . For sampling broader parabolas coarser grids are needed and vice versa, to remain within the harmonic region. Indeed it is evident from Table 7.1 that the choice of  $\Delta k$  can drastically affect

	$m_h^*$	$m_e^*$	Coefficient of determination ( $R^2$ ) for $m_h^*$ and $m_e^*$ respectively
$\Delta k = \vec{b}/100$	0.05	0.35	0.67, 0.87
$\Delta k' = \vec{b}/400$	0.19	0.32	0.93, 0.9
$\Delta k'' = \vec{b}/800$	18.66	0.03	0.80, 0.71

Table 7.1: Average  $m^*$  for MAPbI<sub>3</sub> using different grid sizes for fitting.  $\Delta k'$  is giving the best  $R^2$  value showing the significance of grid size on fitting procedure, grid is symmetric around the extremum which in the case of MAPbI<sub>3</sub> is slightly shifted from  $\Gamma$  point.

the value of  $m^*$ .

Erroneous values as large as 18.7  $m_0$  can appear solely by using wrong grid sizes (illustrated by the fitness function for different grids in Figure 7.1). In fact, since there is no strict control on the directional growth of perovskites, mobilities as high as 11.979  $m_0$  (reported in Reference<sup>205</sup> for orthorhombic MAPbI<sub>3</sub> along [010] direction) or 13.19  $m_0$  (reported in Reference<sup>215</sup> for MASnCl<sub>3</sub>) would hamper the charge mobility significantly. According to Table 7.1, the  $R^2$  (quality of the fit) is maximum for  $\Delta k'$  (0.93, 0.9). The corresponding average  $m^*$  values (highlighted row in Table 7.1) are indeed the correct  $m^*$  also reported elsewhere<sup>199,201</sup>. Brivio et al.<sup>210</sup> correctly address this issue in a quite different approach following the **k.p** scheme. They already report nonparabolic behaviors in a range of  $k_{BT}$  away from the extremum. While the parabolic dispersion can be satisfied by restricting  $k$  points to a narrow vicinity of the extremum, some authors prefer to introduce a  $k$ -dependent effective mass ( $m^*(k)$ ) without any further calculation of its magnitude. In fact, the parabolic limitation of  $m^*$  is the immediate consequence of not including higher order perturbation terms corresponding to higher order derivatives in the **k.p** and Taylor expansion methods, respectively and there is no real need for the introduction of new quantities such as  $k$  dependent masses. Having said that, we show in this work that one can calculate accurate  $m^*$  for halide perovskites within the conventional definition of effective masses (second order perturbation) provided that the  $\Delta k$  are chosen in such a way to remain within the parabolic region.

### 7.2.2 Effective mass calculation and significance of $\Delta k$ value for fitting

For each system the band diagram was obtained using a regular  $4 \times 4 \times 4$  Monkhorst pack grid for sampling the BZ along the high symmetry points. After locating the real extremum point for both TVB and the BCB, a set of grid points ( $3 \times 3 \times 3$ ,  $4 \times 4 \times 4$ ,  $5 \times 5 \times 5$ ) were generated around the extremum with different mesh sizes  $\Delta k$ . In most cases the fitness was converged with 20-27 points and no further modification was added by including more grid points. Therefore for the screening purpose, we continued with 27 points ( $3 \times 3 \times 3$ ). The mesh size on the other hand was crucial to the results. Each and every single system depending on the dispersion shape of its band structure needed finer or broader  $\Delta k$  value. Generally  $\Delta k$  was varying between  $\vec{b}/100$  to  $\vec{b}/400$ , for sampling the broader and finer curvatures, respectively.

## Chapter 7. Computational study of carrier transport in halide perovskites via a semiclassical model of electron and hole dynamics

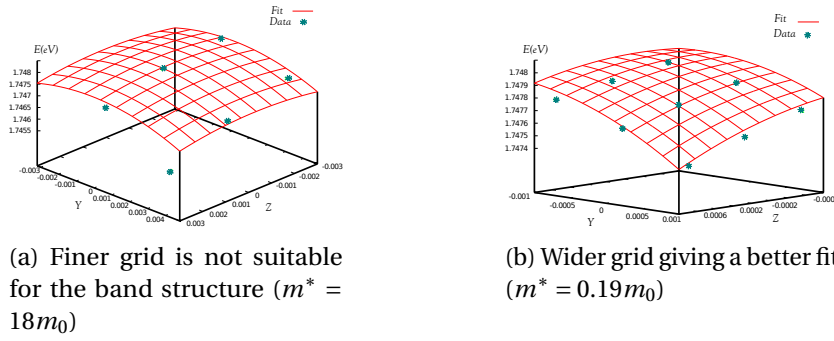


Figure 7.1: Importance of the grid size for fitting: The projection of the energy function on the  $x$  plane is demonstrated.

We used two different fitting functions, in one, only the tensor of the Hessian matrix was fitted giving the extremum as an initial value and in the second one, both the location of the extremum as well as the Hessian matrix was fitted. This way we could assess the quality of the fit once more with comparing the extremum point values. The significance of the  $\Delta k$  value is shown with an example of  $\text{CH}_3\text{NH}_3\text{PbI}_3$  in Figure 7.1.

### 7.2.3 GGA Vs. GGA+SOC for Cubic $\text{CsSnI}_3$ band diagrams with $C_{3v}$ symmetry

According to the matrix element theorem, the matrix element between an operator  $p$  and two wave functions  $\psi_1$  and  $\psi_2$  can differ from zero only when the direct product of the representations of  $p$  and  $\psi_2$  contains an irreducible representation of  $\psi_1$ . The operator  $p$  has a translational symmetry so according to the character table it has  $A_1$  irreducible representation. As demonstrated in Figure 7.2a, the BCB has  $A_1$  symmetry, thus  $p|BCB\rangle$  would have  $A_1 \otimes A_1$  symmetry which according to the product table of the  $c_{3v}$  point group is  $A_1$  (Tables 7.2.3 and 7.2). Therefore the momentum matrix element of TVB (with  $A_1$ ) with the BCB is nonzero. On the other hand, higher conduction bands belong to  $E$  representations which has no common component with  $A_1$ . Meaning that upper conduction band matrix elements with the BCB vanish to zero. The same argument holds for the SOC band structure. Except for the use of double group notations for including the spin symmetry as convention.

## 7.3 Results and Discussion

### 7.3.1 Lower gaps result in lower effective masses

Using the techniques explained above, we performed high-throughput ab initio screening to monitor the variations of the effective masses under different chemical and structural changes. While previous computational studies have been published on the effective masses of individual HOP systems, we believe this work is the first to address a wide range of compounds (possible HOP candidates) for assessment of their transport properties. In addition, exploring

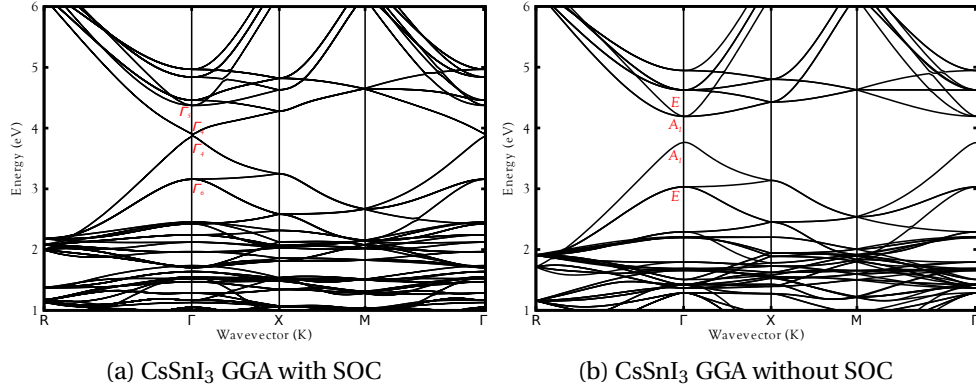


Figure 7.2: Band diagrams with and without SOC correction. Band splitting occurs when SOC is applied.

	$E$	$2C_3(z)$	$\sigma_v$	Linear, rotations	quadratic
$A_1$	1	1	1	$z$	$x^2 + y^2$
$A_2$	1	1	-1	$R_z$	
$E$	2	-1	0	$(x,y)(R_x, R_y)$	$(x^2 - y^2, xy) (xz, yz)$

Table 7.2: Character table of  $c_{3v}$  point group

a wide range of compounds allows for realization of dominant hidden correlations among different variables. Figure 7.4 shows the effective masses versus the band gap for tin-based HOPs. Both electron and hole effective masses decrease as the band gap shrinks. The gap shrinks symmetrically from bottom and top (viz. TVB and the BCB approach each other with the same rate-see Figure 7.4 and 7.5). This linear correlation seems to be intrinsic to halide perovskites (or more general to covalently bonded semiconductors<sup>217</sup>).

In Reference<sup>218</sup> Hautier et al. performed a similar study to propose low effective mass-high band gap oxides for the purpose of efficient transparent conductive oxides (TCOs). However, in the case of TCOs, this relation does not hold in general for all chemical compositions while in HOPs more general trends can be established. The evident correlation between the gap and  $m^*$  is indeed in line with what is predicted by band structure methods. Here we will benefit from two in principle contradictory though complementary band structure theories to explain our results. In a halide perovskite there are two kinds of electronic states. As discussed in Chapter 6, in HOPs both TVB and the BCB are mainly composed of B-X atomic orbitals. While TVB is mostly of a covalent nature, electrons in the conduction band are more delocalized.

	$A_1$	$A_2$	$E$
$A_1$	$A_1$	$A_2$	$E$
$A_2$	$A_2$	$A_1$	$E$
$E$	$E$	$E$	$A_1 + A_2 + E$

Table 7.3: Product table of  $c_{3v}$  point group

## Chapter 7. Computational study of carrier transport in halide perovskites via a semiclassical model of electron and hole dynamics

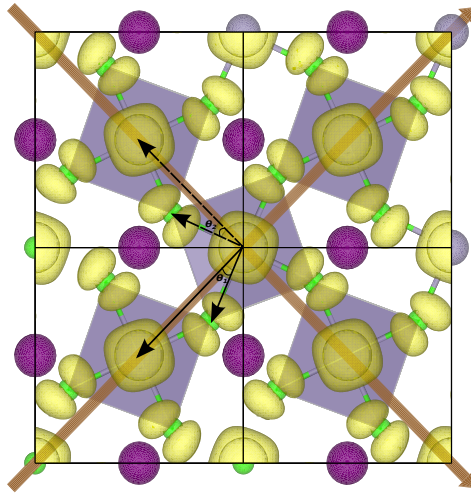
---

These electrons are less bound to the nuclei (belonging to higher angular momentums) and so can be approximated well by nearly free electrons. Therefore pseudopotential based frameworks can serve for interpreting the behavior of these particles (**k.p** theory). While **k.p** theory can explain the conduction band behavior quite accurately (vide infra), the covalence nature of TVB, suggests the use of a completely different though complementary tight binding model. Atomic orbitals can indeed give a precise picture for describing the hole carriers.

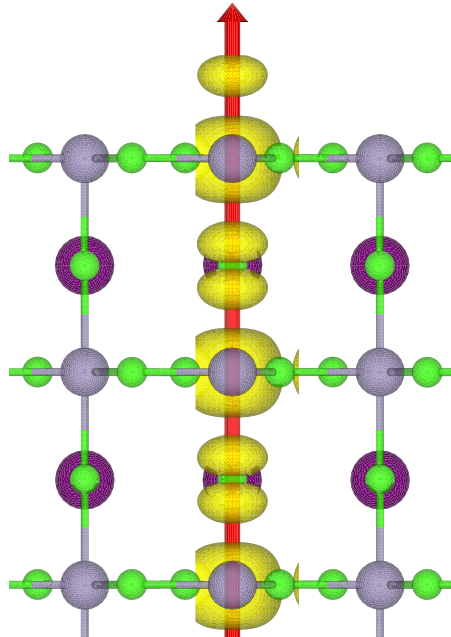
In a tight binding (TB) framework, each band is composed of atomic orbitals. As discussed in Chapter 6, the antibonding overlap between B s orbital and X p orbital is maximum in structures with the lowest distortion (lowest deviation from cubic structure). Accordingly the hole masses are lower in these structures. In a covalent structure it is plausible to think higher orbital overlap would boost carrier transport in line with what the TB approach predicts<sup>213</sup> (Look at the tight binding relation with orbital overlap in Appendix C). Indeed the eigenvector corresponding to the lowest effective mass is along the direction where the overlap is maximal (Figure 7.3). Likewise, the energy of the valence band rises as the antibonding overlap increases (Figure 7.6), which partially accounts for the decrease in the band gap (the other part as discussed in Chapter 6 emerges from the partial charge on B atom which reduces  $E_{BCB}$ ). The effects of different chemical and structural variations can thereby be explained as a function of orbital overlap and partial charges as mentioned vide supra. Cubic structures with the lowest distortion, and thus highest orbital overlap, give the lowest effective masses. Tetragonal structures (tilting in one direction) and orthorhombic structures (tilting in two directions) have slightly higher effective masses. Among halogens (with similar crystal structure and similar cations), iodide based compounds has the lowest masses followed by bromide and chloride, respectively (see the band diagrams B). Monovalent cations mostly affect the partial charges and thus the energy of the bottom of the conduction band. At the same time, smaller cations can distort the structure more easily when applied with highly electronegative halogens like chloride. As an example, combination of Li and Na with Cl often flattens the TVB and results in relatively high effective masses for holes (Figure B.5a).

The effective mass of electrons in the conduction band is defined by Equation 7.4 according to the **k.p** theory. Dispersion of a non-degenerate band is expressed as superposition of all the bands at that specific  $k$  point. In practice, however, only the nearest bands with not so big denominators (small energy difference) will be important and yet among them, those with proper symmetry properties can have nonzero coupling with the BCB. That is, according to Equation 7.1, the curvature of the BCB at the extremum ( $\Gamma$  or  $R$  point) is a function of the energy gap between the two bands and their corresponding momentum matrix element. The latter vanishes for most of the upper conduction bands due to the symmetry selection rules (see the character tables in 7.2.3 and 7.2), whereas TVB has a nonzero momentum matrix element with the BCB and, therefore, the effective mass shows a linear dependence on the band gap ( $E_{n'} - E_n$ ).

$$\frac{1}{m^*} = \frac{1}{m} + \frac{2}{m^2 k^2} + \sum_{n' \neq n} \frac{|k \cdot \langle u_0^{(n)} | p | u_0^{(n')} \rangle|^2}{E_0^n - E_0^{n'}} \quad (7.4)$$



(a) Transversal principle axes of transport for holes shown with brown arrows



(b) Tetragonal axis, longitudinal hole effective mass along the red eigenvector

Figure 7.3: Two transversal and one longitudinal eigenvectors (principle axes of carrier transport) are shown. Lowest  $m^*$  in the highest overlap direction.

**Chapter 7. Computational study of carrier transport in halide perovskites via a semiclassical model of electron and hole dynamics**

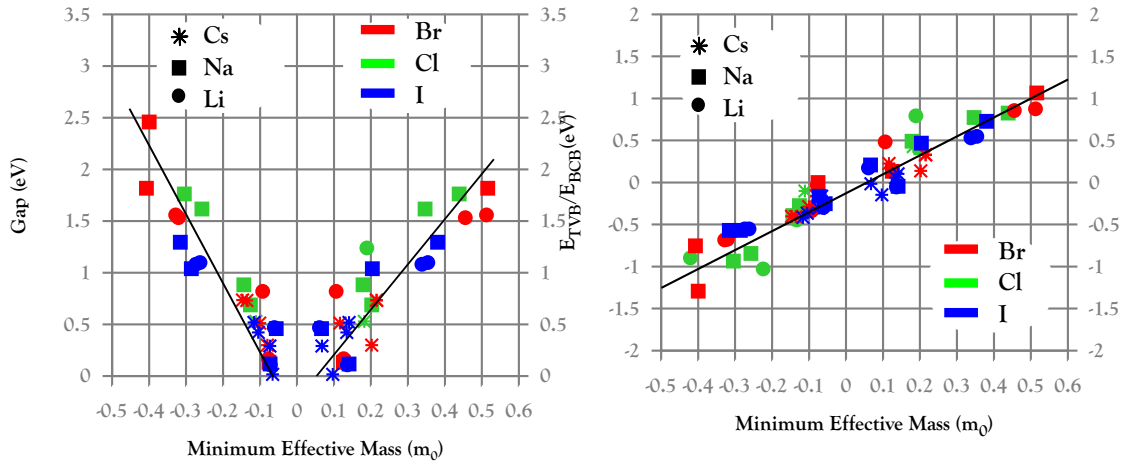


Figure 7.4: Gap and band edge energies versus minimum effective mass for Sn-based compounds

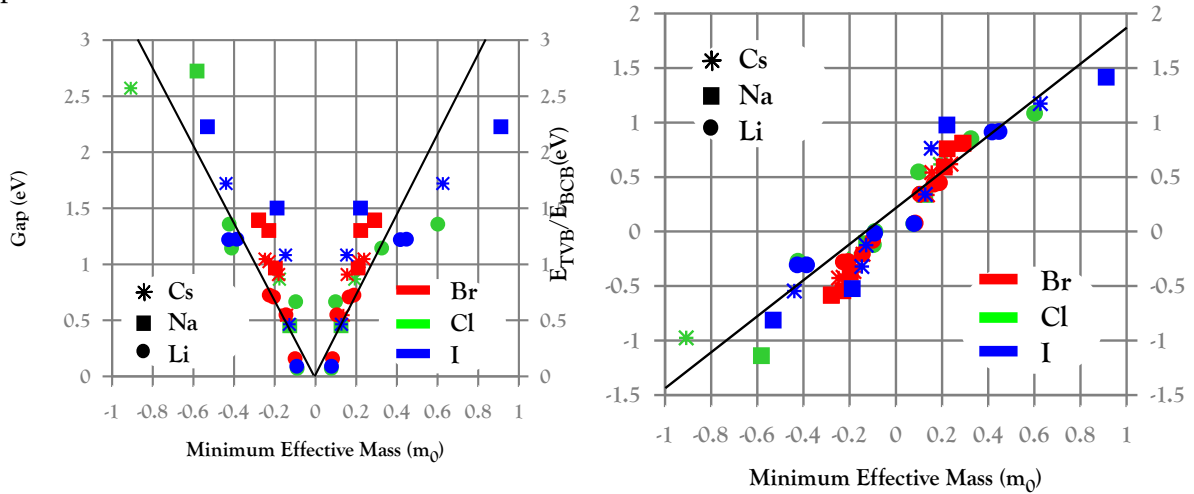


Figure 7.5: Gap and band edge energies versus minimum effective mass for Pb-based compounds

**7.3.2 Effect of hydrogen bonding**

Hydrogen bonding can induce distortions to the structure. A clear example can be seen in  $\text{NH}_4\text{PbI}_3$  where the cubic structure is deformed and as mentioned in our previous work the effective orbital overlap is significantly reduced (see Figure 7.7e and 7.7c). As a result TVB is flattened compared to that of the non-deformed  $\text{PH}_4\text{PbI}_3$  (see Figure 7.7f and 7.7d) with effective masses 10 times larger than that of  $\text{PH}_4\text{PbI}_3$  (yet smaller than  $1.5 m_0$ ).

**7.3.3 Effects of dopants and defects**

The results presented so far have been based on ideal crystals where the electronic states can be described in terms of the Bloch theorem. For these cases, we saw that the effective masses and superb carrier transport properties are basically maintained over a large range of



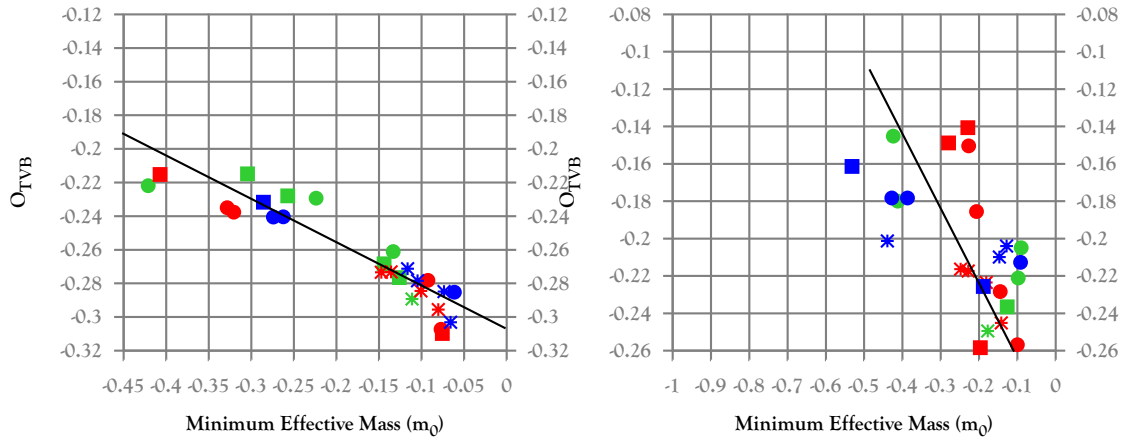


Figure 7.6: Antibonding overlap of the TVB orbitals versus the minimum hole effective masses  $m_e^*$  for tin-based (left) and lead-based (right) compounds

chemical compositions and structural variations. Real crystals however, contain defects that destroy the perfect periodicity. Therefore, it is important to establish how the electronic and charge transport properties are affected in systems containing defects or dopants. We should point out that, strictly speaking, with this we are already going beyond the validity limits of the applied methodology. That is, on one hand, for what concerns the doping, computational limitations do not allow us to work in the limits of infinitesimal diluted concentration of defects (e.g. to include hundreds of unit cells). On the other hand, to satisfy periodic boundary conditions we are accounting for an artificial extra periodicity of the defects. While the latter is a common assumption made in almost all ab initio calculations<sup>219,220</sup>, the former is somehow closer to reality when considering the liquid-based fabrication process of perovskites which happens in conditions far from the equilibrium and thus results in higher concentration of defects.

#### Effects of dopants: $\text{CsSn}_x\text{D}_{1-x}\text{I}_3$ , $\text{D}=\text{Zn, Sr}$

We substituted Sn with Zn and Sr with [8:1] ratio. Both dopants widen up the band gap (0.7 eV for Zn and 0.3 eV for Sr) and split some degenerate states by breaking the symmetry (look at Figure B.14 in B). While in Sr-doped system, the main features of  $\text{CsSnI}_3$  are preserved, the band diagram of Zn doped systems change drastically. Zinc puts an empty independent, discontinuous band within the band gap (n-dopant like) and changes the dispersion shape of the BCB considerably. This new band is composed of Sn p, I s, and a tiny contribution of Zn p orbital, being discontinuous, this band is not able to transfer charge. Presence of Zn, suppresses the neighboring iodide ions to contribute, an effect that can be seen in the asymmetry of the electron density in the Zn vicinity (Figure 7.8). Unlike strontium, the curvature of the BCB is affected quite a lot giving rise to relatively higher  $m_e^* = 1.7 m_0$ . The TVB dispersion, on the other hand is pretty much sustained with both dopants (with average  $m_h^* = 0.05 m_0$ ).

**Chapter 7. Computational study of carrier transport in halide perovskites via a semiclassical model of electron and hole dynamics**

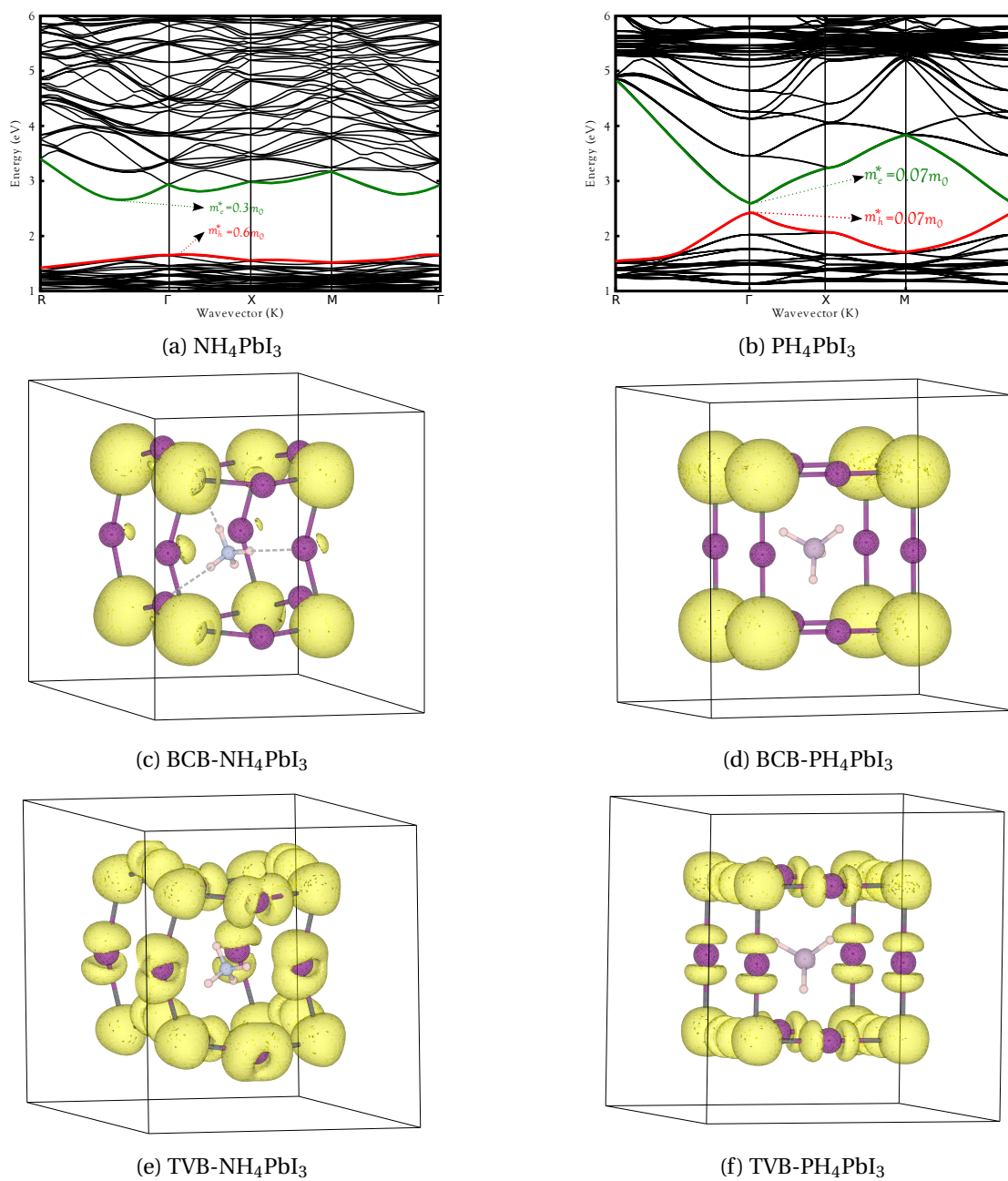


Figure 7.7: Effect of hydrogen bonding on effective masses.

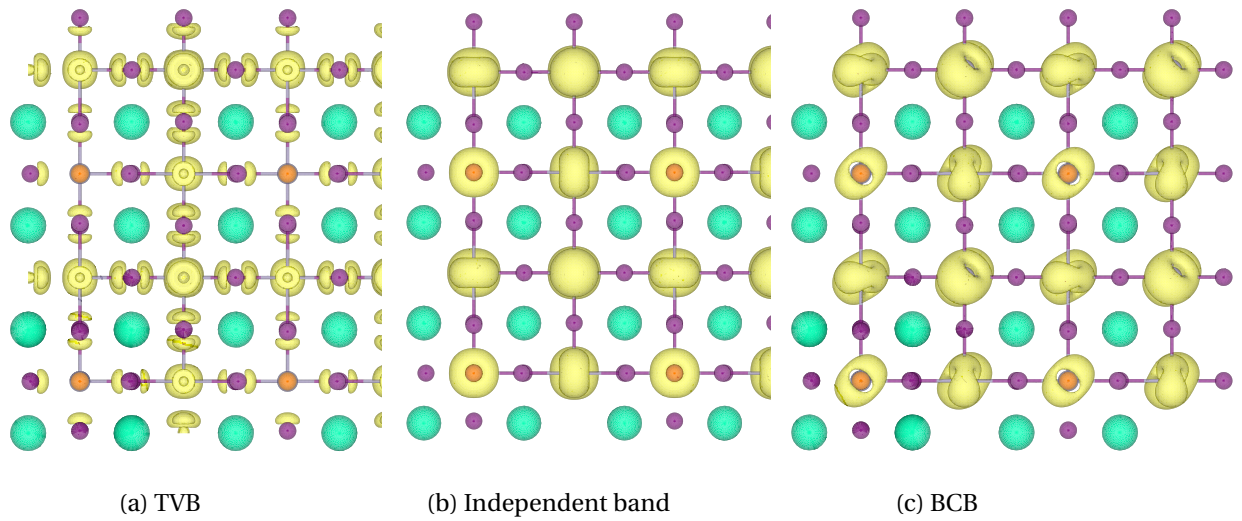


Figure 7.8: Effect of Zn(II) dopant on the orbitals of the band edges

### Vacancy defects in CsPbI<sub>3</sub>

Band structure plots of tetragonal CsPbI<sub>3</sub> with different vacancies suggest that the curvature is only slightly sensitive to vacancy defects (Figure B.16). Except for normal splitting of degenerate states (due to the broken symmetry), only Pb vacancies seem to affect the bands (mostly TVB). Pb vacancies flatten the TVB resulting in relatively heavy holes:  $m_h^* = 0.9 m_0$ . In absence of Pb, the contribution of equatorial iodide p orbitals to TVB significantly decreases (Figure 7.9).

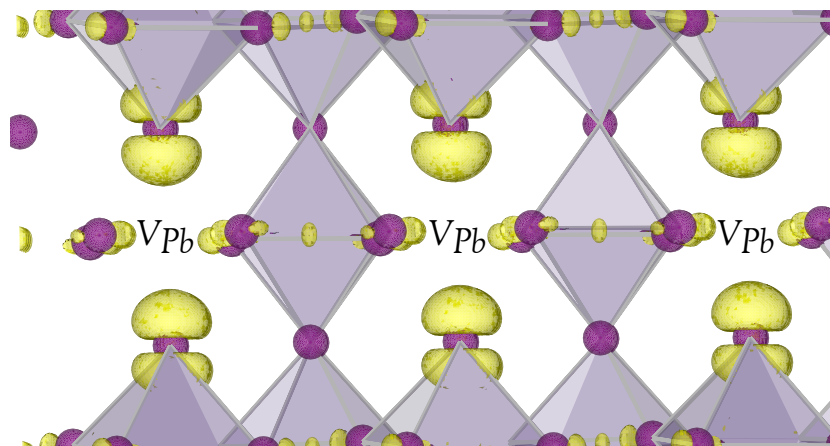


Figure 7.9: Pb vacancy: depletion of equatorial iodide p orbitals that significantly affects TVB.

## **7.4 Conclusion**

We performed a series of ab initio calculations over a broad range of HOPs and calculated the effective masses. Effective masses are strongly correlated with the band gap which can be explained by means of **k.p** theory and a tight binding model for the BCB and TVB, respectively. Zinc dopants add an independent band inside the gap and flatten the band edges (mostly BCB) resulting in higher effective masses. Likewise, lead vacancies flatten the TVB by depleting the orbital contributions from neighboring iodide ions.

## 8 Conclusions and outlook

In this thesis, I tried to rationalize the design of liquid-based and solid-state DSSCs using computational techniques.

In Chapter 3, many sensitizers were systematically studied, which allowed to establish some general design principles for efficient dye sensitizer based on their electronic structure and absorption spectra.

More macroscopic and physical aspects of a DSSC, like dye packing, dye-dye and dye-electrolyte interactions were explored in Chapter 4, where a specialized force field for DSSCs was developed and applied for the aforementioned analysis.

As a proof of principle, we investigated solvation effects on simple carbocations, as prototypical models for dye cations generated after injection of an electron into the  $\text{TiO}_2$  semiconductor. In Chapter 5, we were able to show that different solvents can alter the stability of different isomers of carbocations.

In the last two chapters, the origins of the band gap in halide perovskites was investigated and related to orbital overlaps in the states at the band edges (Chapter 6). Finally in Chapter 7, the carrier transport in perovskites was studied using a semi-classical approach.

This computational work can be continued in many ways motivated by the rapid advances in the of DSSCs. Semitransparent DSSCs based on liquid electrolytes remain commercially interesting due to their aesthetic and flexible nature. Many pilot and large scale companies such as G24i, 3G Solar, AISIN SEIKI, Toyota, and Dyesol are pursuing the module production and installation of these colorful cells such as the prototypical case installed at the EPFL *convention center*. Moreover, the flexibility of these cells makes them in particular interesting for indoor use, installed on everyday objects. New applications of DSSCs, for example as light absorbers for hydrogen generation, are equally encouraging and are attracting more attention everyday.

Likewise, the current status of solid-state DSSC research provides a promising outlook for future commercial applications. Recently, perovskites surpassed the competing efficiency of 20.1%<sup>27</sup>. However, there is still a considerable lag between the module size of commercially available perovskites with highest reported efficiencies of 11% (produced by the IMEC nanotechnology center<sup>221</sup>) and the ones produced on a lab scale. Larger area processing

## Chapter 8. Conclusions and outlook

---

and narrow interconnections are prerequisites for processing efficient thin-film modules. Moreover, many fabrication processes need to be replaced by their module scale equivalent. An example for such an upscaling is the lab-scale spin coating process that had to be replaced by blade or spray coating.

The big hitch even on a lab-scale is the issue of durability and stability of perovskites. Two sources of degradation have been identified for these materials. One is humidity and the other one is the light itself!

While these devices need to meet the limit of 24-year stability, their current status is around thousands of hours. Under working conditions, perovskites degrade to  $\text{PbI}_2$  grains, which are piling up on the grain boundaries which significantly limits the charge transport processes<sup>222</sup>. Thankfully the progress on the issue of durability seems to be as fast as that in the "efficiency marathon". New studies suggest many passivation methods (polymer encapsulation) with hydrophobic compounds together with the use of thicker oxide layers (e.g.  $\text{TiO}_2$ ) that can keep water outside the perovskite layer. While most of these precautions are empirical methods inherited from other thin-film technologies, understanding the exact mechanism of decomposition via heat or water is essential for perovskites to become commercially viable.

In this context, a comprehensive atomic -level study can be of great help. In particular, phase diagrams of perovskites can picture the stability ranges for different phases of these materials in different phases for different temperatures. We are currently developing a polarizable force field for this purpose. Rotation of organic cations ( $\text{CH}_3\text{NH}_3^+$ ) can induce polarization to the crystal. Polarizable force fields can capture this behavior via the calculation of induced multipole moments in the course of the simulation. The complete phase diagram can be calculated in this way. Moreover the collective movements of  $\text{CH}_3\text{NH}_3^+$  (if there exist any) can be analyzed with the classical approach. Many hypotheses relate this collective movements to ferro electricity<sup>223,224</sup>. Classical force fields can be a way for assessing such a hypothesis.

Using ab initio techniques one can study the mechanism of water diffusion in perovskites and the subsequent damage it causes. Furthermore, using time-propagation time-dependent DFT simulations within an Ehrenfest framework, electron injection at the perovskite/ $\text{TiO}_2$  interface can be studied.

## Bibliography

- [1] Wenger, S. Strategies to optimizing dye-sensitized solar cells: organic sensitizers, tandem device structures, and numerical device modeling. Ph.D. thesis, ÉCOLE POLYTECHNIQUE FÉDÉRALE DE LAUSANNE, 2010.
- [2] Chang, Y.-C.; Wang, C.-L.; Pan, T.-Y.; Hong, S.-H.; Lan, C.-M.; Kuo, H.-H.; Lo, C.-F.; Hsu, H.-Y.; Lin, C.-Y.; Diau, E. W.-G. *Chemical Communications* **2011**, 47, 8910–8912.
- [3] Yella, A.; Lee, H.-W.; Tsao, H. N.; Yi, C.; Chandiran, A. K.; Nazeeruddin, M. K.; Diau, E. W.-G.; Yeh, C.-Y.; Zakeeruddin, S. M.; Grätzel, M. *Science* **2011**, 334, 629–34.
- [4] Chung, I.; Song, J.-H.; Im, J.; Androulakis, J.; Malliakas, C. D.; Li, H.; Freeman, A. J.; Kenney, J. T.; Kanatzidis, M. G. *Journal of the American Chemical Society* **2012**, 134, 8579–8587.
- [5] Heyd, J.; Scuseria, G. E.; Ernzerhof, M. *The Journal of Chemical Physics* **2006**, 124, 219906.
- [6] Chung, I.; Lee, B.; He, J.; Chang, R. P.; Kanatzidis, M. G. *Nature* **2012**, 485, 486–489.
- [7] Goldemberg, J. *World Energy Assessment: Energy and the challenge of sustainability*; United Nations Pubns, 2000.
- [8] Hoffert, M. I.; Caldeira, K.; Jain, A. K.; Haites, E. F.; Harvey, L. D.; Potter, S. D.; Schlesinger, M. E.; Schneider, S. H.; Watts, R. G.; Wigley, T. M. *Nature* **1998**, 395, 881–884.
- [9] Wikipedia, World energy consumption — Wikipedia, The Free Encyclopedia. 2015; [https://en.wikipedia.org/w/index.php?title=World\\_energy\\_consumption&oldid=669551246](https://en.wikipedia.org/w/index.php?title=World_energy_consumption&oldid=669551246), [Online; accessed 13-July-2015].
- [10] Morton, O. *Nature* **2006**, 443, 19–22.
- [11] Wikipedia, Renewable energy — Wikipedia, The Free Encyclopedia. 2015; [https://en.wikipedia.org/w/index.php?title=Renewable\\_energy&oldid=670703399](https://en.wikipedia.org/w/index.php?title=Renewable_energy&oldid=670703399), [Online; accessed 13-July-2015].
- [12] Wikipedia, Polycrystalline silicon — Wikipedia, The Free Encyclopedia. 2015; [https://en.wikipedia.org/w/index.php?title=Polycrystalline\\_silicon&oldid=667688513](https://en.wikipedia.org/w/index.php?title=Polycrystalline_silicon&oldid=667688513), [Online; accessed 19-July-2015].

## Bibliography

---

- [13] Shockley, W.; Queisser, H. J. *Journal of Applied Physics* **1961**, *32*, 510–519.
- [14] Chiu, P.; Law, D.; Woo, R.; Singer, S.; Bhusari, D.; Hong, W.; Zakaria, A.; Boisvert, J.; Mesropian, S.; King, R. *Photovoltaic Specialist Conference (PVSC), 2014 IEEE 40th*; 2014; pp 0011–0013.
- [15] Gupta, M. C.; Ballato, J. *The handbook of photonics*; CRC press, 2006.
- [16] O'regan, B.; Grätzel, M. *Nature* **1991**, *353*, 737–740.
- [17] Kruger, J.; Plass, R.; Cevey, L.; Piccirelli, M.; Gratzel, M.; Bach, U. *Applied Physics Letters* **2001**, *79*, 2085–2087.
- [18] Wang, M.; Moon, S.-J.; Xu, M.; Chittibabu, K.; Wang, P.; Cevey-Ha, N.-L.; Humphry-Baker, R.; Zakeeruddin, S. M.; Grätzel, M. *Small* **2010**, *6*, 319–324.
- [19] Cai, N.; Moon, S.-J.; Cevey-Ha, L.; Moehl, T.; Humphry-Baker, R.; Wang, P.; Zakeeruddin, S. M.; Gratzel, M. *Nano Letters* **2011**, *11*, 1452–1456.
- [20] Burschka, J.; Dualeh, A.; Kessler, E.; Baranoff, E.; Cevey-Ha, N.-L.; Yi, C.; Nazeeruddin, M. K.; Gratzel, M. *Journal of the American Chemical Society* **2011**, *133*, 18042–18045.
- [21] Chang, J. A.; Rhee, J. H.; Im, S. H.; Lee, Y. H.; Kim, H.-j.; Seok, S. I.; Nazeeruddin, M. K.; Gratzel, M. *Nano Letters* **2010**, *10*, 2609–2612.
- [22] Kim, H.-S.; Lee, C.-R.; Im, J.-H.; Lee, K.-B.; Moehl, T.; Marchioro, A.; Moon, S.-J.; Humphry-Baker, R.; Yum, J.-H.; Moser, J. E. *Scientific Reports* **2012**, *2*.
- [23] Kojima, A.; Teshima, K.; Shirai, Y.; Miyasaka, T. *Journal of the American Chemical Society* **2009**, *131*, 6050–6051.
- [24] Im, J.-H.; Lee, C.-R.; Lee, J.-W.; Park, S.-W.; Park, N.-G. *Nanoscale* **2011**, *3*, 4088–4093.
- [25] Dar, M. I.; Arora, N.; Gao, P.; Ahmad, S.; Gratzel, M.; Nazeeruddin, M. K. *Nano Letters* **2014**, *14*, 6991–6996.
- [26] Lee, M. M.; Teuscher, J.; Miyasaka, T.; Murakami, T. N.; Snaith, H. J. *Science* **2012**, *338*, 643–647.
- [27] Yang, W. S.; Noh, J. H.; Jeon, N. J.; Kim, Y. C.; Ryu, S.; Seo, J.; Seok, S. I. *Science* **2015**, *aaa9272*.
- [28] Park, N.-G. *The Journal of Physical Chemistry Letters* **2013**, *4*, 2423–2429.
- [29] Etgar, L.; Gao, P.; Xue, Z.; Peng, Q.; Chandiran, A. K.; Liu, B.; Nazeeruddin, M. K.; Gratzel, M. *Journal of the American Chemical Society* **2012**, *134*, 17396–17399.
- [30] Zhou, H.; Chen, Q.; Li, G.; Luo, S.; Song, T.-b.; Duan, H.-S.; Hong, Z.; You, J.; Liu, Y.; Yang, Y. *Science* **2014**, *345*, 542–546.



- [31] Jeon, N. J.; Noh, J. H.; Yang, W. S.; Kim, Y. C.; Ryu, S.; Seo, J.; Seok, S. I. *Nature* **2015**, *517*, 476–480.
- [32] Ullrich, C. *Time-Dependent Density-Functional Theory: Concepts and Applications*; Oxford Graduate Texts; OUP Oxford, 2011.
- [33] Marx, D.; Hutter, J. *Modern Methods and Algorithms of Quantum Chemistry* **2000**, *1*, 301–449.
- [34] Chipot, C.; Pohorille, A. *Free energy calculations*; Springer, 2007.
- [35] Brunk, E.; Rothlisberger, U. *Chemical Reviews* **2015**,
- [36] Yu, P. Y.; Cardona, M.; Sham, L. J. *Physics Today* **1997**, *50*, 76.
- [37] Kittel, C. *Introduction to solid state physics*; Wiley, 2005.
- [38] Ashcroft, N. W.; Mermin, N. D. *Solid State Physics*; Holt, Rinehart and Winston, New York, 2005; pp 490–495.
- [39] Hohenberg, P.; Kohn, W. *Physical Review* **1964**, *136*, B864.
- [40] Dreizler, R. M.; Gross, E. K. *Density functional theory: an approach to the quantum many-body problem*; Springer Science & Business Media, 2012.
- [41] Kato, T. *Pure Applied Math* **1957**, *10*, 16.
- [42] Bright-Wilson, E.; Rich, A.; David, N. **1968**,
- [43] Levy, M. *Physical Review A* **1982**, *26*, 1200.
- [44] van Leeuwen, R. *Advances in Quantum Chemistry* **2003**, *43*, 25–94.
- [45] Thomas, L. H. *Mathematical Proceedings of the Cambridge Philosophical Society*; 1927; Vol. 23; pp 542–548.
- [46] Fermi, E. *Journal fur Physics* **1928**, *48*, 73–79.
- [47] Schwinger, J. *Physical Review A* **1981**, *24*, 2353.
- [48] Sham, L.; Marcus, P.; Janak, J.; Williams, A. *New York* **1971**, 458.
- [49] Becke, A. D. *Physical Review A* **1988**, *38*, 3098.
- [50] Lee, C.; Yang, W.; Parr, R. *Physical Review A* **1988**, *38*, 3098.
- [51] Perdew, J. P.; Wang, Y. *Physical Review B* **1992**, *46*, 12947.
- [52] Perdew, J. P.; Burke, K.; Wang, Y. *Physical Review B* **1996**, *54*, 16533.
- [53] Runge, E.; Gross, E. K. *Physical Review Letters* **1984**, *52*, 997.

## Bibliography

---

- [54] Yabana, K.; Bertsch, G. *Physical Review B* **1996**, *54*, 4484.
- [55] Casida, M. E. *Physical Review A* **1995**, *51*, 2005.
- [56] Dreuw, A.; Weisman, J. L.; Head-Gordon, M. *The Journal of Chemical Physics* **2003**, *119*, 2943–2946.
- [57] Iikura, H.; Tsuneda, T.; Yanai, T.; Hirao, K. *The Journal of Chemical Physics* **2001**, *115*, 3540–3544.
- [58] Yanai, T.; Tew, D. P.; Handy, N. C. *Chemical Physics Letters* **2004**, *393*, 51–57.
- [59] Savin A, D. P., Chong *Recent advances in density functional methods*; World Scientific, 1995; Vol. 1.
- [60] Tawada, Y.; Tsuneda, T.; Yanagisawa, S.; Yanai, T.; Hirao, K. *The Journal of Chemical Physics* **2004**, *120*, 8425–8433.
- [61] Zhao, Y.; Truhlar, D. G. *Theoretical Chemistry Accounts* **2008**, *120*, 215–241.
- [62] Li, R.; Zheng, J.; Truhlar, D. G. *Physical Chemistry Chemical Physics* **2010**, *12*, 12697–12701.
- [63] Koopmans, T. *Physica* **1933**, *1*, 104–113.
- [64] Gratzel, M.; O'Regan, B. *Nature* **1991**, *353*, 737 – 740.
- [65] Polander, L.; Yella, A. *Angewandte Chemie International Edition* **2013**, 8731–8735.
- [66] Nazeeruddin, M. *Advanced Functional Materials* **2006**, 189–194.
- [67] Kimura, M.; Nomoto, H. *Angewandte Chemie International Edition* **2012**, 4371–4374.
- [68] Negre, C. F. A.; Milot, R. L.; Martini, L. A.; Ding, W.; Crabtree, R. H.; Schmittenmaer, C. A.; Batista, V. S. *The Journal of Physical Chemistry C* **2013**, *117*, 24462–24470.
- [69] Imahori, H.; Kang, S.; Hayashi, H.; Haruta, M.; Kurata, H.; Isoda, S.; Canton, S. E.; Infahsaeng, Y.; Kathiravan, A.; Pascher, T.; Chábera, P.; Yartsev, A. P.; Sundström, V. *The Journal of Physical Chemistry A* **2011**, *115*, 3679–90.
- [70] Yella, A.; Humphry-Baker, R. *Chemistry of Materials* **2013**, *25*, 2733–2739.
- [71] Mathew, S.; Yella, A.; Gao, P.; Humphry-Baker, R.; Curchod, B. F.; Ashari-Astani, N.; Tavernelli, I.; Rothlisberger, U.; Nazeeruddin, M. K.; Grätzel, M. *Nature Chemistry* **2014**, *6*, 242–247.
- [72] Milot, R. L.; Moore, G. F.; Crabtree, R. H.; Brudvig, G. W.; Schmittenmaer, C. A. *The Journal of Physical Chemistry C* **2013**, *117*, 21662–21670.

- [73] Zdanowicz, T.; Rodziewicz, T.; Zabkowska-Waclawek, M. *Solar Energy Materials and Solar Cells* **2005**, *87*, 757–769.
- [74] Hay, P. J.; Wadt, W. R. *The Journal of Chemical Physics*. **1985**, *82*, 299.
- [75] Hehre, W. J. *The Journal of Chemical Physics*. **1972**, *56*, 2257.
- [76] Petersson, a.; Bennett, A.; Tensfeldt, T. G.; Al-Laham, M. A.; Shirley, W. A.; Mantzaris, J. *The Journal of Chemical Physics* **1988**, *89*, 2193–2218.
- [77] Frisch, M. J. et al. Gaussian 09 Revision D.01. 2009; Gaussian Inc. Wallingford CT 2009.
- [78] Cossi, M.; Rega, N.; Scalmani, G.; Barone, V. *Journal of Computational Chemistry* **2003**, *24*, 669–681.
- [79] Humphrey, W.; Dalke, a.; Schulten, K. *Journal of Molecular Graphics*. **1996**, *14*, 33–8, 27–8.
- [80] Salvatori, P.; Amat, A.; Pastore, M.; Vitillaro, G.; Sudhakar, K.; Giribabu, L.; Soujanya, Y.; Angelis, F. D. *Computational and Theoretical Chemistry* **2014**, *1030*, 59–66.
- [81] Lobello, M.; Wu, K.; Reddy, M. *Dalton Transactions* **2014**, *43*, 2726–2732.
- [82] Wang, C.; Chang, Y.; Lan, C. *Energy and Environmental Science* **2011**, *4*, 1788–1795.
- [83] Xu, J.; Zhu, L.; Fang, D.; Chen, B.; Liu, L.; Wang, L.; Xu, W. *Chemphyschem* **2012**, *13*, 3320–9.
- [84] Tozer, D. J. *The Journal of Chemical Physics*. **2003**, *119*, 12697.
- [85] Röhr, M. I.; Petersen, J.; Wohlgemuth, M.; Bonačić-Koutecký, V.; Mitrić, R. *ChemPhysChem* **2013**, *14*, 1377–1386.
- [86] Tripathy, U.; Kowalska, D.; Liu, X.; Velate, S.; Steer, R. P. *The Journal of Physical Chemistry A* **2008**, *112*, 5824–5833, PMID: 18537232.
- [87] Vydrov, O. A.; Scuseria, G. E. *The Journal of Chemical Physics*. **2006**, *125*, 234109.
- [88] Yanai, T.; Tew, D. P.; Handy, N. C. *Chemical Physics Letters* **2004**, *393*, 51–57.
- [89] Zhao, Y.; Truhlar, D. G. *Theoretical Chemistry Accounts* **2008**, *120*, 215–241.
- [90] Peach, M. J. G.; Benfield, P.; Helgaker, T.; Tozer, D. J. *The Journal of Chemical Physics* **2008**, *128*, –.
- [91] Koopmans, T. *Physica* **1933**, *1*, 104.
- [92] Perdew, J.; Parr, R.; Levy, M.; Jr, J. B. *Physical Review Letters* **1982**, *49*, 1691–1694.
- [93] Teale, A. M.; De Proft, F.; Tozer, D. J. *The Journal of Chemical Physics*. **2008**, *129*, 044110.

## Bibliography

---

- [94] Mennucci, B.; Cammi, R. *Continuum Solvation Models in Chemical Physics*; John Wiley & Sons, 2007.
- [95] Scalmani, G.; Frisch, M. J.; Mennucci, B.; Tomasi, J.; Cammi, R.; Barone, V. *The Journal of Chemical Physics* **2006**, *124*, –.
- [96] Santoro, F.; Barone, V.; Benzi, C.; Improta, R. *Theoretical Chemistry Accounts* **2007**, *117*, 1073–1084.
- [97] Brady, J. E.; Carr, P. W. *The Journal of Physical Chemistry* **1985**, *89*, 5759–5766.
- [98] Pastore, M.; De Angelis, F. In *Modeling materials and processes in dye-sensitized solar cells: understanding the mechanism, improving the efficiency*; Beljonne, D., Cornil, J., Eds.; Topics in Current Chemistry; Springer Berlin Heidelberg, 2014; Vol. 352; pp 151–236.
- [99] Giribabu, L.; Singh, V. K.; Jella, T.; Soujanya, Y.; Amat, A.; Angelis, F. D.; Yella, A.; Gao, P.; Nazeeruddin, M. K. *Dyes and Pigments* **2013**, *98*, 518 – 529.
- [100] Khoudiakov, M.; Parise, A. R.; Brunshwig, B. S. *Journal of the American Chemical Society* **2003**, *125*, 4637–4642, PMID: 12683836.
- [101] Hansch, C.; Leo, A.; Taft, R. *Chemical Reviews* **1991**, *91*, 165–195.
- [102] Li, G.; Bomben, P. G.; Robson, K. C. D.; Gorelsky, S. I.; Berlinguette, C. P.; Shatruk, M. *Chemical Communications* **2012**, *48*, 8790–2.
- [103] Tsao, H. N.; Yi, C.; Moehl, T.; Yum, J.-H.; Zakeeruddin, S. M.; Nazeeruddin, M. K.; Grätzel, M. *ChemSusChem* **2011**, *4*, 591–4.
- [104] Lo, C.-E.; Hsu, S.-J.; Wang, C.-L.; Cheng, Y.-H.; Lu, H.-P.; Diau, E. W.-G.; Lin, C.-Y. *The Journal of Physical Chemistry C* **2010**, *114*, 12018–12023.
- [105] Delcamp, J. H.; Yella, A.; Holcombe, T. W.; Nazeeruddin, M. K.; Grätzel, M. *Angewandte Chemie International Edition Engl.* **2013**, *52*, 376–80.
- [106] Feng, J.; Jiao, Y.; Ma, W.; Nazeeruddin, M. K.; Grätzel, M.; Meng, S. *The Journal of Physical Chemistry C* **2013**, *117*, 3772–3778.
- [107] Lee, C.; Yang, W.; Parr, R. G. *Physical Review B* **1988**, *37*, 785–789.
- [108] Becke, A. D. *Physical Review A* **1988**, *38*, 3098–3100.
- [109] Grimme, S. *Journal of Computational Chemistry* **2006**, *27*, 1787–1799.
- [110] Burnham, B. F.; Zuckerman, J. J. *Journal of the American Chemical Society* **1970**, *92*, 1547–1550, PMID: 5418445.
- [111] Sessler, J. L.; Tomat, E. *Accounts of Chemical Research* **2007**, *40*, 371–379, PMID: 17397134.

- [112] Liu, F.; Cunningham, K. L.; Uphues, W.; Fink, G. W.; Schmolt, J.; McMillin, D. R. *Inorganic Chemistry* **1995**, *34*, 2015–2018.
- [113] Plater, M. J.; Aiken, S.; Bourhill, G. *Tetrahedron* **2002**, *58*, 2415 – 2422.
- [114] Tang, H.; Yin, H.; Wang, J.; Yang, N.; Wang, D.; Tang, Z. *Angewandte Chemie* **2013**, *125*, 5695–5699.
- [115] Wiberg, J.; Marinado, T.; Hagberg, D. P.; Sun, L.; Hagfeldt, A.; Albinsson, B. *The Journal of Physical Chemistry B* **2010**, *114*, 14358–63.
- [116] Voitchovsky, K.; Ashari Astani, N.; Tavernelli, I.; Tetreault, N.; Rothlisberger, U.; Stellacci, F.; Grätzel, M.; Harms, H. A. *ACS Applied Materials & Interfaces* **2015**,
- [117] O'Regan, B. C.; Durrant, J. R. *Accounts of Chemical Research* **2009**, *42*, 1799–1808.
- [118] Park, N.-G.; Kim, K. *Physica Status Solidi (a)* **2008**, *205*, 1895–1904.
- [119] De Angelis, F.; Fantacci, S.; Selloni, A. *Nanotechnology* **2008**, *19*, 424002.
- [120] De Angelis, F. *Chemical Physics Letters* **2010**, *493*, 323–327.
- [121] Pearlman, D. A.; Case, D. A.; Caldwell, J. W.; Ross, W. S.; Cheatham, T. E.; DeBolt, S.; Ferguson, D.; Seibel, G.; Kollman, P. *Computer Physics Communications* **1995**, *91*, 1–41.
- [122] Hay, P. J.; Wadt, W. R. *The Journal of Chemical Physics* **1985**, *82*, 270–283.
- [123] Tang, W.; Sanville, E.; Henkelman, G. *Journal of Physics: Condensed Matter* **2009**, *21*, 084204.
- [124] Bayly, C. I.; Cieplak, P.; Cornell, W.; Kollman, P. A. *The Journal of Physical Chemistry* **1993**, *97*, 10269–10280.
- [125] für Festkörperforschung Stuttgart 1997-2001, C. M. Copyright IBM Corp 1990-2015. 1997-2015; <http://www.cpmf.org/>.
- [126] Segall, M.; Linda, P.; Probert, M.; Pickard, C.; Hasnip, P.; Clark, S.; Payne, M. *Accelrys: San Diego, CA* **2002**,
- [127] Car, R.; Parrinello, M. *Physical Review Letters* **1985**, *55*, 2471.
- [128] Lee, C.; Yang, W.; Parr, R. G. *Physical Review B* **1988**, *37*, 785.
- [129] Troullier, N.; Martins, J. *Solid State Communications* **1990**, *74*, 613–616.
- [130] Humphrey, W.; Dalke, A.; Schulten, K. *Journal of Molecular Graphics* **1996**, *14*, 33–38.
- [131] Sushko, M. L.; Gal, A. Y.; Shluger, A. L. *The Journal of Physical Chemistry B* **2006**, *110*, 4853–4862.

## Bibliography

---

- [132] Giammona, D. A. An examination of conformational flexibility in porphyrins and bulky-ligand binding in myoglobin. Ph.D. thesis, 1984.
- [133] Nusbaumer, H.; Zakeeruddin, S. M.; Moser, J.-E.; Grätzel, M. *Chemistry-A European Journal* **2003**, *9*, 3756–3763.
- [134] Hamann, T. W. *Dalton Transactions* **2012**, *41*, 3111–3115.
- [135] Moret, M.-E.; Tavernelli, I.; Rothlisberger, U. *The Journal of Physical Chemistry B* **2009**, *113*, 7737–7744.
- [136] Wu, X.; Liu, Z.; Huang, S.; Wang, W. *Physical Chemistry Chemical Physics* **2005**, *7*, 2771–2779.
- [137] Alimohammadi, M.; Fichthorn, K. A. *The Journal of Physical Chemistry C* **2011**, *115*, 24206–24214.
- [138] Jorgensen, W. L.; Briggs, J. M. *Molecular Physics* **1988**, *63*, 547–558.
- [139] Sakai, N.; Wang, R.; Fujishima, A.; Watanabe, T.; Hashimoto, K. *Langmuir* **1998**, *14*, 5918–5920.
- [140] He, Y.; Tilocca, A.; Dulub, O.; Selloni, A.; Diebold, U. *Nature Materials* **2009**, *8*, 585–589.
- [141] Gong, X.-Q.; Selloni, A. *The Journal of Physical Chemistry B* **2005**, *109*, 19560–19562.
- [142] Hara, K.; Dan-oh, Y.; Kasada, C.; Ohga, Y.; Shinpo, A.; Suga, S.; Sayama, K.; Arakawa, H. *Langmuir* **2004**, *20*, 4205–4210.
- [143] Wang, J.; Wolf, R. M.; Caldwell, J. W.; Kollman, P. A.; Case, D. A. *Journal of computational chemistry* **2004**, *25*, 1157–1174.
- [144] Jorgensen, W. L.; Maxwell, D. S.; Tirado-Rives, J. *Journal of the American Chemical Society* **1996**, *118*, 11225–11236.
- [145] Bandura, A.; Kubicki, J. *The Journal of Physical Chemistry B* **2003**, *107*, 11072–11081.
- [146] Yella, A.; Lee, H.-W.; Tsao, H. N.; Yi, C.; Chandiran, A. K.; Nazeeruddin, M. K.; Diau, E. W.-G.; Yeh, C.-Y.; Zakeeruddin, S. M.; Grätzel, M. *Science* **2011**, *334*, 629–634.
- [147] Struebing, H.; Ganase, Z.; Karamertzanis, P. G.; Sioumkrou, E.; Haycock, P.; Piccione, P. M.; Armstrong, A.; Galindo, A.; Adjiman, C. S. *Nature Chemistry* **2013**, *5*, 952–957.
- [148] Truhlar, D. G. *Nature Chemistry* **2013**, *5*, 902–903.
- [149] Dong, G.; Teo, P.; Wickens, Z. K.; Grubbs, R. H. *Science* **2011**, *333*, 1609–1612.
- [150] Lee, D.-H.; Kwon, K.-H.; Chae, S. Y. *Science* **2011**, *333*, 1613–1616.

- [151] Olah, G. A.; Tolgyesi, W. S.; Kuhn, S. J.; Moffatt, M. E.; Bastien, I. J.; Baker, E. B. *Journal of the American Chemical Society* **1963**, *85*, 1328–1334.
- [152] Sieber, S.; Buzek, P.; Schleyer, P. v. R.; Koch, W.; Carneiro, J. W. d. M. *Journal of the American Chemical Society* **1993**, *115*, 259–270.
- [153] Prakash, G. S.; Schleyer, P. v. R. *Stable carbocation chemistry*; John Wiley & Sons, 1997.
- [154] O’Ferrall, R. M. *Advances in Physical Organic Chemistry* **2010**, *44*, 19.
- [155] Duncan, M. A. *The Journal of Physical Chemistry A* **2012**, *116*, 11477–11491.
- [156] Dinér, P. *The Journal of Physical Chemistry A* **2012**, *116*, 9979–9984.
- [157] Rasul, G.; Prakash, G. S.; Olah, G. A. *The Journal of Physical Chemistry A* **2015**,
- [158] Kirkwood, J. G. *The Journal of Chemical Physics* **1935**, *3*, 300–313.
- [159] Martínez, A. G.; de la Moya Cerero, S.; Vilar, E. T.; Fraile, A. G. *Tetrahedron* **2012**, *68*, 2892–2898.
- [160] Wang, J.; Cieplak, P.; Kollman, P. A. *Journal of Computational Chemistry* **2000**, *21*, 1049–1074.
- [161] Darden, T.; York, D.; Pedersen, L. *The Journal of Chemical Physics* **1993**, *98*, 10089–10092.
- [162] Nosé, S. *The Journal of Chemical Physics* **1984**, *81*, 511–519.
- [163] Martyna, G. J.; Tobias, D. J.; Klein, M. L. *The Journal of Chemical Physics* **1994**, *101*, 4177–4189.
- [164] Feller, S. E.; Zhang, Y.; Pastor, R. W.; Brooks, B. R. *The Journal of Chemical Physics* **1995**, *103*, 4613–4621.
- [165] Laio, A.; VandeVondele, J.; Rothlisberger, U. *The Journal of Physical Chemistry B* **2002**, *106*, 7300–7307.
- [166] Molteni, C.; Parrinello, M. *Journal of the American Chemical Society* **1998**, *120*, 2168–2171.
- [167] Piana, S.; Carloni, P. *Proteins: Structure, Function, and Bioinformatics* **2000**, *39*, 26–36.
- [168] Selloni, A.; Carnevali, P.; Car, R.; Parrinello, M. *Physical Review Letters* **1987**, *59*, 823.
- [169] Troullier, N.; Martins, J. L. *Physical Review B* **1991**, *43*, 1993.
- [170] Martyna, G. J.; Tuckerman, M. E. *The Journal of Chemical Physics* **1999**, *110*, 2810–2821.
- [171] Tuckerman, M.; Laasonen, K.; Sprik, M.; Parrinello, M. *The Journal of Chemical Physics* **1995**, *103*, 150–161.

## Bibliography

---

- [172] Burschka, J.; Pellet, N.; Moon, S.-J.; Humphry-Baker, R.; Gao, P.; Nazeeruddin, M. K.; Grätzel, M. *Nature* **2013**, *499*, 316–319.
- [173] Liu, M.; Johnston, M. B.; Snaith, H. J. *Nature* **2013**, *501*, 395–398.
- [174] Kazim, S.; Nazeeruddin, M. K.; Grätzel, M.; Ahmad, S. *Angewandte Chemie International Edition* **2014**, *53*, 2812–2824.
- [175] NREL, National renewable energy laboratory. 2015; <http://www.nrel.gov/ncpv/>, [Online; accessed 13-July-2015].
- [176] Noh, J. H.; Im, S. H.; Heo, J. H.; Mandal, T. N.; Seok, S. I. *Nano Letters* **2013**, *13*, 1764–1769.
- [177] Pellet, N.; Gao, P.; Gregori, G.; Yang, T.-Y.; Nazeeruddin, M. K.; Maier, J.; Grätzel, M. *Angewandte Chemie International Edition* **2014**, *53*, 3151–3157.
- [178] Eperon, G. E.; Stranks, S. D.; Menelaou, C.; Johnston, M. B.; Herz, L. M.; Snaith, H. J. *Energy & Environmental Science* **2014**, *7*, 982–988.
- [179] Hao, F.; Stoumpos, C. C.; Cao, D. H.; Chang, R. P.; Kanatzidis, M. G. *Nature Photonics* **2014**, *8*, 489–494.
- [180] Amat, A.; Mosconi, E.; Ronca, E.; Quarti, C.; Umari, P.; Nazeeruddin, M. K.; Grätzel, M.; De Angelis, F. *Nano Letters* **2014**, *14*, 3608–3616.
- [181] Verma, A.; Kumar, A.; Bhardwaj, S. *Physica Status Solidi (b)* **2008**, *245*, 1520–1526.
- [182] Yin, W.-J.; Shi, T.; Yan, Y. *Applied Physics Letters* **2014**, *104*, 063903.
- [183] Giannozzi, P.; Baroni, S.; Bonini, N.; Calandra, M.; Car, R.; Cavazzoni, C.; Ceresoli, D.; Chiarotti, G. L.; Cococcioni, M.; Dabo, I. *Journal of Physics: Condensed Matter* **2009**, *21*, 395502.
- [184] Monkhorst, H. J.; Pack, J. D. *Physical Review B* **1976**, *13*, 5188.
- [185] Stoumpos, C. C.; Malliakas, C. D.; Kanatzidis, M. G. *Inorganic chemistry* **2013**, *52*, 9019–9038.
- [186] Trots, D.; Myagkota, S. *Journal of Physics and Chemistry of Solids* **2008**, *69*, 2520–2526.
- [187] Umari, P.; Mosconi, E.; De Angelis, F. *Scientific Reports* **2014**, *4*.
- [188] Mathews, S.; Ramesh, R.; Venkatesan, T.; Benedetto, J. *Science* **1997**, *276*, 238–240.
- [189] Mitzi, D. B. *Progress in Inorganic Chemistry*; John Wiley & Sons, Inc., 2007; pp 1–121.
- [190] Tanaka, K.; Takahashi, T.; Kondo, T.; Umeda, K.; Ema, K.; Umebayashi, T.; Asai, K.; Uchida, K.; Miura, N. *Japanese Journal of Applied Physics* **2005**, *44*, 5923.
- [191] Snaith, H. J. *The Journal of Physical Chemistry Letters* **2013**, *4*, 3623–3630.



- [192] Jeon, N. J.; Noh, J. H.; Yang, W. S.; Kim, Y. C.; Ryu, S.; Seo, J.; Seok, S. I. *Nature* **2015**, *517*, 476–480.
- [193] Edri, E.; Kirmayer, S.; Kulbak, M.; Hodes, G.; Cahen, D. *The Journal of Physical Chemistry Letters* **2014**, *5*, 429–433.
- [194] Zhang, M.; Yu, H.; Lyu, M.; Wang, Q.; Yun, J.-H.; Wang, L. *Chemical Communications* **2014**, *50*, 11727–11730.
- [195] Zhou, H.; Chen, Q.; Li, G.; Luo, S.; Song, T.-b.; Duan, H.-S.; Hong, Z.; You, J.; Liu, Y.; Yang, Y. *Science* **2014**, *345*, 542–546.
- [196] Mosconi, E.; Umari, P.; De Angelis, F. *Journal of Materials Chemistry A* **2015**, –.
- [197] Even, J.; Pedesseau, L.; Katan, C.; Kepenekian, M.; Lauret, J.-S.; Saponi, D.; Deleporte, E. *The Journal of Physical Chemistry C* **2015**, *119*, 10161–10177.
- [198] Butler, K. T.; Frost, J. M.; Walsh, A. *Materials Horizons* **2015**, *2*, 228–231.
- [199] Umari, P.; Mosconi, E.; De Angelis, F. *Scientific Reports* **2014**, *4*, 4467.
- [200] Vurgaftman, I.; Meyer, J. R.; Ram-Mohan, L. R. *Journal of Applied Physics* **2001**, *89*, 5815–5875.
- [201] Du, M. H. *Journal of Materials Chemistry A* **2014**, *2*, 9091–9098.
- [202] Menéndez-Proupin, E.; Palacios, P.; Wahnón, P.; Conesa, J. *Physical Review B* **2014**, *90*, 045207.
- [203] Chang, Y.; Park, C.; Matsuishi, K. *Journal-Korean Physical Society* **2004**, *44*, 889–893.
- [204] Giorgi, G.; Fujisawa, J.-I.; Segawa, H.; Yamashita, K. *The Journal of Physical Chemistry Letters* **2013**, *4*, 4213–4216.
- [205] Feng, J.; Xiao, B. *The Journal of Physical Chemistry Letters* **2014**, *5*, 1278–1282.
- [206] Even, J.; Pedesseau, L.; Jancu, J.-M.; Katan, C. *Physica Status Solidi (RRL)-Rapid Research Letters* **2014**, *8*, 31–35.
- [207] Yin, W.-J.; Shi, T.; Yan, Y. *Advanced Materials* **2014**, *26*, 4653–4658.
- [208] He, Y.; Galli, G. *Chemistry of Materials* **2014**, *26*, 5394–5400.
- [209] Geng, W.; Zhang, L.; Zhang, Y.-N.; Lau, W.-M.; Liu, L.-M. *The Journal of Physical Chemistry C* **2014**, *118*, 19565–19571.
- [210] Brivio, F.; Butler, K. T.; Walsh, A.; van Schilfgaarde, M. *Physical Review B* **2014**, *89*, 155204.
- [211] Stoumpos, C. C.; Malliakas, C. D.; Kanatzidis, M. G. *Inorganic Chemistry* **2013**, *52*, 9019–9038.

## Bibliography

---

- [212] MATLAB, *version 7.10.0 (R2010a)*; The MathWorks Inc.: Natick, Massachusetts, 2010.
- [213] Harrison, W. A. *Solid State Theory*; Courier Corporation, 1970.
- [214] Noel, N. K.; Stranks, S. D.; Abate, A.; Wehrenfennig, C.; Guarnera, S.; Haghighirad, A.-A.; Sadhanala, A.; Eperon, G. E.; Pathak, S. K.; Johnston, M. B. *Energy & Environmental Science* **2014**, 7, 3061–3068.
- [215] Feng, J.; Xiao, B. *The Journal of Physical Chemistry C* **2014**, 118, 19655–19660.
- [216] Feng, J.; Xiao, B. *The Journal of Physical Chemistry Letters* **2014**, 5, 1719–1720.
- [217] Yu, P. Y.; Cardona, M. *Fundamentals of Semiconductors*; Springer, 1996.
- [218] Hautier, G.; Miglio, A.; Ceder, G.; Rignanese, G.-M.; Gonze, X. *Nature communications* **2013**, 4.
- [219] Kumar, M. H.; Dharani, S.; Leong, W. L.; Boix, P. P.; Prabhakar, R. R.; Baikie, T.; Shi, C.; Ding, H.; Ramesh, R.; Asta, M. *Advanced Materials* **2014**, 26, 7122–7127.
- [220] Shi, D.; Adinolfi, V.; Comin, R.; Yuan, M.; Alarousu, E.; Buin, A.; Chen, Y.; Hoogland, S.; Rothenberger, A.; Katsiev, K. *Science* **2015**, 347, 519–522.
- [221] IMEC, Module perovskites with 11% efficiency. 2015; <http://phys.org/news/2015-07-perovskite-photovoltaic-module-percent-conversion.html>.
- [222] Yin, J.; Cao, J.; He, X.; Yuan, S.; Sun, S.; Li, J.; Zheng, N.; Lin, L. *Journal of Materials Chemistry A* **2015**,
- [223] Liu, S.; Zheng, F.; Koocher, N. Z.; Takenaka, H.; Wang, F.; Rappe, A. M. *The Journal of Physical Chemistry Letters* **2015**, 6, 693–699.
- [224] Frost, J. M.; Butler, K. T.; Walsh, A. *Apl Materials* **2014**, 2, 081506.

# **Appendices**



## **A Tables for Chapter 4**

## Appendix A. Tables for Chapter 4

Atom types	Parameters		
Zn	$R_{vdW} = 1.10, \varepsilon = 0.0125$		
CD=CC=CF=CN	$R_{vdW} = 1.908, \varepsilon = 0.086$		
DU	$R_{vdW} = 1.5, \varepsilon = 0.0$		
NP=NO	$R_{vdW} = , \varepsilon = ,$		
Bonds	Parameters	Bonds	Parameters
ZN-NP	$r_{ij} = 2.02, k_r = 50.0$	DU-CC	$r_{ij} = 1.39, k_r = 0.0$
ZN-NO	$r_{ij} = 2.02, k_r = 50.0$	DU-CA	$r_{ij} = 1.40, k_r = 0.0$
NP-CC	$r_{ij} = 1.42, k_r = 316.0$	CF-H4	$r_{ij} = 1.08, k_r = 367.0$
NO-CC	$r_{ij} = 1.42, k_r = 316.0$	CA-H4	$r_{ij} = 1.08, k_r = 367.0$
CC-CB	$r_{ij} = 1.50, k_r = 273.0$	CA-CA	$r_{ij} = 1.41, k_r = 469.0$
CC-CD	$r_{ij} = 1.42, k_r = 391.0$	CF-CA	$r_{ij} = 1.41, k_r = 469.0$
CB-CB	$r_{ij} = 1.39, k_r = 418.0$	CN-CA	$r_{ij} = 1.41, k_r = 469.0$
CB-HC	$r_{ij} = 1.07, k_r = 367.0$	CA-C	$r_{ij} = 1.52, k_r = 469.0$
CA-OS	$r_{ij} = 1.37, k_r = 470.0$	C-OH	$r_{ij} = 1.36, k_r = 450.0$
CD-CA	$r_{ij} = 1.52, k_r = 270.0$	C-O2	$r_{ij} = 1.24, k_r = 656.0$
CD-N2	$r_{ij} = 1.46, k_r = 340.0$	OH-HO	$r_{ij} = 1.02, k_r = 553.0$
CZ-CD	$r_{ij} = 1.42, k_r = 273.0$	CT-OS	$r_{ij} = 1.46, k_r = 320.0$
CZ-CN	$r_{ij} = 1.42, k_r = 273.0$	CT-CA	$r_{ij} = 1.54, k_r = 317.0$
CZ-CZ	$r_{ij} = 1.25, k_r = 600.0$	N2-CA	$r_{ij} = 1.43, k_r = 481.0$
DU-DU	$r_{ij} = 4.04, k_r = 0.0$	CT-HC	$r_{ij} = 1.10, k_r = 340.0$
Angles	Parameters	Angles	Parameters
CD-DU-DU	$K_\theta = 0.00 \theta_{eq} = 180.000$	CC-NO-CC	$K_\theta = 70.00 \theta_{eq} = 105.400$
CN-DU-DU	$K_\theta = 0.00 \theta_{eq} = 180.000$	CC-CB-CB	$K_\theta = 70.00 \theta_{eq} = 107.000$
CN-CA-H4	$K_\theta = 50.0 \theta_{eq} = 120.000$	CC-CD-CC	$K_\theta = 70.00 \theta_{eq} = 124.100$
DU-CD-CC	$K_\theta = 0.00 \theta_{eq} = 117.530$	CB-CC-CD	$K_\theta = 70.00 \theta_{eq} = 125.400$
CC-DU-CD	$K_\theta = 0.00 \theta_{eq} = 42.460$	CC-CB-CT	$K_\theta = 70.00 \theta_{eq} = 124.900$
DU-CC-CD	$K_\theta = 0.00 \theta_{eq} = 20.160$	CB-CB-CT	$K_\theta = 70.00 \theta_{eq} = 128.200$
CA-CN-CA	$K_\theta = 63.0 \theta_{eq} = 120.000$	CC-CD-HC	$K_\theta = 30.00 \theta_{eq} = 118.000$
CA-CA-CN	$K_\theta = 63.0 \theta_{eq} = 120.000$	CB-CT-HC	$K_\theta = 35.00 \theta_{eq} = 109.500$
CN-CA-DU	$K_\theta = 0.00 \theta_{eq} = 20.160$	CB-CT-CT	$K_\theta = 63.00 \theta_{eq} = 114.000$
CA-DU-CN	$K_\theta = 0.00 \theta_{eq} = 42.460$	OS-CT-HC	$K_\theta = 60.00 \theta_{eq} = 111.200$
DU-CN-CA	$K_\theta = 0.00 \theta_{eq} = 117.530$	CC-CB-HC	$K_\theta = 50.00 \theta_{eq} = 109.500$
CN-CZ-CZ	$K_\theta = 80.0 \theta_{eq} = 179.650$	CB-CB-HC	$K_\theta = 50.00 \theta_{eq} = 109.500$
CZ-CN-DU	$K_\theta = 0.00 \theta_{eq} = 0.000$	OH-C-O2	$K_\theta = 80.00 \theta_{eq} = 121.260$
CZ-CD-DU	$K_\theta = 0.00 \theta_{eq} = 0.000$	CA-OS-CT	$K_\theta = 60.00 \theta_{eq} = 117.960$
CA-DU-CA	$K_\theta = 0.00 \theta_{eq} = 84.920$	CA-CA-OS	$K_\theta = 80.00 \theta_{eq} = 123.850$
CC-DU-CC	$K_\theta = 0.00 \theta_{eq} = 84.920$	CA-CD-CC	$K_\theta = 63.00 \theta_{eq} = 117.140$
CA-CA-DU	$K_\theta = 0.00 \theta_{eq} = 139.360$	CD-CA-CA	$K_\theta = 63.00 \theta_{eq} = 120.890$

---

H4-CA-DU	$K_\theta = 0.00 \theta_{eq} = 100.650$	CA-N2-CA	$K_\theta = 50.00 \theta_{eq} = 122.110$
NP-CC-DU	$K_\theta = 0.00 \theta_{eq} = 125.500$	N2-CD-CC	$K_\theta = 70.00 \theta_{eq} = 116.640$
CC-DU-DU	$K_\theta = 0.00 \theta_{eq} = 117.260$	N2-CA-CA	$K_\theta = 70.00 \theta_{eq} = 121.170$
CB-CC-DU	$K_\theta = 0.00 \theta_{eq} = 125.400$	CD-N2-CA	$K_\theta = 70.00 \theta_{eq} = 118.590$
NO-CC-DU	$K_\theta = 0.00 \theta_{eq} = 125.500$	CC-CD-CA	$K_\theta = 70.00 \theta_{eq} = 117.260$
CC-DU-DU	$K_\theta = 0.00 \theta_{eq} = 117.260$	CC-CD-N2	$K_\theta = 70.00 \theta_{eq} = 116.640$
CD-CC-DU	$K_\theta = 0.00 \theta_{eq} = 0.000$	CZ-CD-CC	$K_\theta = 63.00 \theta_{eq} = 117.070$
CA-DU-DU	$K_\theta = 0.00 \theta_{eq} = 117.260$	CZ-CZ-CD	$K_\theta = 80.00 \theta_{eq} = 179.680$
CA-CN-CZ	$K_\theta = 63.00 \theta_{eq} = 120.330$	CA-CA-CZ	$K_\theta = 63.00 \theta_{eq} = 120.330$
NP-ZN-NP	$K_\theta = 0.00 \theta_{eq} = 90.000$	CA-CZ-CZ	$K_\theta = 80.00 \theta_{eq} = 179.650$
NO-ZN-NO	$K_\theta = 0.00 \theta_{eq} = 90.000$	CA-C-O2	$K_\theta = 70.00 \theta_{eq} = 124.780$
NO-ZN-NP	$K_\theta = 50.00 \theta_{eq} = 90.000$	CA-CF-H4	$K_\theta = 50.00 \theta_{eq} = 120.000$
ZN-NP-CC	$K_\theta = 30.00 \theta_{eq} = 127.400$	CF-CA-OS	$K_\theta = 80.00 \theta_{eq} = 123.850$
ZN-NO-CC	$K_\theta = 30.00 \theta_{eq} = 127.400$	CF-CA-H4	$K_\theta = 50.00 \theta_{eq} = 120.000$
NO-CC-CB	$K_\theta = 70.00 \theta_{eq} = 110.300$	CA-CF-CA	$K_\theta = 63.00 \theta_{eq} = 120.000$
NP-CC-CB	$K_\theta = 70.00 \theta_{eq} = 110.300$	CF-CA-CF	$K_\theta = 63.00 \theta_{eq} = 120.000$
NO-CC-CD	$K_\theta = 70.00 \theta_{eq} = 125.500$	CA-CA-H4	$K_\theta = 50.00 \theta_{eq} = 120.000$
NP-CC-CD	$K_\theta = 70.00 \theta_{eq} = 125.500$	CA-CA-CA	$K_\theta = 63.00 \theta_{eq} = 120.000$
CC-NP-CC	$K_\theta = 70.00 \theta_{eq} = 105.400$	CA-CA-CF	$K_\theta = 63.00 \theta_{eq} = 120.000$

---

Dihedrals

---

X -CN-CZ-X	$IDIVF = 1, \frac{V}{2} = 0.000,$	$\gamma = 180.000,$	$PN = 2.000$
CN-CZ-CZ-X	$IDIVF = 1, \frac{V}{2} = 0.000,$	$\gamma = 180.000,$	$PN = 2.000$
X -CC-DU-X	$IDIVF = 1, \frac{V}{2} = 0.000,$	$\gamma = 180.000,$	$PN = 2.000$
X -CA-DU-X	$IDIVF = 1, \frac{V}{2} = 0.000,$	$\gamma = 180.000,$	$PN = 2.000$
X -CN-DU-X	$IDIVF = 1, \frac{V}{2} = 0.000,$	$\gamma = 180.000,$	$PN = 2.000$
X -NO-ZN-X	$IDIVF = 1, \frac{V}{2} = 0.000,$	$\gamma = 180.000,$	$PN = 2.000$
X -NP-ZN-X	$IDIVF = 1, \frac{V}{2} = 0.000,$	$\gamma = 180.000,$	$PN = 2.000$
X -NO-CC-X	$IDIVF = 4, \frac{V}{2} = 5.700,$	$\gamma = 180.000,$	$PN = 2.000$
X -NP-CC-X	$IDIVF = 4, \frac{V}{2} = 5.700,$	$\gamma = 180.000,$	$PN = 2.000$
X -CC-CB-X	$IDIVF = 4, \frac{V}{2} = 3.150,$	$\gamma = 180.000,$	$PN = 2.000$
X -CB-CB-X	$IDIVF = 4, \frac{V}{2} = 21.500,$	$\gamma = 180.000,$	$PN = 2.000$
X -CD-CC-X	$IDIVF = 4, \frac{V}{2} = 7.900,$	$\gamma = 180.000,$	$PN = 2.000$
X -CB-CT-X	$IDIVF = 1, \frac{V}{2} = 0.000,$	$\gamma = 180.000,$	$PN = 2.000$
X -CA-CA-X	$IDIVF = 4, \frac{V}{2} = 14.500,$	$\gamma = 180.000,$	$PN = 2.000$
X -CA-CN-X	$IDIVF = 4, \frac{V}{2} = 14.500,$	$\gamma = 180.000,$	$PN = 2.000$
CA-CA-CD-CC	$IDIVF = 1, \frac{V}{2} = 5.000,$	$\gamma = 10.000,$	$PN = 2.000$
CA-DU-DU-CC	$IDIVF = 1, \frac{V}{2} = 1.200,$	$\gamma = 180.000,$	$PN = 2.000$
CZ-CZ-CD-CC	$IDIVF = 1, \frac{V}{2} = 0.000,$	$\gamma = 0.000,$	$PN = 1.000$
CA-CN-CZ-CZ	$IDIVF = 1, \frac{V}{2} = 0.000,$	$\gamma = 0.000,$	$PN = 1.000$
CT-OS-CA-CA	$IDIVF = 1, \frac{V}{2} = 32.970,$	$\gamma = 0.000,$	$PN = 1.000$
CC-CD-N2-CA	$IDIVF = 1, \frac{V}{2} = 0.360,$	$\gamma = 160.000,$	$PN = 2.000$

## Appendix A. Tables for Chapter 4

CA-CZ-CZ-CD	$IDIVF = 1, \frac{V}{2} = 0.000,$	$\gamma = 0.000,$	$PN = 1.000$
CF-CA-OS-CT	$IDIVF = 1, \frac{V}{2} = 0.000,$	$\gamma = 0.000,$	$PN = 1.000$
X-CA-CF-X	$IDIVF = 4, \frac{V}{2} = 14.500,$	$\gamma = 180.000,$	$PN = 2.000$
Improper dihedrals			
CA-CZ-CN-CA	$IDIVF = 0, \frac{V}{2} = 1.000$	$\gamma = 180.000,$	$PN = 2.000$
CA-C-CA-CA	$IDIVF = 0, \frac{V}{2} = 1.000$	$\gamma = 180.000,$	$PN = 2.000$
X-X-CC-X	$IDIVF = 0, \frac{V}{2} = 1.000$	$\gamma = 180.000,$	$PN = 2.000$
X-X-CB-X	$IDIVF = 0, \frac{V}{2} = 1.000$	$\gamma = 180.000,$	$PN = 2.000$
X-X-NP-X	$IDIVF = 0, \frac{V}{2} = 1.000$	$\gamma = 180.000,$	$PN = 2.000$
X-X-NO-X	$IDIVF = 0, \frac{V}{2} = 1.000$	$\gamma = 180.000,$	$PN = 2.000$
CA-OS-CA-CA	$IDIVF = 0, \frac{V}{2} = 1.000$	$\gamma = 180.000,$	$PN = 2.000$

Table A.1: Force field parameters implemented in this work for YD2-o-C8.

Atom types	Parameters		
CO	$R_{vdW} = 2.900, \epsilon = 0.5600$		
N5	$R_{vdW} = 1.8240, \epsilon = 0.1700$		
N6	$R_{vdW} = 1.8240, \epsilon = 0.1700$		
N7	$R_{vdW} = 1.8240, \epsilon = 0.1700$		
N8	$R_{vdW} = 1.8240, \epsilon = 0.1700$		
N0	$R_{vdW} = 1.8240, \epsilon = 0.1700$		
N9	$R_{vdW} = 1.8240, \epsilon = 0.1700$		
HA	$R_{vdW} = 1.4590, \epsilon = 0.0150$		
CA	$R_{vdW} = 1.9080, \epsilon = 0.0860$		
Bonds	Parameters	Bonds	Parameters
CO-N5	$r_{ij} = 283.4, k_r = 2.07$	CA-N6	$r_{ij} = 427.0, k_r = 1.381$
CO-N6	$r_{ij} = 283.4, k_r = 2.07$	CA-N7	$r_{ij} = 427.0, k_r = 1.381$
CO-N7	$r_{ij} = 283.4, k_r = 2.07$	CA-N8	$r_{ij} = 427.0, k_r = 1.381$
CO-N8	$r_{ij} = 283.4, k_r = 2.07$	CA-N0	$r_{ij} = 427.0, k_r = 1.381$
CO-N9	$r_{ij} = 283.4, k_r = 2.07$	CA-N9	$r_{ij} = 427.0, k_r = 1.381$
CO-N0	$r_{ij} = 283.4, k_r = 2.07$	CA-CA	$r_{ij} = 469.0, k_r = 1.400$
CA-N5	$r_{ij} = 427.0, k_r = 1.381$	CA-HA	$r_{ij} = 367.0, k_r = 1.080$
Angles	Parameters	Angles	Parameters
N0-CO-N7	$K_\theta = 80.0, \theta_{eq} = 180.00$	CO-N9-CA	$K_\theta = 50.0, \theta_{eq} = 120.00$
N0-CO-N5	$K_\theta = 80.0, \theta_{eq} = 90.00$	CA-N5-CA	$K_\theta = 70.7, \theta_{eq} = 109.95$
N0-CO-N8	$K_\theta = 80.0, \theta_{eq} = 90.00$	CA-N6-CA	$K_\theta = 70.7, \theta_{eq} = 109.95$
N0-CO-N5	$K_\theta = 80.0, \theta_{eq} = 90.00$	CA-N7-CA	$K_\theta = 70.7, \theta_{eq} = 109.95$
N0-CO-N6	$K_\theta = 80.0, \theta_{eq} = 90.00$	CA-N8-CA	$K_\theta = 70.7, \theta_{eq} = 109.95$



---

N9-CO-N8	$K_\theta = 80.0, \theta_{eq} = 90.00$	CA-N9-CA	$K_\theta = 70.7, \theta_{eq} = 109.95$
N9-CO-N7	$K_\theta = 80.0, \theta_{eq} = 90.00$	CA-N0-CA	$K_\theta = 70.7, \theta_{eq} = 109.95$
N9-CO-N5	$K_\theta = 80.0, \theta_{eq} = 90.00$	N5-CA-HA	$K_\theta = 52.4, \theta_{eq} = 120.40$
N9-CO-N8	$K_\theta = 80.0, \theta_{eq} = 90.00$	N6-CA-HA	$K_\theta = 52.4, \theta_{eq} = 120.40$
N9-CO-N5	$K_\theta = 80.0, \theta_{eq} = 90.00$	N7-CA-HA	$K_\theta = 52.4, \theta_{eq} = 120.40$
N9-CO-N6	$K_\theta = 80.0, \theta_{eq} = 180.00$	N8-CA-HA	$K_\theta = 52.4, \theta_{eq} = 120.40$
N5-CO-N6	$K_\theta = 80.0, \theta_{eq} = 90.00$	N9-CA-HA	$K_\theta = 52.4, \theta_{eq} = 120.40$
N5-CO-N7	$K_\theta = 80.0, \theta_{eq} = 90.00$	N0-CA-HA	$K_\theta = 52.4, \theta_{eq} = 120.40$
N6-CO-N8	$K_\theta = 80.0, \theta_{eq} = 90.00$	N5-CA-CA	$K_\theta = 70.1, \theta_{eq} = 119.72$
N6-CO-N7	$K_\theta = 80.0, \theta_{eq} = 90.00$	N6-CA-CA	$K_\theta = 70.1, \theta_{eq} = 119.72$
N7-CO-N8	$K_\theta = 80.0, \theta_{eq} = 90.00$	N7-CA-CA	$K_\theta = 70.1, \theta_{eq} = 119.72$
N5-CO-N8	$K_\theta = 90.0, \theta_{eq} = 180.00$	N8-CA-CA	$K_\theta = 70.1, \theta_{eq} = 119.72$
CO-N6-CA	$K_\theta = 50.0, \theta_{eq} = 120.00$	N0-CA-CA	$K_\theta = 70.1, \theta_{eq} = 119.72$
CO-N7-CA	$K_\theta = 50.0, \theta_{eq} = 120.00$	N9-CA-CA	$K_\theta = 70.1, \theta_{eq} = 119.72$
CO-N8-CA	$K_\theta = 50.0, \theta_{eq} = 120.00$	CA-CA-CA	$K_\theta = 67.2, \theta_{eq} = 119.970$
CO-N5-CA	$K_\theta = 50.0, \theta_{eq} = 120.00$	CA-CA-HA	$K_\theta = 50.3, \theta_{eq} = 119.700$

---

Dihedrals

---

N7-CA-CA-N8	$IDIVF = 1, \frac{V}{2} = 3.625,$	$\gamma = 180.000,$	$PN = 2.$
N5-CA-CA-N6	$IDIVF = 1, \frac{V}{2} = 3.625,$	$\gamma = 180.000,$	$PN = 2.$
N0-CA-CA-N9	$IDIVF = 1, \frac{V}{2} = 3.625,$	$\gamma = 180.000,$	$PN = 2.$
X-CO-X-CA	$IDIVF = 1, \frac{V}{2} = 5.0,$	$\gamma = 180.000,$	$PN = 4.$
N0-CO-N7-CA	$IDIVF = 1, \frac{V}{2} = 1.000,$	$\gamma = 60.000,$	$PN = 0.$
N0-CO-N8-CA	$IDIVF = 1, \frac{V}{2} = 1.000,$	$\gamma = 60.000,$	$PN = 0.$
N0-CO-N6-CA	$IDIVF = 1, \frac{V}{2} = 1.000,$	$\gamma = 60.000,$	$PN = 0.$
N0-CO-N9-CA	$IDIVF = 1, \frac{V}{2} = 1.000,$	$\gamma = 60.000,$	$PN = 0.$
N0-CO-N5-CA	$IDIVF = 1, \frac{V}{2} = 1.000,$	$\gamma = 60.000,$	$PN = 0.$
N9-CO-N7-CA	$IDIVF = 1, \frac{V}{2} = 1.000,$	$\gamma = 60.000,$	$PN = 0.$
N9-CO-N8-CA	$IDIVF = 1, \frac{V}{2} = 1.000,$	$\gamma = 60.000,$	$PN = 0.$
N9-CO-N0-CA	$IDIVF = 1, \frac{V}{2} = 1.000,$	$\gamma = 60.000,$	$PN = 0.$
N9-CO-N6-CA	$IDIVF = 1, \frac{V}{2} = 1.000,$	$\gamma = 60.000,$	$PN = 0.$
N9-CO-N5-CA	$IDIVF = 1, \frac{V}{2} = 1.000,$	$\gamma = 60.000,$	$PN = 0.$
N5-CO-N6-CA	$IDIVF = 1, \frac{V}{2} = 1.000,$	$\gamma = 60.000,$	$PN = 0.$
N5-CO-N7-CA	$IDIVF = 1, \frac{V}{2} = 1.000,$	$\gamma = 60.000,$	$PN = 0.$
N5-CO-N8-CA	$IDIVF = 1, \frac{V}{2} = 1.000,$	$\gamma = 60.000,$	$PN = 0.$
N5-CO-N0-CA	$IDIVF = 1, \frac{V}{2} = 1.000,$	$\gamma = 60.000,$	$PN = 0.$
N5-CO-N9-CA	$IDIVF = 1, \frac{V}{2} = 1.000,$	$\gamma = 60.000,$	$PN = 0.$
N6-CO-N5-CA	$IDIVF = 1, \frac{V}{2} = 1.000,$	$\gamma = 60.000,$	$PN = 0.$
N6-CO-N7-CA	$IDIVF = 1, \frac{V}{2} = 1.000,$	$\gamma = 60.000,$	$PN = 0.$
N6-CO-N8-CA	$IDIVF = 1, \frac{V}{2} = 1.000,$	$\gamma = 60.000,$	$PN = 0.$
N6-CO-N0-CA	$IDIVF = 1, \frac{V}{2} = 1.000,$	$\gamma = 60.000,$	$PN = 0.$
N6-CO-N9-CA	$IDIVF = 1, \frac{V}{2} = 1.000,$	$\gamma = 60.000,$	$PN = 0.$

**Appendix A. Tables for Chapter 4**

---

N7-CO-N5-CA	$IDIVF = 1, \frac{V}{2} = 1.000,$	$\gamma = 60.000,$	$PN = 0.$
N7-CO-N6-CA	$IDIVF = 1, \frac{V}{2} = 1.000,$	$\gamma = 60.000,$	$PN = 0.$
N7-CO-N8-CA	$IDIVF = 1, \frac{V}{2} = 1.000,$	$\gamma = 60.000,$	$PN = 0.$
N7-CO-N0-CA	$IDIVF = 1, \frac{V}{2} = 1.000,$	$\gamma = 60.000,$	$PN = 0.$
N7-CO-N9-CA	$IDIVF = 1, \frac{V}{2} = 1.000,$	$\gamma = 60.000,$	$PN = 0.$
N8-CO-N5-CA	$IDIVF = 1, \frac{V}{2} = 1.000,$	$\gamma = 60.000,$	$PN = 0.$
N8-CO-N6-CA	$IDIVF = 1, \frac{V}{2} = 1.000,$	$\gamma = 60.000,$	$PN = 0.$
N8-CO-N7-CA	$IDIVF = 1, \frac{V}{2} = 1.000,$	$\gamma = 60.000,$	$PN = 0.$
N8-CO-N0-CA	$IDIVF = 1, \frac{V}{2} = 1.000,$	$\gamma = 60.000,$	$PN = 0.$
N8-CO-N9-CA	$IDIVF = 1, \frac{V}{2} = 1.000,$	$\gamma = 60.000,$	$PN = 0.$
CA-CA-N6-CO	$IDIVF = 1, \frac{V}{2} = 1.000,$	$\gamma = 180.000,$	$PN = 0.$
CA-CA-N5-CO	$IDIVF = 1, \frac{V}{2} = 1.000,$	$\gamma = 180.000,$	$PN = 0.$
CA-CA-N7-CO	$IDIVF = 1, \frac{V}{2} = 1.000,$	$\gamma = 180.000,$	$PN = 0.$
CA-CA-N8-CO	$IDIVF = 1, \frac{V}{2} = 1.000,$	$\gamma = 180.000,$	$PN = 0.$
CA-CA-N0-CO	$IDIVF = 1, \frac{V}{2} = 1.000,$	$\gamma = 180.000,$	$PN = 0.$
CA-CA-N9-CO	$IDIVF = 1, \frac{V}{2} = 1.000,$	$\gamma = 180.000,$	$PN = 0.$
HA-CA-N6-CO	$IDIVF = 1, \frac{V}{2} = 1.000,$	$\gamma = 0.000,$	$PN = 0.$
HA-CA-N5-CO	$IDIVF = 1, \frac{V}{2} = 1.000,$	$\gamma = 0.000,$	$PN = 0.$
HA-CA-N7-CO	$IDIVF = 1, \frac{V}{2} = 1.000,$	$\gamma = 0.000,$	$PN = 0.$
HA-CA-N8-CO	$IDIVF = 1, \frac{V}{2} = 1.000,$	$\gamma = 0.000,$	$PN = 0.$
HA-CA-N0-CO	$IDIVF = 1, \frac{V}{2} = 1.000,$	$\gamma = 0.000,$	$PN = 0.$
HA-CA-N9-CO	$IDIVF = 1, \frac{V}{2} = 1.000,$	$\gamma = 0.000,$	$PN = 0.$
CA-CA-CA-N5	$IDIVF = 1, \frac{V}{2} = 3.625,$	$\gamma = 180.000,$	$PN = 2.$
CA-CA-CA-N7	$IDIVF = 1, \frac{V}{2} = 3.625,$	$\gamma = 180.000,$	$PN = 2.$
CA-CA-CA-N8	$IDIVF = 1, \frac{V}{2} = 3.625,$	$\gamma = 180.000,$	$PN = 2.$
CA-CA-CA-N6	$IDIVF = 1, \frac{V}{2} = 3.625,$	$\gamma = 180.000,$	$PN = 2.$
CA-CA-CA-N0	$IDIVF = 1, \frac{V}{2} = 3.625,$	$\gamma = 180.000,$	$PN = 2.$
CA-CA-CA-N9	$IDIVF = 1, \frac{V}{2} = 3.625,$	$\gamma = 180.000,$	$PN = 2.$
CA-N5-CA-CA	$IDIVF = 1, \frac{V}{2} = 4.800,$	$\gamma = 180.000,$	$PN = 2.$
CA-N6-CA-CA	$IDIVF = 1, \frac{V}{2} = 4.800,$	$\gamma = 180.000,$	$PN = 2.$
CA-N7-CA-CA	$IDIVF = 1, \frac{V}{2} = 4.800,$	$\gamma = 180.000,$	$PN = 2.$
CA-N8-CA-CA	$IDIVF = 1, \frac{V}{2} = 4.800,$	$\gamma = 180.000,$	$PN = 2.$
CA-N0-CA-CA	$IDIVF = 1, \frac{V}{2} = 4.800,$	$\gamma = 180.000,$	$PN = 2.$
CA-N9-CA-CA	$IDIVF = 1, \frac{V}{2} = 4.800,$	$\gamma = 180.000,$	$PN = 2.$
CA-N6-CA-HA	$IDIVF = 1, \frac{V}{2} = 4.150,$	$\gamma = 180.000,$	$PN = 2.$
CA-N5-CA-HA	$IDIVF = 1, \frac{V}{2} = 4.150,$	$\gamma = 180.000,$	$PN = 2.$
CA-N7-CA-HA	$IDIVF = 1, \frac{V}{2} = 4.150,$	$\gamma = 180.000,$	$PN = 2.$
CA-N8-CA-HA	$IDIVF = 1, \frac{V}{2} = 4.150,$	$\gamma = 180.000,$	$PN = 2.$
CA-N0-CA-HA	$IDIVF = 1, \frac{V}{2} = 4.150,$	$\gamma = 180.000,$	$PN = 2.$
CA-N9-CA-HA	$IDIVF = 1, \frac{V}{2} = 4.150,$	$\gamma = 180.000,$	$PN = 2.$
N5-CA-CA-HA	$IDIVF = 1, \frac{V}{2} = 6.650,$	$\gamma = 180.0,$	$PN = 2.$
N6-CA-CA-HA	$IDIVF = 1, \frac{V}{2} = 6.650,$	$\gamma = 180.0,$	$PN = 2.$

N7-CA-CA-HA	$IDIVF = 1, \frac{V}{2} = 6.650,$	$\gamma = 180.0,$	$PN = 2.$
N8-CA-CA-HA	$IDIVF = 1, \frac{V}{2} = 6.650,$	$\gamma = 180.0,$	$PN = 2.$
N0-CA-CA-HA	$IDIVF = 1, \frac{V}{2} = 6.650,$	$\gamma = 180.0,$	$PN = 2.$
N9-CA-CA-HA	$IDIVF = 1, \frac{V}{2} = 6.650,$	$\gamma = 180.0,$	$PN = 2.$
CA-CA-CA-CA	$IDIVF = 1, \frac{V}{2} = 3.625,$	$\gamma = 180.0,$	$PN = 2.$
CA-CA-CA-HA	$IDIVF = 1, \frac{V}{2} = 6.650,$	$\gamma = 180.0,$	$PN = 2.$
HA-CA-CA-HA	$IDIVF = 1, \frac{V}{2} = 6.650,$	$\gamma = 180.0,$	$PN = 2.$
Improper dihedrals			
CA-N5-CA-CA	$IDIVF = 0, \frac{V}{2} = 1.1,$	$\gamma = 180. ,$	$PN = 2.$
CA-N6-CA-CA	$IDIVF = 0, \frac{V}{2} = 1.1,$	$\gamma = 180. ,$	$PN = 2.$
CA-N7-CA-CA	$IDIVF = 0, \frac{V}{2} = 1.1,$	$\gamma = 180. ,$	$PN = 2.$
CA-N8-CA-CA	$IDIVF = 0, \frac{V}{2} = 1.1,$	$\gamma = 180. ,$	$PN = 2.$
CA-N0-CA-CA	$IDIVF = 0, \frac{V}{2} = 1.1,$	$\gamma = 180. ,$	$PN = 2.$
CA-N9-CA-CA	$IDIVF = 0, \frac{V}{2} = 1.1,$	$\gamma = 180. ,$	$PN = 2.$
CA-CA-CA-HA	$IDIVF = 0, \frac{V}{2} = 1.1,$	$\gamma = 180. ,$	$PN = 2.$
CA-N5-CA-HA	$IDIVF = 0, \frac{V}{2} = 1.1,$	$\gamma = 180. ,$	$PN = 2.$
CA-N6-CA-HA	$IDIVF = 0, \frac{V}{2} = 1.1,$	$\gamma = 180. ,$	$PN = 2.$
CA-N7-CA-HA	$IDIVF = 0, \frac{V}{2} = 1.1,$	$\gamma = 180. ,$	$PN = 2.$
CA-N8-CA-HA	$IDIVF = 0, \frac{V}{2} = 1.1,$	$\gamma = 180. ,$	$PN = 2.$
CA-N0-CA-HA	$IDIVF = 0, \frac{V}{2} = 1.1,$	$\gamma = 180. ,$	$PN = 2.$
CA-N9-CA-HA	$IDIVF = 0, \frac{V}{2} = 1.1,$	$\gamma = 180. ,$	$PN = 2.$

Table A.2: Force field parameters implemented in this work for the cobalt bipyridine complex.



## **B** Band diagrams for Chapter 7

Systematic variations in CsSnI<sub>3</sub>: Figures (B.1, B.2, B.3, B.4, B.5, B.6, B.7, B.8, B.9, B.10, B.11 and B.12)

## Appendix B. Band diagrams for Chapter 7

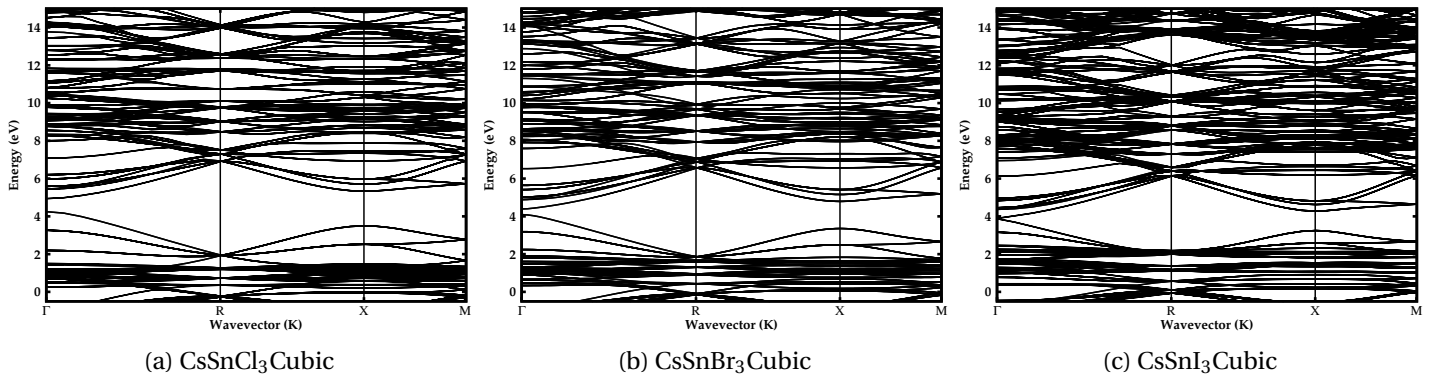


Figure B.1: Sn-Cubic structures

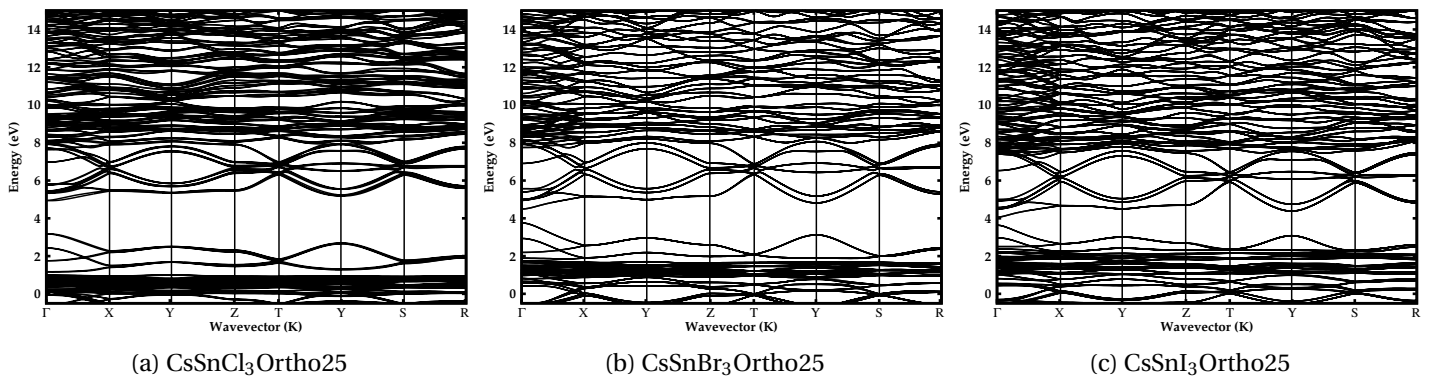


Figure B.2: Sn-Ortho25 structures

### B.1 Effect of doping

Effect of doping in the band structure for Sr dopant with and without oxygen in Figures B.15a, B.13b, B.14c, B.13e, B.13d

## B.1. Effect of doping

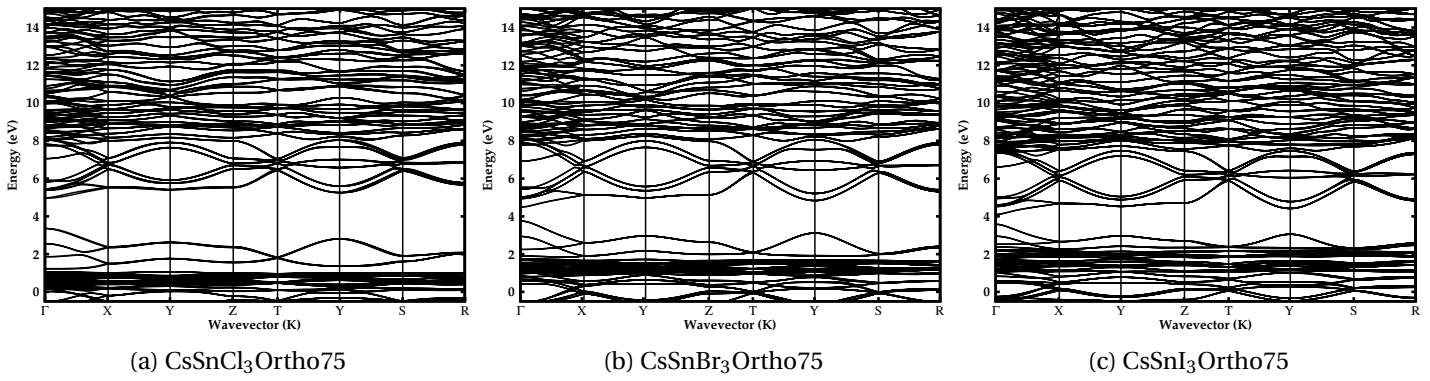


Figure B.3: Sn-Ortho75 structures

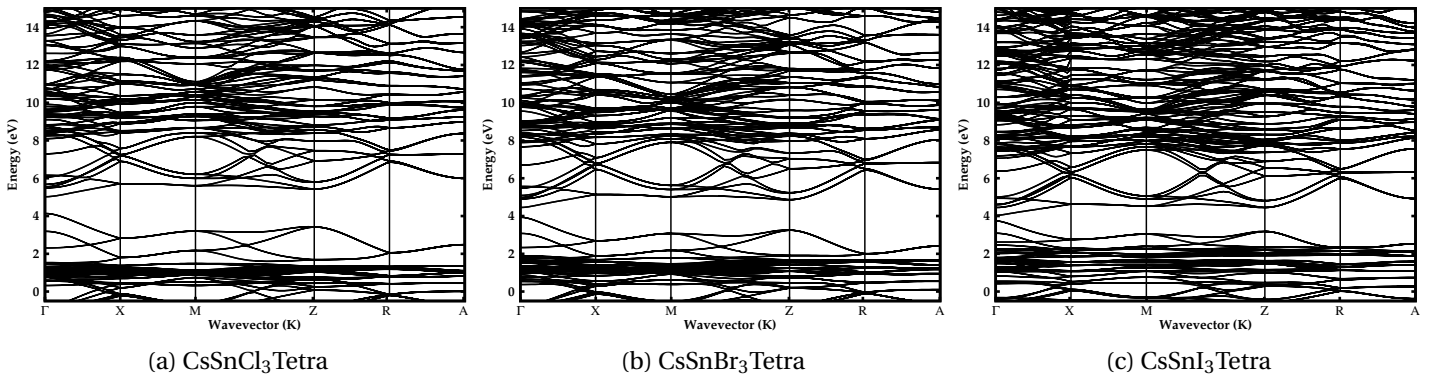


Figure B.4: Sn-Tetra structures

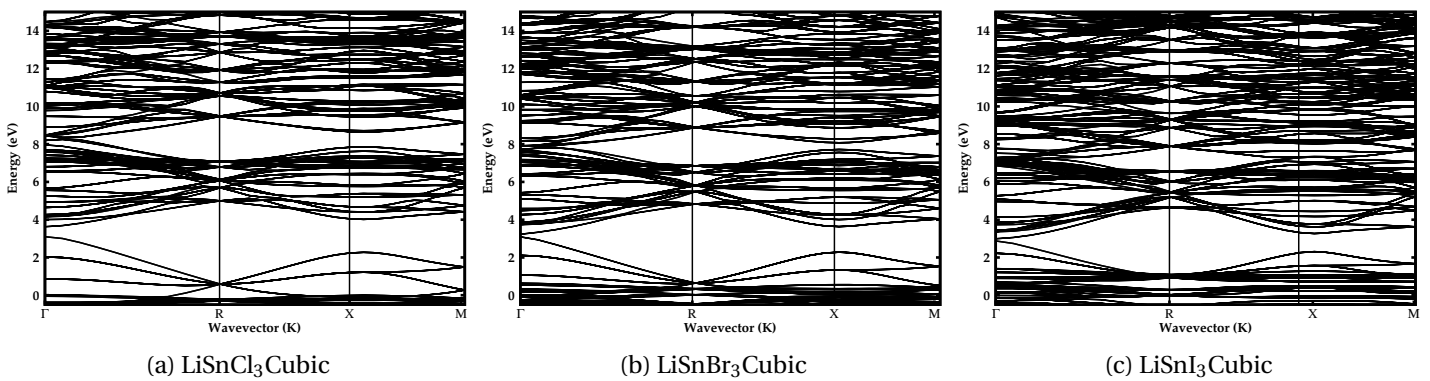


Figure B.5: Sn-Cubic structures

## Appendix B. Band diagrams for Chapter 7

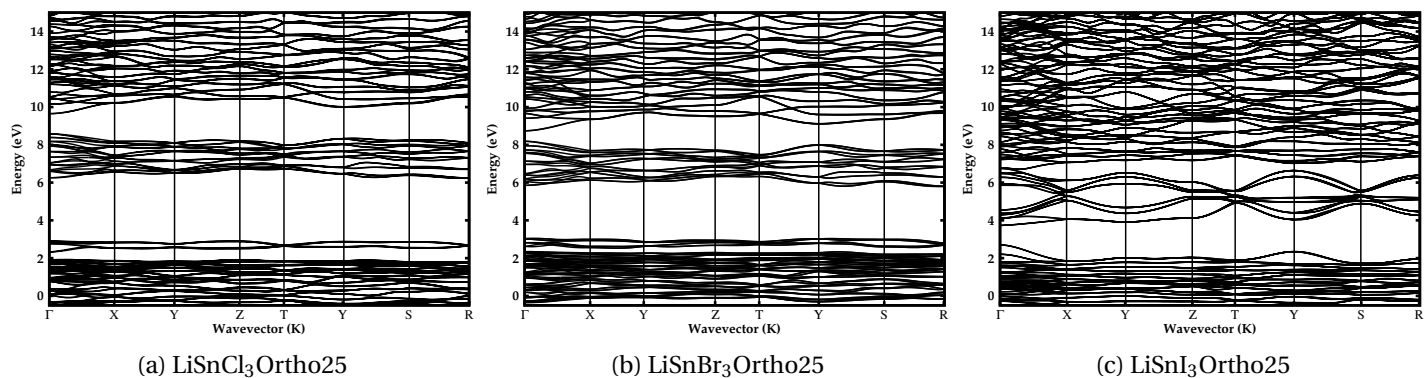


Figure B.6: Sn-Ortho25 structures

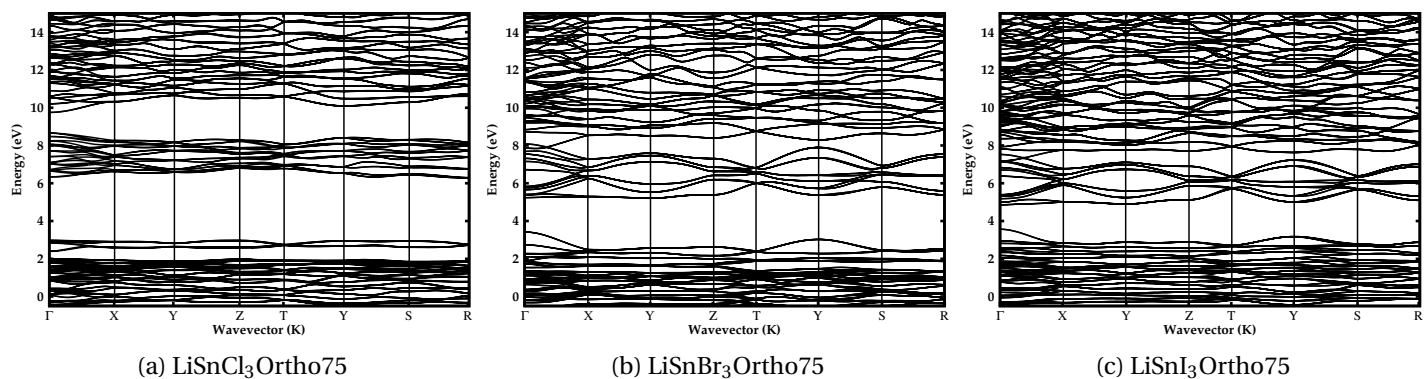


Figure B.7: Sn-Ortho75 structures

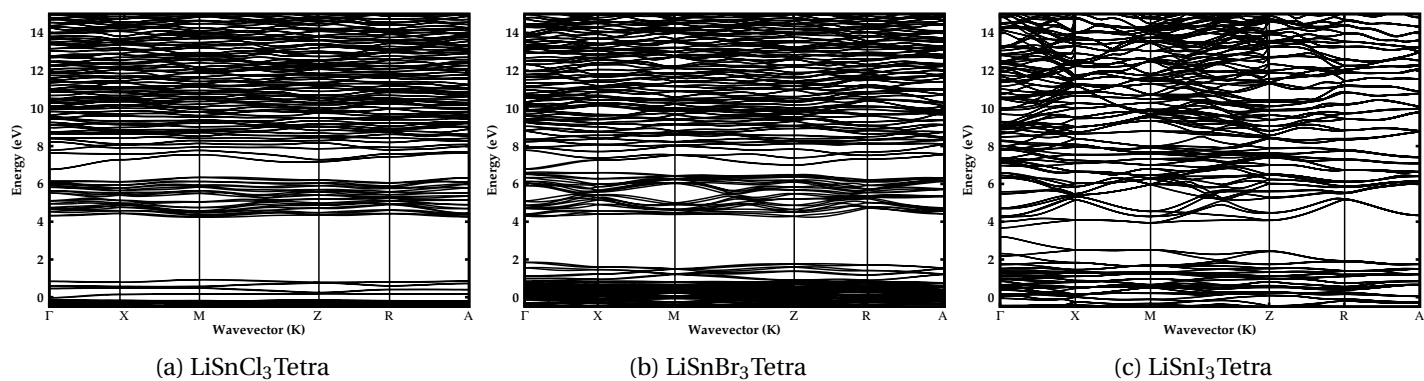


Figure B.8: Sn-Tetra structures



## B.1. Effect of doping

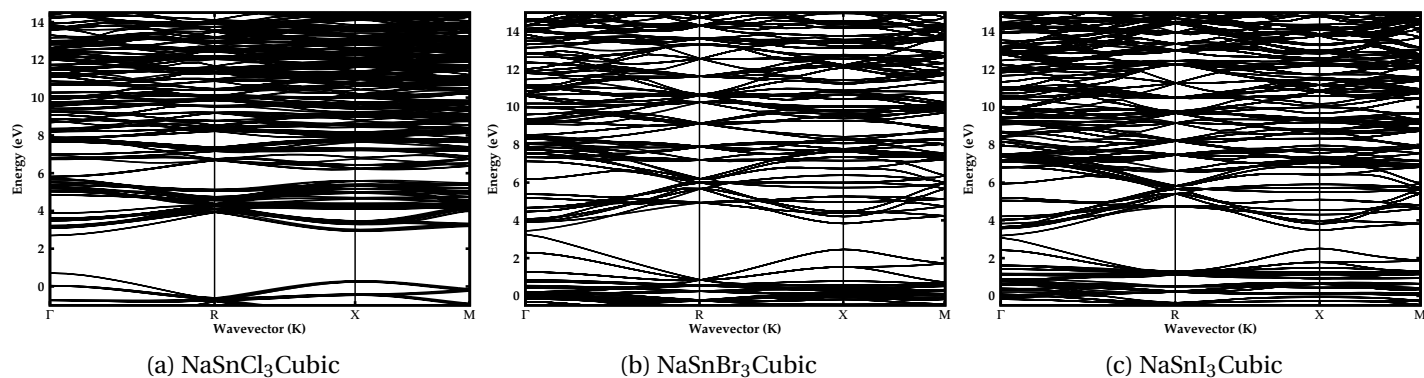


Figure B.9: Sn-Cubic structures

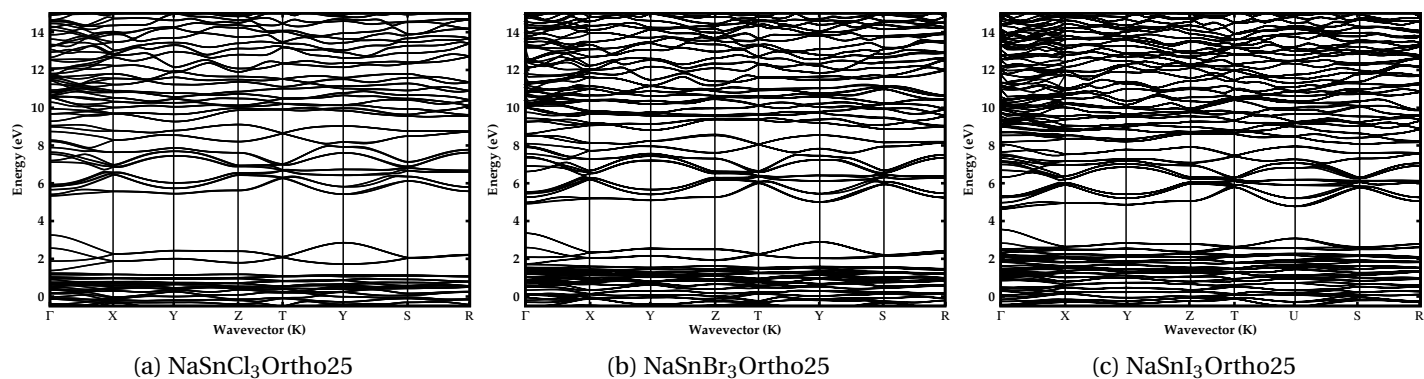


Figure B.10: Sn-Ortho25 structures

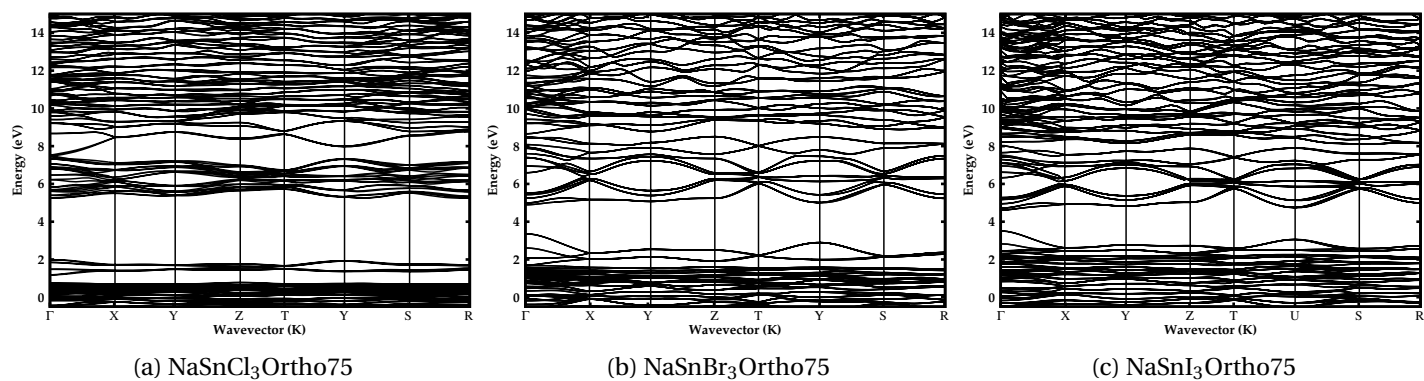
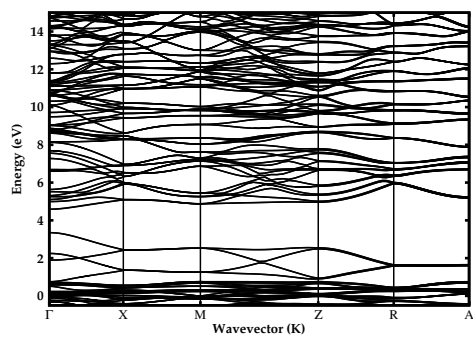


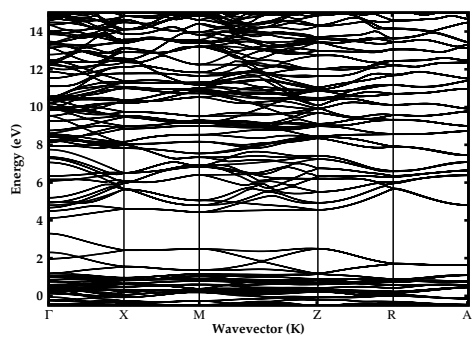
Figure B.11: Sn-Ortho75 structures

## Appendix B. Band diagrams for Chapter 7

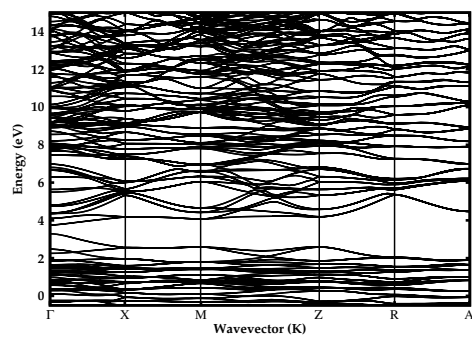
---



(a) NaSnCl<sub>3</sub> Tetra



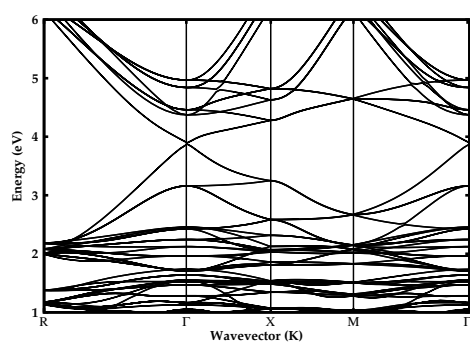
(b) NaSnBr<sub>3</sub> Tetra



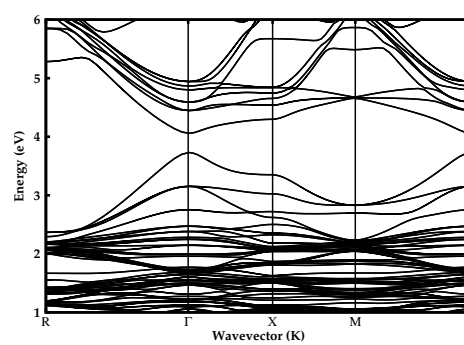
(c) NaSnI<sub>3</sub> Tetra

Figure B.12: Sn-Tetra structures

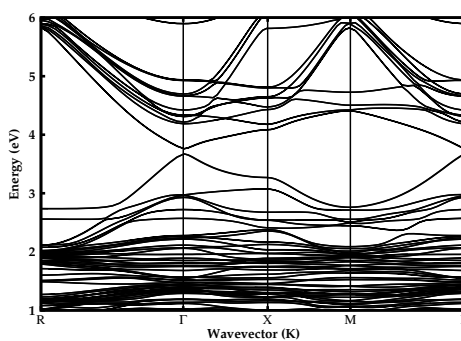
## B.1. Effect of doping



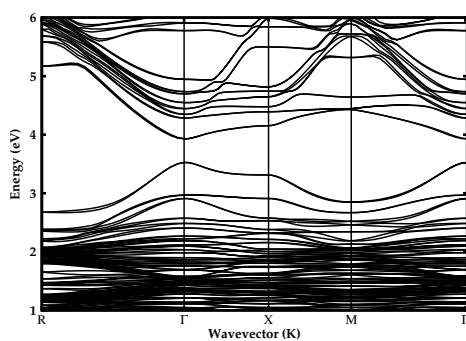
(a) Pure  $\text{CsSnI}_3$



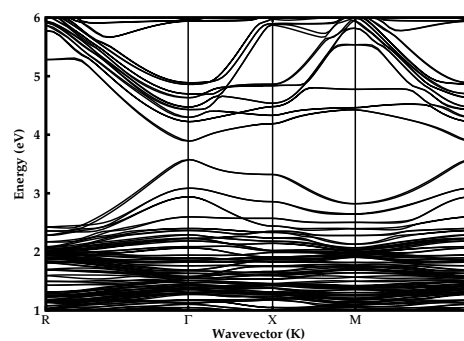
(b) Sr-doped  $\text{CsSnI}_3$



(c) Oxide  $\text{CsSnI}_3$



(d) Sr-doped oxide  $\text{CsSnI}_3$ , O connected to Sn



(e) Sr-doped oxide  $\text{CsSnI}_3$ , O connected to Sr

Figure B.13: Effect of Sr dopant on band structure

Appendix B. Band diagrams for Chapter 7

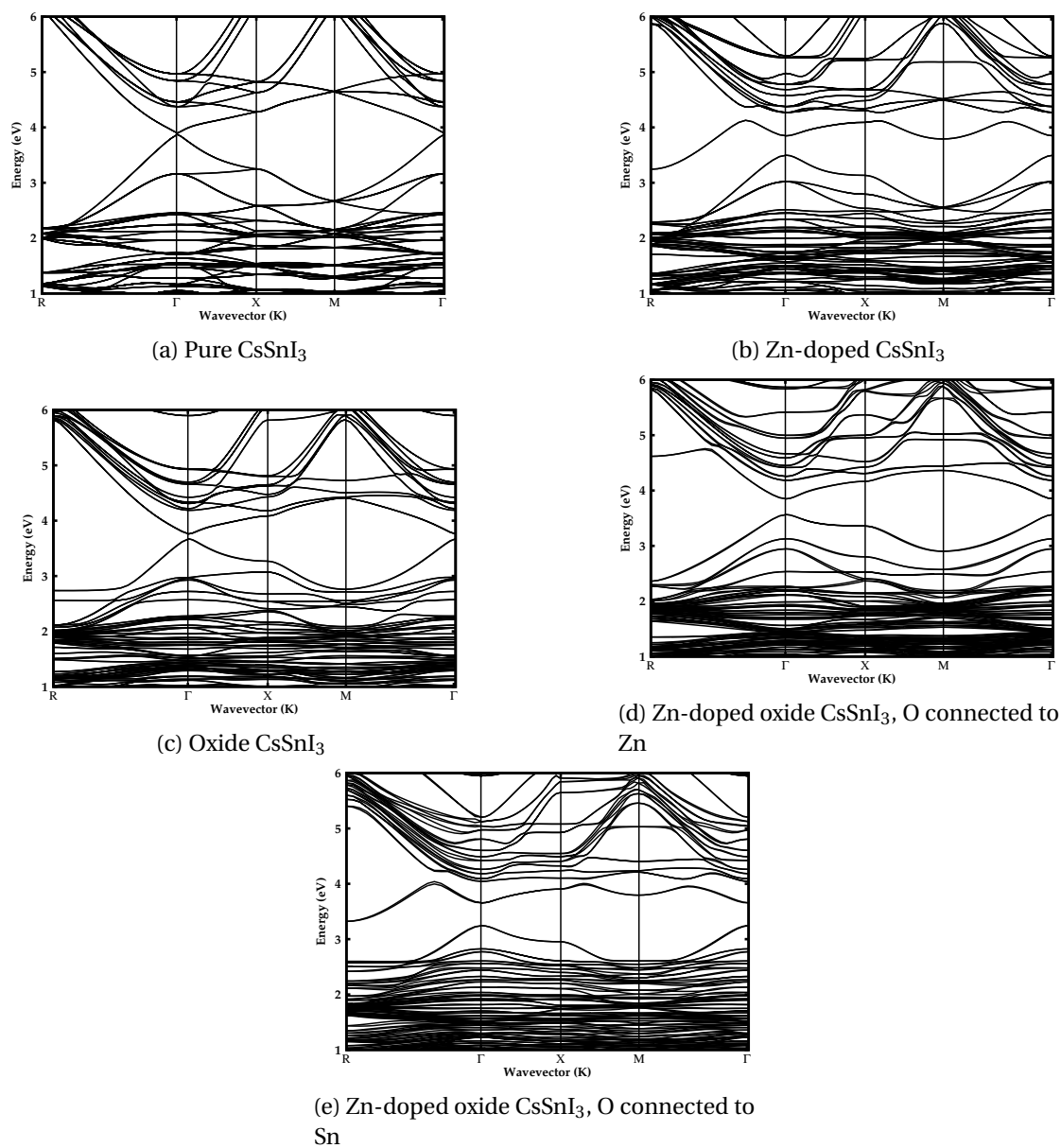
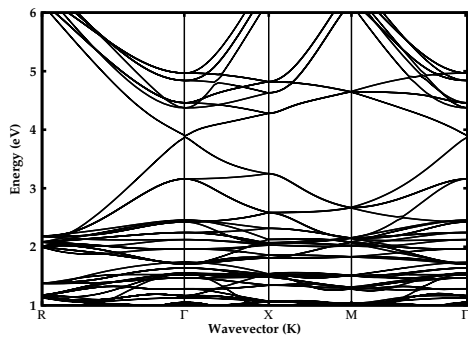
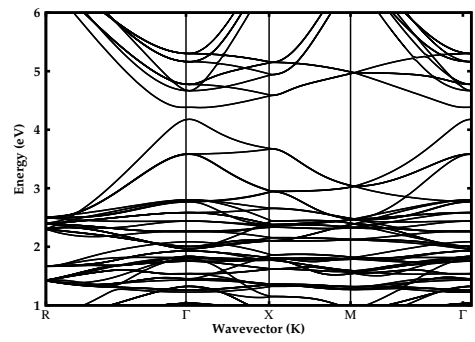


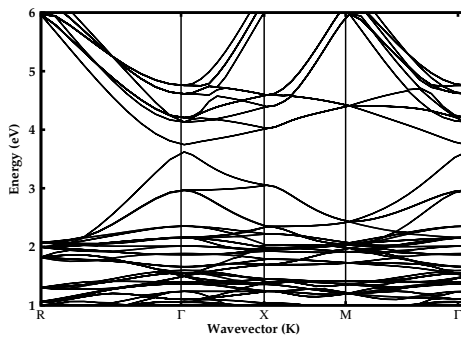
Figure B.14: Effect of Zn(II) dopant on band structure



(a) Pure CsSnI<sub>3</sub>



(b) Charge defect (Sn4+) in CsSnI<sub>3</sub>



(c) Charge defect (Sn16+) in CsSnI<sub>3</sub>

Figure B.15: Charge defects

## Appendix B. Band diagrams for Chapter 7

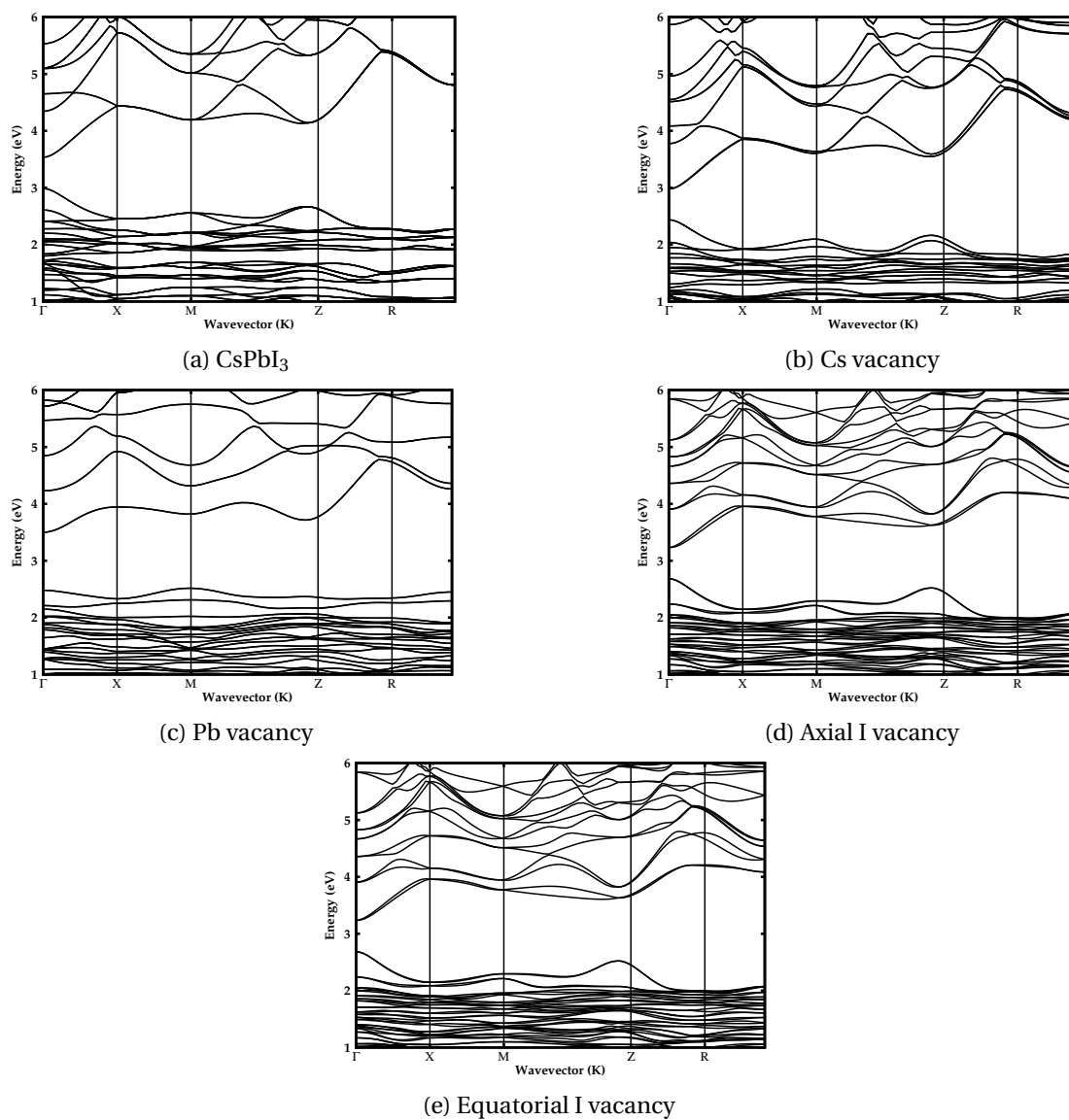
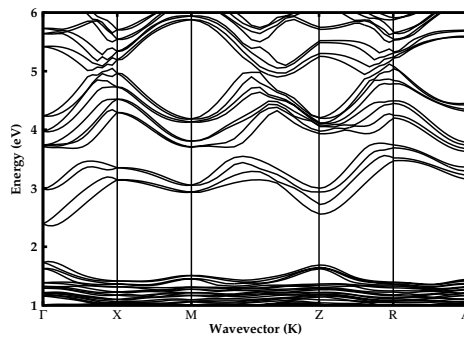
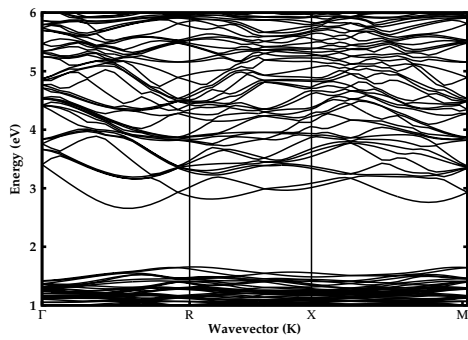


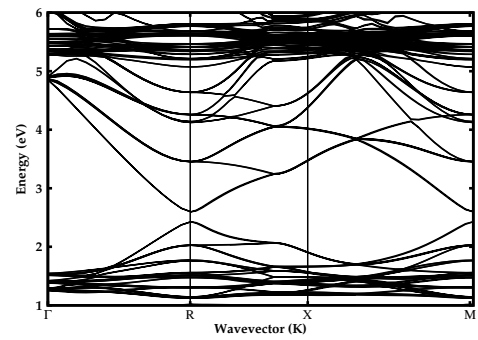
Figure B.16: Vacancy defects in CsPbI<sub>3</sub>



(a)  $\text{CH}_3\text{NH}_3\text{PbI}_3$



(b)  $\text{NH}_4\text{PbI}_3$



(c)  $\text{PH}_4\text{PbI}_3$

Figure B.17: Band diagrams of organic monovalent cation perovskites





## C Tight-binding formulation for simple cubic crystal of Na atoms (linear combination of s orbitals)

The expectation value of the energy:

$$\psi = \sum_j c_j \psi_t(r - r_j) \quad (\text{C.1})$$

$$T\psi(r) = e^{-ik \cdot T} \psi(r) \quad (\text{C.2})$$

$$\psi_{k,t} = \frac{1}{\sqrt{N}} \sum_j \psi(r - r_j) e^{-ik \cdot r_j} \quad (\text{C.3})$$

$$\langle E \rangle = \frac{\int \psi_{k,t}^*(r) [-(\hbar^2/2m)\nabla^2 + V(r)] \psi_{k,t}(r) d\tau}{\int \psi_{k,t}^*(r) \psi_{k,t}(r) d\tau} \quad (\text{C.4})$$

$$\left[-\frac{\hbar^2}{2m}\nabla^2 + v(r - r_j)\right] \psi_t(r - r_j) = \epsilon_t \psi_t(r - r_j) \quad (\text{C.5})$$

$$\left(-\frac{\hbar^2}{2m}\nabla^2 + V\right) \psi_{k,t} = \frac{1}{\sqrt{N}} \sum_j [\epsilon_t + \sum_{i \neq j} v(r - r_j)] \psi_t(r - r_j) e^{-ik \cdot r_j} \quad (\text{C.6})$$

$$\langle E \rangle = \epsilon_t + \frac{1/N \sum_{j,t} e^{-ik \cdot (r_j - r_l)} \int \psi_t^*(r - r_l) \sum_{i \neq j} v(r - r_i) \psi_t(r - r_j) d\tau}{\int \psi_{k,t}^* \psi_{k,t} d\tau} \quad (\text{C.7})$$

For the simple cubic case where the band is only composed of s orbitals, the  $k$ -dependent terms would have the following format:

$$\lambda = \int \psi_t^*(\mathbf{r} - \mathbf{r}_i) v(\mathbf{r} - \mathbf{r}_i) \psi_t(\mathbf{r}) d\tau \quad (\text{C.8})$$

$$\lambda \sum e^{-ik \cdot r_i} = 2\lambda (\cos k_x a + \cos k_y a + \cos k_z a) \quad (\text{C.9})$$

$$= 6\lambda + \frac{\hbar^2 k^2}{2m^*} + \dots \quad (\text{C.10})$$

$$\frac{m^*}{m} = -\frac{1}{\lambda} \frac{\hbar^2 (1/a)^2}{2m} \quad (\text{C.11})$$



## Negar Ashari-Astani



---

<b>CONTACT INFORMATION</b>	36, Av. d'Echallens 1004 Lausanne Switzerland	0788864643 negar.ashariastani@epfl.ch
<b>SUMMARY</b>	<b>Computational chemist (QM, MM, QM/MM), working on dye sensitized and perovskite solar cells in close contact with experimentalists, Organizer of conferences, love teaching, Great passion for our environment</b>	
<b>RESEARCH INTERESTS</b>	Green chemistry (solar cells), Classical and ab initio molecular dynamics, Time dependent density functional theory, Solid state physics, Dye-sensitized solar cells, Thermodynamic integration molecular dynamics, Photochemistry.	
<b>EDUCATION</b>	<b>EPFL</b> , École Polytechnique Fédérale de Lausanne  Ph.D., <b>LABORATORY OF COMPUTATIONAL CHEMISTRY AND BIOCHEMISTRY</b> , <i>Expected:</i> March 2015 <ul style="list-style-type: none"><li>• Thesis Topic: <i>Rational computational design of Dye Sensitized and Perovskite based solar cells</i></li><li>• Advisor: Ursula Röthlisberger</li></ul> Minor., <b>LABORATORY OF COMPUTATIONAL CHEMISTRY AND BIOCHEMISTRY</b> , 2010-2011 <ul style="list-style-type: none"><li>• Topic: <i>Computational Chemistry</i></li></ul> <b>Amirkabir University of Technology</b> , Iran  M.S., <b>EXTRACTIVE METALLURGY LABORATORY</b> <i>Received:</i> October 2009 <ul style="list-style-type: none"><li>• Thesis Topic: <i>Molecular Dynamics simulation of potential distribution along electrochemical cells</i></li><li>• Advisor: Seyed Hadi Tabaian</li></ul> B.S., <b>FINITE ELEMENT SIMULATIONS LABORATORY</b> <i>Received:</i> October 2007 <ul style="list-style-type: none"><li>• Thesis Topic: <i>Effect of thermal fatigue on cast Iron GGG25</i></li><li>• Advisor: Seyed Mohammad Mirbagheri</li></ul>	
<b>AWARDS</b>	Computational grant <ul style="list-style-type: none"><li>• HPC-Europa2: Pan-European Research Infrastructure for High Performance Computing grant in University of Edinburgh, Scotland Summer 2011</li></ul> Teaching award <ul style="list-style-type: none"><li>• EPFL: La prime spéciale pour prestations d'une valeur exceptionnelle dans l'enseignement October 2014</li></ul>	

**EXPERIENCES**

- Holding conferences** 2014  
Organizer of the first Computational chemistry and biochemistry conference in Iran, IPM  
Invited speakers: Michele Parinello, Ursula Roethlisberger, Paolo Carloni, Matteo Dalperaro, Maria Ramos Task: Organizer
- Project mentor** 2012-2014  
Mentored 3 undergraduate semester students. Task: Mentor
- Research Assistant** 2008-2009  
Lab. of Statics and Strengths of the Materials  
Amirkabir University of Technology  
Supervisor: Morteza Naderpour Task: Teaching, Making exercises
- Trainee** 2010  
Lab. of Computational chemistry and Biochemistry  
EPFL  
Supervisor: Ursula Röethlisberger

**TEACHING  
EXPERIENCE**

- Teaching Assistant Falls 2011-2012  
Electronic structural methods  
Instructor: Ursula Röthlisberger  
Computational chemistry,  
EPFL
- Teaching Assistant Springs 2012-2013  
Molecular dynamics and Monte Carlo simulations  
Instructor: Ursula Röthlisberger  
Computational chemistry,  
EPFL
- Co-instructor Fall 2009-2010  
Statics and strength of materials  
with Morteza Naderpour  
Material Science,  
Amirkabir University of Technology

**PUBLISHED  
JOURNAL  
PUBLICATIONS**

- Mathew, S.; Yella, A.; Gao, P.; Humphry-Baker, R.; Curchod, B. F. E.; **Ashari-Astani, N.**; Tavernelli, I.; Rothlisberger, U.; Nazeeruddin, Md. K.; Grätzel, M. "Dye-Sensitized Solar Cells with 13% Efficiency Achieved Through the Molecular Engineering of Porphyrin Sensitizers" *Nature Chem.* (2014), 6, 242-247;
- K. Voitchovsky, **N. Ashari-Astani**, I. Tavernelli, B. Curchod, N. Ttreault, U. Rothlisberger, F. Stellacci, M. Grätzel, H. A. Harms "In-situ mapping of the molecular arrangement of amphiphilic dye molecules at the TiO<sub>2</sub> surface of dye sensitized solar cells." *ACS Applied Materials & Interfaces* (2015).
- E. Bozkurt, **N. Ashari**, N. Browning, E. Brunk, P. Campomanes, M. A. S. Perez, U. Röthlisberger. "Lessons from Nature: Computational Design of Biomimetic Compounds and Processes" *Chimia*, (2014), 68, 642-647 ;
- Yella, A.; Humphry-Baker, R.; Curchod, B. F. E.; **Ashari-Astani, N. S.**; Teuscher, J.; Polander, L. E.; Mathew, S.; Moser, J.-E.; Tavernelli, I.; Röthlisberger, U.; Grätzel, M.; Nazeeruddin, M. K.; Frey, J. "Molecular Engineering of a Fluorene Donor for Dye-Sensitized Solar Cells" *Chem. Mater.* (2013), 25, 2733-2739;
- Polander, L. E.; Yella, A.; Teuscher, J.; Humphry-Baker, R.; Curchod, B. F. E.; **Ashari Astani, N.**; Gao, P.; Moser, J.-E.; Tavernelli, I.; Röthlisberger, U.; Grätzel, M.; Nazeeruddin, M. K.; Frey, J. *Chem. Mater.* (2013), 25, 2642;

6. L. E. Polander, A. Yella, B. F. E. Curchod, A. **N. Ashari-Astani**, J. Teuscher, R. Scopelliti, P. Gao, S. Mathew, J.-E. Moser, I. Tavernelli, U. R othlisberger, M. Gr atzel, M. K. Nazeeruddin, J. Frey. "Unraveling the Potential for Dithienopyrrole Sensitizers in Dye-Sensitized Solar Cells" *Angew. Chem. Int. Ed.* (2013), 52, 87318735;
7. E. Brunk, **N. Ashari**, P. Athri, P. Campomanes, F.F. de Carvalho, B.F.E. Curchod, P. Diamantis, M. Doemer, J. Garrec, A. Laktionov, M. Micciarelli, M. Neri, G. Palermo, T.J. Penfold, S. Vanni, I. Tavernelli and U. Rothlisberger "Pushing the frontiers of first-principles based computer simulations of chemical and biological systems" *Chimia*, (2011), 65, 667-671;
8. S. Meloni, G. Palermo, **N. Ashari Astani**, B. F.E. Curchod, Michael Graetzel, U. Roethlisberger. "Valence and conduction bands engineering in halide perovskites for solar cell applications" (2014) *arXiv:1412.3659* [cond-mat.mtrl-sci]
9. S. M. H. Mirbagheri, M. Bari, **N. Ashari Astani**. "Thermal fatigue mechanism in the GG25 Gray Iron" , *Journal of school of engineering* , (2010).
10. **N. Ashari Astani**, G. Ackland. " A comparison between electrical field screening efficiency of two most famous couple redoxes used in Gratzel cells" *Journal of hpc-europa* 78 (2010).

COMPLETE PAPERS  
IN SUBMISSION  
PROCESS

1. S. Mathew, **N. Ashari Astani**, B. Curchod, U. R othlisberger, M. Gra tzel. "Synthesis and Characterization of a UllazinePorphyrin Dyad and investigation as a photosensitizer in Dye-Sensitized Solar Cells". (Complete and in the process of submission to EES (RSC))
2. E. Brunk, **N. Ashari-Astani**, U. R othlisberger. "Making use of solvent effects to tune carbocation regioselectivity".(Complete and in the process of submission to Angw.)
3. **N. Ashari Astani**, B. F.E. Curchod, S. Mathew, C. Yi, G. Palermo, I. Tavernelli, M. Gra tzel, U. R othlisberger. "A theoretical review on porphyrin-based sensitizers All the way up to 13% efficiency" (Complete and in the process of submission to Phy. Chem.)
4. **N. Ashari-Astani**, Simone Meloni, Amir Hesam Salavati, Giulia Palermo, M. Gra tzel, U. R othlisberger. "Classical description of electron and hole transportation in halide perovskites" (Complete, Journal not decided yet)
5. **N. Ashari Astani**, E. Brunk, B. Curchod, I. Tavernelli, U. R othlisberger. "Classical molecular dynamics simulation of porphyrin-based dye-sensitized solar cells".

ONGOING  
PROJECTS AND  
CORRESPONDING  
PAPERS IN  
PREPARATION

1. C. Yi, **N. Ashari Astani**, B. Curchod, I. Tavernelli, U. R othlisberger, M. Gra tzel. "Y789, the porphyrin-based dye with 12,7% efficiency"
2. **N. Ashari Astani**, A. Boziki, M. Gra tzel, U. R othlisberger. "Halide perovskites phase diagram: a classical polarizable force-field approach"
3. **N. Ashari Astani**, S. Meloni, U. R othlisberger. "Investigation of hydrated  $TiO_2$  anatase (101) surface"
4. **N. Ashari Astani**, U. R othlisberger. "Crystal structure prediction of perovskites using Meta dynamics approach"
5. Peng Qin, Simone Meloni, **N. Ashari Astani**, Ursula Roethlisberger, Michael Graetzel. "Tin-based Zn and Sr alloy halide perovskites"

## LANGUAGES

- Persian (Farsi): Native
- English: Fluent
- French: Intermediate in reading, beginner in speaking.
- Arabic: Intermediate in reading, beginner in speaking.

## REFERENCES

Ursula Röthlisberger  
Full Professor  
LCBC  
EPFL

Phone: +41 (0)21 693 03 21  
E-mail: ursula.roethlisberger@epfl.ch

Michael Grätzel  
Full Professor  
LPI  
EPFL

Phone: +41 21 69 33112  
E-mail: michael.graetzel@epfl.ch

Simone Meloni  
Post doctoral researcher  
LCBC  
EPFL

Phone: +41 21 69 30328  
E-mail: simone.meloni@epfl.ch